UNIVERSITY OF STRATHCLYDE
DEPARTMENT OF PHYSICS

Self-generated magnetic fields in intense laser-solid interactions relevant to relativistic plasma astrophysics

by

Nicholas Mark Henry Butler

in partial fulfilment of the requirements for the degree of Doctor of Philosophy in Physics

2018

Copyright Declaration

Signed:

Date:

Abstract

This thesis reports on self-generated magnetic fields in ultra-intense laser interactions with dense plasma and the role that these play in the dynamics of relativistic electrons, and, subsequently, ion acceleration. This includes an investigation of resistive magnetic fields generated within solids and their influence on the transport of multi-mega-Ampere currents of energetic electrons. It also includes investigations of magnetic fields in foils expanded to near-critical density, produced by the Biermann battery and Weibel instability mechanisms.

The first part of the thesis explores the transport of relativistic electrons in relatively thick solids, specifically, different allotropes of lithium, silicon and carbon. This is initially explored numerically. Simulations, performed using a three-dimensional hybrid-particle-in-cell codes are used to investigate how the material resistivity-temperature profile affects fast electron transport via self-generated magnetic fields. The degree of lattice order in the material strongly affects electrical resistivity at low temperatures. By considering resistivity-temperature profiles intermediate to those of ordered and disordered arrangements of ions, it is shown that the magnitude and shape of the resistivity-temperature profile at low temperatures strongly affects the growth of self-generated resistive magnetic fields and the onset of resistive transport instabilities. The scaling of these effects to scenarios relevant to the fast ignition scheme for inertial confinement fusion is also discussed. Following this, the influence of the low temperature electrical resistivity on the onset of the resistive filamentation instability is investigated, both experimentally and numerically, in targets consisting of layers of ordered and disordered forms of carbon. It is demonstrated that the thickness of the disordered carbon layer influences the degree of filamentation of the fast electron beam, with strong filamentation produced for thickness of the order of 60 μm or greater. Furthermore, it is also shown that the position of the disordered carbon layer (within the layered target) has a minimal influence on the growth of the resistive

filamentation instability.

The second part of the thesis explores the influence of self-generated magnetic fields on the dynamics of electron motion in ultrathin foil targets expanding to near-critical-density and undergoing relativistic induced transparency. The generation of a plasma jet, supported by a self-generated azimuthal magnetic field is explored. The parameters of the jet and its sensitivity to the experimental parameters are characterised. Following this, the onset of Weibel instability-generated magnetic fields is investigated, as diagnosed by the formation of bubble-like structures in the beam of protons accelerated from the foil. The sensitivity of the Weibel-generated magnetic fields to the decompression of the target is explored. An analysis of the scaling of the relativistic plasma jet is presented, exploring the possibility of employing these laboratory-generated structures as analogues of astrophysical relativistic plasma jet phenomena.

Acknowledgements

The work presented in this thesis is the culmination of over three years of work, including numerous nights spent in the laboratory, countless hours analysing data obtained from experiments and simulations, 22,000 miles on board flights, culminating in a total distance of 86.5% of the circumference of the earth, 3 tattoos (and counting) and a great deal more grey hairs than when I first commenced my studies!

First and foremost, I would like to extend my deepest gratitude to my supervisor, Professor Paul McKenna, without whom the completion of this work would not have been possible. I am extremely grateful to him for providing me with the opportunity to conduct my research within such an enthusiastic, vibrant research group, but for also being the perfect example of a supervisor and a scientist: patient, energetic, enthusiastic and possessing a passion for the discovery of new knowledge. His constant support and guidance have been invaluable.

Next, I would like to thank the people that I've had the pleasure to have worked with over the years. To the colleagues that I had the pleasure of meeting when I commenced this journey, Robbie, Bruno, Ross, Haydn, Harry, Rachel, Martin, David and Remi, I would like to take this opportunity to thank you for welcoming me into the group. Also, for your infectious enthusiasm for science and research, which demonstrated to me that undertaking a PhD is not solely a matter of knowledge and intelligence, but also hard work, passion and drive. In particular I would like to extend my thanks to Dr. Ross Gray and Dr. Martin King: Ross, for his vast depths of experience and knowledge, and experimental nous. He is an exemplary scientist and one of the best experimental physicists I have had the pleasure of working with. And Martin, for his cooperation in obtaining the complex particle-in-cell simulations presented in this these, and his stellar analysis of the results garnered from these. A special mention must be made to Robbie Wilson for being a great peer and friend throughout my PhD, in addition to being an excellent flatmate. A notable

mention must be made to Dr. Bruno Gonzalez-Izquierdo for his extremely helpful Spanish tuition!

I would also like to take this opportunity to express my gratitude to the others that I have had the pleasure of working with: Adam, John, Sam, Zoe, Jonathan, Dean, Chris, Graeme, Ceri and Professor David Neely. Furthermore, I sincerely thank Robbie and Matthew Duff for taking time out of their busy schedules to proof-read this thesis and for their valuable input into the content.

In addition, I would like to acknowledge the staff at both the Central Laser Facility and the PHELIX laser system for their expertise and dedication, without which none of the experimental investigations presented in this thesis would not have been possible. To those I have collaborated with, or had the pleasure of meeting, from outwith Strathclyde - Dr. Ellie Tubman from the University of York, and Reza Mirfayzi and Rory Garland from Queens University Belfast - I would also like to extend my thanks.

A nod to those great friends, old and new, scientists and non-scientists, who provided many a happy distraction to see me through the last year; you know who you are - thank you.

Finally, and most importantly, I would like to extend a heartfelt thank you to my parents Mark and Fiona, brothers Jonny and Stefan, and to my girlfriend, Lauren, for supporting me throughout this journey. It would not have been possible without your support and encouragement, and for that I am forever grateful. Also, Stefan, now you've finished school you can start buying your share of the games on the XBOX!

Role of Author

The results presented in this thesis are the work of the author over several experimental campaigns, performed as part of a team of researchers led by Prof. McKenna. The author had a lead role at each step: experimental planning and execution, data analysis, numerical simulations and interpretation of results. In addition, the author made significant contributions to the preparation of the publications arising from this work.

Chapter 5: The author actively contributed to the planning and execution of the experiment. The proton dosimetry film stacks were designed, assembled and digitised by the author, in addition to the preparation of targetry prior to installation in the target chamber. The author took a leading role in the analysis of all data. The analytical model used to estimate the proton spatial-intensity distributions from the TNSA electric field distribution was based on a code originally written by Dr. M. N. Quinn (University of Strathclyde) and subsequently developed by the author. The calculation of the electrical resistivity of the materials featured was performed by Dr. M. P. Desjarlais (Sandia National Laboratory). The three-dimensional hybrid-PIC simulations were performed by the author and Dr. D. A. Maclellan under the supervision of Dr. A. P. L. Robinson and Prof. P. McKenna.

Chapter 6: The author actively contributed to the planning and execution of the experimental campaign. The two-beam, transverse optical probe diagnostic was designed by Dr. R. J. Gray (University of Strathclyde), with assistance from the author. The diagnostic was assembled by Dr. R. J. Gray and the author. The proton dosimetry film stacks corresponding to the initial investigation were designed and digitised by the author, and were assembled by Mr. S. D. R. Williamson (University of Strathclyde). Targetry was prepared by the author, with assistance from Mr. P. Martin (Queens University Belfast). In the following investigation, the design, assembly and digitisation of the proton dosimetry film diagnostic was performed primarily by Dr. H. W. Powell (University of Strathclyde),

with assistance from Dr. L. C. Stockhausen (CPLU), Dr. D. R. Rusby (Central Laser Facility) and Dr. B. Gonzalez-Izquierdo (University of Strathclyde). The author took a leading role in the analysis of all data. Particle-in-Cell simulations were performed by Dr. M. King (University of Strathclyde) and analysed by the author.

List of publications

Publications directly resulting from the work presented in this thesis

1. **Influence of low-temperature resistivity on fast electron transport in solids: scaling to fast ignition electron beam parameters**
   P. McKenna, D. A. MacLellan, **N. M. H. Butler**, R. J. Dance, R. J. Gray, A. P. L. Robinson, D. Neely, and M. P. Desjarlais, *Plasma Physics and Controlled Fusion*, **57**, 064001 (2015)

2. **Measurement of the angle, temperature and flux of fast electrons emitted from intense laser-solid interactions**
   D. R. Rusby, L. A. Wilson, R. J. Gray, R. J. Dance, **N. M. H. Butler**, D. A. Maclellan, G. G. Scott, V. Bagnoud, B. Zielbauer, P. McKenna and D. Neely, *Journal of Plasma Physics*, **81**, 5 (2015)

3. **Role of lattice structure and low temperature resistivity in fast-electron-beam filamentation in carbon**
   R. J. Dance, **N. M. H. Butler**, R. J. Gray, D. A. MacLellan, D. R. Rusby, G. G. Scott, B. Zielbauer, V. Bagnoud, H. Xu, A. P. L. Robinson, M. P. Desjarlais, D. Neely, and P. McKenna, *Plasma Physics and Controlled Fusion*, **58**, 014027 (2016)

4. **Near-100 MeV protons via a laser-driven transparency-enhanced hybrid acceleration scheme**
   A. Higginson, R. J. Gray, M. King, S. D. R. Williamson, **N. M. H. Butler**, R. Wilson, R. Capdessus, C. Armstrong, J. S. Green, S. J. Hawkes, P. Martin, W. Q. Wei, S. R. Mirfayzi, X. H. Yuan, S. Kar, M. Borghesi, R. J. Clarke, D. Neely and P. McKenna, *Nature Communications*, **9**, 724 (2018)

5. **Escaping electrons from intense laser-solid interactions as a function of laser spot size**

   D. R. Rusby, R. J. Gray, **N. M. H. Butler**, R. J. Dance, G. G. Scott, V. Bagnoud, B. Zielbauer, P. McKenna and D. Neely, *European Physical Journal*, **167**, 02001 (2018)

Additional publications resulting from PhD work

1. **Laser-driven x-ray and neutron source development for industrial applications of plasma accelerators**

   C. M. Brenner, S. R. Mirfayzi, D. R. Rusby, C. Armstrong, A. Alejo, L. A. Wilson, R. Clarke, H. Ahmed, **N. M. H. Butler**, D. Haddock, A. Higginson, A. McClymont, C. D. Murphy, M. Notley, P. Oliver, R. Allott, C. Hernandez-Gomez, S. Kar, P. McKenna and D. Neely, *Plasma Physics and Controlled Fusion*, **58**, 014039 (2016)

2. **Optically controlled dense current structures driven by relativistic plasma aperture-induced diffraction**

   B. Gonzalez-Izquierdo, R. J. Gray, M. King, R. J. Dance, R. Wilson, J. McCreadie, **N. M. H. Butler**, R. Capdessus, S. Hawkes, J. S. Green, M. Borghesi, D. Neely, and P. McKenna, *Nature Physics*, **12**, 505-215 (2016)

3. **Evidence of high-n hollow ion emission from Si ions pumped by ultraintense x-rays from relativistic laser plasma**

   J. Colgan, A. Ya. Faenov, S. A. Pikuz, E. Tubman, **N. M. H. Butler**, J. Abdallah Jr, R. J. Dance, T. A. Pikuz, I. Y. Skobelev, M. A. Alkhimova, N. Booth, J. S. Green, C. D. Gregory, A. Andreev, R. Lotzsch, I. Uschmann, A. Zhidkov, R. Kodama, P. Mckenna, and N. Woolsey, *Europhysics Letters*, **114**, 3 (2016)

4. **Intra-pulse transition between ion acceleration mechanisms in intense laser-foil interactions**

   H. Padda, M. King, R. J. Gray, H. W. Powell, B. Gonzalez-Izquierdo, L. C. Stockhausen, R. Wilson, D. C. Carroll, R. J. Dance, D. A. MacLellan, X. H. Yuan, **N. M. H. Butler**, R. Capdessus, M. Borghesi, D. Neely and P. McKenna, *Physics of Plasmas*, **23**, 063116 (2016)

5. **Towards optical polarization control of laser-driven proton acceleration in foils undergoing relativistic transparency**

B. Gonzalez-Izquierdo, M. King, R. J. Gray, R. Wilson, R. J. Dance, H. W. Powell, D. A. Maclellan, J. McCreadie, **N. M. H. Butler**, S. Hawkes, J. S. Green, C. D. Murphy, L. C. Stockhausen, D. C. Carroll, N. Booth, G. G. Scott, M. Borghesi, D. Neely and P. McKenna, *Nature Communications*, **7** 12891 (2016)

6. **Influence of laser polarization on collective electron dynamics in ultraintense laser-foil interactions**

   B. Gonzalez-Izquierdo, R. J. Gray, M. King, R. Wilson, R. J. Dance, H. W. Powell, D. A. Maclellan, J. McCreadie, **N. M. H. Butler**, S. Hawkes, J. S. Green, C. D. Murphy, L. C. Stockhausen, D. C. Carroll, N. Booth, G. G. Scott, M. Borghesi, D. Neely and P. McKenna, *High Power Laser Science and Engineering*, **4**, 33 (2016)

7. **Detector for imaging and dosimetry of laser-driven epithermal neutrons by alpha conversion**

   S. R. Mirfayzi, A. Alejo, H. Ahmed, L. A. Wilson, S. Ansell, C. Armstrong, **N. M. H. Butler**, R. Clarke, A. Higginson, M. Notley, D. Raspino, D. R. Rusby, M. Borghesi, N. Rhodes, P. McKenna, D. Neely, C. M. Brenner, and S. Kar, *Journal of Instrumentation*, **11** C10008 (2016)

8. **Pulsed x-ray imaging of high-density objects using a ten picosecond high-intensity laser driver**

   D. R. Rusby, C. M. Brenner, C. Armstrong, L. A. Wilson, R. Clarke, A. Alejo, H. Ahmed, **N. M. H. Butler**, D. Haddock, A. Higginson, A. McClymont, S. R. Mirfayzi, C. D. Murphy, M. Notley, P. Oliver, R. Allott, C. Hernandez-Gomez, S. Kar, P. McKenna, and D. Neely, *Proceedings of SPIE*, **9992**, 99920E-99920e-8 (2016)

9. **Evaluating laser-driven Bremsstrahlung radiation sources for imaging and analysis of nuclear waste packages**

   C. P. Jones, C. M. Brenner, C. A. Stitt, C. Armstrong, D. R. Rusby, S. R. Mirfayzi, L. A. Wilson, A. Alejo, H. Ahmed, R. Allott, **N. M. H. Butler**, R. Clarke, D. Haddock, C. Hernandez-Gomez, A. Higginson, C. D. Murphy, M. Notley, C. Paraskevoulakos, J. Jowsey, P. McKenna, D. Neely, S. Kar, and T. B. Scott, *Journal of Hazardous Materials*, **318**, 694-701 (2016)

10. **Using X-ray spectroscopy of relativistic laser plasma interaction to reveal parametric decay instabilities: a modeling tool for astrophysics**

E. Oks, E. Dalimier, A. Ya. Faenov, P. Angelo, S. A. Pikuz, E. Tubman, **N. M. H. Butler**, R. J. Dance, T. A. Pikuz, I. Skobelev, M. Alkhimova, N. Booth, J. S. Green, C. D. Gregory, A. Andreev, A. Zhidkov, R. Kodama, P. McKenna and N. Woolsey, *Optics Express*, **25**, 1958 (2017)

11. **X-ray spectroscopy of super-intense laser-produced plasmas for the study of nonlinear processes. Comparison with PIC simulations**
    E. Dalimier, A. Ya. Faenov, E. Oks, P. Angelo, T. A. Pikuz, Y. Fukuda, A. Andreev, J. Koga, H. Sakaki, H. Kotaki, A. Pirozhkov, Y. Hayashi, I. Y. Skobelev, S. A. Pikuz, T. Kawachi, M. Kando, K. Kondo, A. Zhidkov, E. Tubman, **N. M. H. Butler**, R. J. Dance, M. A. Alkhimova, N. Booth, J. S. Green, C. D. Gregory, P. McKenna, N. Woolsey, and R. Kodama, *Journal of Physics: Conference Series*, **810**, 012004 (2017)

12. **Experimental demonstration of a compact epithermal neutron source based on a high power laser**
    S. R. Mirfayzi, A. Alejo, H. Ahmed, D. Raspino, S. Ansell, L. A. Wilson, C. Armstrong, **N. M. H. Butler**, R. Clarke, A. Higginson, J. Kelleher, C. D. Murphy, M. Notley, D. R. Rusby, E. Schooneveld, M. Borghesi, P. McKenna, N. J. Rhodes, D. Neely, C. M. Brenner and S. Kar, *Applied Physics Letters*, **111**, 044101 (2017)

13. **Development of focusing plasma mirrors for ultraintense laser-driven particle and radiation sources**
    R. Wilson, M. King, R. J. Gray, D. C. Carroll, R. J. Dance, **N. M. H. Butler**, C. Armstrong, S. J. Hawkes, R. J. Clarke, D. J. Robertson, C. Bourgenot, D. Neely and P. McKenna, *Quantum Beam Science*, **2**, 1 (2018)

14. **Radiation pressure-driven plasma surface dynamics in ultra-intense laser pulse interactions with ultra-thin foils**
    B. Gonzalez-Izquierdo, R. Capdessus, M. King, R. J. Gray, R. Wilson, R. J. Dance, J. McCreadie, **N. M. H. Butler**, S. J. Hawkes, J. S. Green, N. Booth, M. Borghesi, D. Neely and P. McKenna, *Applied Sciences*, **8**, 336 (2018)

List of symbols and abbreviations

The following is a brief glossary of some of the terms employed throughout this thesis. Unless otherwise stated in the text, the symbols and abbreviations below represent the following:

Abbreviations

AGNs - Active Galactic Nuclei

ASE - Amplified Spontaneous Emission

CH - Plastic target material

CPA - Chirped Pulse Amplification

D - Diamond

DT - Deuterium-Tritium fuel

FI - The Fast Ignition scheme for ICF

FWHM - Full Width Half Maximum

GRBs - Gamma Ray Bursts

HH - Herbig-Haro

ICF - Inertial Confinement Fusion

IGM - Intergalactic Medium

IP - Image Plate

ISM - Interstellar Medium

LA - Laser Axis

MCF - Magnetic Confinement Fusion

MFP - Mean Free Path

OPCPA - Optical Parametric Chirped Pulse Amplification

PIC - Particle-in-Cell

PM - Plasma Mirror

QMD - Quantum Molecular Dynamics

RCF - Radiochromic Film

RPA - Radiation Pressure Acceleration

RSIT - Relativistic Self-Induced Transparency

RT - Rayleigh-Taylor

SNe - Supernovae

SNIe - Type 1 Supernova

SNR - Supernova Remnant

TAP - Target Area Petawatt, Vulcan petawatt beamline

TN - Target Normal

TNSA - Target Normal Sheath Acceleration

VC - Vitreous Carbon

WDM - Warm Dense Matter

WI - Weibel Instability

YSOs - Young Stellar Objects

Greek

β - Dimensionless measure of velocity, $\beta = v/c$

ε_0 - Permittivity of free space

η - Electrical resistivity

γ - Lorentz factor

λ - Wavelength

λ_D - Debye Length

μ_0 - Permeability of free space

∇ - $\hat{x}\frac{\partial}{dx} + \hat{y}\frac{\partial}{dy} + \hat{z}\frac{\partial}{dz}$

ν - Frequency

ω - Angular frequency

ϕ - Faraday rotation

ρ - Density

τ - Duration

θ - Angle

Latin

a_0 - Dimensionless laser amplitude

c - Speed of light

c_0 - Ion sound velocity

E - Electric field strength

E - Energy

e - Elementary electric charge

F - Force

F_L - Lorentz force

F_P - Ponderomotive force

$F/\#$ - Ratio of focal length to beam diameter

h - Planck's constant

$\hbar$ - Reduced Plank's constant

I - Intensity

J, **j** - Current density

k - Wavenumber

k_B - Boltzmann's constant

L, l - Length

L_s, l_s - Scale length

m - Mass

n - Number density

n_c - Critical density

P - Pressure

p - Momentum

r - Radius

t - Duration

T - Temperature

v - Velocity

V - Verdet constant

X, Y, Z - Cartesian coordinates

Z - Atomic number

Z^* - Effective charge state

Subscripts

0 - Initial, unperturbed

e - Electron

f - Fast electron

i - Ion

ion - Ionisation potential

L - Laser

p - Plasma

rad - Radiation

RE - Rising edge

x, y, z - Cartesian coordinates

List of Figures

List of Tables

Contents

Chapter 1

Introduction

Magnetism is an effect generated by the motion of charged particles, and comprises one of the two aspects of the electromagnetic force (the other being the electrostatic force). The existence of magnetic fields has been long known, though for many years the only sign of such phenomena was the attraction or repulsion of certain metals (iron, nickel, cobalt) by permanent magnets, as recorded by Thales of Miletus in the 6^{th} century BC [1] and in the Chinese "Book of the Devil Valley Master" in the 4^{th} century BC. For the following 2000 years, knowledge of magnetism was restricted to the use of lodestone compasses for navigation, until William Gilbert investigated the phenomenon systematically, and demonstrated that Earth was magnetised [2]. Following this discovery, significant work was undertaken in the study of magnetism including Gauss's studies of the nature of Earth's magnetism, and Coulomb's verification that the strength of magnetic fields diminished as an inverse square law with distance from the source, and that magnetic fields must exist as dipoles.

The 19^{th} century led to many advancements in the understanding of the nature of magnetic fields: firstly, Ørsted's observation that electric currents were accompanied by azimuthal magnetic fields was the initial discovery which demonstrated the interlinked nature of electricity and magnetism. Ampère subsequently showed that parallel wires, with co-propagating currents attracted one another, and Biot and Savart produced the Biot-Savart law, calculating the magnetic field strength surrounding any current. These investigations resulted in Ampère's theorem of magnetism in 1861 [3], in which it was proposed that magnetism was equivalent to loops of electric current.

Further understanding was made in the 1830s when Michael Faraday proposed that one body could interact with another via electric and magnetic forces through 'lines of

force', or 'action at a distance'. Through experimental demonstration, he showed that an evolving electric field induced an encircling magnetic field, now known as Faraday's law of induction. Furthermore, he demonstrated that the polarisation plane of linearly polarised light was altered after propagating through a parallel magnetic field, a phenomenon later termed "Faraday rotation". This was the first evidence of the relationship between light and electromagnetic fields.

This connection was later studied in 1855 when Scottish physicist James Clerk Maxwell developed and published his famous "Maxwell's equations", formally uniting electricity and magnetism, although his theory was as yet incomplete. It was with the publication of his 1864 paper, the "Electromagnetic theory of light" in which he exhibited that, in the absence of any charges, that not all the solutions to his formulated equations were zero and that the velocity of electrical and magnetic waves in such a scenario was 3×10^8 m/s.

Magnetic fields are now known to be ubiquitous throughout the known universe. The nearest example is the Earth's magnetic field, which is not only exploited for navigation, but also essential for protecting us from hazardous cosmic rays and solar winds. Further, magnetic fields play an important role in various branches of astrophysics. They are particularly critical for angular momentum transport, without which the solar-type stars would not spin as slowly as they do today. Magnetic fields are responsible for the coronal loops observed from the solar corona. They play a crucial role in driving turbulence in accretion discs, in which they provide the stresses needed for accretion. Large scale fields in these discs are also thought to be involved in launching jets of plasma. Fields permeating a rotating black hole are postulated to provide an efficient method of extracting energy to power these jets from active galactic nuclei. Magnetic fields with micro-gauss strength and coherence scales of order several kilo-parsecs are also observed in nearby galaxies, and also on the scales of galactic clusters. Understanding the origin of magnetic fields relevant to astrophysical phenomena is a topic of great importance. However due to the distances and timescales involved in astrophysical systems, measurements and observations have proven difficult.

The study of laboratory analogues of astrophysical phenomena is one method by which the investigation of astrophysically relevant magnetic fields may be accomplished. High power laser laboratory experiments, taking place on timescales of femtoseconds to nanoseconds and length scales of micrometres to millimetres, can offer insight to parsec-sized phenomena that endure for millions of years, due to the applicability of "scaling laws".

These enable comparison between the two systems of vastly different parameters. Intense laser-solid interactions offer a promising avenue for the study of systems associated with astrophysical magnetic fields due to the large magnetic fields generated (10^5 T in the region of the laser focal spot). Experimental measurements reported in Borghesi *et al.* [4] demonstrate distinct mechanisms of magnetic field generation throughout the target, which was confirmed in numerical simulations by Mason and Tabak [5]. The potential to tailor the dynamics of interactions by selection of the laser and target parameters result in such experiments being attractive for the recreation of astrophysical phenomena in laboratory environments.

Just as the foundations of the understanding of magnetism was the result of increasing numbers of investigations, the work presented in this thesis builds upon a solid set of foundations laid by countless others. A brief historical review of the field of laser-plasma physics, and more specifically, the field of intense laser-solid interactions, is surmised below.

1.1 History and motivation

In 1917, Albert Einstein first considered the concept of the stimulated emission of light [6]. He proposed that, through spontaneous emission, an excited, isolated electron could return to a lower energy state. This concept remained hypothetical for many years until the midst of the Cold War. It was to this backdrop that, in 1960, Theodore Maiman unveiled his prototype laser using a synthetic ruby crystal [7]. This was the first demonstration of the generation of coherent optical light, and built upon the previous development of a maser for the US Army Signal Corps in 1955 [8].

People at the time could be forgiven for not appreciating the full ramifications of this development. In fact, Maiman himself was quoted as saying "the laser is a solution looking for a problem". Nearly 60 years on the laser has revolutionised the world. The fundamental properties of light amplified via the stimulated emission of radiation (LASER) are its monochromaticity, coherence, high brightness and high directionality. It is these properties which have resulted in its utilisation in a broad range of applications: including in the home (CD/DVD/Blu-ray players and fibre optic communication), industry (precision laser machining and liquid screening at airports), space science (topographic measurements of the Earth, gravitational wave detection), medicine (optometry and surgical incisions) and fundamental physics (laser cooling of atoms, optical levitation and high field physics).

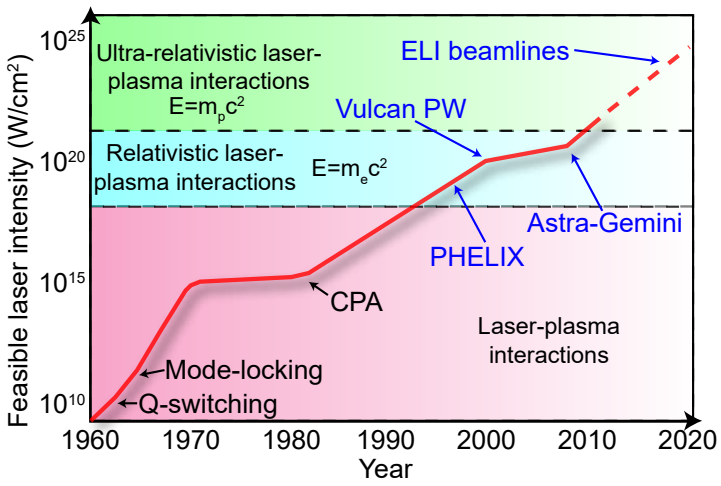

Figure 1.1: Progession of maximum achieved laser intensity over time. Significant events in the field of laser development are shown, and the regimes of laser-plasma interactions are highlighted. The expected progression of future development is shown.

Following Maiman's demonstration, rapid progress was made in the field of laser physics; the first helium-neon (HeNe) laser [9] and laser diode [10] were demonstrated shortly after, and these designs were quickly improved and developed. In 1962, Q-switching [11], a technique for obtaining higher energy and short pulses of light, was invented. Through this technique, pulses of energy in the kilo-Joule range and nanosecond duration were made feasible. A new regime of ultrashort, down-to-femtosecond duration pulses was achieved following the demonstration of mode-locking in 1964 [12]. When focused, these ultra-short, high energy pulses resulted in intensities of 10^{14}-10^{16} W/cm^2. These intensities, at values greater than the ionisation potential of hydrogen, when combined with the inherent properties of lasers, make them ideal drivers of high energy density physics. Thus, the study of laser-plasma interaction physics was conceived in the 1970s and 1980s [13].

In 1985, the peak achievable intensity was increased yet further with the invention of chirped pulse amplification (CPA) [14], which has led to intensities of up to 10^{21} W/cm^2 now being achievable. Presently, new facilities, such as Extreme Light Infrastructure (ELI) [15] or the proposed Omega EP OPAL upgrade [16], are seeking to push the frontier further to above 10^{23} W/cm^2. The progression of high-power laser systems since the time of their inception is illustrated in figure 1.1.

Such rapid advancements in laser technology have brought similarly large leaps forward in the field of laser-matter interactions, with multiple new avenues of investigations and applications opened up to researchers. More specific to the theme of this thesis are the investigations undertaken in interactions between an intense laser pulse and an initially

solid target, or more succinctly, intense laser-solid interactions. These research avenues encompass a myriad of numerous possibilities from fundamental physics research, to studies of employing these tools for use in applications outside of the laboratory. Studies of fundamental high energy density physics incorporate a huge range of topics. Some salient examples are: investigations of the transport of large currents of fast electrons, generated by an intense laser pulse, within dense matter; studies of the different mechanisms by which ions are accelerated to high energy in the interaction, and the generation of intense X-ray radiation. Perhaps the most well known is that of inertial confinement fusion (ICF). ICF is an alternative to the magnetic confinement fusion (MCF) scheme for achieving nuclear fusion in the laboratory. The use of lasers to drive controlled nuclear fusion was proposed in 1972 in Nuckolls *et al.* [17], and is described by the following steps: intense lasers (typically with wavelengths in the ultraviolet region of the electromagnetic spectrum) heat and compress a speherical fuel capsule. The capsule is composed of an outer ablator shell with an inner layer of cryogenic deuterium-tritium (DT) solid, filled with DT gas fuel. A schematic of the capsule design in shown in figure 1.2 (a). As the lasers ablate the outer shell, the inner material radially compresses due to the conservation of momentum, resulting in the formation of a central "hot spot", surrounded by a dense, cooler region [18]. As the interaction progresses, the density of the central core reaches ∼20 times the density of lead, and ignites at temperatures of 1×10^6 K. This scheme is more commonly known as the central hot spot (CHS) ignition scheme for ICF and is illustrated in figure 1.2 (b).

In 1994, Tabak *et al.* [19], proposed the "fast ignitor" scheme for ICF, utilising a combination of long (ns) and short (ps) pulse lasers. The fast ignition (FI) concept is a variant of ICF in which the compression and ignition stages of the interaction are decoupled; in the CHS scheme, the long pulse beams compress the fuel pellet to the point of ignition, whilst in the FI scheme, long pulse lasers compress the capsule to high densities ∼600 g/cm^3 and a separate short pulse laser generates a large flux of fast electrons that ignite the fuel. The generation of a central hot spot is not necessary in FI; the fusion reaction occurs due to heating by the fast electron population. Additionally, FI also offers the advantage that the level of compression required is reduced, compared to the CHS scenario. Thus, the laser energy requirements are reduced. Two main techniques currently exist for FI: hole-boring and cone-guided FI [20, 21]. Hole-boring involves the direct interaction of the ignitor pulse with the compressed fuel capsule, whilst in the cone-guided scheme a hollow guiding cone (typically of a high atomic number material, e.g. gold) is

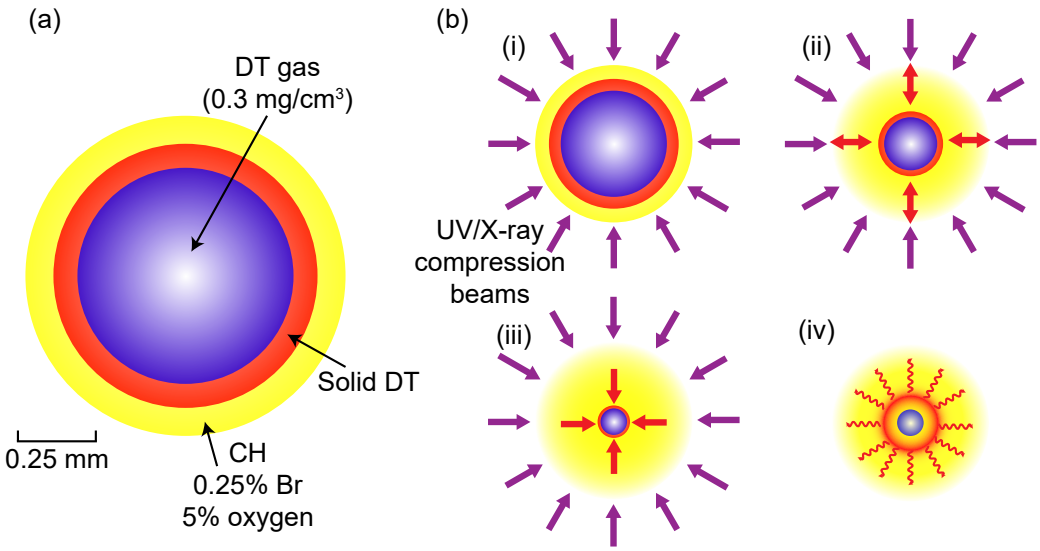

Figure 1.2: (a) Schematic illustration of the fuel capsule design employed in intertial confinement fusion; (b) Stages of the central hot-spot scheme for ICF: (i) UV/X-ray laser pulses rapidly heat the surface of the capsule forming an enveloping plasma; (ii) The fuel is compressed by the rocket-like ablation of the surface material; (iii) During the final phase of the interaction, the fuel core has a density ∼20 times that of lead, and ignites at 10^6 K; (iv) The thermonuclear burn spreads rapidly throughout the compressed fuel, yielding many times the input energy.

embedded within the fuel capsule. The short pulse beam is then focused onto the cone, avoiding the low-density, expanding plasma, and fast electrons are generated at the tip of the cone. The fast electrons propagate over a distance of the order ∼300-400 μm through the cone into the fuel, and thus control of the transport properties of the fast electrons in the dense plasma is paramount. The results presented in **Chapter 5** of this thesis are directly relevant to the cone-guiding method.

Significant research effort has also been devoted to other potential applications of laser-solid interactions, such as hadron therapy. The high flux of energetic ions accelerated in the interactions are potentially attractive for oncology purposes. However, the necessary spatial and spectral control of the ion beams have not yet been obtained. Promising research into advanced ion acceleration schemes may meet these criteria in the future [22, 23]. Furthermore, the use of intense laser-solid interactions as sources of radiation, ions and neutrons for the imaging or detection of scientific or industrial objects has been demonstrated. The tunable, bright, broadband, relatively small source size, high particle and radiation fluxes may be particularly relevant for industrial purposes, for example in non-destructive testing. Resolutions of $\ll$1 mm have been demonstrated, whilst the advent of high-repetition rate laser systems would enable rapidly moving objects, such as turbines or vacuum pumps to be examined for defects [24]. Demonstrations of laser-generated X-

rays and neutrons for the imaging and analysis of nuclear waste have been performed [25], whilst X-ray backscatter imaging has been proposed for the detection of objects, such as landmines [26].

1.2 Laboratory astrophysics

The application of intense laser-solid interactions that is perhaps most relevant to the overarching theme of this thesis is that of laboratory astrophysics. During the past several decades, the emergence of new high-energy density (HED) experimental capabilities, including high power lasers, has stimulated the pursuit of studies of astrophysical analogues generated in the laboratory environment [27–30]. HED laboratory astrophysics differs from traditional studies of astrophysical analogues, where parameters such as the low-energy nuclear cross section are measured. It enables macroscopic collections of matter to be investigated in extreme conditions, such as high temperatures, densities and velocities [31]. The major aims of such laboratory simulations are: the study of astrophysical systems, albeit on a smaller scale; and the validation of simulation codes for theoretical/computational astrophysics. The latter case of experiments need not bear strong similarities to the analogous astrophysical scenarios, but must probe some well-defined physical problem. Through "benchmarking" computational codes against experimental results, the ability to simulate the complicated physics of astrophysical phenomena can be improved.

Examples of physical processes which are generated in the interaction between an intense laser pulse and a solid-density target are warm dense matter (WDM) states [32], relativistic plasmas [33], high Mach-number plasma jets [34] and photo-ionised plasmas [35,36]. These examples are relevant to a wide range of astrophysical phenomena, the details of which will be discussed in turn below, in the context of potential laboratory astrophysics experiments.

1) Supernovae

Supernova (SNe) explosions represent some of the most extreme, bright events in the known universe, often outshining their host galaxy. Two fundamental mechanisms for the formation of supernovae are known, classified as Type Ia (SNIe) and Type II. SNIe are associated with the accretion of matter from a massive star to a relatively more compact, denser white dwarf. White dwarfs are post-main sequence stellar objects, composed of the remnants of a stellar core. They are formed primarily of electron-degenerate matter and

are extremely dense: the mass of a white dwarf is comparable to a solar mass, whilst its volume is comparable to that of the Earth. White dwarfs are limited to a maximum of 1.44 solar masses [37], referred to as the Chandrasekhar mass limit. Beyond this point, the white dwarf's core reignites, driving thermonuclear reactions. The electron degeneracy pressure generated with the recommencement of fusion results in the accreting material being driven off in an SNe explosion. Type II SNe, in contrast, originate from singular star systems and result from the rapid collapse of the core of a massive star. As the lifetime of such a star progresses, it will eventually exhaust its supply of hydrogen, and begin fusing successively heavier elements. The star will become increasingly more metallic as heavier elements are formed, until the production of iron, at which point fusion can no longer take place. When this occurs, the electron degeneracy pressure supporting the core ceases, and the core collapses under the gravitational weight of the outer layers, until it exceeds the Chandrasekhar limit. At this point, the core implodes violently, until the collapse is halted via neutron degeneracy. The resulting shockwave propagates radially outwards from the core, blasting off the star's outer layers at significant fractions of the speed of light. Figure 1.3 illustrates the two mechanisms of SNe occurence. The energy released in such events is on the order of 10^{44} J, with the energy originating from the region of the central core, transported to the outer surface via a complex combination of hydrodynamic flows and radiative transport. As optical observations are impossible beyond the expanding photosphere, laboratory investigations of plasma opacity and radiation transport [38–40] are crucial for understanding the energy transfer from the core region. Additionally, lasers employed for ICF experiments, such as the National Ignition Facility (NIF), may also enable the study of thermonuclear ignition relevant to SNIe to be undertaken. Furthermore, the onset of fusion in these experiments may also result in the production of neutron fluxes, perhaps relevant to nucleosynthesis of heavy elements during these phenomena.

2) Supernova Remnants

The final result of an SNe explosion is the formation of an SNe remnant (SNR); huge molecular nebulae which persist for many millennia, in contrast to the progenitor blast which created them, that occurs on durations of seconds. The remnant is bounded by an expanding shockwave, and is composed of stellar ejecta, in addition to accelerated interstellar medium (ISM). The interaction of the expanding material with the ISM leads

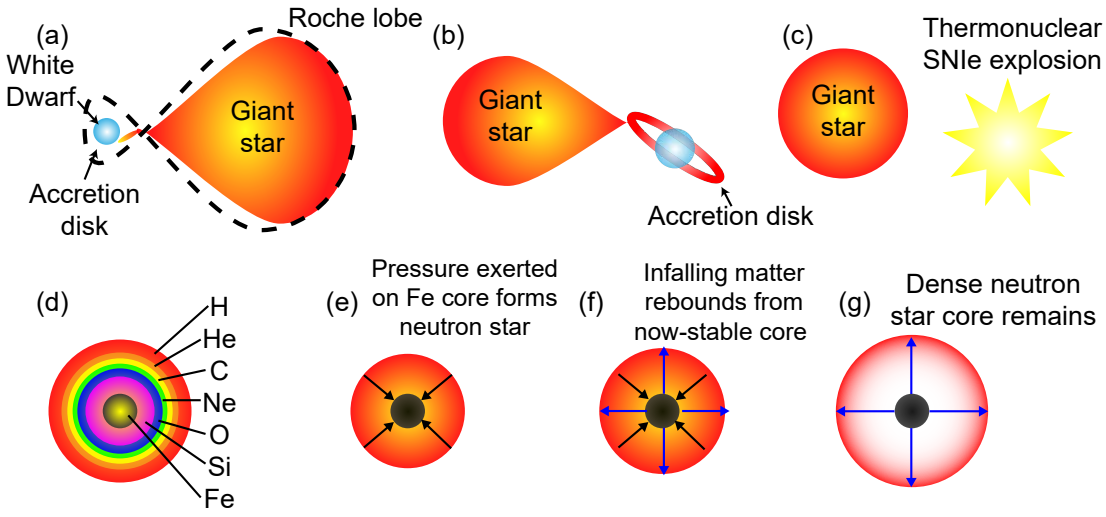

Figure 1.3: Illustration of the processes by which Type 1a and II supernovae occur: (a)-(c) Type Ia supernova, showing (a) a massive giant star exists in a binary system with a denser, white dwarf. The giant star loses material to the white dwarf, (b) generating an accretion disk. The accretion of matter continues until the disk reaches the Chandrasekhar limit, at which point (c) thermonuclear fusion, and a type Ia supernova occurs; (d)-(g) Type II supernova, showing (d) a massive, evolved star has undergone nuclear fusion until, forming an iron core. At this point, fusion can no longer take place and the star begins to collapse (e). The pressure exerted on the core by the collapsing matter compresses it into neutrons. A combination of a shockwave generated by the rebounding matter and a neutrino flux from the core blast the outer layers into space (f), leaving behind a supernova remnant and dense neutron star (g).

to the production of observable structures [41] and are believed to account for significant proportion of cosmic rays [42, 43]. Experimental investigations of Rayleigh-Taylor-like instabilities [44] and magnetic field growth driven by the Weibel instability [45] may provide evidence for the large degrees of structure observed in many SNR, for example the Crab nebula [46] (shown in figure 1.4). In addition, experiments relevant to hydrodynamics at early times following the SNe have been performed [47], and collisionless shock experiments have also examined the amplification of magnetic fields and synchrotron generation in the interior of the expanding material [48–50].

The growth of self-generated magnetic fields, driven by the growth of the Weibel instability resulting from the interaction of a propagating energetic electron current flowing into an expanding background plasma is particularly relevant to the study reported in **Chapter 6** of this thesis.

3) Planetary interiors

WDM states generated in laboratory conditions are often important to studies of planetary interiors, due to their relevance to the conditions found in the cores of Jovian planets and

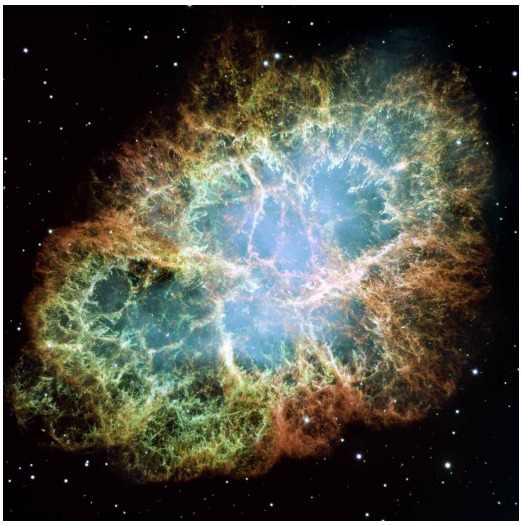

Figure 1.4: Optical image of the Crab Nebula, with visible filamentary structure present. At the centre of the nebula lies a pulsar, with a rotational frequency of 30 Hz. Image Credit: NASA, ESA, J. Hester, A. Loll (ASU)

brown dwarfs, and terrestrial planets. Understanding the nature of the material located in the cores of these objects is important for many reasons, including the understanding of the generation of planetary magnetic fields [51], determination of the composition of the core, and for the evolution of the object in question. Such studies are not only important for determining the formation, and future, of Earth and the other Solar System planets, but also for the study of exotic extrasolar objects, many of which tend to be "hot jupiters", giant gas planets with small, highly eccentric orbits; "super earths", large terrestrial planets with similar composition to Earth; and brown dwarfs, massive "failed stars" occupying the mass range between Jovian planets and small stellar objects that do not possess the requisite mass necessary to achieve thermonuclear ignition. Denoeud *et al.* [52] demonstrated the applicability of laser compression for studying the physics of compressed iron at planetary temperatures and pressures; whilst Booth *et al.* [32] investigated the resistivity of WDM in conditions relevant to those found in brown dwarfs. The transport of energetic electron currents in transient states of WDM has been studied extensively, with some salient examples reported in Quinn *et al.* [53] and McKenna *et al.* [54].

The influence of transient-WDM states on energetic electron transport is particularly relevant to the results presented in **Chapter 5**.

4) Astrophysical jets

Highly collimated, high Mach-number, bipolar plasma jets are routinely observed propagating from compact sources such as active galactic nuclei (AGNs) [55] and young stellar objects (YSOs) [56]. Observations have shown that they are associated with rotating accretion disks and it is postulated that the twisting of an ordered magnetic field threading accretion disks acts to accelerate jets [57]. These structures have been measured to extend out from parsec scales (for YSOs) to many mega-parsecs (for AGNs), with velocities approaching the speed of light, c, for the case of AGN launched jets. Thus, they represent some of the largest known singular structures in the observable universe. Polarimetric measurements of these objects has demonstrated the presence of an azimuthal, helical magnetic field enveloping the jet as it propagates into the low density medium surrounding it [58]. Measurements of the jet launch region near the central dense object are difficult due to the presence of the accretion disk, gas and dust clouds, the host planetary nebulae (in the case of YSOs) and the galactic disk (for AGNs). Furthermore, the timescales over which these structures evolve result in added difficulties for observations and measurements. Thus, laboratory analogues of relativistic plasma jets would enable great insight into the physical processes surrounding them.

Experimental demonstrations of the generation and propagation of plasma jets have been previously performed in the laboratory with intense lasers. Logory *et al.* [59] investigated the propagation of a plasma jet into a carbon foam via the irradiation of a gold hohlraum coupled to a concave, hemispherical ablator, demonstrating the presence of a jet of plasma. Following this, Foster *et al.* [60] employed the Omega laser to drive a titanium target through a washer, in order to generate a narrow jet of plasma that was propagated into a hydrocarbon foam, simulating the propagation of an astrophysical jet into the ISM. In 2006, Nilson *et al.* [61] investigated the role of magnetic reconnection in jet formation by employing two beams of the Vulcan laser to irradiate two areas on the front surface of a solid foil. It was concluded that jet formation could not be explained hydrodynamically, and that magnetic reconnection between the two plasmas generated at the rear surface was the driver. More recently, Gregory *et al.* [62] investigated jet formation due to two colliding plasmas, and the effects of propagation in a low-density background gas, whilst Sarri *et al.* [63] investigated the dynamics of strong, self-generated magnetic fields relevant to those observed in the collimation of relativistic astrophysical jets.

In experiments utilising ultrathin, nanometre-scale foils, Powell *et al.* [34] demonstrated

the presence of a relativistic plasma jet, generated at the onset of relativistically self-induced transparency during the intense laser-solid interaction, whilst Gonzalez-Izquierdo *et al.* [64] numerically explored the existence of precessing, helical magnetic field structures which could act to collimate jets, formed via the rotation of a diffraction pattern of intense laser light transmitted through a relativistic plasma aperture.

The physical processes relating to the generation of jets launched from AGNs and YSOs are particularly relevant to the results presented in **Chapter 6**.

The above discussion is not a comprehensive list of the range of relativistic plasma astrophysical phenomena reproducible in the laboratory. Other potential scenarios that have been investigated in the laboratory include the dynamics of radiatively-driven molecular clouds [65] and the physics of gamma-ray bursts (GRBs) [66]. Radiatively-driven molecular clouds are cold, dense molecular clouds illuminated by massive, bright stars. The intense stellar radiation incident on the cloud generates a high pressure source at the surface via photoevaporation, and Klein *et al.* [67] and Robey *et al.* [68] have investigated the reproduction of the photoevaporation-front hydrodynamics relevant to these scenarios. GRBs are some of the most energetic phenomena in the observable universe, with the characteristic emission of a 'flash' of gamma rays, followed by an afterglow of longer wavelength radiation lasting from several milliseconds to hours. All GRBs observed so far have been located at extreme distances to earth, and thus provide an opportunity for the study of the early universe. Models of the formation of these phenomena often refer to the 'fireball' model [66], where an initial mixture of electrons, positrons and photons expands relativstically. The gamma ray burst then results from synchrotron emission from reverse shocks within the beam of electrons and positrons [69]. Sarri *et al.* [70] demonstrated the generation of electron/positron pair plasmas in an experiment employing the Astra-Gemini laser system. An analysis of the electron/positron plasma generated experimentally showed similarities to observations of relativistic astrophysical jets [71].

1.3 Thesis outline

Common to all the above scenarios is the ubiquitous presence of magnetic fields. This thesis presents several experimental and numerical studies on self-generated magnetic fields and their influence on the dynamics of relativistic electrons in both solids and foils expanding to near-critical density.

The thesis consists of eight chapters, with the first half primarily focused on a discussion of the fundamentals of intense laser-solid interactions and the diagnostics tools employed to obtain the data presented in the latter half. A brief summary of each chapter follows:

- **Chapter 2** - explores the underpinning physics of intense laser-solid interactions.
- **Chapter 3** - provides a review of relevant literature relating to laboratory astrophysics experiments specific to relativistic laser-solid interactions, along with a detailed overview of the scaling relations enabling laboratory analogues of astrophysical phenomena to be studied.
- **Chapter 4** - describes the experimental and numerical techniques employed to obtain and analyse the results presented in the results chapters.
- **Chapter 5** - reports on an investigation of the influence of self-generated magnetic field growth on fast electron transport in solid targets using a combination of experimental measurements and 3D hybrid-PIC simulations.
- **Chapter 6** - presents investigations of astrophysically relevant magnetic field structures in foils expanding to near-critical density using a combination of experimental measurements and PIC simulations.
- **Chapter 7** - summarises the results of the investigations presented in **Chapters 5** and **6**, and discusses potential directions for future research.

Chapter 2

Fundamentals of laser-plasma interactions

Before discussing the results presented later in this thesis, it is helpful to first discuss the physical processes relevant to the field of laser-solid interaction physics. This includes a range of phenomena including the basic electromagnetic theory of a propagating wave, the methods by which these waves interact with matter, and the resultant generation of energetic particles and radiation via these mechanisms.

2.1 Description of an electromagnetic wave

It is instructive to begin the discussion of the fundamental principles of laser-solid interactions with a brief description of electromagnetic waves and the equations by which they are governed.

The classical description of an electromagnetic wave is one of synchronised oscillations of perpendicularly-oriented electric and magnetic fields, the properties of which can be fully described by a combination of the four Maxwell's equations and the Lorentz force equation. It has been over 150 years since James Clerk Maxwell published his theory on the classical nature of electromagnetic radiation [3, 72], in which he established the equations that have been ubiquitous in the description of the interaction of light with matter since, whilst also unifying the theories of Gauss, Ampére, Faraday and Coulomb. These can be summarised by the following:

$$\nabla \cdot \mathbf{E} = \frac{\rho}{\varepsilon_0} \tag{2.1}$$

$$\nabla \cdot \mathbf{B} = 0 \tag{2.2}$$

$$\nabla \times \mathbf{E} = -\frac{\partial \mathbf{B}}{\partial t} \tag{2.3}$$

$$\nabla \times \mathbf{B} = \mu_0 \mathbf{J} + \frac{1}{c}\frac{\partial \mathbf{E}}{\partial t} \tag{2.4}$$

where equations (2.1) and (2.2) are Gauss's laws for electric fields and magnetic fields, respectively, and $\mathbf{E}$ is the electric field strength, $\mathbf{B}$ is the magnetic flux density, ρ is the charge density, and ε_0 is the permittivity of free space.

Equation (2.3) is Faraday's law of induction, and governs the interaction of an external magnetic field with an electrical current; and lastly, Ampére's circuital law (equation 2.4), where μ_0 is the permeability of free space and $\mathbf{J}$ is the current density flowing around a closed loop of current.

The above equations offer a full description of electromagnetism and the generation of time varying electric and magnetic fields. Maxwell's equations state that an electric charge generates a field, and that this field acts as to mediate the interactions with this charge and neighbouring charges.

2.1.1 Polarisation of an electromagnetic wave

Polarisation is the property that is applied to transversely-oscillating waves, including electromagnetic waves, that describes the overall orientation of the plane of the oscillations of the electric field of the wave. This property can be applied solely to transverse waves as the direction of oscillation is always perpendicular to the direction of motion of the wave. Light emitted from thermal sources, for example, incandescent lightbulbs or the Sun, is said to be unpolarised due to its lack of specific plane of oscillation. In contrast, the high power laser systems employed in the experimental campaigns featured in this thesis emit pulses of polarised light, specifically linearly polarised light. In linear polarisation, the fields that comprise the electromagnetic wave oscillate along a single plane. Waves that are horizontally polarised, with respect to the surface of a target, are P-polarised, whilst vertically polarised waves are S-polarised. The terms P and S arise from the German term for parallel and perpendicular, respectively. Figure 2.1 illustrates the differences between these two cases.

Mathematically, for an infinite, plane-wave electromagnetic wave propagating in the x-direction, the electric field can be expressed as the superposition of two orthogonal linear

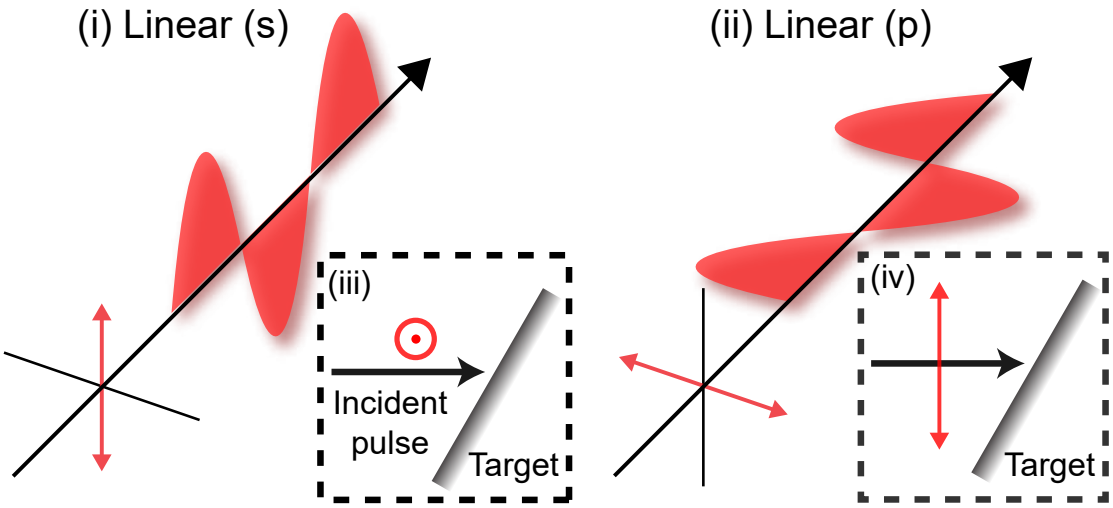

Figure 2.1: Illustration of polarisation states of electromagnetic radiation, showing (i) vertically and (ii) horizontally polarised light. Inset: (iii) Schematic illustrating vertically polarised light with respect to a target surface, showing the incident pulse (black) and the plane of polarisation (red); (iv) Same, but for horizontally polarised light.

components:

$$\mathbf{E}_y = E_{0y} sin(\phi)\hat{y} \tag{2.5}$$

and:

$$\mathbf{E}_z = E_{0z} sin(\phi - |\Delta\theta)\hat{z} \tag{2.6}$$

If $E_{0z} = 0$, and the phase difference between the two components is $\Delta\theta = 0$, the wave oscillates in one specific plane, and the wave is linearly polarised. The same is true if $E_{0y} = 0$ and $\Delta\theta = 0$. If the electric fields of the two perpendicular, linear components, E_{0y} and E_{0z} are equal in magnitude, but possess a phase difference of $\Delta\theta = \pi/2$, the resultant electric field follows a circular trajectory as it oscillates, giving circular polarisation. For any other combination of the two linear electric field components, or a phase difference $\Delta\theta \neq 0, \pi/2$, the resultant polarisation state is defined as elliptical polarisation. In the cases of circular and elliptical polarisation, the rotation of the electric fields as they propagate can have two possible directions, right or left. The state that the wave possesses is dependent on the rotation of the fields with respect to the direction of propagation of the wave.

2.2 Description of a plasma

Another topic of paramount importance to the concepts introduced throughout this thesis is the fundamental description of plasma.

Plasma is ubiquitous throughout the known universe: it is the primary component of stellar interiors and atmospheres; planetary nebulae and interstellar gas clouds; the upper layers of the atmosphere of our planet and others; and stellar winds and astrophysical jet-like phenomena. On a terrestrial scale, plasma is, by comparison, a great deal more sparse. Examples include lightning, neon lighting and St. Elmo's fire.

The interaction of a tightly focused, high power laser pulse with solid density matter is one such situation where a rapid change of state from solid matter to plasma occurs via heating and ionisation (as will be covered in section 2.3). As the material undergoes heating, it first boils and transitions to a gaseous state, before electrons are then stripped from their constituent ions, and it transitions to a plasma. Although they may appear similar, ionised gas cannot be called a plasma. Plasmas must abide by the following definition: "*A plasma is a quasineutral gas of charged and neutral particles which exhibits collective behaviour*". "Quasineutral" means that plasma is, locally, an electrically neutral medium of positive and negative particles. More specifically, a positive test charge introduced to a plasma, with no particles undergoing thermal motion, would be screened by surrounding negative test charges present in the vicinity of the positive charge. Thus, no electric field would be experienced by other charged particles at the edge of the plasma. "Collective" behaviour describes the concept that the motion of particles in plasma is dominated, not by collisions, but by the global action of electric and magnetic fields generated by the motion of charged particles elsewhere in the plasma system. In turn these particles are subsequently influenced by the fields generated by the particles influenced by them [73,74]. In contrast, particle motion in an ionised gas is governed primarily by collisional behaviour.

Furthermore, to be designated as a plasma, there are certain criteria that must be satisfied [75].

1. $\lambda_D << L$ - the Debye screening distance, λ_D, is shorter than the dimensions of the plasma, L. The Debye length of a plasma defines the distance over which a point charge can influence other charges, and the distance past which charges are shielded

from external fields. This can be written as:

$$\lambda_D = \sqrt{\left(\frac{\epsilon_0 k_B T_e}{e^2 n_e}\right)} \tag{2.7}$$

where ϵ_0 is the permittivity of free space, k_B is Boltzmann's constant, T_e is the electron temperature, e is the electronic charge, and n_e is the electron density in the plasma. This arises from the following: consider a scalar potential resulting from a test charge, ϕ. Using Gauss's law we obtain:

$$\nabla^2 \phi = \frac{\rho}{\varepsilon_0} \tag{2.8}$$

where $\rho = e n_e$. Assuming that the number density of the electron cloud n_e is given by a Boltzmann distribution of the form $n_e = n \cdot \exp(\frac{e\phi}{k_B T_e})$ results in the following:

$$\nabla^2 \phi = \frac{en}{\varepsilon_0}(\exp \frac{e\phi}{k_B T_e} - 1) \tag{2.9}$$

Expanding equation (2.9) in a Taylor series in the first order around 0, by assuming a potential energy much lower than the electron temperature, it is found that:

$$\nabla^2 \phi = \frac{e^2 n \phi}{\varepsilon_0 k_B T_e} = \nabla^2 \phi = \frac{\phi}{\lambda_D^2} \tag{2.10}$$

This characteristic of plasmas enables the quasi-neutrality of the system to be maintained: local charge imbalances are shielded and cancelled out within a distance much less than the spatial dimensions of the system, meaning that, on a macroscopic scale, the plasma is essentially charge neutral.

Physically, plasmas do not exist in only one dimension, and thus the Debye length represents the radius of a spherical volume, known as a "*Debye sphere*", where the electric field generated by the charge separation of the charged particles in the plasma only interacts with other charged particles inside this volume.

Furthermore, the Debye length defines the extent as to which the electric fields of an incident laser pulse can propagate past the critical surface of the plasma (see section 2.5).

2. $N_D >> 1$ - Debye shielding, and quasi-neutrality, is only valid if there are a significant number of electrons present inside a sphere with a radius equal to the size

of the Debye screening distance, the *Debye sphere*. The number of electrons N_D is given by:

$$N_D = \frac{4}{3} n_e \pi \lambda_D^3 = 1.38 \times 10^6 T_e^{3/2} n_e^{-1/2} \tag{2.11}$$

3. $\omega_p \tau > 1$ - Collective effects dominate the particle dynamics over collisional effects, where τ is the mean time between collisions.

   Charged particles comprising a plasma are subject to both local and global perturbations. However, when compared to the collective response of plasma electrons acting in response to charge imbalances in a plasma, local disturbances or perturbations from collisions can be considered negligible.

   The collective response of a plasma is the final characteristic used to differentiate a plasma from an ionised gas. This describes the oscillations generated in response to an imbalance of charge, for example, an electron being displaced from its equilibrium position. In order to return the electron to its initial state, and maintain quasi-neutrality, an electric field is generated which, when coupled with the inertia of the electrons influenced by this field, sets up electron oscillations about their equilibrium positions. These oscillations occur at a characteristic frequency, known as the plasma frequency, ω_p. Using Gauss's law of electric field generation in one dimension ($\mathbf{E} = n_e e x/\varepsilon_0$), these oscillations can be described by the following method:

   Electron dynamics are governed by the Lorentz force for which, in the case of small electron oscillations, the $\mathbf{v} \times \mathbf{B}$ term can be neglected (see section 2.4.1):

$$F_L = -e\mathbf{E} = m_e \frac{d^2 x}{dt^2} \tag{2.12}$$

   Substituting the form of Gauss's law in one dimension into equation (2.12) results in the equation of motion of electrons in a plasma:

$$\frac{d^2 x}{dt^2} + \frac{n_e e^2}{\varepsilon_0 m_e} x = 0 \tag{2.13}$$

   From equation (2.13) it can be seen that electrons in a plasma will oscillate around their rest position with simple harmonic motion, with a natural frequency of:

$$\omega_p = \frac{(k_B T_e)^{1/2}}{\lambda_D m_e^{1/2}} = \sqrt{\frac{n_e e^2}{\varepsilon_0 m_e}} \tag{2.14}$$

The product of $\omega_p\tau$ being greater than unity represents the influence of collisional effects being relatively weak and unimportant in comparison to collective effects. In an ionised gas, $\omega_p\tau$ would be defined as being less than unity.

2.3 Ionisation

When a high-power laser pulse is focused onto the surface of a solid target, plasma is generated through ionisation of the target material. As a result of the photoelectric effect, incident photons can ionise atoms via photoionisation; the act of imparting a photon's energy to a bound electron and giving it enough energy to escape its parent atoms potential well. The energy of the incident photons must be, at least, the same as the binding energy of the electrons to their parent atom. The quantum energy of a photon was determined by Planck, and is given by $E = h\nu$.

For the laser systems presented in this thesis, where the central wavelength is approximately 1 μm (for more information, see section 4.2.7), and frequency 300 THz, the energy possessed by each photon is ≈ 1.2 eV. The binding energies of atoms is dependent on the element in question. However, even the weakest binding energies are of the order of tens of eV. Thus, it is not possible for classical photoionisation to occur with the lasers employed. However, ionisation can emerge as a consequence of numerous mechanisms when intense laser beams interact with matter. This can be demonstrated by considering the ionisation of hydrogen, with a binding energy of 13.6 eV. The Bohr radius of the hydrogen atom is given by:

$$a_B = \frac{4\pi\varepsilon_0\hbar^2}{m_e e^2} = 0.053 \text{ nm} \tag{2.15}$$

which results in a binding electric field of:

$$E_a = \frac{e}{4\pi\varepsilon_0 a_B^2} = 5 \times 10^{11} \text{ V/m} \tag{2.16}$$

The magnitude of the electric field of the laser is intensity dependent, given by $E_0 = a_0 m_e c\omega_L/e$, where a_0 is known as the dimensionless laser amplitude (see section 2.4.1). Thus, the intensity required for laser ionisation to occur is given by:

$$I_a = \frac{\varepsilon_0 c}{2} E_a^2 \approx 10^{16} \text{ W/cm}^2 \tag{2.17}$$

Depending on the particular parameters of the laser, diverse ionisation processes can occur

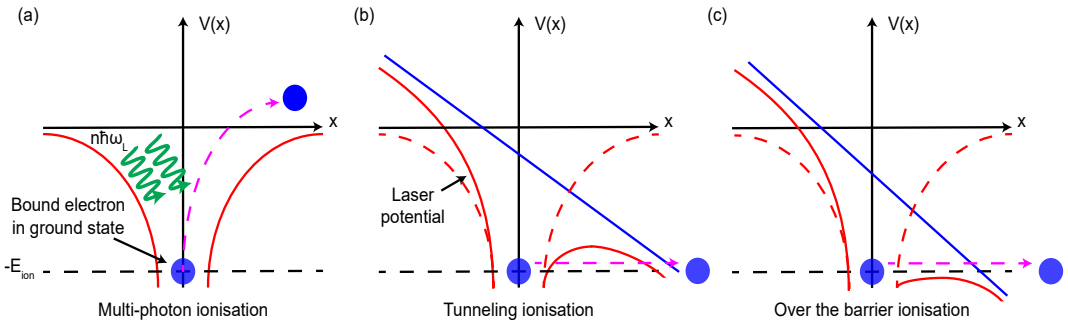

Figure 2.2: Ionisation processes relevant to laser-solid interactions. (a) Multi-photon ionisation; (b) Tunneling ionisation; (c) Barrier suppression ionisation.

at lower intensities than this. These processes are illustrated in figure 2.2

At lower laser intensities, ionisation can be achieved via multi-photon ionisation. Multi-photon ionisation (MPI) can proceed from $\sim 10^{10}$ W/cm^2 and, rather than photo-ionisation by a single photon as required by the previously discussed photo-electric effect, if the laser intensity is of the order of $\sim 10^{10}$ W/cm^2, then the flux of incoming photons is large enough to cause ionisation through the absorption of multiple photons, for example, the ionisation of the ground state of hydrogen would require 12 photons of 1 μm within a timescale of 0.5 fs. One caveat exists for this process however: the photons absorbed by the electron must be absorbed over the timescale of one laser cycle.

The kinetic energy of the electron ejected from the atom depends on the net number of photons absorbed, analogous to the photoelectric effect.

$$E_f = (n + s)\hbar\omega_L - E_{ion} \tag{2.18}$$

where n is the number of photons required to induce ionisation and s is the excess number of photons absorbed, $\hbar$ is Planck's constant, ω_L is the angular frequency of the absorbed photons and E_{ion} is the ionisation potential.

The second ionisation mechanism, important to laser-solid interactions, takes place at higher intensities and is a result of the electric field of the laser distorting the potential well of the atom, suppressing the Coulomb barrier preventing ionisation. The resultant potential is then given by:

$$V(x) = \frac{-Ze^2}{x} - eE_0x \tag{2.19}$$

where E_0 is the laser electric field.

There are two possible mechanisms for ionisation via suppression of the potential barrier:

tunnelling ionisation, which is the case described above; and barrier suppression, where the potential barrier is completely suppressed. The latter occurs at higher intensities; typically in situations where $I_L > 10^{14}$ W/cm^2.

The act of suppressing the Coulomb barrier results in the minimum laser intensity required for ionisation being reduced, i.e.

$$I_{BSI} = \frac{\varepsilon_0 c}{2} E_{BSI}^2 = \frac{4 \times 10^9}{Z^2} \frac{E_{ion}^4}{[eV]} \tag{2.20}$$

where E_ion is the ionisation energy. Considering the ground state of hydrogen, this would result in a minimum intensity for ionisation of $\sim 10^{14}$ W/cm^2.

In order to discriminate between ionisation mechanisms, Keldysh *et al.* proposed a parameter that determined the boundary between multiphoton and tunneling ionisation in terms of laser intensity: the *Keldysh adiabaticity parameter*, γ_k [76, 77]. This is given by:

$$\gamma_k = \omega_L \sqrt{\frac{2E_{ion}}{I_L}} \tag{2.21}$$

In the context of laser-solid interactions, a Keldysh parameter of $\gamma_k \gg 1$ indicates that the dominant ionisation process is mulitphoton ionisation. This can be thought of as the case when the target is irradiated by a high frequency, low field strength laser. Alternatively, this is also described by the case when the laser intensity at the front surface of the target is relatively low or moderate, for example, ionisation induced by the pedestal of the laser pulse intensity profile (see section 4.2.4 for further discussion on the properties of the pulse contrast of a high-power laser pulse).

Conversely, a Keldysh parameter of $\gamma_k \ll 1$ dictates that the barrier suppression ionisation mechanisms are dominant. This condition indicates that the laser intensity is large enough that the electric field of the laser is large enough to suppress the binding potential of the well trapping the electron to its parent atom through one of the two methods previously detailed.

Moreover, in addition to the direct field ionisation processes discussed, collisional processes are also prevalent in laser interactions with a solid density target. Recall our discussion of the kinetic energy transferred to the electron via multi-photon ionisation allowing it to escape its potential well. In this instance, the freed electron possessed excess kinetic energy after its escape; this energy may be large enough that, should the freed electron collide with a neighbouring atom in the dense material comprising the target, additional

atoms could be ionised. Collisional ionisation is increasingly important in solid-density targets once electrons have been freed through field-driven processes. Furthermore, inside the interior of the target, additional ionisation takes place; in part due to the generation of a return current to support the propagation of fast electrons [78, 79] and due to collisions involving the cold return current electrons, and also due to the high electric fields generated on the rear surface of the target [80–82]. These situations will be discussed in detail in section 2.6 and 2.9.1.

Finally, it is of interest to note that recent studies [83] have shown that the traditional boundary signified by the Keldysh parameter is not the most realistic picture of the photoionisation process that occurs in the a laser-solid interaction, and that coupling the Keldysh parameter with a scaled laser frequency parameter, Ω, which considers the range of frequencies and peak intensities possible, leads to a more realistic description of laser-induced ionisation processes.

2.4 Laser propagation in plasma

Our discussion of the interaction of a high-power laser pulse with a plasma should begin with a overview of the characteristics of the laser pulse itself. This will be covered in greater detail in **Chapter 4** (section 4.2.4) and thus will only be discussed briefly at this stage.

The main pulse of a high-power laser is often preceeded by a nanosecond long pedestal, known as amplified spontaneous emission (ASE), inherently generated in conventional laser amplification techniques (this will be covered in greater detail in section 4.2.4). In addition to this, several less intense pre-pulses and uncompensated dispersion may also be present. When focused, the intensity of this pedestal can be of the order of $\sim 10^{12}$ W/cm^2, which is sufficient to ionise the target prior to the arrival of the main ultra-intense pulse. An illustration of the temporal intensity profile of a typical laser pulse is shown in figure 4.3 in section 4.2.4.

As the ASE portion of the laser pulse interacts with the front surface of a target, ionisation, via one of the aforementioned mechanisms (see section 2.3), will occur. The material in the region of the focal spot expands outwards into vacuum, as illustrated in figure 2.3. Figure 2.3 (a) shows the density profile of the expanding plasma into vacuum, where the density falls off exponentially away from the target. At a distance z from a

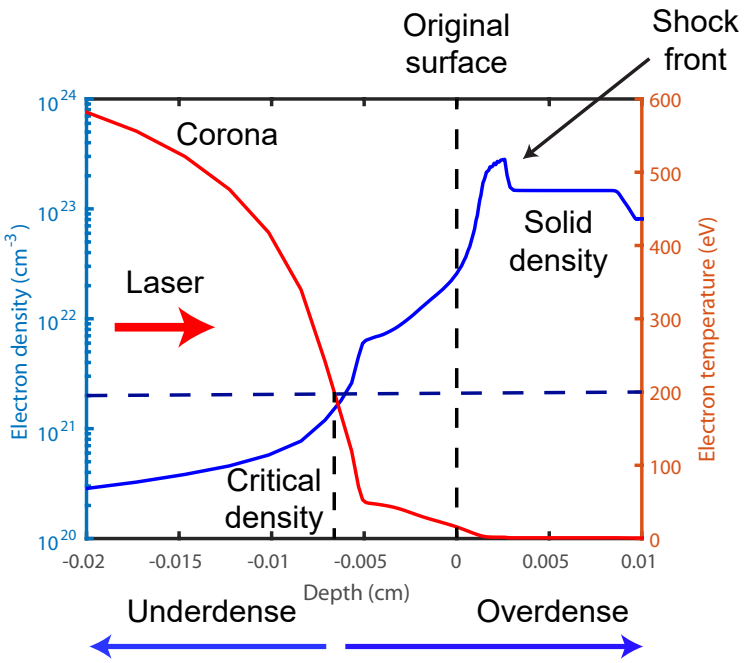

Figure 2.3: (a) Plot from a hydrodynamic simulation (using Helios-CR) showing temperature and density profiles produced by the interaction of a solid-density target and a laser pulse, with intensity $I_L = 5 \times 10^{12}$ W/cm^2.

solid density target, the plasma density profile can be expressed as [75]:

$$n_e(z) = n_0 e^{(-z/L_s)} \tag{2.22}$$

As this plasma expands outwards, a shock wave is launched into the target. The laser cannot propagate past a certain plasma density, denoted as the critical density, n_c, and the point where the laser is reflected or interacts with the plasma is known as the critical surface (discussed later in section 2.4).

The spatial extent of the pre-plasma generated in the initial interaction of the target and the preceding light is a critical factor in determining the absorption of energy from the laser into the target (discussed in section 2.5). This parameter is denoted by the plasma density scale length, L_s, and can be approximated as a function of the duration of the laser pulse, τ_L, and the ion sound velocity, c_0.

$$L_s \approx c_0 \tau_L \tag{2.23}$$

and where the ion sound velocity is given by:

$$c_0 = \sqrt{\left(\frac{Z_* k_B T_e}{m_i}\right)} \tag{2.24}$$

where Z^* is the charge state of the ion being considered, and m_i is the ion mass.

The shock wave mentioned previously is generated as a result of the rapid thermal expansion of the plasma into vacuum. It propagates into the target with a velocity given by [84]:

$$v_s = \frac{c_0}{2}\sqrt{1 + \frac{4\alpha}{\rho_0 c_0^2}P} + 1 \tag{2.25}$$

where α is a constant specific to the material under irradiation, P is the pressure exerted by the incident laser pulse, and ρ_0 is the solid density of the target. For ASE possessing an intensity of the order of $\sim 10^{12}$ W/cm^2, the velocity of the shock is approximately tens of microns per nanosecond and as such, dependent on the target thickness, the shock will reach the rear surface of the target within a few nanoseconds, leading to decompression, altering the interaction dynamics [84].

2.4.1 Electron motion in an electromagnetic field

From a fundamental perspective, the interaction of a laser with a plasma involves the acceleration of electrons due to the action of the electromagnetic nature of light [85, 86]. A good starting point for discussing this topic is the interaction of an electromagnetic plane wave and a single electron [87]. The motion of an electron in the presence of an electromagnetic field is described by the Lorentz force equation, $F_L = \frac{d\mathbf{p}}{dt} = e(\mathbf{E} + \mathbf{v} \times \mathbf{B})$. Here, $\mathbf{p} = \gamma m_e \mathbf{v}_e$ is the relativistically corrected electron momentum. Once an electron has been freed from its parent atom, it can then interact via the Lorentz force with an electromagnetic wave. This interaction typically takes the form of an oscillation due to the electric and magnetic field components.

By considering the electron velocity in the laser field, (composed of the electric and magnetic field components), the effects on the electron dynamics can be distinguished. Through rearrangement of the Lorentz force equation, the velocity of the particles can be written as:

$$\frac{d\mathbf{p}}{dt} = m_e \frac{d\mathbf{v}}{dt} = e(\mathbf{E} + \mathbf{v} \times \mathbf{B}) \tag{2.26}$$

The components of the electric and magnetic fields can then be separated by considering $\mathbf{B}$ to be equal to ~ 1 and $\mathbf{E}$ to be equal to c, i.e. the magnitude of $\mathbf{B} \ll \mathbf{E}$.

$$m_e \frac{d\mathbf{v}}{dt} = e\mathbf{E} \tag{2.27}$$

Equation (2.27) can be rewritten as shown in equation (2.28). This is due to the fact that the electric field can be represented as a plane wave (i.e. a simple harmonic oscillator, $\mathbf{E}(x,t) = \mathbf{E}_0(x)\sin(\omega_L t)$ and by making the assumption that $x = 0$:

$$\mathbf{v} = \frac{e\mathbf{E}_0}{m_e \omega_L}\cos(\omega_L t) \tag{2.28}$$

The constant terms on the right hand side of equation (2.28), $eE_0/m_e\omega_L$, can be represented by a dimensionless parameter known as the dimensionless laser amplitude, $a_0 = \mathbf{v}/c$. The dimensionless laser amplitude allows the qualification of whether the peak laser intensity is sufficiently large such that relativistic effects must be considered, i.e. whether the laser can be considered relativistically intense, such that the energy gained in one laser cycle by the electron oscillating in the electric field of the laser has a kinetic energy equal to, or greater than, the rest mass energy of an electron. The form of a_0 can be defined as:

$$a_0 = \frac{eE_0}{m_e c \omega_L} = \sqrt{\left(\frac{I\lambda_L^2}{1.37 \times 10^{18}}\right)} \tag{2.29}$$

where I is in W/cm^2 and λ_L is in microns. The terms on the right hand side of equation (2.29) allow for a simple determination of whether the laser can be classed as relativistically intense or not; if $a_0 \gg 1$ then the velocity gained by the oscillating electron becomes large enough that the contribution of the magnetic field of the laser must be included. Figure 2.4 shows the motion of an electron oscillating under the influence of the electromagnetic field of a laser for the cases of $a_0 \ll 1$ and $a_0 \gg 1$, i.e. the non-relativistic limit and the relativistic limit, respectively.

An electron interacting with a laser field in the non-relativistic limit will have an oscillation velocity $\ll c$ and consequently, the $\mathbf{v} \times \mathbf{B}$ term can be neglected. Thus, the electron will oscillate primarily due to the electric field of the laser in the direction of polarisation, at an oscillation frequency equal to that of the frequency of the laser. In contrast, when the electron oscillation velocity is increased such that $v \to c$, the influence of the magnetic field becomes significant to the motion of the electron. In this situation, the electric field

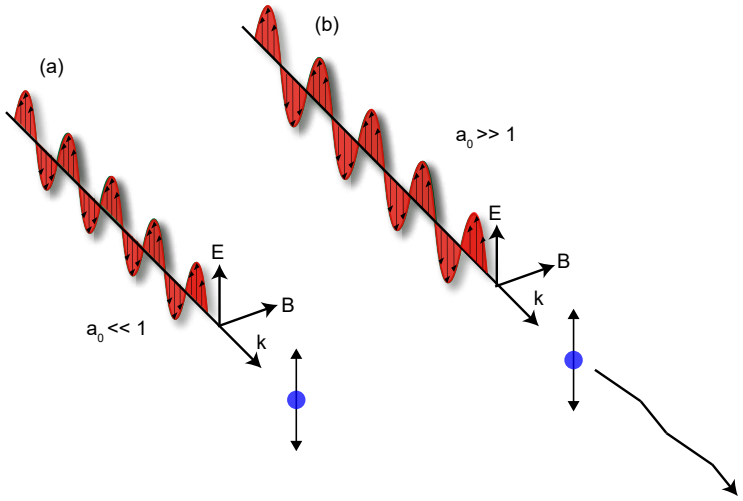

Figure 2.4: Motion of a single electron oscillating in an intense laser electromagnetic field for the cases of a (a) non-relativistic laser intensity ($a_0 \ll 1$) and (b) a relativistic intensity ($a_0 \gg 1$).

produces a transverse oscillation in the direction of polarisation. The $\mathbf{v} \times \mathbf{B}$ force term results in a force exerted on the electron directed along the laser propagation direction. The electric field reverses, as before, but the Lorentz force exerted on the electron is still directed along the direction of propagation. This motion results in the electron moving along a figure-of-eight trajectory in the laboratory frame due to the longitudinal momentum becoming comparable with the transverse momentum. This process occurs at twice the laser frequency, in contrast to the non-relativistic case that oscillated at the laser frequency.

The above is only valid for a spatially-infinite plane wave and electron in vacuum, where the electron gains no net energy from its interaction with the laser, a theory known as the Lawson-Woodward theorem [88]. The Lawson-Woodward theorem states that for a relativistic electron interacting with an infinite plane wave in an infinite region of vacuum, with no boundaries present, the electron would merely return to its original position upon the end of the interaction, with no net energy gained in the process. However, in reality, an electromagnetic wave is finite both spatially and temporally. This leads to variations in the gradients in the laser field, and results in a phenomenon known as the ponderomotive force, discussed in the following section (section 2.4.2), thus violating one of the key assumptions of the Lawson-Woodward theorem, summarised by Gibbon [89].

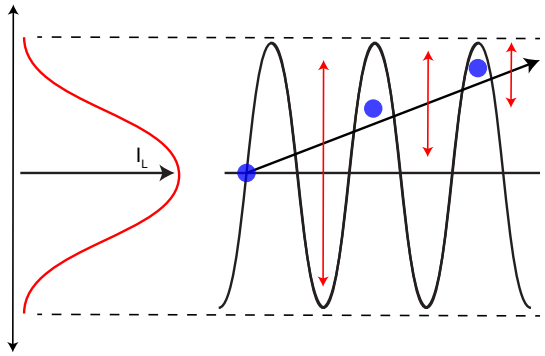

Figure 2.5: Illustration of electrons being driven to regions of lower intensity due to the action of the ponderomotive force.

2.4.2 The ponderomotive force

In a realistic interaction between a laser pulse and a plasma, the pulse has a transverse spatial-intensity profile, and a duration much longer than the period of the electromagnetic wave. As for the case of a plane wave, the combined effects of the electric and magnetic fields of the laser impart momentum to the electrons, causing them to drift from their initial position. Here, however, there exists a spatial intensity gradient across the pulse, and this results in the electron being driven from regions of high intensity, to lower intensities during the first half of its oscillation. As the electric field reverses over the second half of the laser period, the electron still feels a force driving it in the opposite direction but, due to the lower intensity at the wings of the pulse, this restoring force is weaker and thus the electron does not return to its initial position. Consequently, energy is gained by the electron, breaking the Lawson-Woodward theorem, whilst it is also driven out of the high intensity region of the pulse. The force acting to drive the electron to regions of lower intensity is often referred to as the *ponderomotive force*, illustrated in figure 2.5.

In the non-relativistic limit, i.e. when $a_0 \ll 1$ and the influence of the electric field dominates, the ponderomotive force can be expressed as [89]:

$$\mathbf{F}_p = \frac{-e^2}{4m_e\omega_L^2}\nabla\mathbf{E}^2 \tag{2.30}$$

It should be noted that the electric charge term is squared. Hence, it can be taken that the ponderomotive force drives all particles, regardless of charge, in the same direction from regions of higher to lower intensity.

As the intensity of the incident laser is increased a_0 approaches 1. With the velocity of the oscillating electron also approaching c, the contribution of the magnetic field to the

electron motion must be considered [90]:

$$\mathbf{F}_p = -m_e c^2 \nabla \sqrt{1 + \frac{a_0^2}{2}} \tag{2.31}$$

As previously discussed in section 2.4.1, the increased contribution of the magnetic field produces a force along the laser propagation direction, launching the electron into the target material; a process known as $\mathbf{j} \times \mathbf{B}$ heating, which will be described in greater detail in section 2.5.3.

2.4.3 Multi-electron motion in a laser field

Expanding upon the previous case of a plane-wave pulse interacting with a single electron, the case where a laser pulse interacts with many electrons is now considered.

Analogous to the situation where one electron encounters an electromagnetic wave and experiences a force resulting in an oscillation in the laser field, and along the laser propagation direction, an intense laser pulse interacting with the large number of electrons liberated during the ionisation processes discussed in section 2.3 sets up electron oscillations similar to the case discussed in the previous section. However, as previously discussed in section 2.2, a key phenomena of a plasma is its ability to collectively respond to electron displacement via plasma oscillations. The frequency of the plasma oscillations is characteristic of the plasma electrons (equation (2.14)).

As the laser pulse propagates through the expanding plasma, interacting with the freed electron population, the laser propagation is determined by the refractive index of the plasma. The refractive index is, in turn, governed by the density of the plasma, which as previously discussed in section 2.4 decreases exponentially out from the front surface of the target. This propagation is governed by the dispersion relation for electromagnetic waves in plasma, which can be derived via the method introuced by Macchi [90], summarised here:

First the wave equation for the electric field is obtained:

$$\left(\nabla^2 - \mu_0 \epsilon_0 \frac{\partial^2}{\partial t^2}\right) \mathbf{E} = \frac{1}{\epsilon_0} \nabla \rho - \mu_0 \frac{\partial \mathbf{J}}{\partial t} \tag{2.32}$$

The case under consideration here is that of a cold, homogeneous unmagnetised plasma, where the response to electromagnetic fields is due to the action of electrons only, a valid assumption on the timescales relevant to laser-solid interactions. Furthermore, the elec-

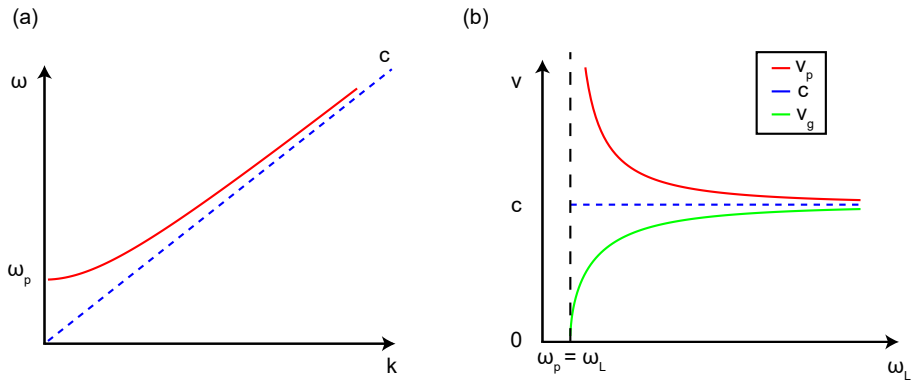

Figure 2.6: (a) Dispersion relation of an electromagnetic wave propagating through a plasma. The wave can only propagate if it has an angular frequency greater than ω_p. (b) Group and phase velocities of a wave propagating through a plasma as a function of its angular frequency. When $\omega_L = \omega_p$, the phase velocity tends to infinity, whilst the group velocity tends to zero. If $\omega_L > \omega_p$, the plasma is said to be underdense. Conversely, if $\omega_L < \omega_p$, the plasma is overdense.

tromagnetic wave propagating through the plasma is considered to be monochromatic. A dispersion relation, describing the propagation of laser light through a plasma, is obtained as:

$$\omega_L^2 = \omega_p^2 + c^2 k^2 \tag{2.33}$$

where ω_L is the laser frequency. A graphical depiction of the dispersion relation is shown in figure 2.6

The boundary condition marked as $\omega_L = \omega_p$ (in figure 2.6 (b)) is known as the "critical surface", and is associated with the electron density past which the laser can no longer propagate, known as the "critical density", given by:

$$n_c = \frac{\varepsilon_0 m_e \omega_L^2}{e^2} \approx 1.1 \times 10^{21} \, (\lambda_L[\mu m]) \tag{2.34}$$

The critical density is defined as the point at which the characteristic oscillation frequency of the plasma electrons, represented by the density dependent plasma frequency, is equal to the laser frequency, i.e. $\omega_L = \omega_p$. When this condition is met, the electrons can respond to the incoming laser and screen it, reflecting it. It is shown in figure 2.6 that, at this point, the phase velocity, $v_p = \omega/k$, of the laser tends to infinity, whilst the group velocity, $v_g = d\omega/dk$, tends to zero.

For the condition where $\omega_L > \omega_p$, the electron oscillations are too slow to respond to the laser and it can propagate. Regions satisfying this criteria are known as *underdense*, and have $n_e < n_c$. In contrast, should $\omega_L < \omega_p$, then the region of plasma would be termed

overdense. It is the phenomena originating in this region, at and beyond the boundary of the critical density, that is of greatest relevance to the results presented in this thesis, and several of the fundamental physical processes relevant to this case will be discussed in the coming sections.

In addition, in the context of the following section (section 2.5), it should be stated that there is a component of the electric field of the laser which is able to penetrate beyond the critical density of the plasma. This evanescent component is observed to decay exponentially and is diminished over a distance, characterised as the collisionless skin depth, l_s, given by:

$$l_s = \frac{c}{\omega_p} \tag{2.35}$$

Furthermore, figure 2.6 also shows the case of a relativistically intense electromagnetic wave, i.e. when $a_0 \gg 1$. The first thing to notice is that the value of the plasma frequency in the relativistic case is lowered when compared to the plasma frequency in the lower intensity limit. This can be explained through the relativistic mass increase experienced by the electrons via the Lorentz factor, γ as they are driven to velocities comparable to c. The relativistically corrected plasma frequency is given as:

$$\omega_p' = \sqrt{\frac{n_e e^2}{\varepsilon_0 \gamma m_e}} = \frac{\omega_p}{\sqrt{\gamma}} \tag{2.36}$$

This reduction in the plasma frequency, and the reduced ability of the electrons to respond with a similar level of effectiveness to the incoming laser pulse, in turn effectively alters the critical density value. This alteration can be thought of as the critical surface of the plasma being pushed back into the target, allowing the laser to propagate to higher densities, deeper into the target material. This phenomena is not classically allowed. The relativistically corrected critical density is given as:

$$n_c' = \frac{\varepsilon_0 \gamma m_e \omega_L}{e^2} = \gamma n_c \tag{2.37}$$

It can be seen from equation (2.37) that the critical density of the plasma increases by the same factor, γ. The plasma skin depth (equation (2.35)), is also increased by the same factor, (corrected as: $l_s' = c/\omega_p'$). Thus, the evanescent component of the electric field of the laser can also penetrate deeper into the target, beyond the corrected critical surface. Should the Lorentz factor of the electron population increase such that l_s' is of the order

of the target thickness, relativistic induced transparency (RIT) occurs [91–93].

Pure relativistically induced transparency, however, is currently impossible to achieve with solid-density targets using current state-of-the-art high-power laser systems in use today; for example, to successfully enable laser propagation through a solid density aluminium target a laser intensity of $I_L > 10^{23}$ W/cm^2 would be required. This is clearly an order of 10^2 times greater than the current peak intensities available.

However, the onset of RIT is still possible through a combination of laser-induced target expansion (discussed in section 2.4) and relativistic effects. In this way, it is possible, using current state-of-the-art technology to achieve the condition for RIT: $n_e/\gamma n_c < 1$. One corollary to this statement is that, in addition to achieving this condition, the onset of RIT is also dependent on the thickness of the foil under irradiation as it approaches, or has dimensions smaller than, one laser wavelength. A transparency threshold can then be obtained incorporating the foil thickness, l [94, 95],

$$a_0 > \pi \frac{n_e l}{n_c \lambda} \tag{2.38}$$

The relevance of RIT in the context of its importance to ion acceleration in the ultrathin target regime explored in this thesis, and the physical processes by which the combination of target expansion and relativistic effects lead to its onset will be discussed in detail in section 2.9.

2.5 Laser energy absorption to plasma

The previous section was concerned with the collective electron dynamics associated with the interaction of a laser pulse and a plasma, the expansion of a solid-density target, and the propagation of an electromagnetic wave through this expanding plasma. However, there must exist an energy transfer between the electromagnetic fields and the plasma electrons freed from the target in order that these processes occur. This section will discuss the mechanisms by which laser energy can be transferred to the plasma, a process fundamental to the acceleration of electrons, and the resulting physical processes arising due to them.

There are two regimes in which absorption of the laser energy occurs; the first that is described is the collisional transfer of energy, relevant at lower laser intensities (i.e. $< 10^{14}$ W/cm^2), present in the light preceding the main pulse. The collisional process responsible

for the initial bulk heating of the target, prior to the arrival of the main part of the pulse, is inverse bremsstrahlung [96]. Despite the terminology of "collisional", in this regime electrons still gain energy from the electric field of the laser. However, due to collisions with ions this energy is absorbed into the plasma before the electrons can return to their original positions and recouple their energy to the pulse. Mechanisms in this regime are dependent on the mean free path of the electrons being less than the dimensions of the plasma, ensuring collisions dominate over field effects.

As the intensity at the critical surface of the target increases over the pulse temporal intensity profile, a transition from collisional to collisionless absorption processes occurs [97], where field driven electron oscillations dominate. The magnitude of the electromagnetic fields of the laser is comparatively greater than before, and hence the oscillations of the electrons in the laser field are large enough to drive them beyond the critical surface of the target and consequently, the influence of the laser. Due to the increased velocity gained by the electrons in the interaction, the mean free path can be considered larger than the spatial extent of the plasma. Thus, collisional processes are trivial compared to field-driven effects at intensities $> 10^{12}$ W/cm^2. At relativistic intensities ponderomotive $\mathbf{J} \times \mathbf{B}$ heating, driven by the ponderomotive force, dominates [98]. Intermediate to collisional inverse bremsstrahlung and $\mathbf{J} \times \mathbf{B}$ heating lies two important electric field-driven processes: resonance absorption and vacuum heating [99].

2.5.1 Resonance absorption

At the intensities considered in this thesis ($> 10^{18}$ W/cm^2), i.e. relativistic laser intensities, collisionless absorption mechanisms dominate electron production. The first collisionless process by which laser-energy is coupled into the target is resonance absorption. In this mechanism, a p-polarised laser pulse interacts with the front surface of a solid-density target at an oblique angle [100]. Crucially, the density gradient of the pre-plasma in front of the target must be relatively shallow, i.e. $L_S > \lambda_S$, where L_S is the density scale length of the plasma. This process is prevalent for linearly polarised pulses where the plane of polarisation of the pulse is normal to the target surface, i.e. p-polarised (see section 2.1.1), and becomes significant at intensites $> 10^{12}$ W/cm^2. In resonance absorption, the parallel component of the electric field tunnels through to the critical surface, where it excites a plasma wave in the form of density perturbations. The terminology of "resonance" arises from the optimum conditions for the generation of the plasma wave: at resonance, when

the laser frequency equals the plasma frequency, i.e. at the critical surface.

The efficiency of this process is dependent on the angle of the incident laser pulse [101]:

$$sin\theta = (\frac{c}{2\omega_L L_s})^{1/3} \tag{2.39}$$

where the optimum angle of incidence of the pulse can be determined for the laser frequency and plasma scale length under consideration.

The pulse propagates through the expanding plasma, up to the critical density surface, where it is reflected. However, due to the oblique incidence the pulse, the point of reflection is modified to $n_{crit}cos^2(\theta)$. This is due to the need to include the k-vector of the laser in the dispersion relation (equation (2.33)). This can be rewritten as:

$$\omega_L^2 = \omega_p^2 + c^2k_x^2 + \omega_L^2 sin^2(\theta) \tag{2.40}$$

At the point of reflection, the electric field of the pulse acts normal to the surface of the target and it can tunnel through the critical surface, setting up resonant plasma waves in the material. These plasma waves are driven at the laser frequency beyond the critical surface where the restoring force on the electrons is reduced due to the evanescent decay of the laser electric field beyond this point. An illustration of resonance absorption is shown in figure 2.7 (a).

The efficiency of resonance absorption tends to decrease with increasing laser intensity: as the intensity increases, the ponderomotive force steepens the density profile, and the plasma scale length decreases, so that $L_s < \lambda_L$. Upon entering this regime, vacuum heating begins to dominate over resonance heating, as discussed below.

2.5.2 Vacuum (Brunel) heating

In vacuum heating, as with resonance heating, there is an angular dependence on the absorption efficiency but due to the decreased scale length, the generation of resonant plasma waves is inhibited. As was the case previously, Vacuum heating is dominant for p-polarised pulses but, crucially, increases in importance at intensities above 10^{17} W/cm^2, and an illustration of the process is shown in figure 2.7 (b).

In this process, electrons oscillate in the electric field of the laser, but in contrast to the case of resonance absorption, plasma waves cannot be generated due to the sharp plasma boundary. Instead, electrons are dragged out of the target by the laser field in the first

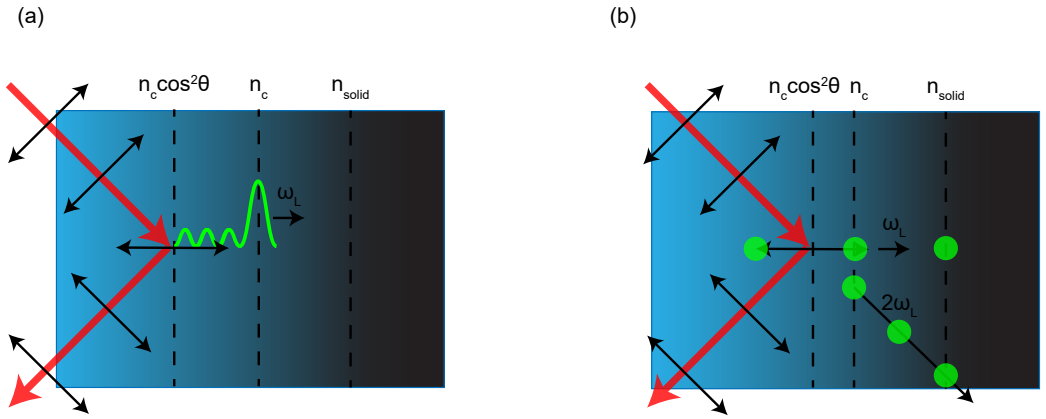

Figure 2.7: (a) Schematic illustrating the resonance absorption process. The incident pulse is p-polarised (with respect to to the target surface) onto a long density scale length pre-plasma. Energy is transferred to the electrons via resonant plasma waves. (b) Schematic of the vacuum and $\boldsymbol{J} \times \boldsymbol{B}$ absorption mechanisms. Here, the pulse is incident on a relatively steeper density scale length pre-plasma. In vacuum heating, electrons are pulled from target surface by the parallel component of the electric field and accelerated back into the target as the direction of the field reverses. In $\boldsymbol{J} \times \boldsymbol{B}$ heating, electron bunches are launched into the target along the laser propagation direction, at twice the laser frequency.

half of the cycle and then, as the field changes direction in the second half of the laser cycle, re-accelerated into the target. Once they have crossed the critical density surface, the strength of the laser electric field decays up to a skin depth into the material, and so the restoring force acting on the electrons is reduced. This leads to a net gain of energy by the electrons, and as such, results in a current of energetic electrons injected into the target along the target normal axis [102].

2.5.3 J × B heating

The third and final absorption process discussed is pondermotive $\mathbf{J} \times \mathbf{B}$ heating, which dominates in the relativistic regime. Here, electrons are directly accelerated by the laser-field - they are accelerated along the axis of laser propagation via the ponderomotive force at twice the laser, whereas in the previous cases, the electrons have been primarily accelerated along the target normal direction by interaction with the laser field.

Recalling sections 2.4.1 and 2.4.2, the oscillating $\mathbf{v} \times \mathbf{B}$ component of the laser field begins to dominate the motion of electrons for intensities greater than 10^{18} W/cm^2, at which point the electrons motion becomes relativistic and experience a force along the laser propagation direction. $\mathbf{J} \times \mathbf{B}$ heating is a similar process: the ponderomotive force moves electrons from regions of high intensity to lower intensity but, in addition, they are

also heated by the $\mathbf{v} \times \mathbf{B}$ component. The force exerted on the electrons along the laser propagation direction is given as:

$$\mathbf{F} = \frac{-m_e \partial v_{os}^2(x)}{\partial x}(1 - cos2\omega_L t) \tag{2.41}$$

where v_{os} is the electron quiver velocity. The first term on the right hand side of equation (2.41) represents the ponderomotive force, as described previously. The second term in equation (2.41) is the fast oscillating component that contains the high frequency term $2\omega_L$, arising from the $\mathbf{v} \times \mathbf{B}$ term of the Lorentz force. Thus, as this term acts to oscillate electrons at twice the laser frequency, they are driven into the target in bunches at $2\omega_L$. An illustration of this mechanism is shown in figure 2.7 (b).

2.6 Fast electron transport

The previous section discussed the mechanisms by which energy is transferred from the laser to the electrons at the critical density surface. Beyond this point, the electrons injected into the target no longer feel the influence of the laser as they continue to propagate. This population of energetic electrons is accelerated to relativistic velocities via the laser pulse, and are referred to as "fast" electrons.

Of key importance to the physics of fast electron transport is the electrical resistivity of the target, which influences the transport of the fast electrons via the generation of magnetic fields. In addition, the electrical resistivity is also significant due to its role in the growth of instability processes that affect the beam transport. The properties of the fast electron beam and the influence of the electrical resistivity of the target on the transport of fast electrons will be discussed in this section.

2.6.1 Fast electron spectrum

The absorption mechanisms discussed in the previous section accelerate a population of the plasma electrons into a target material at relativistic velocities. The sheer number of electrons accelerated by the laser pulse is such that currents of many mega-Amperes are reached. At non-relativistic intensities, the fast electron distribution is Maxwellian in nature:

$$f(E_f) = N_f \sqrt{\frac{4E_f}{\pi(k_B T_e)^3}} exp(-\frac{E_f}{k_B T_e}) \tag{2.42}$$

where E_f is the fast electron energy and $k_B T_e$ is the fast electron temperature.

When the regime of relativistically intense interactions is entered into however and collective heating via collisionless absorption mechanisms begins to dominate over collisional processes, the single-temperature Maxwellian distribution becomes a relativistic, bi-maxwellian electron distribution [103]. The fast electrons can then be represented by a Maxwell-Juttner distribution, i.e.:

$$f(\gamma) = N_f \frac{\gamma^2 \beta}{\frac{k_B T_e}{m_e c^2} K_2(m_e c^2 / k_B T_e)} \exp\left(-\gamma \frac{k_B T_e}{m_e c^2}\right) \tag{2.43}$$

where $\beta = v/c$, $\gamma = \frac{1}{\sqrt{1-\beta^2}}$ and K_2 is the modified Bessel function of the second order. N_f is the number of fast electrons generated in the interaction between the pulse and the target material, i.e.

$$N_f = \frac{\eta_{L\to e} E_L}{k_B T_e} \tag{2.44}$$

where $\eta_{L\to e}$ is the laser to fast electron energy conversion efficiency. Evaluations of $\eta_{L\to e}$ are still a subject of many investigations in the field, but the total absorption of the laser energy by the fast electrons has been studied by Davies [99] and Ping *et al.* [104] on solid-density foils irradiated by short laser pulses.

In the above, $k_B T_e$ is the fast electron temperature, a key characteristic for fast electron and magnetic field generation studies. Several investigations of the scaling of this parameter with the intensity of the incident pulse have been carried out over the years, with two significant models arising from this work, the first for laser intensities below 10^{17} W/cm^2, and the second for relatively higher laser intensities.

At the lower range of laser intensities, Beg *et al.* [79] demonstrated experimentally that the fast electron temperature scaled with irradiance as $k_B T_e \propto \left(I_L \lambda_L^2\right)^{1/3}$. Numerically, Gibbon *et al.* [105] derived the same scaling for similar interaction conditions. At relativistic laser intensities, Wilks *et al.* [101] determined that the temperature of the fast electron population scales as $k_B T_e \propto (I_L \lambda_L^2)^{1/2}$. Numerical studies of the fast electron temperature scaling at these intensities arrived at the following:

$$k_B T_e = m_e c^2 \left(\sqrt{1 + a_0^2} - 1\right) \tag{2.45}$$

which can be simplified as:

$$k_B T_e = m_e c^2 \left(\sqrt{1 + \frac{I_L \lambda_L^2}{1.37 \times 10^{18} \text{ Wcm}^{-2} \mu\text{m}^2}} - 1 \right) \tag{2.46}$$

2.6.2 Current neutrality

The crux of the studies of the transport of fast electrons in conditions relevant to the interaction of a high-power laser pulse and a solid-density foil is the assumption of the neutrality of the electric currents propagating through the material. This is stated by the following:

$$\mathbf{j}_f + \mathbf{j}_r \approx 0 \tag{2.47}$$

where $\mathbf{j}_f$ and $\mathbf{j}_r$ are the fast electron and return current densities, respectively. The necessity of current neutrality can be demonstrated by the following example.

If typical parameters of an intense laser-solid interaction are considered, for example, a pulse energy of 100 J and pulse length of 1 ps, the current carried by the fast electron beam is of the order of mega-Amperes. The electric fields generated by these currents have been seen to be of the order of 10^{15} V/m, and are given by Ohm's law:

$$\mathbf{E} = -\eta \mathbf{j}_f \tag{2.48}$$

For the same laser parameters outlined above, the typical values of the velocity of the fast electron beam and its density are approximately c and 10^{26} m^{-3}, respectively. The resultant current density is calculated as:

$$j_f = e n_e \mathbf{v}_f \approx 10^{16} \text{ A/m}^2 \tag{2.49}$$

and if we consider the area of the beam to be the same as the area defined by the radius of the laser focus (~ 5 μm), then the resultant current is of the order of mega Amperes. Currents of this magnitude will lead to the growth of electric fields, such as those discussed above, on the timescales of a few femtoseconds. Electric fields of the magnitude discussed will thus act to halt electron propagation within a few microns [106]. The maximum current that can propagate through a solid target is given by the Alfvén-Lawson limit [107], which can be written as:

$$I_A = \frac{\beta\gamma m_e c^2}{e} = 17000 \beta\gamma \text{A} \tag{2.50}$$

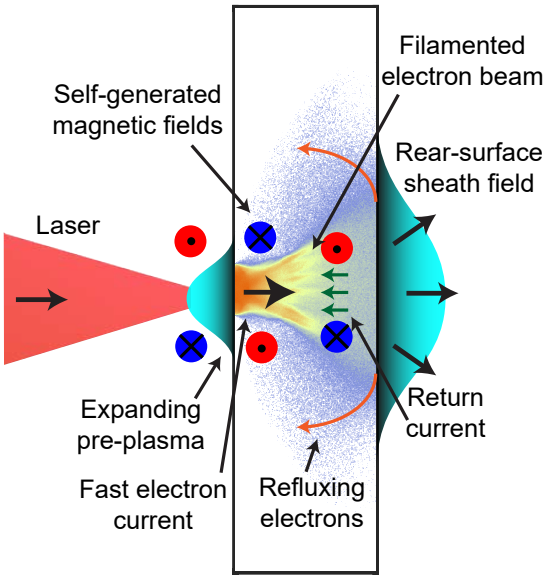

Figure 2.8: Mid-plane view of fast electron transport in a target, obtained via a numerical simulation performed using the hybrid-PIC code, Zephyros. Note the injection of the fast electron population into the target, with the spatially-localised return counter-propgating with respect to it. Furthermore, evidence of beam filamentation is visible in the latter half of the target.

where $\beta = v/c$ and $\gamma = \frac{1}{\sqrt{1-\frac{v^2}{c^2}}}$. Should the current exceed the Alfvén-Lawson limit, the strength of the self-generated magnetic field will be such that the electrons will be turned back towards its source. Using typical experimental parameters, this limit is of the order of 10s of kilo-Amperes, orders of magnitudes lower than the expected current of the fast electron beam.

Thus, in the relativistically-intense regimes relevant to this thesis, there will be no propagation throughout the target unless local charge neutrality is achieved. This charge neutrality is made possible by the generation of a counter-propagating, return current. [108]. This current must have a density approximately equal to the fast electron beam, as shown in equation (2.47). Figure 2.8 demonstrates the current neutralisation process.

The timescale for charge neutralisation to occur is given by $t_{f-r} = 2\pi/\omega_{pe}$. This is approximately less than 1 fs, although this can vary depending upon the target [109]

In addition, the return current must be spatially localised with the fast electron beam to avoid runaway magnetic field growth. Bell *et al.* [110] demonstrated this by considering the conservation of energy, as follows: suppose, for a fast electron beam injected into a target at an angle normal to the surface, with a radius r_f, the return current, moving in opposition to it, has a slightly larger radius $r_r = r_f + \Delta r$. Both populations carry the same current, I to ensure current neutralisation, but possess current densities $j_f = I_f/\pi r_f^2$, and

$j_r = I_r/\pi r_r^2$, for the fast and return currents, respectively. The magnetic field generated in the target is then given by:

$$B = \frac{\mu_0 I}{2\pi} = \begin{cases} r(r_f^{-2} - r_r^{-2}), & \text{if } r < r_f \\ r^{-1} - r r_r^{-2}, & \text{if } r_f < r < r_f \\ 0, & \text{if } r_r < r \end{cases} \tag{2.51}$$

If $\Delta r \ll r_f$, then the peak magnetic field is $B_{max} = \mu_0 I(\Delta r/r_f)/\pi r_f$. The corresponding energy contained within the beam of electrons is then $E_{BL} = \mu_0 I_f^2(\Delta r/r_f^2)/4\pi$.

Considering some typical parameters of laser-driven fast electron currents, i.e. $r_f = 5$ μm and $I = 20$ MA, the maximum magnetic field is approximately $10^6(\Delta r/r_f)$ T and the energy is $\sim 40(\Delta r/r_f^2)^2$ J/μm. Thus, Δr must be much smaller than r_f for the conservation of energy to hold: the magnetic energy can not be greater than the absorbed laser energy. This illustrates how the return current cannot follow a vastly different path from that taken by the fast electron current, and why local current neutrality must hold true.

2.6.3 Collisions, heating and electrical resistivity

As the fast electron population propagates through the target, its transport may be affected by collisions with the background populations of electrons and ions. These interactions may occur via elastic and inelastic scattering, which may take the form of "electron-electron" or "electron-ion" collisions. In addition, energy may also be lost via excitation, ionisation and radiation emission (i.e. bremsstrahlung) [111]. Furthermore, the generation of electric and magnetic fields is also a factor in the loss of energy experienced by the fast electrons, although the contribution from collisions and radiation dominate.

The loss of energy from the fast electrons is quantified by the stopping power dE/ds. The stopping power is calculated by summing the individual contributions from each mechanism by which energy is lost, i.e.:

$$\left(\frac{dE}{ds}\right)_{total} = \left(\frac{dE}{ds}\right)_{collisions} + \left(\frac{dE}{ds}\right)_{radiative} \tag{2.52}$$

To illustrate the contributions to the total stopping power of the collisional and radiative components, electron stopping curves were generated using the ESTAR stopping tables

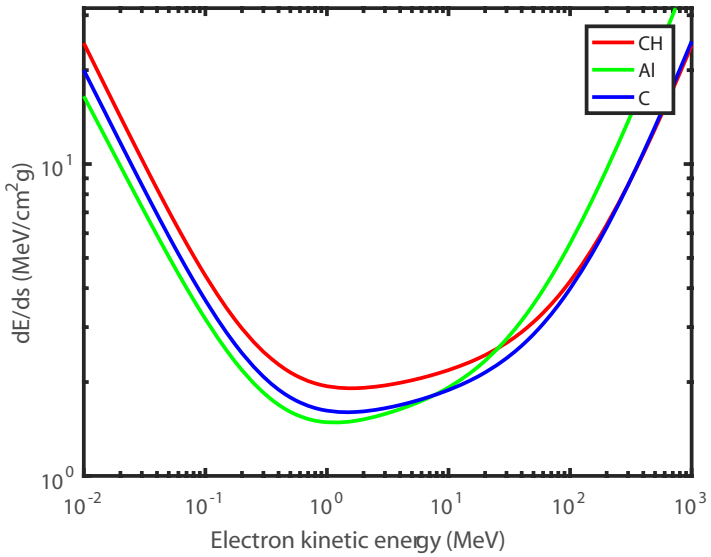

Figure 2.9: Example stopping curves generated generated in ESTAR [112] for carbon (blue), aluminium (green) and plastic (red) as a function of fast electron energy. At lower energies the dominant loss mechanism is via collisional stopping, whilst radiative losses dominate above ~ 1 *MeV.*

database [112]. The calculations performed by ESTAR employ the Bethe theory of particle stopping to calculate the collisonal component, whilst theoretical bremsstrahlung cross section were used to obtain the radiative losses. The example stopping curves are shown in figure 2.9.

Studying these stopping curves highlights that collisional losses dominate for lower energy electrons (i.e. 0.01 to 1 MeV), whereas higher energy electrons are more susceptible to radiative losses. Mean fast electron energies generated in laser-solid foil interactions are typically > 1 MeV, and thus the fast electron current is effectively collisionless.

The same cannot be said of the return current drawn locally opposite to it, which is composed of thermal electrons and is highly collisional. Therefore, the propagation of the return current heats the background plasma through Ohmic heating, governed by the relation:

$$\mathbf{j}_r \mathbf{E} \approx -\eta \mathbf{j}_f^2 \tag{2.53}$$

Equation (2.53) is proportional to the current density of the return current, and thus, heating predominantly occurs in region of highest current density, i.e. along the fast electron propagation axis.

Ohmic heating of the target by the return current is of critical importance to fast electron

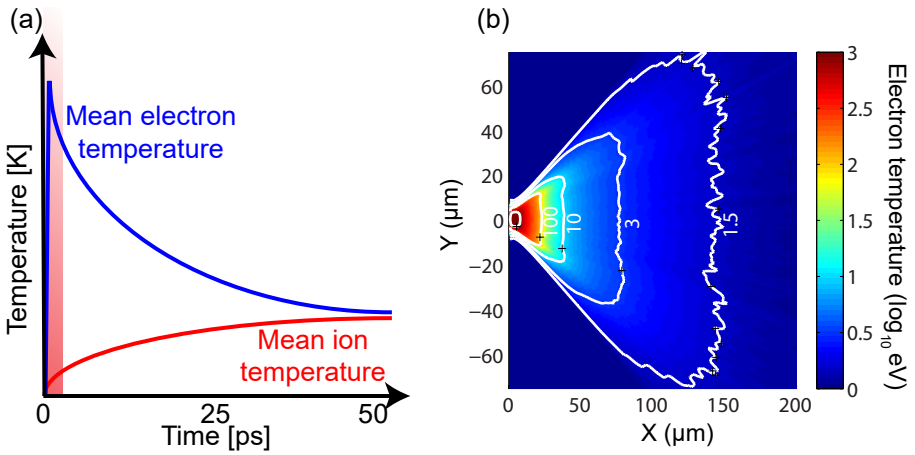

Figure 2.10: (a) Illustration of the temperature evolution of electrons and ions in a target irradiated by an intense laser pulse. Adapted from Mazevet et al. [113]. The highlighted region represents the transient WDM regime of interest, and marks approximately 1 ps after the interaction; (b) Example midplane [X-Y] view of the the electron temperature in a target, generated via a hybrid-PIC code. Contours are drawn for isothermals corresponding to 1.5, 3, 10 and 100 eV.

transport due to its role in changing the background electrical resistivity, via heating the background electrons. Crucially, the heating induced by the return current results in spatial variations of electrical resistivity which in turn generates large self-generated magnetic fields (explored in section 2.7.1), influencing the transport of the fast electrons.

Due to the mass differences between electrons and the ions that make up the background plasma, electron heating occurs on far faster timescales than that of ions [113]. This has the effect of creating an intermediate "transient Warm Dense Matter (WDM)" state over the duration of the laser pulse and thus, the fast electron generation, where the material temporarily retains its solid structure during the rapid thermal excitation of the target material [114]. Figure 2.10 highlights the timescales for the heating of the background plasma. The highlighted region illustrates the disparity in temperatures between the electron and ion populations and the timescales over which this regime is important ($\sim$ over the first picosecond after the interaction).

The temperature of the background plasma in the WDM state is relatively cool (< 20 eV) and, as shown in figure 2.11 (an example resistivity-temperature profile for aluminium) the resistivity of the material varies strongly with temperature in these conditions, despite continuing to possess solid structure. In a solid, atoms are arranged into a crystalline, lattice-like structure, for materials described as "ordered", or a non-crystalline structure, lacking long-range order, in the case of materials termed "disordered".

Solids may be categorised into metals, insulators and semiconductors depending on their

electronic behaviour at room temperature. These classifications arise from characteristic properties of the materials themselves, where the energy levels available to the electrons in the material are no longer discrete, as in the case of a single atom, but instead form "bands". In the state where the electrons are still bound to their parent atoms, this band is known as the "valence band", whilst freed electrons exist in the "conduction band".

An important parameter in the band structure theory of solid resistivity is the the "Fermi energy". The Fermi energy is the maximum energy of the highest occupied state at a temperature of absolute zero. In solid density metals, this energy is approximately 10 eV, implying that, at typical room temperatures, metallic electrons are able to move freely to the conduction band. The Fermi energy is important when considering semiconductors as doping the material with electrons enables the position of the Fermi energy level to be controlled. This can be illustrated by the relatively narrower band gaps for semiconducting materials as opposed to insulators.

Recent work investigating fast electron transport in thick targets (on the scale of tens-to-hundreds of microns) [115,116] demonstrated that the low-temperature electrical resistivity is of critical importance to the electron beam transport physics due to the sensitivity of transport to variations in resistivity, and, as a result of this sensitivity, the instabilities which are seeded [117]. At these low temperatures (tens of eV), the resistivity-temperature profile is defined by the degree of lattice structure of the material [118] (i.e. the level of how ordered or disordered a material is, for example, the difference between diamond and vitreous carbon). Comparing metals, insulators and semiconductors, vast differences have been observed; demonstrated in figure 2.11.

The interaction of an intense laser pulse with a solid-density foil will result in the interaction region becoming superheated to temperatures of the order of 1000s of eV (as shown in figure 2.10). Depending on the material, this will result in the ionisation of this region. In areas of the target located outside of here however, the temperature continually decreases with increasing distance. The temperature can be an order of $\sim 10^2 - 10^3$ lower in the deeper sections of the target. In the hot interaction region, the resistivity of the background plasma can be accurately described using the Spitzer model of resistivity [119], where the collisional cross-section decreases due to the increase in the electron mean free path.

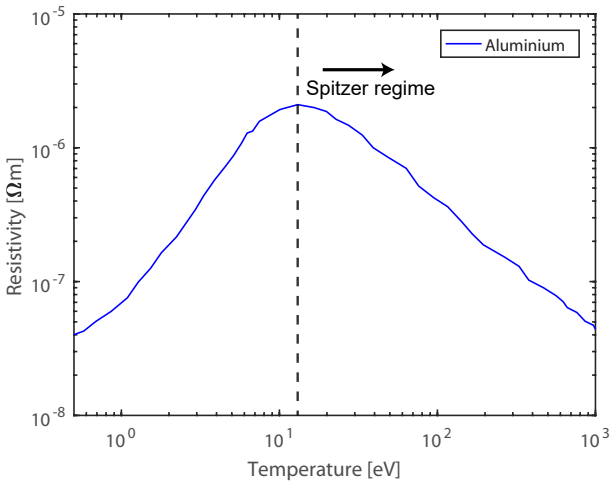

Figure 2.11: Electrical resistivity-temperature profiles for an example metal, aluminium. The transition to the Spitzer regime is observed at ~ 11 *eV.*

The relationship between electrical resistivity, η, and temperature, T_e, is given by:

$$\eta = \frac{Z\pi e^2 m_e^{1/2}}{(4\pi\varepsilon_0)^2 k_B T_e^{3/2}} \ln\Lambda \tag{2.54}$$

where η is dependent on the target material, given by the atomic number, Z; the electron temperature, and contributions of collisions to the heating of the material, $\ln\Lambda$, named the Coulomb logarithm. The Coulomb logarithm has been estimated to be $\ln\Lambda \geq 2$ [120]. The Spitzer model of electrical resistivity is only valid for a fully ionised, non-degenerate plasma. Thus, in the cooler regions beyond the first tens of microns, application of the Spitzer model to describe the resistivity is incorrect [121].

In the regions of the target where intermediate states of WDM are present, the relationship between electrical resistivity and temperature is not fully described by either the band theory of solid conductivity, or by the high-temperature Spitzer model; application of the Spitzer model to low-temperature plasmas results in incorrect resistivity predictions. Recent theoretical studies have shown that the use of *ab initio* quantum molecular dynamics (QMD) simulations based on density functional theory (DFT) [122,123], coupled with the Kubo Greenwood equation [124] provides a more accurate description of the behaviour of the resistivity-temperature relationship at low temperatures. The detailed discussion of the QMD-Kubo Greenwood method is beyond the scope of this thesis, however, a brief summary of the process is laid out in section 5.2.1.

2.7 Self-generated magnetic fields

The generation of strong magnetic fields in intense laser-solid interactions has been extensively studied [4, 5, 63, 101, 125–127]. A number of mechanisms exist by which magnetic fields are generated over the course of intense laser-solid interactions, relevant to the themes of this thesis. These include resistively-generated magnetic fields that strongly influence the propagation of fast electrons [54, 128]; magnetic fields generated by the Weibel instability (WI) [129]; and via the Biermann battery mechanism [130]. Understanding the processes surrounding these magnetic field generation mechanisms, and what influences them, is of crucial importance for applications such as FI ICF [126], and investigations of relativistic plasma astrophysics including jet formation [131] and the dynamics of SNe remnants [45]. This section explores the schemes relevant to this thesis by which the generation of magnetic fields are generated.

2.7.1 Resistive magnetic fields in solids

To paraphrase reference [118], it may be expected that the sheer number of fast electrons produced by an intense laser pulse would flood the target. However, this is not the case. Realistically, the current neutrality relation (equation (2.47)) does not depict a total cancellation of the fast electron current (as shown by $\mathbf{j}_f + \mathbf{j}_r \approx 0$) and, as such, resulting current imbalances lead to the growth of large magnetic fields. The magnetic field associated with such an imbalance can be determined via Ampere's law (equation (2.4)), i.e.:

$$\nabla \times \mathbf{B} = \mu_0(\mathbf{j}_f + \mathbf{j}_r) + \mu_0\varepsilon_0\frac{\partial \mathbf{E}}{\partial t} \tag{2.55}$$

where the displacement current term on the right hand side of equation (2.55) can be neglected. Magnetic field generation during the propagation of a large current of fast electrons can be described by combining Ohm's law and Faraday's law. Recall that Ohm's law (equation (2.48)) is $\mathbf{E} = -\eta\mathbf{j}_r$, and Faraday's law (equation (2.3)) is $\nabla \times \mathbf{E} = \dfrac{\partial \mathbf{B}}{\partial t}$. Substituting Ohm's law into equation (2.55) results in:

$$\mathbf{E} = \eta\mathbf{j}_f - \frac{\eta}{\mu_0}\nabla \times \mathbf{B} \tag{2.56}$$

where the $\nabla \times \mathbf{B}$ term corresponds to the resistive diffusion of the magnetic field, which in the limit of strong heating becomes negligible. Thus, $\mathbf{E} = \eta\mathbf{j}_f$.

The self-generated magnetic field can be shown to evolve with time as:

$$\frac{\partial \mathbf{B}}{\partial t} = \nabla \times \eta \mathbf{j}_f \tag{2.57}$$

$$\frac{\partial \mathbf{B}}{\partial t} = \eta \nabla \times \mathbf{j}_f + \nabla \eta \times \mathbf{j}_f \tag{2.58}$$

In equation (2.58), the first term acts to produce a magnetic field that moves electrons to regions of higher current density, whereas the second term is indicative of a magnetic field that will move electrons towards regions of higher resistivity [132]. As the spatial intensity profile of the laser focal spot is typically Gaussian in nature, this will result in the highest current density being located along the central axis of propagation. Thus, the first results in an azimuthal magnetic field which acts to pinch the electron beam [118]. The second term in equation (2.58) generates a magnetic field that exists due to transverse gradients in the electrical resistivity across the beam. These gradients arise from Ohmic heating by the return current population which, as previously discussed, is greatest along the axis of the beam, diminishing towards the edge of the beam. As the return current is spatially-localised with the fast electron beam, the level of Ohmic heating beyond the edges of the beam is minimal, and therefore a large temperature gradient exists in this region. The magnetic fields generated by this temperature gradient will force electrons to regions of higher resistivity, which will result in either the hollowing or the collimation of the beam, depending on the resistivity gradients of the material.

Investigations of beam hollowing and collimation of fast electron currents by self-generated magnetic fields have been carried out by Davies *et al.* [133, 134], Norreys *et al.* [135] and Maclellan *et al.* [128], and Bell and Kingham [118].

2.7.2 Biermann battery process

In astrophysics, the Biermann battery mechanism is a process by which a weak seed magnetic field can be generated in the absence of a seed field. The process was proposed by Ludwig Biermann in 1951 [130], and arises to the existence of perpendicular electron density and temperature gradients [136, 137]. It is commonly thought to be the progenitor of cosmic magnetic fields that are then amplified via turbulent flows and kinetic instabilities, such as the Weibel Instability (WI), resulting in the microGauss magnetic fields observed in the interstellar medium [138].

The Biermann battery mechanism is also proposed to be the driver of self-generated

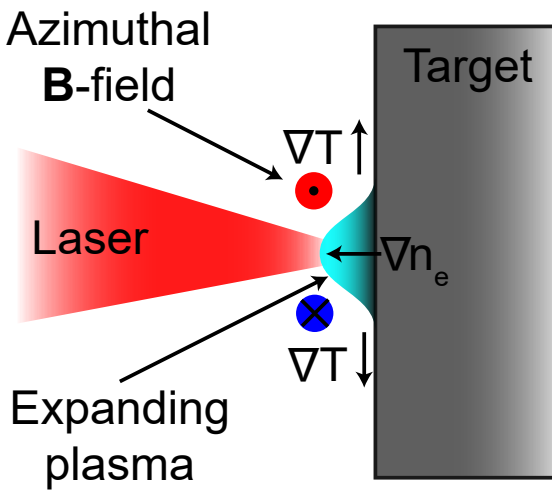

*Figure 2.12: Illustration of the development magnetic fields via the Biermann battery mechanism. The intense laser pulse induces heating and expansion of the target, producing density and temperature gradients. When the angle between the gradients is misaligned, an azimuthal **B**-field is generated.*

magnetic fields in intense laser-solid interactions [125, 139]. An illustration of the process of magnetic field generation via the Biermann battery mechanism is shown in figure 2.12. The expanding plasma generated when the intense laser pulse irradiates a target possesses a density gradient in the target normal direction (see section 2.4) and a temperature gradient perpendicular to this (with the temperature being greatest on-axis). This results in a charge separation, thus generating an electric field, i.e.:

$$en_e\mathbf{E} = -\nabla P_e \tag{2.59}$$

where $P_e = n_e k_B T_e$. Substituting equation (2.59) into Faraday's law (equation (2.3)), results in:

$$\nabla \times \frac{1}{en_e}\nabla P_e = \frac{\partial \mathbf{B}}{\partial t} \tag{2.60}$$

which is rewritten as:

$$\frac{\partial \mathbf{B}}{\partial t} = k_B \frac{\nabla T_e \times \nabla n_e}{en_e} \tag{2.61}$$

where T_e and n_e are the electron temperature and density, respectively. The Biermann battery mechanism is the dominant magnetic field generation mechanism for scenarios where the electron density and temperature gradients (∇n_e and ∇T_e, respectively) are not aligned. Whilst it offers a small contribution to the magnetic field growth when compared the other terms in the generalised form of Faraday's law of induction (equation

(2.62)) as it is the only term independent of **B**, and thus dominates for small values of magnetic field and small system sizes [136].

$$\frac{\partial \mathbf{B}}{\partial t} = \nabla \times (\mathbf{v} \times \mathbf{B}) + \frac{\eta c^2}{4\pi}\nabla^2 \mathbf{B} - \frac{\nabla \times (\mathbf{j} \times \mathbf{B})}{n_e e} - k_B \frac{\nabla T_e \times \nabla n_e}{n_e e} \tag{2.62}$$

where the terms on the right-hand-side correspond to magnetic field generation via convection, resistivity gradients, the Hall effect and the Biermann battery.

If the assumption that the density gradient is directly primarily along the target normal is true, and the magnetic field is initially zero, i.e. **B**=0, then, via the Biermann battery mechanism, the magnetic field grows linearly with time. The magnitude of such a field is shown:

$$\mathbf{B} = \frac{2\tau k_B T_e}{L_\perp L_\parallel} \tag{2.63}$$

where $L_\perp$ and $L_\parallel$ are the lengths of the perpendicular (temperature) and parallel (electron density) gradients, respectively. The time at which the field strength is calculated is denoted by τ and the field strength is given in MegaGauss. The length-scale of the gradients is assumed to be comparable. This linear growth continues as long as the two comparable gradients exist; hot electrons propagate down $L_\perp$, whilst a cold return current propagates against it. This will occur within a transit time, $t = L_\perp / \mathbf{v}_{th}$, where $\mathbf{v}_{th}$ is the electron thermal velocity. Thus, the final value of the magnetic field strength is defined by the electron transit time, resulting in the condition that the Biermann battery mechanism saturates when $r_L \sim L_\parallel$, where r_L is the electron Larmor radius. This can be rewritten in terms of the electron plasma beta velocity ($\beta_e = \mathbf{v}/c$), enabling the final magnetic field strength value to be written as:

$$\frac{\mathbf{B}}{\sqrt{8\pi P_e}} = \beta_e^{-1/2} \approx \frac{d_e}{\sqrt{2} L_\parallel} \tag{2.64}$$

where $d_e = c/\omega_p$ is the electron inertial length. Large values of $L_\parallel / d_e$ are typical of astrophysical systems and, from equation (2.64), this implies that the final magnetic field generated by this mechanism is small: $\sim 10^{-20}$ G [138].

The scenario where both the density and temperature gradients are of fixed dimensions is considered. This is valid for the case of intense laser-solid interactions employing a laser with a temporal duration (∼1 ps), which is short compared to hydrodynamic timescales, and in astrophysical shock scenarios where the magnetic field growth is sustained. In cases

such as these, the effects of magnetic convection begin to dominate over the Biermann battery, in the absence of a dynamo mechanism. If the rate of convection is greater than the growth of the magnetic field via the Biermann battery, then balance is achieved, resulting in the following scaling for a saturated magnetic field [136]:

$$\frac{\mathbf{B}}{\sqrt{8\pi P_e}} = \beta_e^{-1/2} \approx \frac{d_i}{\sqrt{2}L} \tag{2.65}$$

where $d_i = c/\omega_{pi}$ is the ion inertial length, and $L \sim L_\perp = L_\parallel$. As was shown in equation (2.64), the magnetic field strength scales as d_e/L, as predicted by Haines [140]. Furthermore, Haines [140] also proposed the dominance of the Biermann battery mechanism for $L/d_i \gtrsim 1$.

2.7.3 Weibel process

The Weibel instability (WI) [129] is a collisionless, transverse instability present in homogeneous, or nearly homogeneous electromagnetic plasmas. It has been the subject of extensive study in the context of intense laser-solid interaction physics due to its influence on fast electron transport due to the interaction with the counter-streaming cold return current [141, 142]. In this scenario, small modulations in the density profile of one of the populations leads to perturbations in the local self-generated magnetic field, resulting in the filamentation of the population of fast electrons. However, Weibel also considered the case of the growth of an instability driven by velocity anisotropies in a fast electron beam, propagating into a background of a static ion population [129]. As in the case of two-counter propagating electron beams, the signature of this instability is a pattern of filaments present in the beam of accelerated protons (see section 2.9.1). The scenario of a collisionless, relativistic electron population propagating into a static ion population is particularly relevant for intense laser-solid interaction physics, as discussed in section 2.6.3.

The WI is important for the generation and amplification of magnetic fields [142]. It has long been known that instabilities can generate strong magnetic fields, even in the absence of seed fields, and thus the WI has often been proposed as the mechanism by which relatively small cosmological magnetic fields, generated by the Biermann battery mechanism, have been amplified to their currently observed microgauss levels. The configuration of density and temperature gradients discussed in section 2.7.2 is also relevant to the con-

ditions required for the onset of the WI [143]. In this scenario, the intense laser pulse generates a plasma expansion, and produces an electron flow down the density gradient, driving the Biermann battery mechanism. The velocity of the current of electrons varies across the non-parallel temperature gradient, with the highest velocity electrons being located closest to the central axis. Density and velocity perturbations across the transverse profile of the beam then drive the WI [129]. This behaviour is observed for systems with L/d_e >100 [143]. Furthermore, the magnetic field generated in such a scenario is observed to no longer follow the scaling of the Biermann battery (d_e/L), where $\beta_e \approx 1$. In the case of a large system, the magnetic field strength, in the form of the electron plasma beta velocity appears to tend to a value of $\beta_e \approx 100$ [143].

The growth rate of the WI is indirectly proportional to the electron density of the plasma, in agreement with observations of its influence for large scale length systems where L/d_e >100 [143, 144]. The growth rate of the WI is given as:

$$\Gamma_{WI} = \omega_{pf} \sqrt{\left(\frac{n_f}{\gamma n_e} \right)} \times \frac{v_f}{c} \tag{2.66}$$

where ω_{pf} is the plasma frequency of the fast electrons, n_f is the number density of fast electrons, n_e is the target electron density and v_f is the fast electron velocity.

The magnetic fields associated with the WI are oscillatory. However if the transit time of the electrons is smaller than the oscillation period of the field, they may appear quasi-static. Ramani and Laval [145] calculated the magnitude of the magnetic field strength generated by this instability as:

$$\mathbf{B} \approx \frac{2 n_e^{1/4} T_e^{1/2}}{L} \tag{2.67}$$

Recent experimental investigations have demonstrated the influence of the WI and the interplay with the Biermann battery mechanism. For example, Gode *et al.* [144] demonstrates the measurement of signatures of WI growth when a pre-plasma was present prior to the arrival of the intense laser pulse, corresponding to a long scale-length system. The influence of the WI in the context of fast electron transport is discussed in section 2.7.4. This topic is further discussed, in the context of ion acceleration, in **Chapter 6**.

2.7.4 Effects on transport instabilities

Several distinct instabilities exist that can affect the transport dynamics of the fast electron beam as it propagates within the target. Instabilities may either lead to increased energy

losses, divergence changes or spatial intensity variations to the affected electron population via breakup of the beam. They can in some cases be beneficial, i.e. the two-stream instability [146], caused by the co-streaming of electron and ion populations, where energy is transferred from the electron population to the ions, boosting them to higher energies [146, 147].

The instabilities which typically dominate fast electron transport in high power laser-solid interactions arise due to the interaction of the counter-streaming electron populations of the fast and return currents. The main instabilities relevant to the investigations presented in this thesis are the Weibel instability [129] and the resistive filamentation instability [117, 148]. This does not however discount the effects of other instabilities which may be present in laser-solid interactions. For example, the ionisation instability is the result of the necessity, in insulators, to ionise the material in order to promote free electrons from their parent atoms to form the return current of electrons. Any perturbations in the ionisation rate will lead to electron density modulations along the profile of this beam, leading to the localised non-neutralisation of charge, inhibiting the fast electron beam from propagating, seeding instability growth [149, 150].

Weibel instability

As discussed above (in section 2.7.3) WI is a collisionless, transverse instability, resulting from the interactions between opposing magnetic fields from the primary fast electron population and a counter-propagating return current [53]. Small modulations may develop in the density profile of the fast electron population due to this interaction, resulting in a perturbation of the local self-generated magnetic field at this point. The resultant magnetic field then acts to pinch the region of the beam into filaments, essentially breaking the beam up into numerous beamlets. This, in turn, enforces modulations to grow transversely across the beam, where this process repeats, effectively altering the beam divergence, energy deposition and the efficiency of energy transport.

The WI occurs on timescales of approximately the plasma frequency of the beam, ω_{pf}, and has a spatial scale approximately of the order of the plasma skin depth ($l_s = c/\omega_{pf}$). An illustration of the growth of the WI is depicted in figure 2.13. Krasheninnikov *et al.* [149] showed that the WI exhibits a dependence on target temperature. By increasing the transverse temperatures of the beam, the WI can be mitigated through suppressing its growth rate [151, 152].

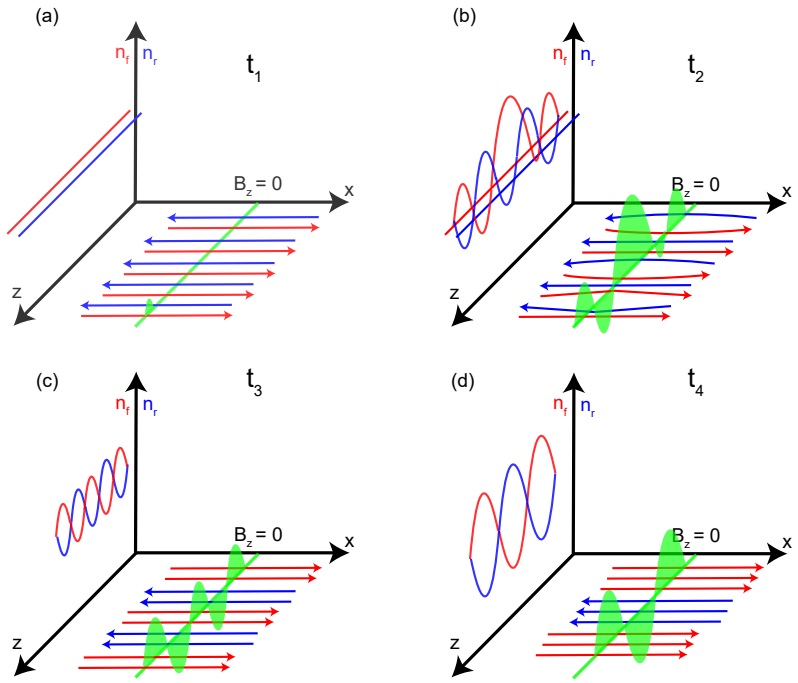

Figure 2.13: Illustration of the development of the Weibel instability involving two counter-propagating electron beams with densities n_f and n_r. (a) A small density fluctuations results in the generation of a transverse magnetic field, which will (b) act to pinch both currents. (c) The field then grows via positive feedback, which (d) leads to beam filamentation.

Furthermore, Evans *et al.* [151] demonstrated that the WI demonstrates a dependence on Z^2, where Z is the atomic number of the target material. This may result in the instability being suppressed in high-atomic number targets, but may be prevalent in lower-atomic number targets, such as lithium [151].

Recent investigations have demonstrated that the effects of the WI may become prominent even in high-power laser interactions with thin (2 to 10 μm thick) targets, where fast electron transport effects are less apparent [144].

Resistive Filamentation

The mechanism for resistive filamentation to occur is broadly similar to the WI, except that the fast electron beam is broken up by the collisional return current. In addition, the growth rate of the magnetic fields enveloping the filaments arising from resistive filamentation is dependent on the electrical resistivity of the target material [153], which depends on the material under irradiation, the level of target heating and spatial variations in the fast electron beam current density (from equation (2.58)) [148].

The timescale of the growth of the resistive filamentation instability is slower in comparison to the WI. Typically, the magnetic fields supporting each filament grow on timescales

determined by the magnetic diffusion time, τ_d:

$$\tau_d = \frac{\mu_0 r_F^2}{\eta} \tag{2.68}$$

where r_F is the radius of the filament under consideration, and is given by $r_F = 2\gamma^{1/2}(\mathbf{v}_{th}/\mathbf{v}_f)(c/\omega_{pf})$ [117, 154]. Here, $\mathbf{v}_{th}$ is thermal velocity of the return current. Finally, η is the electrical resistivity.

The growth rate of the resistive filamentation instability is also dependent on the transverse temperature of the fast electron beam. This dependency arises due to the fact that as the instability grows, the local magnetic field enveloping each filament results in a pinching force. The transverse temperature produces a counter-acting pressure force that causes the filament to expand; if no transverse temperature was present, the filament would simply collapse. Therefore, the filamentation growth rate is sensitive to the balance between the inwards acting magnetic force and the outwards acting pressure force [152]

The growth of the resistive filamentation instability as a function of electrical resistivity (controlled through material lattice structure) in carbon is investigated in **Chapter 5**.

2.8 Plasma Instabilities: Rayleigh-Taylor instability

The Rayleigh-Taylor (RT) instability is a transverse instability at the interface between two fluids of different densities. This instability has been observed in scenarios such as ICF [155] and, famously, the Crab nebula [156]. The interface between the two fluids is initially flat, with the two layers of fluid being plane-parallel [157]. Small localised perturbations in the interface results in pressure variations, leading to the growth of the perturbations, resulting in the characteristic formation of bubble-like structures. Figure 2.14 demonstrates this.

As the low density fluid accelerates into the high density fluid, the boundary separating both becomes unstable. The instability grows exponentially and, for a sinusoidal perturbation (as shown in figure 2.14), the amplitude of the perturbation grows as:

$$\xi = \xi_0 e^{\gamma_0 t} = \xi_0 e^{(Akat)^{1/2}} \tag{2.69}$$

where γ_0 is the instability temporal growth rate and $A = (\rho_1 - \rho_2)/(\rho_1 + \rho_2)$ where ρ_1 and ρ_2 are the densities of the light and heavy fluid, respectively. Additionally, a is the

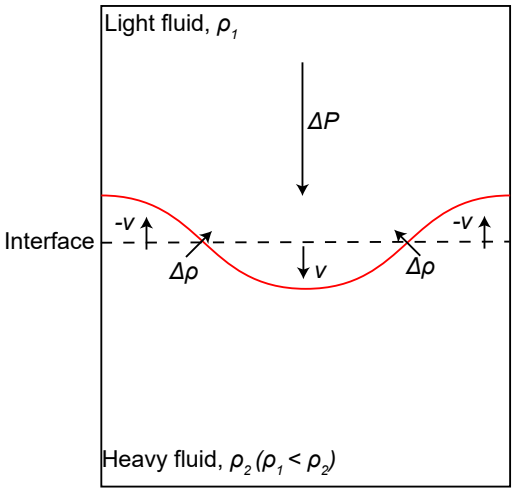

Figure 2.14: Schematic of the Rayleigh-Taylor instability, where two fluids of different densities, ρ_1 and ρ_2 (where $\rho 1 < \rho 2$) are separated by a boundary. The pressure gradient exerted by ρ_1 on $\rho 2$ results in a perturbed interface with the peaks and troughs moving with opposite velocities.

acceleration of the light fluid and k is the spatial wavenumber of the perturbation.

RT-like instabilities are relevant to intense laser-solid interactions, particularly in ultra-thin foil interactions in the radiation pressure regime (see section 2.9.2). Experimentally, Palmer *et al.* [44] proposed RT-like instabilities as the driver for the formation of bubble-like structures observed in the beam of accelerated protons in experiments using ultrathin foils using the Vulcan petawatt laser, whilst Pegoraro *et al.* [158] and Sgattoni *et al.* [159] have investigated this numerically. RT-like instabilities in intense laser-solid interactions can occur because the incident laser photons are effectively a light fluid, pushing into the heavier fluid of target electrons. Both populations can be thought of as planar to each other. As the interaction at the front surface progresses, any perturbations arising from either surface structure or a rippling of the critical density surface leads to the growth of the instability. As the perturbations grow, localised regions of higher laser intensity form, resulting in regions of higher photon pressure. In these higher intensity regions, electrons are expelled more via the ponderomotive force (see section 2.4.2). This results in a a transverse modulation of the electrostatic charge separation field. As a result, the resultant beam of accelerated ions is imprinted with the spatial profile of the electron density.

2.9 Ion acceleration mechanisms

Until now, this chapter has largely focused on the collective response of target electrons to the action of an intense laser pulse. As discussed in section 2.6.3, this is due to the contrasting timescales for electron and ion heating. The relatively more massive ions remain relatively static over the timescales of the oscillating laser electric and magnetic fields. However, ion motion does becomes important at longer timescales in the interaction, or when the electrostatic, charge separation field generated by the collective electron acceleration via the laser is sufficiently high that subsequent ion motion becomes feasible.

As discussed in **Chapter 1**, the acceleration of ions in high power laser-solid foil interactions has been a source of interest since its discovery [160], due to the envisioned applications for these potential compact, tunable ion sources. Indeed, over the years there has been considerable debate over the nature of laser-driven ion acceleration including the location from which the ions where sourced [161–163] and how the energy scaling of the accelerated ion beams [164] depended on the laser parameters employed. This section introduces the schemes of laser-driven ion acceleration relevant to this thesis.

2.9.1 Target normal sheath acceleration (TNSA)

When the fast electrons (described in section 2.6) have reached the rear surface of the target, they can no longer draw a return current to further propagate, and thus, many of the low energy population of the fast electron current are halted, creating a negative charge imbalance. The fastest electrons may possess enough energy to overcome the retarding nature of this field and escape into vacuum. The slowest electrons may also be reflected at the rear surface boundary and recirculate to the front surface, where they generate another charge separation field, similar to the rear. These distributions are referred to as sheath fields

The sheath field extends out to a distance of approximately a Debye length, λ_D, (discussed in section 2.2) from the rear surface of the plasma [80,165], and is sufficiently strong to ionise the atoms present at the rear surface, a thin contamination layer of hydrocarbons. To best describe this scheme, the approximation whereby the sheath field is static, in space and time, is considered. In this approximation, we assume that the ion density in the region of the sheath field drops off sharply; the drop in electronic potential in the sheath is given by $\nabla\Phi_s \sim T_f/e$; and ions, of charge Z, moving in this potential will gain

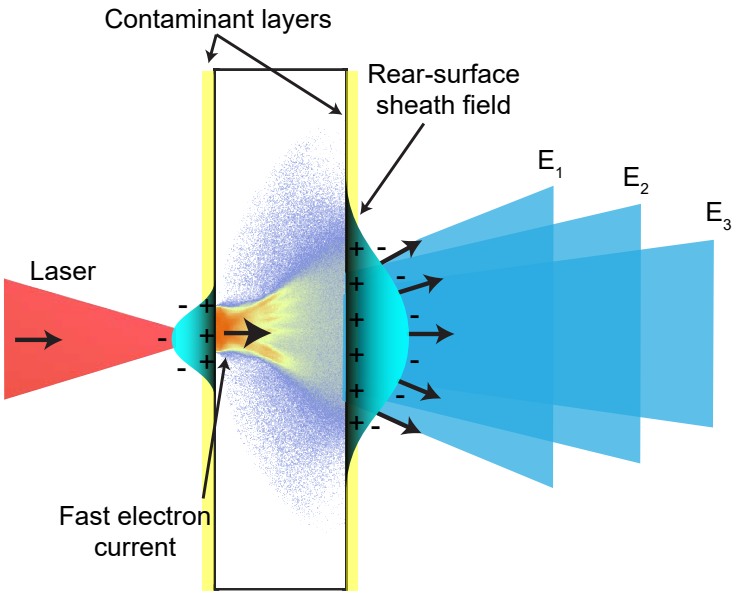

Figure 2.15: Illustration of the acceleration of ions via the TNSA mechanism. The fast electrons generated at the front surface propagate through the target and generate a TV/m field at the rear surface. Protons are subsequently accelerated to multi-MeV energies, normal to the sheath field. The divergence of the ion beam is dependent on the ion energy, where $E_3 > E_2 > E_1$

energy dictated by $\varepsilon_i = Ze\nabla\Phi_s \sim ZT_f$. An illustration of TNSA is shown in figure 2.15. The field strength of the sheath field is given by:

$$E_s \sim \frac{k_B T_e}{e\lambda_D} \tag{2.70}$$

The electron temperature is derived from Wilk's scaling relation [101] (see section 2.6), and the spatial extent of the sheath field is typically on the order of microns in extent [166]. A more thorough treatment of the estimation of the potential and electric field strength is given in Fuchs *et al.* [167, 168].

Substituting the typical values of the electron temperature and the Debye length into equation 2.70, an electric field strength on the order of TV/m is calculated. Fields of this strength are far larger than the ionisation threshold of the atoms on the target rear surface, and hence, they are instantly ionised. The strength of the electric field required to ionise the constituent atoms is given below:

$$E_{ion} = \frac{\pi\varepsilon_0 U_{bind}^2}{e^3 Z} \tag{2.71}$$

where U_{bind} is the binding energy of the atom. Substituting in the values for an atom

of carbon-12 ($U_{bind} = 92.15MeV$ and $Z = 6$), a threshold intensity for ionisation of $E_{ion} = 2.5 \times 10^{11}$ V/m is calculated, far below the electric fields present. The dominant ionisation mechanism in the sheath field is barrier suppression (see section 2.3) [81].

Due to the negative imbalance in charge in the sheath field, the ions are accelerated from the plasma in a short duration (ps) bunch. Space charge effects are limited due to charge neutralisation by a co-moving electron beam. The ions are accelerated preferentially according to their charge to mass ratio (q/m), and thus, protons are accelerated to higher velocities than heavier ions. Experimental investigations of the efficiency of TNSA found higher heavy ion energies when no contaminant layer was present on the target surfaces [169]. As the accelerated ions expand into vacuum, a layering of the species occurs, with the species with the highest charge to mass ratio in the lead.

Per the nomenclature, ions accelerated by this mechanism are ejected at an angle normal to the the local orientation of the sheath field - as shown in figure 2.15. However, if there are any modulations present in the transverse spatial profile of the fast electron beam, arising from the instabilities discussed in section 2.6, these are mapped into the spatial profile of the sheath field. Thus, the spatial profile of the accelerated ion beam is imprinted with the characteristics of spatial profile of the sheath field which relates the fast electron spatial distribution, in addition to the local orientation of the rear surface. Through these properties, measurements of accelerated protons can be employed to infer the dynamics and properties of electrons accelerated in the interaction.

Realistically, however, the sheath field is not static over the course of the timescales of a laser-solid interaction, and TNSA is instead described as the expansion of a locally neutral electron-ion plasma in vacuum. Simply, the expansion of the ion population into vacuum is given as:

$$n_i(x,t) = n_0 e^{(-x/(c_s t)-1)} \tag{2.72}$$

where $c_s = (ZT_e/m_i)^{1/2}$ is the expansion velocity, often called the ion acoustic velocity. It should be noted that $x = -c_s t$ defines a shock wave propagating backwards into the target at a velocity equal to c_s, similar to the scenario depicted in section 2.4 for plasma expansion from the front surface of a target. The resultant charge separation from the expansion of the plasma leads to the generation of an accelerating electric field.

The magnitude of the electric field is greatest at the ion front, due to the charge separation in this region being maximised, and is found to be approximately twice the value

of the sheath field at the initial rear-surface of the target, i.e.:

$$E_i = \frac{2E_0}{w_{pi}t} \tag{2.73}$$

where E_0 is given by the same expressions as for the static case (eq. (2.70)), i.e. $E_s = \frac{k_B T_e}{e\lambda_D}$.

TNSA is a complex process subject to numerous factors, including absorption of the laser energy at the front surface, the transport of fast electrons through the target, and the temporal and spatial evolution of the sheath field at the target rear surface. A number of analytical models have been proposed to enable greater understanding of the evolution of the sheath field and the characteristics of the accelerated ion population. A model devised by Mora [170] is perhaps the most widely used approach, although numerous other models have been developed [171–173].

The Mora model is a one-dimensional, isothermal model of plasma expansion into vacuum. Models of free plasma expansion developed previously to this did not fully explore the effects of charge separation fields or the spatial distribution of the ion front [80,174,175], however, the Mora model incorporates these in order to obtain a temporal description of the peak electric field strength at the ion front. At time $t = 0$, the population of ions present on the rear-surface of the target, of density n_i, are assumed to be initially cold and at rest, for $x < 0$, where x is the position of the target rear-surface. At $x > 0$, the ion density is presumed to be $n_i = 0$, resulting in a step-like density boundary.

The evolution of the electric field strength of the ion front, $E_f(t)$, the position of the ion front, $x_f(t)$, and the velocity of the ion front, $v_f(t)$, can be calculated from the simple model approach:

$$E_f(t) = \frac{2E_0}{\left(2e + \omega_{pi}^2 t^2\right)^{1/2}} \tag{2.74}$$

$$v_f(t) = 2c_s \ln\left(\tau + \sqrt{\tau^2 + 1}\right) \tag{2.75}$$

$$x_f(t) = 2\sqrt{2e}\lambda_{D0}\left(\tau \ln\left(\tau + \sqrt{\tau^2 + 1}\right) - \sqrt{\tau^2 + 1} + 1\right) \tag{2.76}$$

where e in equations 2.74 and 2.76 is Euler's number, and $\tau = \omega_{pi}t/\sqrt{2e}$ is the time, t, normalised to the ion plasma frequency where, again, e is Euler's number. The maximum energy of the accelerated protons, E_{max}, can be obtained by:

$$E_{max} = \frac{1}{2} m_i v_f^2 \approx 2Z k_B T_e \left(\ln\left(\tau + \sqrt{\tau + 1}\right)\right)^2 \tag{2.77}$$

Furthermore, the proton energy spectrum is described by:

$$\frac{dN}{dE_p} = \frac{n_{i0}c_s t}{\sqrt{2E_p Z k_B T_e}} \exp\sqrt{\frac{-2E_p}{Z k_B T_e}} \tag{2.78}$$

One limitation of the Mora model is that there is no upper limit for the time over which the acceleration occurs, thus ions are accelerated indefinitely for increasing time. Thus, an upper limit must be defined for the time over which acceleration takes place. Fuchs *et al.* [167] demonstrated, experimentally and numerically, that the maximum acceleration time is given by:

$$t_{acc} \approx 1.3(\tau_L + 60 \text{ fs}) \tag{2.79}$$

where τ_L is the laser pulse duration. Equation 2.79 is only valid for intensities $> 3 \times 10^{19}$ W/cm^2, and pulse durations on the order of picoseconds.

Typical parameters of TNSA accelerated ion beams include laser-to-proton conversion efficiencies of a few percent, with relatively high conversion efficiencies of up to 15% measured [176]; and a resultant high number of protons per pulse (typically $> 10^{13}$ protons per pulse). Maximum energies of > 85 MeV have previously been observed in bunch lengths of the order of the laser pulse duration [177].

The source size of the ions produced through TNSA has been shown to be $\sim$ 100 μm [178, 179] and thus, the emittance of the beam is extremely low (of a factor of 100 lower than achievable in conventional RF accelerators). In addition, the beam exhibits an energy-dependent divergence angle: the highest energy protons possess the smallest divergence angle, whilst the lowest energy protons are emitted with larger divergence angles. This is a result of the gaussian-spatial profile of the sheath field. Finally, analyses of proton acceleration experiments involving the TNSA mechanism suggest that the energy of the accelerated protons scales with laser intensity as $E_{max} = (I\lambda^2)^{1/2}$ up to $I\lambda^2 = 3 \times 10^{20}$ W/cm^2 μm^2 [164, 166, 167]. This is valid for picosecond laser systems.

2.9.2 Radiation pressure acceleration

The acceleration of objects via the pressure exerted on them from radiation has long been known in the context of astronomy and astrophysics, from the acceleration of spacecraft via solar radiation incident on a solar sail [180,181] to stellar structure and evolution [182,183]. Extending the concept of utilising the momentum of the photons incident on a target in a laser-solid interaction has been discussed in the context of ion acceleration for many

years, [184] as a means by which the shortcomings of the TNSA mechanism, namely the broad energy spectrum, large divergence and unfavourable intensity scaling, could be addressed.

Radiation pressure acceleration (RPA) was proposed, at intensities of $> 10^{23}$ W/cm^2 by Esirkopov [185] and, in a more currently achievable intensity regime by Robinson [184]. It is expected to dominate in interactions between ultra-intense laser pulses ($> 10^{21}$ W/cm^2) and ultra-thin targets (on the order of tens to hundreds of nanometres) [22, 186–188].

Electromagnetic waves carry momentum, $\hbar k$, and energy, $\hbar\omega$, and radiation pressure is the flow of photon momentum delivered per unit surface to a target. The flux of photons can be calculated as:

$$F_{ph} = \frac{I}{\hbar\omega} \tag{2.80}$$

where F_{ph} is the flux in units of cm^{-2}s^{-1}, I is the peak laser intensity, $\hbar$ is the reduced Planck's constant and ω is the angular frequency of the laser. In laser-solid interactions, the momentum carried by the flux of laser photons is, generally, delivered to a non-transparent surface, i.e. one that is either absorbent or reflective. The pressure exerted transferred to the target can then be shown to be:

$$P_{rad} = \hbar k F_{ph} = \frac{I}{c} \tag{2.81}$$

However, equation (2.81) is valid only for the case of a perfectly absorbing target and does not take into account the fact that realistic pulses can be also reflected and transmitted. Considering these factors leads to a general description for the radiation pressure exerted upon the target:

$$P_{rad} = (1 + R - T)\frac{I}{c} = (2R + A)\frac{I}{c} \tag{2.82}$$

where R, T and A are the reflection, transmission and absorption coefficients, respectively, and where $(R + T + A) = 1$. At the surface of a solid-density target, electrons are pushed inwards by an exchange of momentum with the incident photons, resulting in the electrons being pushed forward and generating a charge separation layer, creating an electrostatic field which in turn acts on the ion population, accelerating them.

There are two distinct regimes of RPA, dependent on the target thickness. For targets of thickness $\gg l_s$, the regime of RPA is known as "hole boring", whilst when the target thickness is of the order of the skin depth, the RPA mode is known as "light sail"

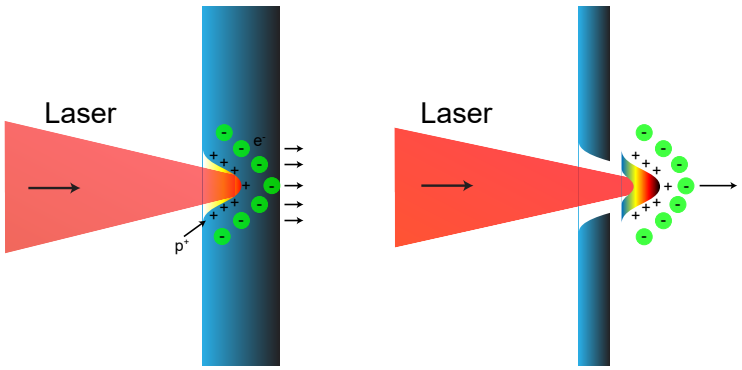

Figure 2.16: (a) Illustration of the hole boring mechanism (b) Illustration of the light sail acceleration mechanism.

acceleration.

In hole boring, the pressure exerted on the critical surface by the light pressure pushes the critical density inwards, acting to steepen the density profile. Electrons are driven forward into a compressed layer, generating a charge separation region that acts to accelerate the ions. The recession velocity of the critical surface, v_{hb}, is referred to as the hole boring velocity [101, 189], and is given by:

$$\frac{v_{hb}}{c} = \left(\frac{n_c I \lambda^2 Z m_e}{n_e 2.74 \times 10^{18} A m_p} \right)^{1/2} \tag{2.83}$$

where n_c is the critical density, n_e is the electron density, I is the laser intensity, λ is the laser wavelength, Z is the ionisation state, A is the mass number, m_e is the electron mass and m_p is the proton mass. The maximum energy of the ions accelerated in the hole boring mode is:

$$\varepsilon_{max} = 2 m_p c^2 \frac{\Pi}{1 + 2\Pi^{1/2}} \tag{2.84}$$

where $\Pi = \frac{Z n_c m_c}{A n_e m_p} a_0^2$. A schematic of the hole boring process is shown in figure 2.16 (a).

If the target has a thickness on the order of the skin depth of the laser, then it may be accelerated as a whole via the light sail mode of RPA [190, 191]. In the hole boring mode, the laser pulse can penetrate deeper into the target as the surface layers are pushed inwards by the pressure of the layer and ion acceleration via the resulting charge separation field. In the light sail mode, however, the target is thin enough that the ion population can be accelerated before the end of the laser pulse duration. As the bulk of the electron population is accelerated as a whole in this case, light sail acceleration has been highlighted as a promising approach for the acceleration of ions in a magnetic bunch to hundreds of

MeV per nucleon [94, 184, 185, 192–194]. The light sail mode is illustrated in figure 2.16 (b). The force exerted by the flux of photons is given as:

$$F_{LS} = (2R + A)S\frac{I}{c} \tag{2.85}$$

where S is the surface area irradiated by the pulse. Then the velocity of the ions accelerated via the light sail mechanism can be determined as:

$$v_i = \frac{(2R + A)\tau I}{\eta c} \propto I\tau\eta^{-1} \tag{2.86}$$

where $\eta = m_i n_i d$ is the areal density of the target and τ is the pulse duration. The maximum ion energy from light sail acceleration can then be found to be:

$$\varepsilon_{max} = \frac{2m_i I^2\tau^2}{\eta c} \tag{2.87}$$

Thus, it can be seen that the maximum ion energy achievable via the light sail mode of RPA scales much more favourably than for TNSA ($E_{max} = (I\lambda^2)^{1/2}$).

Achieving efficient radiation pressure acceleration on ultra-thin foil targets requires the bulk of the target remaining opaque to the laser for the duration of the interaction, and thus the onset of transparency is undesirable. Control of the polarisation of the pulse has been proposed as a method by which plasma expansion and the onset of transparency could be controlled: a circularly polarised pulse lacks an oscillating $\mathbf{J}\times\mathbf{B}$ component of the laser field, minimising the level of electron heating, delaying the onset of transparency. In contrast, for the case of a linearly polarised pulse irradiating a solid-density foil at normal incidence, the oscillating $\mathbf{J}\times\mathbf{B}$ component drives an oscillation of the electron population at 2ω, resulting in strong absorption and fast electron generation [22, 188]. It should also be noted that recent investigations of ion acceleration in thicker foils have reported that tailoring the pulse polarisation becomes less crucial for longer duration pulses and thicker targets [195]. This is due to target deformation occurring early in the interaction, creating a situation whereby regions of the pulse are always incident non-normal to the target, resulting in electron heating.

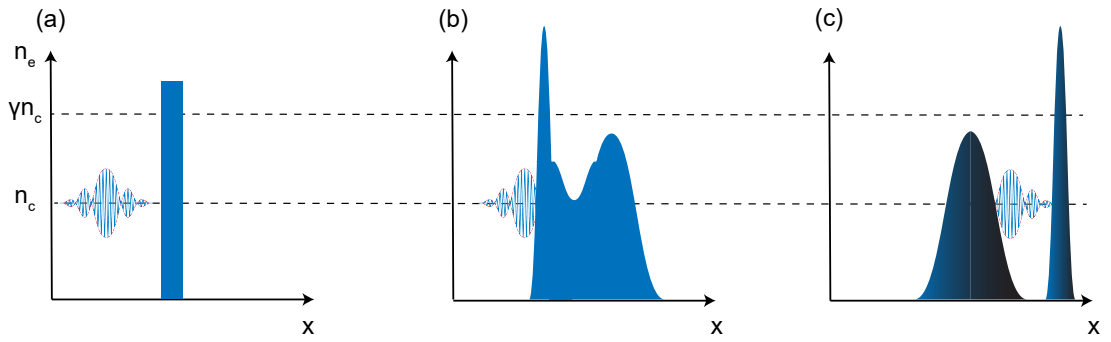

Figure 2.17: Schematic detailing the temporal evolution of the electron density of a solid density foil target undergoing RSIT. (a) Prior to the arrival of the main pulse, the target density exceeds the critical density value. The rising edge of the pulse heats the electrons, resulting in expansion. (b) The peak intensities of the pulse ponderomotively drive electrons forward into the plasma, from the relativistically corrected critical density surface. The electron density directly ahead of the pulse is increased due to bunching of the electron population. (c) A combination of plasma expansion and increasing critical density due to the increasing γ factor, result in the target becoming relativistically transparent. Thus, the laser can propagate through the target, volumetrically interacting with the electrons.

2.9.3 Relativistic self-induced transparency (RSIT) acceleration

Recalling section 2.4.3, when the laser frequency is larger than the plasma frequency the electrons oscillating in the electric field of the laser cannot respond fast enough to the action of the laser and the target becomes transparent. Thus, the laser can propagate through the target, beyond the skin depth.

It is also prudent to recall that the expression for the plasma frequency and the plasma critical density are $\omega_p = \sqrt{e^2 n_e/\varepsilon_0 \gamma m_e}$ and $n_c = \omega_L^2 \varepsilon_0 \gamma m_e/e^2$, respectively.

In previous sections, mechanisms for ion acceleration were presented in isolation. However, in realistic laser-solid foil interactions, the heating of the target electrons (via the absorption mechanisms detailed in section 2.5), and the acceleration of electrons, and ions by the TNSA (section 2.9.1) and RPA (section 2.9.2) mechanisms, lead to a decrease in the density of the target through expansion. Simultaneously, an increase in the relativistically-corrected critical density on the rising edge of the laser (spatial and temporal) intensity profile contributes to the onset of transparency: a process termed Relativistic Self-Induced Transparency (RSIT) [196]. Thus, when considering the impact of RSIT on acceleration schemes, an "intra-pulse transition" [197] between ion acceleration mechanisms must be accounted for. An illustration of the onset of RSIT in intense laser-solid foil interactions is shown in figure 2.17.

The physical picture of the onset of RSIT can be summarised as follows: initially the laser pulse interacts with the front of the target, heating electrons via the absorption mech-

anisms detailed in section 2.5. This results in a decompression of the target, effectively lowering the electron density within the target. At this point the target remains opaque to the laser, and it is reflected or absorbed (recall equation (2.82) in section 2.9.2). As the rising edge of the temporal intensity profile of the pulse increases, the intensity incident on the target increases. This leads to the oscillation velocity of the plasma electrons being on the order of relativistic levels. The increase in the Lorentz factor, γ, as the electron velocity increases effectively increases their mass in the laboratory frame of the interaction, slowing them down and decreasing the plasma frequency (increasing the critical density). When the frequency of the laser exceeds the plasma frequency, the electrons are unable to respond to the propagation of the pulse, and the target is deemed transparent. Propagation of the pulse through the target results in the initiation of several phenomena relevant to ion acceleration. Considering the efficiency of RPA firstly, the onset of transparency leads to the transparency term in equation (2.82) becoming important. As equation (2.82) takes the form $P_{rad} = (1 + R - T)I/c$, where T is the fraction of the pulse transmitted, it can be seen that the onset of transparency diminishes the force exerted upon the target, resulting in less efficient acceleration.

However, the transmission of the laser pulse also enables volumetric heating of the electrons within the target. This has been shown to enhance the maximum energy of ions accelerated via the TNSA mechanism [34, 198–200]. The onset of transparency, and the resultant volumetric heating of the electrons by the co-propagating, transmitted portion of the laser has been shown to be the driver for the formation of a jet of super-thermal electrons, supported by a self-generated quasi-static azimuthal magnetic field [33,34]. The accelerated electrons comprising the jet then stream into the layer of protons accelerated via the TNSA mechanism, enhancing the energy of the proton population in the vicinity of the jet via coupling by its longitudinal electric field. The generation of the electron jet and the collimating, azimuthal magnetic field form part of the investigation presented in **Chapter 6**.

Chapter 3

Laboratory analogues of astrophysical phenomena

As the main theme of this thesis is the investigation of laboratory-produced self-generated magnetic fields relevant to astrophysical phenomena, before proceeding, it is prudent to first review the similarities, and differences, between plasmas generated in intense laser-solid interactions and relevant astrophysical scenarios. Figure 3.1 illustrates relevant conditions in which plasma is generated throughout the known universe. Clearly, there is a vast difference between the temporal and spatial scales of astrophysical plasmas compared to laser-produced laboratory plasmas. Astrophysical plasmas, in general, are observed to exist on timescales ranging from tens of thousands of years to millions of years, and are often found to encompass many parsecs. In contrast, plasmas generated in intense laser-solid interactions, are observed for tens of nanoseconds, and have spatial dimensions of millimetres. Furthermore, intense laser-solid interaction experiments often produce high density plasmas that are strongly magnetised, whilst astrophysical plasmas can be relatively tenuous or even more dense, in the case of stellar surface conditions, and the conditions experienced in stellar interiors, respectively. This chapter explores the nature and evolution of selected astrophysical phenomena; how the differences in scale between these cases and laboratory analogues generated in intense laser-solid interactions can be reconciled; and finally, previous examples of successful intense laser-solid interaction laboratory astrophysics experiments.

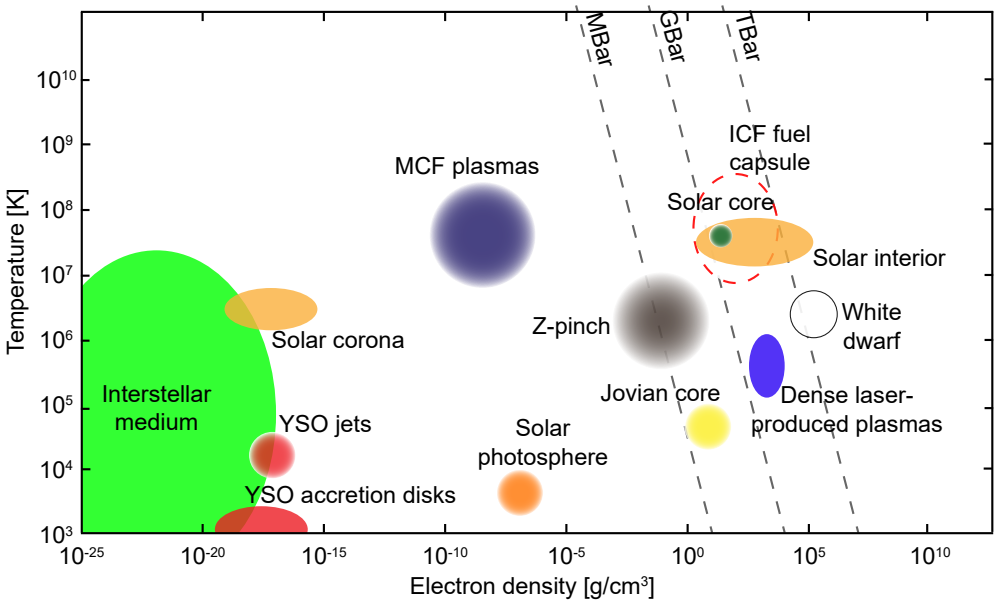

Figure 3.1: Plot of plasma temperature as a function of electron density for various laboratory and astrophysical scenarios. The regime of plasmas generated in intense laser-solid interactions is highlighted in blue. Adapted from A. Ciardi, Laboratory Studies of Astrophysical Jets, Springer Berlin Heidelberg, 2010.

3.1 Magnetised astrophysical phenomena

The generation of magnetic fields is prevalent in numerous scenarios and systems across the known universe, commonly associated with stellar prominences (magnetic filaments of plasma extending from stellar surfaces far into the atmosphere), accretion mechanisms (the gravitational mechanism by which mass is transferred from a relatively more massive object to a denser one) and the dynamo mechanism (the mechanism by which stars or planets generate magnetic field). Phenomena resulting from the presence of strong magnetic fields include directed plasma jets or collisionless shock formation. The magnetic fields required for the formation of plasma jets or collisionless shocks may be initially present, for example in supernova remnants or young galaxies, or they may be self-generated in systems such as inward-flowing accretion mechanisms [45]. Another mechanism resulting in the self-generation of magnetic fields, even in the absence of a seed field, is the Weibel instability [129]. In section 2.7.3, the growth of the Weibel instability due to the interaction of magnetic fields from two counter-propagating currents was discussed. In this scenario, small modulations in the density profile of one of the populations leads to perturbations in the local self-generated magnetic field, resulting in the filamentation of the population of fast electrons. However, Weibel also considered the case of the growth of an instability driven by velocity anisotropies in a fast electron beam, propagating into a background of

Parameter	AGN	YSO
Length (pc)	10^6	1
Lifetime (years)	$\sim 10^7$-10^8	10^4
Velocity (km/s)	$\sim 3\times 10^5$	$\sim$100s
Radius (m)	10^{15}	10^{12}
Mach number	50	20
Electron temperature (eV)	10^7	10^4

Table 3.1: Comparison of properties of astrophyical jets, launched from AGNs and YSOs

a static ion population [129]. As in the case of two-counter propagating electron beams, the resultant fast electron transport pattern is filamented. The scenario of a collisionless, relativistic electron population propagating into a static ion population is particularly relevant for intense laser-solid interaction physics, as discussed in section 2.6.3.

Examples of the properties of matter related to strong magnetic field generation that can potentially recreated in astrophysically relevant conditions in laboratory environments include strong shock phenomena [48,201], high mach number jets [34,62,202], equations of state of warm dense matter [113,203] and relativistic plasmas [64]. Due to their relevance to the results presented in **Chapter 6**, an outline of the physics of high mach number jets is now presented:

Directed jets of plasma are prevalent in many astrophysical systems, including young stellar objects (YSOs), gamma ray bursts (GRBs) [204] and active galactic nuclei (AGNs). Such jets are associated with compact central objects, surrounded by a strongly magnetised accretion disk. Jets represent some of the largest continuous structures in the observable universe, with typical properties summarised in table 3.1. Despite the vast differences between the physical properties of jets arising from the multitude of astronomical sources (illustrated in table 3.1), they nonetheless all share common properties: they are highly-collimated and, in most cases, symmetrical on either side of the accretion disk; they originate in compact objects; they exhibit a chain of regularly spaced emission knots; and they often terminate in emission lobes (with line emission in the case of YSOs and synchrotron emission in the case of AGNs).

The formation of relativistic jets is associated with magnetised accretion disks. In the specific case of YSOs, this process occurs during the accretion phase of star formation, where a cloud of material gravitationally collapses to form a protostar [31,205]. Jets originating from AGN are formed due to the accretion of matter onto a rotating supermassive black hole at a galactic centre. YSOs are stars in the early stages of their evolution, and

the term encompasses both protostellar objects and pre-main sequence stars. They are associated with the accretion of matter from nearby planetary nebulae or massive objects, resulting in the formation of an accretion disk and high Mach number bipolar jets. Accretion disks surrounding these objects will eventually result in the formation of a planetary system. AGNs, in contrast, are compact regions at the centre of a galaxy that outshine their host galaxies, in most regions of the electromagnetic spectrum. Again, they are associated with the accretion of matter onto a dense compact object which, in this instance, is a rotating supermassive black hole. As before, the accretion of matter results in the formation of an orbiting accretion disk and bipolar jets.

The links between accretion mechanisms and jet production are postulated as the jet outflow rate appears proportional to the accretion rate [206] and jets are always directed perpendicular to the plane of the disk. The angular momentum of the accreting matter must be conserved resulting in the formation of a rotating ring of material orbiting the central object. Models of astrophysical jet collimation and launching involve magnetic fields arising from the rotation of the matter in the accretion disk as the collimating mechanism [207–210]. Unfortunately, observations of the central object and the jet launch region are often difficult. The accretion disk, gas and dust clouds, the host planetary nebulae (in the case of YSOs) and the galactic disk (for AGNs) all act to mask optical observations. Furthermore, magnetic fields in this region are difficult to measure as magnetic shocks closely resemble non-magnetic shocks with lower shock velocities [211].

One magnetic model commonly employed to explain the directed momentum of jets is the steady-state "fling" model [57], or magneto-centrifugal acceleration. In this model, the flux of matter launched from the dense core is sustained by centrifugal and toroidal magnetic field pressure forces, directed along the poloidal field. Figure 3.2 illustrates this process schematically. This can be summed up as follows: matter is accreted from a relatively more massive object to the small, compact progenitor, where an accretion disk forms to conserve the angular momentum of the infalling matter (figure 3.2 (a)); the accretion disk is threaded by a poloidal magnetic field, ejecting matter from the disk along the resultant field lines (figure 3.2 (b)). As the disk rotates, the material ejected to larger radii is accelerated by the magneto-centrifugal force. At these large radii, the magnetic fields wind up, generating a collimating, toroidal component of the magnetic field. Outflowing stellar winds interact with these field structures resulting in the formation of a highly-collimated, bipolar jet along the rotation axis (figure 3.2 (c)) [131]. YSO jets

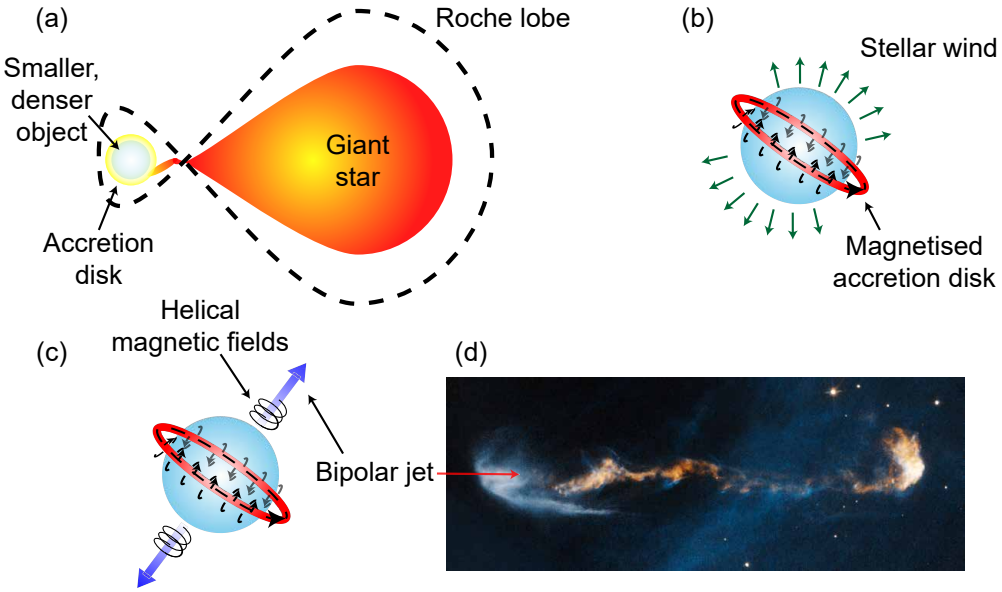

Figure 3.2: Schematic illustrating accretion disk and jet formation, showing (a) the accretion of matter from a relatively massive star onto a smaller, more compact object (i.e. white dwarf, YSO, black hole); (b) Illustration of the magnetic field structure of the rotating disk. The poloidal field ejects matter to larger radii, where the magnetic fields wind up to form a toroidal structure; (c) The stellar wind emanating from the star is swept up and collimated by toroidal fields, forming a bipolar jet, extending to parsec scales; (d) Example bipolar jet emitted from a YSO, Herbig-Haro object HH-47. Credit: NASA, ESA, P. Hartigan (Rice University), G. Bacon (STScI).

propagate with typical properties described in table 3.1.

Whilst magneto-centrifugal acceleration appears to be a candidate for the launching and collimation mechanism of astrophysical jets, other concepts include the explosive "spring" mechanism [212–214] and magnetic tower outflow mechanism [209]. Due to the difficulties involved in making detailed observations of the launch regions of astrophysical jets, no consensus has yet been reached on which scheme is correct.

As the jet propagates away from its progenitor, it remains collimated for distances on parsec scales. Faraday rotation measurements of the jet emanating from the AGN 3C 273 indicate the presence of precessing, helical magnetic field structures along the length of the jet [58]. Figure 3.3 summarises these observations. These observations were repeated for measurements of YSO jets [215], with values much greater than that of the interstellar medium (ISM, 1 G compared to a few μG). The spatial distribution of these fields have been postulated to be generated by the winding up of the magnetic field by the rotation of the accretion disk [216]. A distinct increase in the pitch angle is observed with increasing distance from the source, a feature explained as resulting from shocks as the jet propagates further into the interstellar medium (ISM) or intergalactic medium (IGM).

As the jet expands into the ISM, the ambient gas is excited through collisions at the

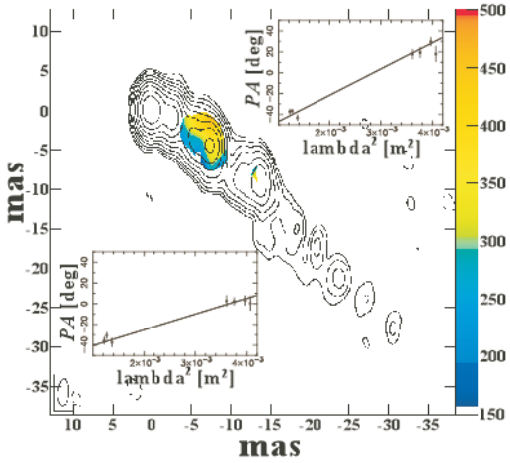

Figure 3.3: Faraday rotation measurements of the jet of AGN 3C 273, depicting a helical magnetic field. [Inset] The pitch angle is plotted as a function of λ^2 for each side of the jet. Credit: K. Asada et al., PNAS 54 (3), 2002, license number: 4206540177144.

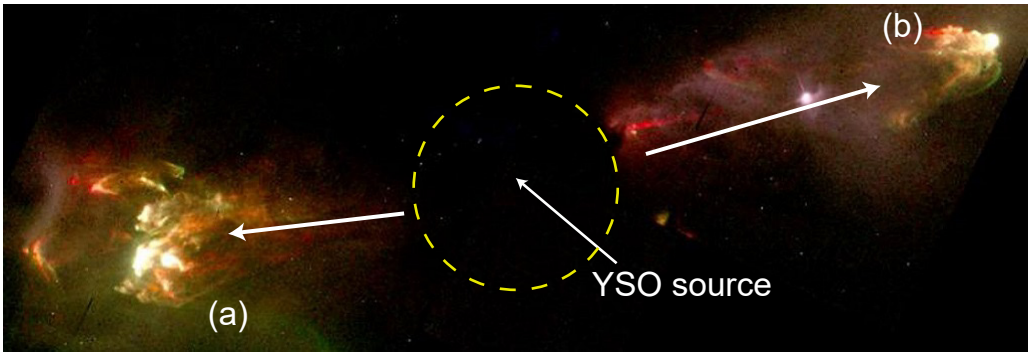

Figure 3.4: Herbig-Haro objects (a) HH1; and (b) HH2, located south of the Orion nebula. The YSO source is obscured by a dark dust cloud. The bright HH-objects are where the jet has excited gas of the ISM. Credit: J. Hester (Arizona State University), WF/PC 2 Investigation Definition team, and NASA.

interface between the leading edge of the jet and the ambient medium. These result in the slowing down of the head of the jet and shock formation. These shocks result in a series of bright emission regions, often symmetrically located on either side of the bipolar jet. These regions are known as Herbig Haro (HH) objects. HH objects enable insight into the properties of the jet at the emission regions. Their rapid transient evolution enables the properties of the jet, including temperatures, densities and velocities, to be probed. [217]. Figure 3.4 illustrates the nature of these objects as seen in observations made of HH objects from the Orion nebula.

Remington *et al* [27, 31] features a comprehensive review of the astrophysical phenomena that offer potential avenues for reproducible measurements in scaled-down laboratory experiments.

Parameter	SN1987a	Typical laboratory experiment
L (m)	3×10^{16}	1×10^{-4}
t (s)	$\sim 1 \times 10^{8}$	$\sim 1 \times 10^{-12}$
ρ (g/cm^3)	7.5×10^{-3}	4.2
Re	2.6×10^{10}	1.9×10^{6}
Pe	2.6×10^{5}	1.8×10^{3}

Table 3.2: Supernova parameters for SN1987a, and corresponding parameters for a typical laboratory laser-solid interaction experiment. From Remington et al. Rev. Mod. Phys. 78:775, 2006.

3.2 Scaling relations

Clearly, there exists massive differences of scale, shown in table 3.2 [31], between plasmas generated in astrophysical scenarios and those generated in intense laser-solid interactions. Reconciling differences of scale between two asymmetrically-sized systems has been investigated for many years. In 1977, Connor and Taylor [218] show that the solution is a set of dimensionless scaling parameters which enable the vastly different regimes to be considered similarly. They showed that if the basic laws that describe a plasma are invariant under a given transformation, then any scaling law derived from such equations must also be invariant. Such scaling laws are routinely applied to scale Magnetic-Confined Fusion (MCF) investigations from comparatively smaller tokamaks, such as JET, up to the next stage in MCF experiments, ITER [219]. They concluded that if the basic laws describing plasmas are invariant under a given transformation, then any scaling laws derived from these laws must also be invariant for the same transformation. Furthering this concept, Ryutov *et al.* [220] proposed a group of transformations for the Euler equations for systems which can be described using ideal magnetohydrodynamics (MHD). The use of MHD equations to describe a system is reliant upon a series of assumptions being satisfied, which describe a system for which the fluid approximation is valid, i.e. they are collisional and generally described by a Maxwell-Boltzmann distribution. However, both the astrophysical and laboratory systems investigated in this thesis are in the plasma state, rather than neutral gas clouds. The specific systems of interest in this thesis generally possess MFPs of a scale far greater than the spatial extent of the system, and thus, the validity of employing MHD equations must be considered. Ryutov *et al.* [221] demonstrated that, in collisionless plasmas, collisionality can be assumed if magnetic fields are present. This process is described as follows: a charged particle, with a component of motion perpendicular to a magnetic field, experiences a force. As a result, the motion of the particle

alters the distribution of the magnetic field. Applying this to the situation where many particles are present, the deflections of the particles contribute to a significant variation of the magnetic field, leading to an effective collisionality over scales on the order of the Larmor radius. Even for relatively weak magnetic field strengths, the spatial scales can be less than the plasma spatial dimensions, enabling a fluid approximation of the plasma to be satisfied. The assumptions of such a system are as follows [221]:

i. The total mass of the system must be conserved:

$$\frac{\partial \rho}{\partial t} + \nabla \cdot \rho \mathbf{v} = 0 \tag{3.1}$$

ii. The total momentum of the system must be conserved:

$$\rho \left(\frac{\partial \rho}{\partial t} + \mathbf{v} \cdot \nabla \mathbf{v} \right) = -\nabla p - \frac{1}{4\pi} \mathbf{B} \times \nabla \times \mathbf{B} \tag{3.2}$$

iii. The magnetic induction is described by:

$$\frac{\partial \mathbf{B}}{\partial t} = \nabla \times \mathbf{v} \times \mathbf{B} \tag{3.3}$$

iv. The total energy of the system must be conserved:

$$\frac{\partial p}{\partial t} + \mathbf{v} \cdot \nabla p = -\gamma p \nabla \cdot \mathbf{v} \tag{3.4}$$

where $\mathbf{v}$, ρ, p and $\mathbf{B}$ are the velocity, density, pressure and the magnetic field strength, respectively. The conservation of energy (equation (3.4)) is defined under the assumption that the fluid is polytropic, i.e. it is governed by the Lane-Emden equation, which presents a solution for the gravitational potential of a Newtonian, spherically symmetric, polytropic fluid. The validity of this assumption requires the stipulation that a system temperature rise does not excite further degrees of freedom; valid for radiation-pressure-dominated systems or systems that are fully ionised. In the above, $\gamma = 1 + 1/C$, and is known as the polytropic index [222], assumed to be constant in space and time.

Equations (3.1)-(3.4) are seen to govern the pressure, density, velocity and magnetic field strength of the system under consideration. A length scale, L^*, can be added to

these parameters, allowing them to be rewritten as:

$$\rho_{(t=0)} = \rho^* F\left(\frac{\mathbf{r}}{L^*}\right) \tag{3.5}$$

$$p_{(t=0)} = p^* G\left(\frac{\mathbf{r}}{L^*}\right) \tag{3.6}$$

$$\mathbf{v}_{(t=0)} = v^* \mathbf{H}\left(\frac{\mathbf{r}}{L^*}\right) \tag{3.7}$$

$$\mathbf{B}_{(t=0)} = B^* \mathbf{I}\left(\frac{\mathbf{r}}{L^*}\right) \tag{3.8}$$

where ρ^*, p^*, v^* and B^* are characteristic, measured values for the density, pressure, velocity and magnetic field strength in a system on the length scale, L^* and $\mathbf{r}$ is the spatial dimension of the system. The functions F, G, $\mathbf{H}$ and $\mathbf{I}$ defined the geometric shape of the distribution at this scale. Any system which is in agreement with the assumptions made previously can then be described by the following five parameters: ρ^*, p^*, v^*, B^* and L^*. By normalising the parameters of the system to these values, a set of dimensionless variables may be defined, i.e:

$$\tilde{\mathbf{r}} = \frac{\mathbf{r}}{L^*} \tag{3.9}$$

$$\tilde{t} = \frac{t}{L^*}\sqrt{\frac{p^*}{\rho^*}} \tag{3.10}$$

$$\tilde{\rho} = \frac{\rho}{\rho^*} \tag{3.11}$$

$$\tilde{p} = \frac{p}{p^*} \tag{3.12}$$

$$\tilde{\mathbf{v}} = \mathbf{v}\sqrt{\frac{\rho^*}{p^*}} \tag{3.13}$$

$$\tilde{\mathbf{B}} = \frac{\mathbf{B}}{\sqrt{p^*}} \tag{3.14}$$

For two systems, of different size $\mathbf{r}$, the initial conditions can be assumed to be identical if the following is true [221]:

$$\mathbf{v}_1\sqrt{\frac{\rho_1}{p_1}} = \mathbf{v}_2\sqrt{\frac{\rho_2}{p_2}} \tag{3.15}$$

$$\frac{\mathbf{B}_1}{\sqrt{p_1}} = \frac{\mathbf{B}_2}{\sqrt{p_2}} \tag{3.16}$$

where equation (3.15) is the Euler number and equation (3.16) is the square root of the plasma beta; the ratio of the plasma pressure to the magnetic pressure. These equations impose two constraints on the five parameters that can describe a system (ρ^*, p^*, v^*, B^* and L^*). Thus, in scaled-down laboratory experiments, a scale ratio of one of ρ^*, p^* or L^* can be chosen. With a scale-ratio between the two systems known, one of the magnetic field strength or the velocity can be examined for similarities, an example of which will be demonstrated in section 3.3.

3.3 Intense laser-solid interaction studies relevant to astrophysics

In recent years, laboratory experiments have opened up new opportunities to study analogues of astrophysical phenomena. Scaling laws, such as those discussed in the previous section have been previously applied to a myriad of laser-plasma interaction experiments. These include experiments investigating plasma jet formation and transport [62, 202], the origin of magnetic fields [48, 201], WDM studies [32, 52, 203], and investigations of astrophysically-relevant radiation [36] and particle production [70].

The most relevant class of laboratory experiments to the work presented in this thesis are those investigating the self-generation of magnetic fields. A key focus is that of plasma jet formation, launching and collimation. Gregory *et al.* [62] employed novel targetry in order to drive the generation of jets: v-shaped foil targets (two thin foils placed at an angle of 140^o to each other) were irradiated, each by separate laser pulses. The plasma generated at the rear of each target expanded into the other, driving plasma jets with velocities of $\sim$300 km/s. It was demonstrated that high velocity, low density plasma jets, with scaling relevant to those launched from YSOs, could be generated and studied. The motivation behind this investigation was the applicability of this experiment for further investigations into the underlying physics of YSOs and the accretion mechanisms associated with them: an ambient gas was employed after the target, thus propagation effects could be isolated from the region of jet formation. In investigations of astrophysical jets it is often observed that the central dense object is obscured by the accretion disk, leading to difficulties when making observations of jet formation. Thus, by isolating propagation effects in ambient

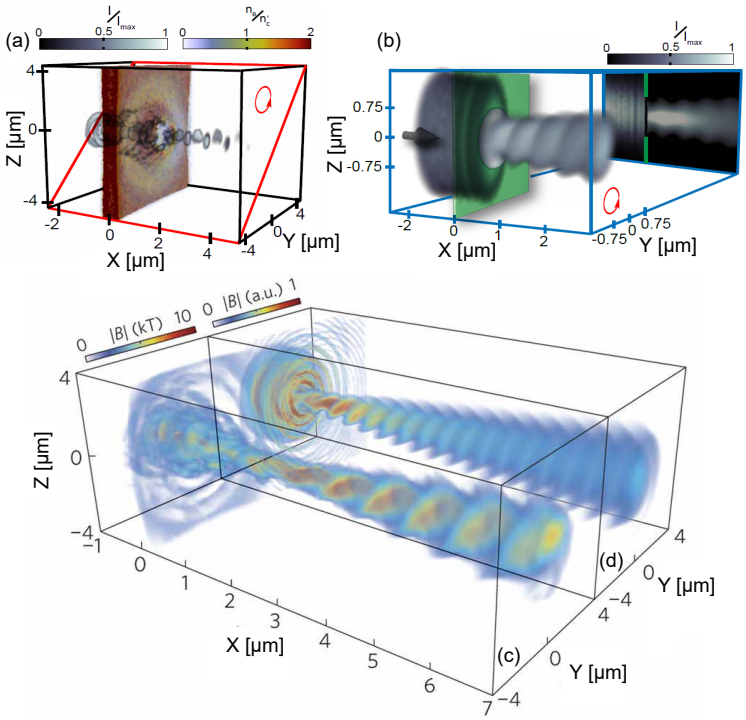

Figure 3.5: Magnetic field structure driven by a rotating diffraction pattern of circularly polarised laser light transmitted through a relativistic plasma aperture self-generated via relativistic induced transparency in an ultrathin foil. (a) 3D PIC simulation result showing the laser diffraction and plasma electron density produced by the relativistic plasma aperture, in the case of a circularly polarised intense laser pulse interacting with a planar foil; (b) 3D simulation profile showing the spatial-intensity variation of the diffraction pattern of a circularly polarised laser pulse through a pre-defined aperture; (c) Magnitude of the magnetic field driven by a circularly polarised laser pulse producing a relativistic plasma aperture in a 10 nm-thick Al target. A helical field structure is produced; (d) Same, but for a lower laser intensity pulse propagating through a fixed, predefined aperture of 0.75 μm radius. Adapted from [64]

medium, such as enhanced collimation or shock structures [223], a deeper insight into the initial collimation and launching mechanism could be gained.

In Foster *et al.* [60] the first measurements of jets and bow shocks in the context of laboratory astrophyiscs were performed, in an investigation of the interaction of supersonic jets with an ambient foam medium using the Omega laser facility. Rosen *et al.* [224], by contrast, was concerned with the interaction of a dense, laser-generated plasma jet with local density perturbation, relevant to Herbig-Haro objects HH34 and HH47A.

More recently, Gonzalez-Izquierdo *et al.* [64,225] reported measurements of the collective response of charged particles to the strong diffraction of laser light transmitted through an ultrathin foil by the self-generation of a relativistic plasma aperture. It was shown that, with circularly polarised laser light, a high current beam of relativistic electrons, with precessing, helical magnetic field structures, could be formed. Similar helical magnetic

field structures have previously been observed in jets launched from AGNs, such as AGN 3C 273 [58]. Furthermore, additional similarities to astrophysical jets were observed in measurements of the distribution of the electron momenta across the beam; with the highest momentum component occurring at the central laser axis. With increasing beam radius, the electron momentum decreases, resulting in an electron beam with properties similar to that of a spine-sheath jet morphology [226]. Detailed analysis of the scaling between the laboratory-produced jet and AGN 3C 273 shows that a length scaling ratio of $\sim 2 \times 10^{21}$ exists between the two systems: from 15 μm to 1 pc [227]. Making the assumption that both jets propagate at velocities $\sim c$, the timescale ratio was estimated to be comparable to the length scale ratio [228], resulting in a calculated interaction timescale of 50 fs. This was found to be in good agreement with the laser pulse duration of 40 fs. Figure 3.5 illustrates the magnetic field structures of the laboratory-produced relativistic electron beams.

Chapter 4

Methods - laser systems, experimental diagnostics, and simulations

In the previous chapter, the underlying physics concepts relevant to the investigations presented in this thesis were discussed. These investigations were only made feasible through the development, and use, of a number of different state-of-the-art technologies and diagnostic equipment.

This chapter details the high power laser technology used to conduct the experiments presented in the latter chapters of this thesis and summarises the diagnostic techniques employed to extract data from these experiments. Finally, a discussion of the simulation techniques used to investigate and interpret the underlying physics of the experimental findings is explored.

4.1 Overview

Experiments conducted at national, high power laser facilities are often allocated in slots of several weeks to over a month. Facilities such as these are utilised by numerous research teams from universities and private companies across not only the country, but occasionally from other institutions across the world. As a result, the allocation of "slots" of beam-time are at a premium.

Once the experiment has commenced, a period of typically a week is set aside to allow the diagnostic and experimental setup to be constructed from scratch. Upon installation

of all the diagnostic equipment required, and successful referencing of the laser focus position, the focus for the remainder of the beamtime shifts to performing as many high quality data shots as possible. Initially, these shots serve mainly to calibrate laser parameters, such as the laser energy incident on the target, or to check the operation of the diagnostics, before progressing to investigating the aims of the experiment. However, this is a very fluid process, and is mainly dictated by analysis of the results as they are acquired. Thus, the shots taken are tailored in-situ, with data scans prioritised that enable better understanding of the interaction, achieve the aims of the experiment and reveal new physics.

4.2 High power laser systems

The experimental investigations presented in this thesis were performed on three separate laser systems at two national-scale facilities located in the United Kingdom and Germany. These are the Astra-Gemini and Vulcan at the Central Laser Facility (CLF) at the Rutherford Appleton Laboratory (RAL) in Oxfordshire, UK; and the PHELIX laser, at the GSI laboratory in Germany. The basic process of generating an ultra-intense laser pulse is, initially, analogous to that of a standard, commonly-owned laser system: coherent amplification of a photon can be achieved when its electromagnetic field acts upon a population inverted gain medium, provided the energy band gap of the medium matches that of the incoming photon. The forthcoming sections will briefly introduce the various concepts that enable the transformation of such technology to produce the high powers required, and the operation of these high power lasers at such high intensities We begin with the technique that has revolutionised the field of laser-plasma interaction physics: chirped pulse amplification (CPA).

4.2.1 Chirped pulse amplification

The technique of chirped pulse amplification (CPA), first demonstrated, in the context of lasers, by Strickland and Mourou in 1985 [14], dramatically altered the field of laser-plasma interactions, allowing relativistic intensities of $\sim 10^{18}$ W/cm^2 to be achieved and opened up new avenues of experimental research that were previously unexplored.

CPA was designed to avoid the damage to optical components that occurs during the amplification of a laser pulse, from the seed pulse, with typical energies of nanoJoules, up

to the tens-to-several hundreds of Joules focused onto the targets employed in laser-solid interactions. Purely amplifying the laser pulse very quickly leads to the beam fluence surpassing the damage threshold of the solid state optics. Further to this, damage can also occur below the damage threshold of the optics in the system due to nonlinear effects, such as self-focusing of the beam [229] and B-integral accumulation, both of which deform the wavefront of the beam. B-integral can be defined by the following equation:

$$B_f = \frac{2\pi}{\lambda} \int n_2 I(z) dz \tag{4.1}$$

where $n_2 I(z)$ is the intensity dependent refractive index of the material.

One approach to minimising this issue of fluence is to increase the diameter of the beam and, consequently, the size of the optics in the system. However, as the demand for higher intensities increases, ever larger and more costly optics will be required to be manufactured. CPA circumvents this issue by not stretching the pulse spatially, but rather by stretching it temporally. It achieves this by introducing what is known as a chirp in the pulse, where a frequency dependent temporal dispersion is introduced by a pair of gratings, known as a "stretcher". The seed pulse is positively chirped. This is to say that longer wavelengths are predominantly dispersed towards the front of the pulse temporal profile. The range of wavelengths present in the laser pulse is known as the "bandwidth"of the pulse, and imposes a limit on the maximum level of temporal stretching and compression achievable: the greater the range of wavelengths available, the shorter the final pulse duration. For example, the Vulcan petawatt laser has a bandwidth of ± 7 nm either side of its central wavelength of 1053 nm, and has a minimum pulse duration on target of ~ 500 fs.

With the intensity of the pulse now far below the damage threshold of the system, amplification can now proceed without any of the aforementioned negative nonlinear effects being encountered. Although the energy density of the pulse is still similar to that of the seed pulse, the total energy contained within the pulse is significantly larger.

The final stage of the CPA process involves compressing the amplified pulse back to its pre-stretched temporal duration. This is achieved by passing the pulse through a grating pair of the opposite dispersion to the initial stretcher pair. At this stage, larger optics are utilised to avoid damage from the now-compressed laser pulse. The result of this final stage is the generation of a short, high energy pulse, suitable for interaction physics, which has circumvented damage to the optics of the system.

Notably, although the seed pulse is typically of the order of a few femtoseconds in

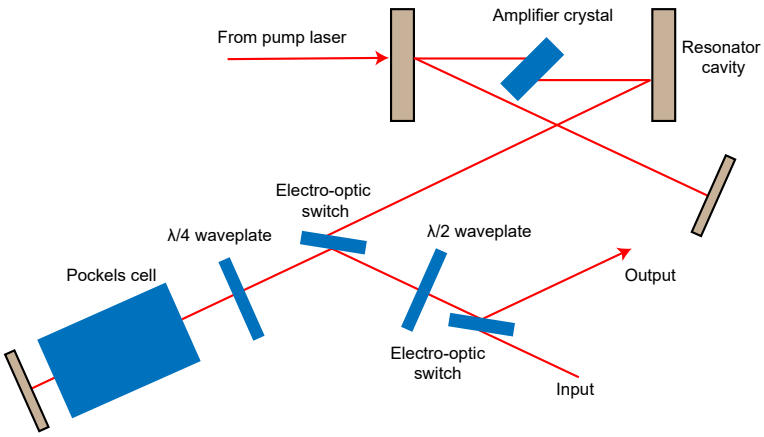

Figure 4.1: Illustration of a typical regenerative amplifier.

duration, re-compression of the amplified pulse does not generally result in an a high-energy pulse of the same temporal duration. This is due to a phenomenon known as "gain narrowing", in which the outer frequencies of the pulse are amplified less efficiently than the central wavelength. Thus, the bandwidth of the pulse is effectively reduced during the amplification process. Thus, re-compressing the pulse back to the duration of the original seed pulse is often impossible due to the gain bandwidth of the amplification medium. Furthermore, the level of gain narrowing is also dependent on the magnitude of the gain.

4.2.2 Amplification techniques

Two common amplification techniques exist and are typically used for conventional laser amplification. The first of these is the use of regenerative amplification. Regenerative amplifiers are typically used in the oscillator or pre-amplification stages with gain achieved on each pass through the gain medium. The gain of regenerative amplifiers is kept relatively low, when compared to the gain of single-pass laser amplifiers, in order to reduce the generation and amplification of spontaneous emission (ASE, see section 4.2.4). A typical schematic of a regenerative amplifier is shown in figure 4.1.

Regenerative amplifiers operate as follows: initially the stretched pulse is injected into the amplifier via a polariser. If the incoming, beam is s-polarised as it enters the amplifier, the waveplate rotates the polarisation of the pulse to p-polarised. The pulse then passes through a Faraday rotator, which again rotates the laser polarisation, this time by an amount that depends on the length of material the pulse passes through, the strength of any external magnetic field present, and the Verdet constant of the material. The resultant pulse exiting the Faraday rotator is s-polarised. This is described by the following relation

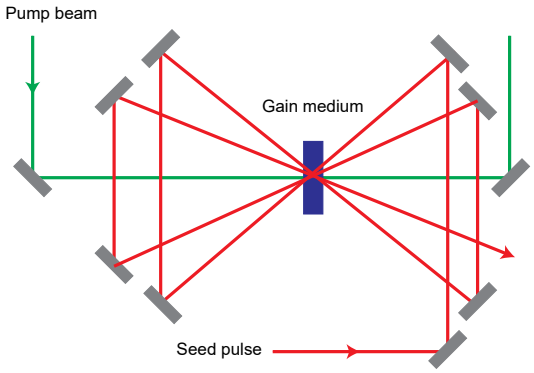

Figure 4.2: Illustration of a typical multi-pass amplifier.

(Eq. 4.5):

$$\theta = \nu B l \tag{4.2}$$

where θ is the angle of rotation of the incident pulse, ν is the Verdet constant of the material, B is the external magnetic field, and l is distance that the pulse propagates through the material.

The pulse is then propagated through a second polariser which acts to reflect s-polarised light and transmits p-polarised light. As the pulse is s-polarised, it is reflected and is injected into a Pockels cell. The Pockels cell is set up with a voltage across it known as the "quarter-wave" voltage, causing it to act as a quarter-wave plate. Thus, the pulse exits the Pockels cell with circular polarisation, and reflects of the cavity mirror, before it passes through the Pockels cell again. Effectively, this has the same effect as a half-wave plate; thus the pulse exits the cell again, this time being p-polarised. As previously discussed, the polariser in the cavity transmits p-polarised light and so the pulse is sent to the gain medium, where it is amplified and reflected off the opposing cavity mirror, back into the cavity. This whole process is repeated *ad infinitum* until the desired number of passes is achieved, at which point the voltage across the Pockels cell is altered, leading to no rotation of the polarisation and the pulse being reflected out of the cavity.

The other amplification technique commonly used is the "multi-pass" amplifier. In this arrangement, as with the regenerative amplifier, the pulse makes multiple passes through the gain medium, however in this case the pulse is confined by a purely geometrical means rather than by optical switching out of a cavity. The pulse is passed multiple times through the gain medium of a series of mirrors as illustrated in figure 4.2.

Due to the fact that the gain medium is not within an optical cavity, larger gains can be achieved per pass of the pulse. Both of these techniques are commonly implemented in CPA laser systems. However, as the highest gain is typically achieved in the pre-amplification stages of the laser system and due to the nature of the amplification and the inherent ASE in these types of amplifiers, alternative amplification techniques are required.

4.2.3 Optical parametric chirped pulse amplification

Optical parametric chirped pulse amplification (OPCPA) is another method of amplification of a high power laser pulse, avoiding damage to optics in the process. With this technique, it is possible to achieve even higher amplified pulse energies than with conventional amplification processes using laser gain media [230, 231].

The initial stage of stretching the pulse remains the same as in the traditional CPA technique. However, rather than proceeding to inject the pulse into a conventional amplifier, it is instead passed through a crystal which exhibits a second-order nonlinearity [232]. Simultaneously, a high energy, high frequency (with respect to the seed pulse) "pump" pulse is also injected into the crystal, resulting in a parametric transfer of energy from the "pump" pulse to the seed pulse. Typical gains of 10^7 have been measured using this technique [233]. The stretched, amplified pulse is then fed into a conventional amplification system and, finally, recompressed as discussed previously in the CPA case.

Optical parametric amplification (OPA) displays several major advantages over conventional laser amplification systems. Firstly, the high level of conversion efficiency from the pump pulse to the seed pulse results in very low heating of the crystal, minimising thermal aberrations in the amplified pulse. This arises from the fact that, upon the correct phase matching conditions, the pump photons are converted to the same frequency as the seed photons. Any excess energy from the pump photon and seed photon is output as a third photon, called the idler, at a frequency which conserves the energy; this is summarised in equation (4.3).

$$\omega_p = \omega s + \omega i \tag{4.3}$$

where ω_p is the frequency of the pump pulse, $omega_s$ is the frequency of the seed pulse and ω_i is the idler frequency.

Furthermore, conventional amplification processes place limits on the shortest achievable pulse duration due to gain-narrowing effects that limit the maximum pulse bandwidth.

Finally, and perhaps most importantly, is that the generation of ASE, (which will be defined and discussed in the section immediately following this) is greatly minimised in optical parametric amplifiers, when compared to conventional techniques. This results from the fact that no energy is stored within the nonlinear crystal itself and that amplification only occurs in the presence of both the signal and pump pulses. It is these reasons that have led to OPA processes being employed as pre-amplifier systems in hydrid OPCPA schemes becoming common procedure for high-power laser systems [234, 235].

4.2.4 Pulse contrast

As discussed in the previous section, amplified spontaneous emission (ASE) production is significantly reduced in OPA processes. In realistic cases of laser amplification, ASE is a background component inherent to conventional laser amplification techniques, whereby photons emitted spontaneously from the excited atoms in the gain medium are amplified in conjunction with the coherent, stimulated emission of the main pulse. The spontaneously emitted photons decay with a spectrum related to the line width of the decay transition, over an emission angle of 4π steradians. Light emitted outside of a small angle from the central axis, quickly leaves the gain medium without a great deal of amplification. However, photons emitted near the central axis of the medium travel along its length and are amplified. A schematic demonstrating this concept is displayed in figure 4.3(a).

ASE manifests itself as a pedestal to the main laser pulse and can be present temporally up to many nanoseconds preceding the main intense laser pulse. With current intensity levels of high power laser pulses being of the order of $\sim 10^{20}$ W/cm^2, even systems where the peak intensity of the ASE pedestal is of the order of 10^8 lower than the peak intensity of the main pulse the effects of the pedestal on laser-solid interactions needs to be seriously considered. The ratio of the intensities of the main pulse to the pedestal is known as the *"laser contrast"*. As demonstrated in figure 4.3(b), this value can vary depending on the time prior to the arrival of the main pulse, and so the contrast ratio is usually quoted with an associated measurement time. In the above example, the peak intensity of the pedestal would be $\sim 10^{12}$ W/cm^2, which, when focused onto a target, would be sufficient to cause ionisation and pre-expansion of the material prior to the arrival of the main pulse. Figure 4.3(b) highlights what is meant by this contrast ratio.

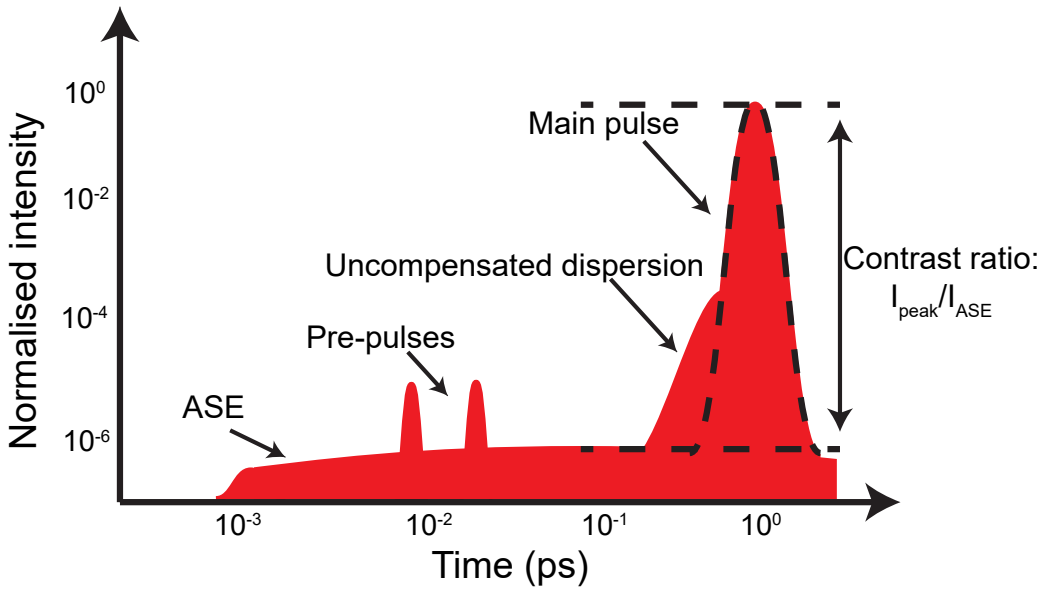

Figure 4.3: Cartoon outlining the temporal intensity profile of a typical laser pulse. In the illustration, the pulse can be thought of as travelling from right to left, with representative times at which features can be observed with respect to the main pulse marked. An example of the contrast ratio between the peak intensity and the ASE is also shown. Adapted from Scott, 2015.

Minimising the degree of spontaneous emission and its subsequent amplification is of key importance in the generation of intense laser pulses. This can be accomplished to a degree passively by implementation of pulse "cleaning" and amplification techniques in the laser chain itself.

One of the amplification techniques employed to enhance the laser contrast is simply to reduce the gain of the amplifier. For a single-pass amplification technique, this might seem counter intuitive as maximum amplification of the pulse is the aim. It is for this reason that regenerative or multi-pass amplification techniques are used as they enable multiple passes through the gain medium operating with a lower gain, extracting energy each time.

An additional approach to pulse "cleaning" is to use a Pockels cell to gate out the ASE pedestal, though this is limited to the nanosecond or hundreds-of-picoseconds time scale. Thus, with this method, there is always a short-timescale level of ASE present in the final amplified pulse.

Finally, the possibility of employing plasma optics in the final focussing beam, just before target, for the purposes of increasing the contrast ratio of the pulse is a desirable method in the high power laser community due to their low cost, disposable nature. This technique will be discussed in much greater detail in 4.2.5.

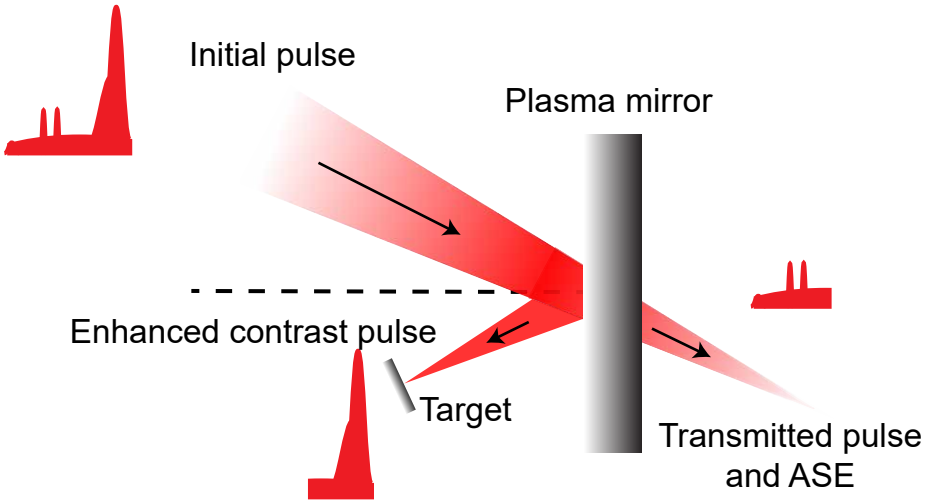

Figure 4.4: Schematic of the principle of operation of a planar plasma mirror under irradiation by an intense laser pulse. The reflection of the main pulse and the transmission of the low intensity ASE is highlighted.

4.2.5 Plasma Mirrors

Plasma optics [236–239] are frequently incorporated into experimental setups in order to minimise laser pre-pulses and ASE inherent in the CPA scheme [14]. These typically take the form of planar slabs of material, though recent studies have explored the possibility of intensity enhancement through the use of small F/#, ellipsoidal focusing plasma mirrors (FPM) [238, 240, 241].

The principle of operation of plasma mirrors is as follows: a thin layer of overdense plasma is created on the surface of a transparent solid. Generally, this is optical quality glass or PMMA, and is often coated with an anti-reflection (AR) coating to enhance transmission when the optic is in its pre-plasma state. The position of the plasma mirror after the final focusing optic is determined such that the ASE and pre-pulses preceding the main pulse fall below the threshold intensity for ionisation of the material and thus, are transmitted. As the main portion of the pulse arrives, and the laser intensity at the surface of the optic increases, it begins to rapidly ionise the optic and is reflected at the critical surface of the resultant overdense plasma. The resultant pulse on target thus has an enhanced contrast ratio than it possessed previous to interaction with the plasma mirror, and possesses a sharper rising edge profile. Figure 4.4 demonstrates this concept.

Several studies have been undertaken to characterise the use of planar plasma mirrors for experimental use [242–244]. The resultant contrast enhancement is improved from the order of $10^6 - 10^7$ by approximately 2 orders of magnitude. One of the drawbacks

in the utilisation of a plasma mirror to enhance contrast is the loss of pulse energy, and thus intensity, of the focused laser pulse on target; resulting from the plasma formation on the surface of the optic, and the fact that 100% of the main pulse is not reflected. Typical losses in the region of 15-30%, and plasma mirror reflectivities of 60-80% have been measured [236, 242, 243]. These losses have been found to be dependent on the incoming laser polarisation on the plasma mirror, with the dominance of absorption mechanisms varying depending on the laser polarisation, as discussed in section 2.5.

Today planar plasma mirrors (PPMs) are almost ubiquitous in laser-solid experiments where targets of thicknesses on the nanometre-scale are irradiated. Their necessity is due to the fragility of these targets: especially large pre-pulses or high-intensity pedestals preceeding the main interaction pulse will vaporise the target before the high intensity main pulse has arrived.

Recently, studies have been undertaken investigating the possible use of plasma mirrors with curved, ellipsoidal geometries which will perform as a secondary, small F/# focusing optic in order to focus the incoming laser pulse to near diffraction-limited spots [238, 240, 241]. In this way, not only will the laser pulse incident on target benefit from an improvement in pulse contrast, but additionally, an increase in peak intensity.

4.2.6 Shack-Hartmann wavefront sensor

The Vulcan petawatt laser system (discussed in detail in the section immediately following this one) is susceptible to several phase aberrations that can result in a loss of peak laser intensity [245]. Such aberrations can lead to several negative effects that present themselves in the laser wavefront, including longitudinal displacements in the final focus position of the pulse.

In order to characterise the magnitude of such aberrations present in the pulse, a Shack-Hartmann wavefront sensor was used to measure the wavefront profile, from which the level of defocus in the final laser focus position from its nominal can be inferred through analysis of the degree of phase aberrations present in the laser wavefront. The measurement could then inform of any deviation from nominal focus on-shot, and thus any drop in the peak laser intensity on target as the target is aligned to nominal focus. An illustration of the operating principle of a Shack-Hartmannn wavefront sensor is shown in figure 4.5.

Shack-Hartmann wavefront sensors are composed of an array of several lenses, often referred to as lenslets, and a CCD with which the light incident on the sensor is imaged.

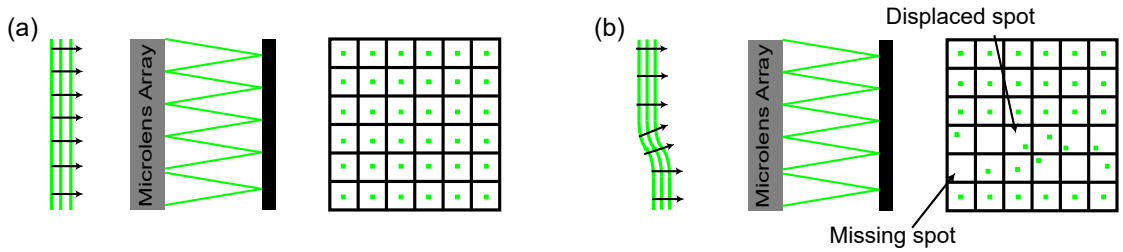

Figure 4.5: Illustration of the operation of a Shack-Hartmann wavefront sensor. (a) Illustrates the case for a planar wavefront with no aberrations, with the spots of light produced on the sensor uniformly spaced. (b) Describes the case with a distorted wavefront, where the position of many spots have been displaced.

The lenslets are of equal focal length, and each spot of light focused onto the CCD by each lenslet can then be analysed to obtain information about the wavefront of the laser [246]. The intensity and position of the spots focused onto the sensor allow calculation of parameters, known as Zernike polynomials, which define several important features of the laser wavefront including the defocus, tilt, astigmatisms and coma. The deviation from the nominal focus is calculated via the following:

$$\Delta\delta = \frac{4Z_3\lambda}{\mathrm{NA}} \tag{4.4}$$

where Z_3 is the third-order Zernike polynomial related to variation from the nominal defocus, measured by the Shack-Hartmann wavefront sensor; λ is the laser wavelength; and NA is the numerical aperture of the laser system, given by $NA = 1/(2F/\#)$.

4.2.7 High power laser facilities

The techniques used to amplify high power laser pulses to enable relativistic intensities on target to be achieved have now been discussed. The following section will describe three high power laser systems used to obtain the results presented in **chapters 5 and 6**, which use several different variations of the aforementioned techniques to achieve intensities in excess of 10^{18} W/cm^2.

4.2.8 Vulcan Petawatt

The Vulcan laser, located at the Central Laser Facility (CLF) based in the Rutherford Appleton Laboratory (RAL), is a Nd:glass based system with eight beam lines which can be directed into two active target areas: Target Area West (TAW) and Target Area Petawatt

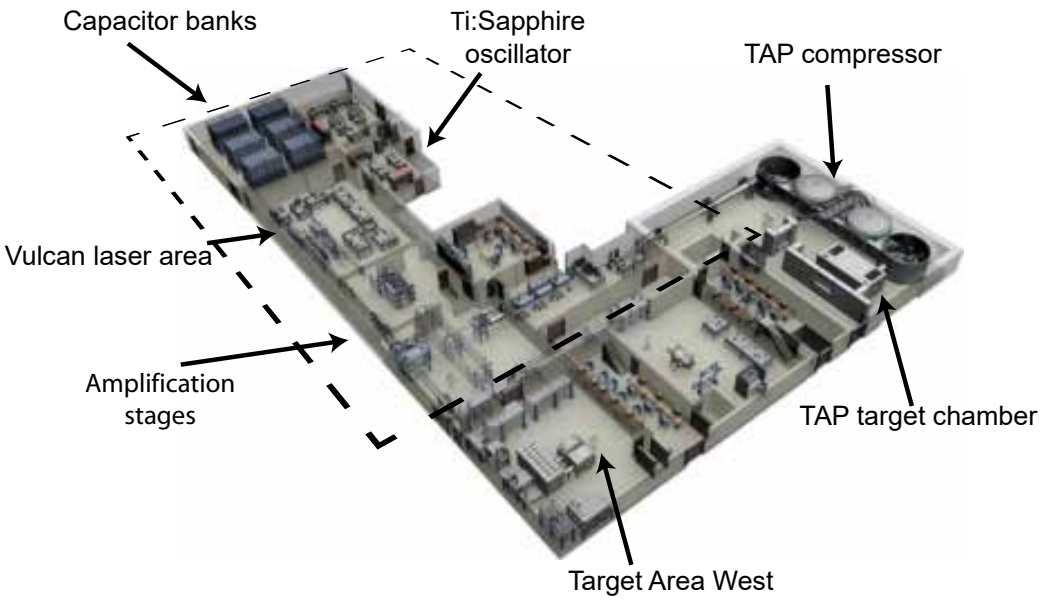

Figure 4.6: Illustration of the Vulcan laser system, with relevant areas highlighted.

(TAP). TAP, and the petawatt arm of the Vulcan laser - known as Vulcan Petawatt is only of relevance to the results presented in this thesis. An illustration of the Vulcan laser facility can be seen in figure 4.6.

In TAP, only two of the eight primary Vulcan beams are employed. Though not employed in this thesis, the first of these is a long pulse beam of approximately 6 ns duration with a delivered energy of 200 J. More important to the results of this thesis is the primary petawatt beam. Optimally, this can deliver 500 J of energy in a pulse duration of 500 fs. Typically however, Vulcan petawatt delivers $\sim$ 200 J to the target in an average focal spot of full width half maximum (FWHM) $\sim$ 4 μm. This results in a final peak intensity on target of $\sim 10^{20}$ W/cm^2.

The Vulcan Petawatt laser starts in the "front end" of the laser system, where $\sim$ 120 fs seed pulses of 5 nJ, each with a bandwidth of 6 nm and a central wavelength of 1053 nm, are generated in a Ti:Sapphire oscillator. Bandwidth, the range of frequencies encompassed by the pulse, is an important parameter as it defines the shortest pulse duration available: the greater the range of frequencies available, the shorter the final pulse duration, i.e. more effective compression using dispersion gratings. Thus, the ability of the laser material to amplify a wide range of frequencies is very important in a laser system. Unfortunately, the range of materials available with broad bandwidth is limited. Nd:glass is one such

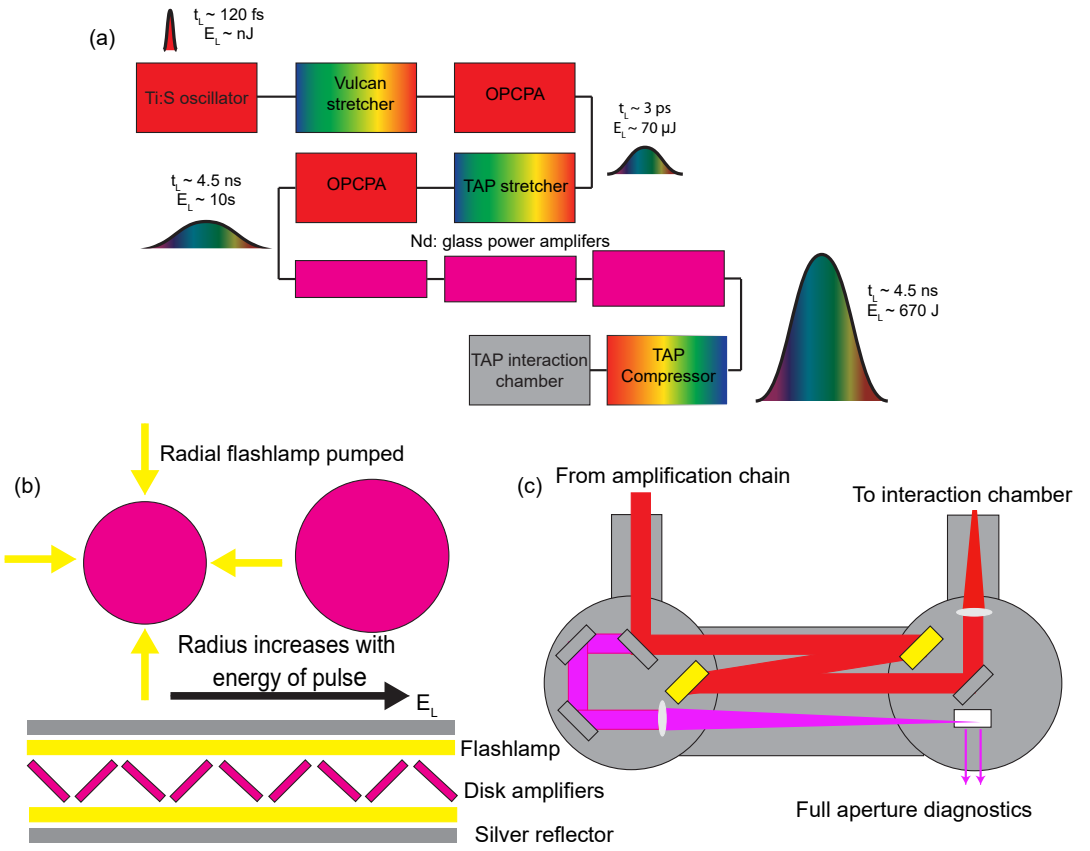

Figure 4.7: (a) Schematic of Vulcan beam line for TAP, (b) illustration of Vulcan Nd:glass rod and disk amplifiers, and (c) schematic of TAP compressor, where the yellow coloured boxes represent the gratings which compress the pulse with a negative dispersion.

material that is capable of broadband amplification, and is the material of choice for the highest energy laser systems, including Vulcan.

Prior to amplification in the Vulcan OPCPA chain, the seed pulse is first stretched in time; typically to the order of nanoseconds. As previously discussed, this reduces the intensity of the pulse below the damage threshold of the optics in the system, preventing non-linear effects from becoming significant. A schematic of the Vulcan laser system and its amplification chain is found in figure 4.7

Once a single seed pulse has been selected for stretching and amplification, it is temporally stretched in an arrangement of reflective diffraction gratings and lenses in a configuration known as an "Offner triplet",which is employed to reduce spectral aberrations in the pulse. The pulse is stretched from the original 120 fs seed pulse duration to approximately 5 ns, at which duration it is of such an intensity that damage to the optics in the system will be avoided, and is thus sent to the OPCPA amplification system.

To achieve the highest energies possible, additional amplification stages are employed. Following the OPCPA pre-amplification stage, the beam is then injected to the rod and disk amplification chain. This consists of, initially, flash lamped Nd:glass rod amplifiers, which increase the energy contained in the pulse to the order of Joules. These are of relatively small diameter ($<$ 50 mm), as inefficiency drops with increasing radius. This is due to increased absorption at the edges of the rod as they are increased in size. As the energy fluence of the beam increases as it passes through the chain, Nd:glass disks are employed to prevent damage. These bring the final energy of the pulse up to the region of $\sim$ 600 J. Figure 4.7(b) demonstrates the layout of the amplifier stage.

After amplification the pulse is expanded, first through focusing in a vacuum spatial filter, to a diameter of 600 mm in order to reduce the energy fluence. Finally, the pulse is injected into the compressor, located inside the TAP target area. Here, a pair of diffraction gratings with the opposite dispersion and configuration to that of the stretcher, that provides the initial chirp to the pulse, recompress the beam from the order of nanoseconds to approximately 500 fs. The compressor layout can be seen in figure 4.7(c). After compression, the final pulse is sent into the target chamber to the final focusing optic: a 0.6m diameter F/3.1 off-axis parabola (OAP). The pulse is then focused down to the target front surface to a diffraction limited spot (FHWM) of $\sim 4\ \mu m$.

Additionally, Vulcan petawatt is also capable of operation in a "double-pulse" mode, enabling two temporally-separated intense laser pulses incident on target. Previously, this regime has been used in investigations of ion acceleration via the TNSA scheme [176, 247] with targets on the order of tens of microns thick.

The dual-pulse mode was employed for the investigation of ion acceleration featured in **chapter 6**. Rather than studying the case of relatively thick targets, the investigation in **chapter 6** focused on the scenario of ultra-thin targets of the orders of tens of nanometres thick. The use of a controlled pre-pulse on targets of these thicknesses can result in the pre-expansion of the target to near-critical densities prior to the arrival of the main pulse.

This scheme will be discussed in greater detail in **chapter 6**, where a detailed discussion of the dual-pulse setup and its use in relation to the investigation of ion acceleration will be presented.

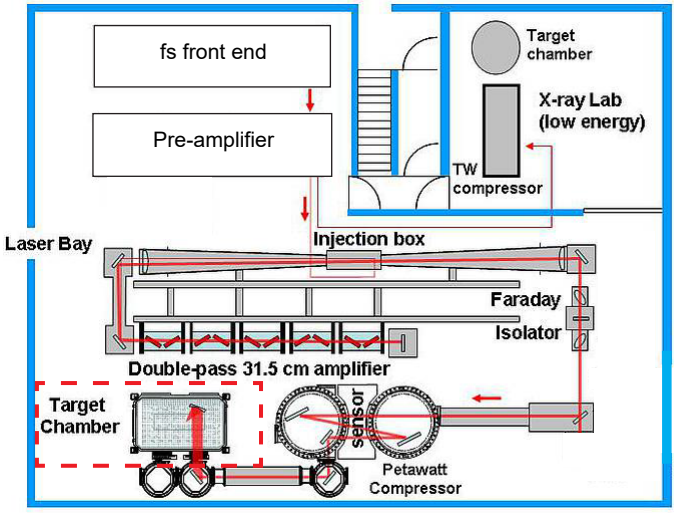

Figure 4.8: PHELIX laser and target area schematic. The target area relevant to the results presented in this thesis has been highlighted for clarity. Adapted from [136].

4.2.9 PHELIX

The Petawatt High Energy Laser for heavy Ion eXperiments, more commonly referred to as PHELIX, at the Gesellschaft für Schwerionenforschung, GSI, facility in Darmstadt, Germany, is a petawatt class laser with similar operating parameters to Vulcan Petawatt. As with Vulcan, it is a flashlamp-pumped Nd:glass system which employs both pre-amplifiers and a main amplifier. Uniquely, PHELIX can be coupled to a conventional LINAC enabling experiments on ion stopping in laser-plasma and warm dense matter to be performed. A schematic of the PHELIX laser and target areas can be found in figure 4.8.

For the experimental data presented in **chapter 5**, the short pulse configuration was used, and thus discussion of the laser parameters and operation will focus solely on this aspect of the system. PHELIX generates pulses with a central wavelength of (1053 ±6) nm, and is capable of producing pulse durations ranging from 0.5 to 20 ps; energies up to 200 J; maximum intensities of 10^{20} W/cm^2; and possesses a pulse contrast ratio of approximately 10^7 [248].

Seed pulses are generated at the femtosecond frontend, with durations of 100 fs and energies of 4 nJ. These are subsequently stretched and amplified via two regenerative amplifiers, with the energy content of the pulse amplified to 30 mJ.

Following this stage, the now 30 mJ pulse is then amplified again in the flashlamp-pumped Nd:glass pre-amplifier to $\sim$ 5 J, and expanded up to 70 mm diameter in order to keep the energy fluence within safe limits for the system, before it is sent to the main

amplifier section. The GSI main amplifier is comprised of five flashlamp-pumped Nd:glass amplifier cassettes, and is based on the designs of Nova and Phebus amplifiers [235]. The maximum energy output of this amplifier chain is 250 J.

The now-amplified, stretched pulse is now recompressed in the compressor down to a minimum pulse length of $\sim$ 700 fs. The maximum output energy after the compressor is $\sim$ 180 J.

Finally, the compressed pulse is injected into the target chamber onto an F/1.5 Cu-coated OAP, that focuses the beam down to a 2.5 μm diameter (FWHM) focal spot, and approximate intensities of $\sim 7 \times 10^{20}$ W/cm^2.

4.3 Laser-plasma diagnostics

The experimental investigations conducted in this thesis sought to characterise specific properties of the plasma electrons, generated in the interaction of the intense laser pulse and a solid density target. A multitude of diagnostic techniques are employed to experimentally measure such properties. However, directly measuring the dynamics inside solid density targets, as is the case in the investigation discussed in **chapter 5** is extremely difficult, and so indirect techniques are required to be used in such instances. Predominantly, three different diagnostic techniques are traditionally used to investigate plasma dynamics and fast electron transport: (1) particle diagnostics; (2) optical probing; and (3) photon (x-ray, γ-ray, transition radiation) emission. The first two techniques are of relevance to the results presented later in this thesis, and thus, only these will be explored over the course of the following sections.

4.3.1 Particle diagnostics

As previously presented in **chapter 2**, during the interaction of an intense laser pulse with solid-density targets the front surface of the target is sufficiently ionised and transformed into plasma. Electrons are ponderomotively accelerated into the target, and via one of the ion acceleration mechanisms previously discussed (see section 2.9), a charge separation field is generated and ions are accelerated away from the rear of the target. Furthermore, the fastest electrons may escape the interaction and, due to the coupling of laser energy into the plasma electrons, may provide direct insight into the underlying dynamics of the interaction. Particle detectors can be separated into two categories, electron and

ion detectors. The experimental measurements presented in this thesis were made using stacked radiochromic film (RCF) detectors and image plate (IP) detectors.

4.3.2 RCF spectroscopy

Whilst measurement techniques which probe or diagnose emission in the optical and X-ray regions of the electromagnetic spectrum provide a valuable insight into the plasma dynamics over the course of laser-foil interactions, these methods have several drawbacks when attempting to diagnose electron dynamics in overdense regions of the interaction. For example, optical probing of plasma is only effective up to some fraction of the plasma critical density, at which point it is opaque to the probe laser, and is refracted out of the line of sight of the detector. Although x-ray diagnostics, such as Cu K-α imagers are able to peer deeper into the plasma, they suffer from issues such as noise produced by refluxing electrons that are confined by the sheath fields generated on the surfaces of the target; whilst transition radiation techniques are only capable of sampling the fastest electrons that overcome these strong fields.

As a result, the use of ion diagnostics primarily measuring the protons accelerated from the rear surface of the target, have been successfully employed in order to characterise the transport and dynamics of electrons inside solid targets [53, 54, 249]. The use of RCF to detect energetic protons is particularly relevant to this thesis [250, 251]. Stacked RCF has advantages over other ion diagnostics, for example, Thomson Parabolas [252], as despite the fact that both approaches give a measure of particle energy, through the stacking multiple layers, RCF also enables the measurement of the proton energy spectrum, beam divergence and spatial-intensity distribution. The spatial-intensity distribution provides insight into fast electron dynamics over the course of the interaction, from TNSA sheath fields generated by electrons which remain inside the target and are affected by the fields present. Furthermore, the protons accelerated in the interaction possess energies on the order of tens of MeV, and are accelerated by electrons in the mean energy region of the fast electron spectrum. These fast electrons are more susceptible to self-generated magnetic fields within the target, enabling a more complete picture of the fast electron dynamics to be inferred. As previously discussed, one of the drawbacks of imaging transition radiation to infer fast electron dynamics is that emission solely originated from the fastest electrons escaping the target, which are less likely to be influenced by self-generated magnetic fields.

Moreover, combined analysis of the energy and spatial-intensity distributions of the

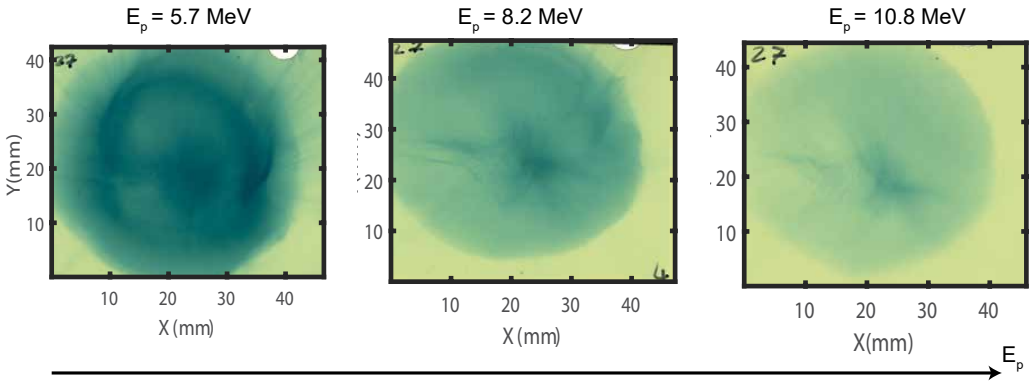

Figure 4.9: Example raw spatial-intensity distributions of protons imaged by RCF from an experimental campaign at PHELIX. The protons shown here were generated from a diamond target of thickness 200 μm

beam of accelerated protons enables the diagnosis of properties of the proton beam which highlight the specific acceleration mechanism or electron dynamics which generated, or influenced, the beam. For example, the transition from a Gaussian to annular structure in the proton beam in silicon targets hundreds of microns thick has been demonstrated to arise due to resistively generated magnetic fields inside the target [128]. In addition, extensive study of the proton spatial-profile from near-critical density targets on the nanometre-scale have shown the presence of ring-like structures [197]. These have been created by an intra-pulse transition of acceleration mechanisms, where a radial deflection force is exerted upon the lowest energy sheath-accelerated protons. Furthermore, the use of stacked RCF has enabled the diagnosis and analysis of various other phenomena to be observed. Examples include a low-divergence, high energy proton component that was observed to vary in position between the target-normal and laser axes, formed due to co-propagation with a relativistic electron jet generated at the onset of relativistic self-induced transparency (RSIT, see section 2.9.3) [34, 253, 254]. Figure 4.9 shows a typical example image of a proton spatial-intensity profile detected by RCF spectroscopy.

RCF is typically comprised of either a single - or double - layer of active material sensitive to ionising radiation. This active layer contains a marker dye, stabilisers, amongst other components, and has a near energy-independent response [255]. When the active component in the RCF is exposed to ionising radiation, it reacts to form a coloured polymer. Depending on the total absorbed dose of protons in the active layer, the polymer is distinctly darker (or lighter) proportional to the level of absorption. The film is self-developing upon exposure, enabling instant access to the data upon removal from the

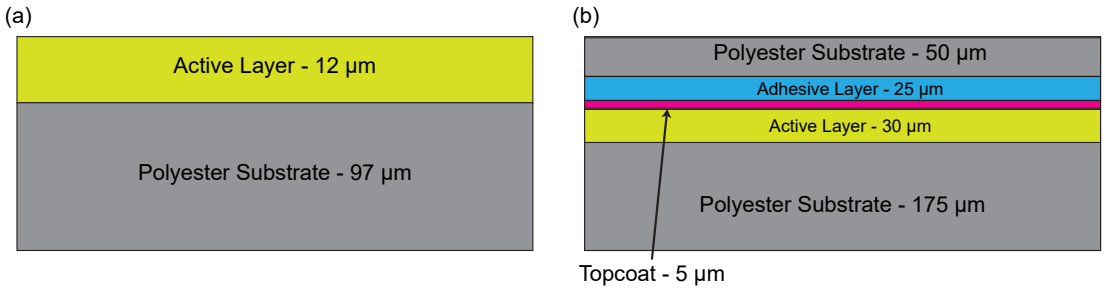

Figure 4.10: Illustration of the cross-section of GAFCHROMIC (a) HD-V2 and (b) EBT2 film, highlighting the composition of each.

interaction chamber.

Two types of RCF were used to make the experimental measurements presented in this thesis: HD-V2 and EBT2. Schematics of the composition of the two types of film are shown in figure 4.10.

HD-V2 has a relatively thinner active layer (12 μm) in comparison to EBT2 (30 μm) and, as such, is less sensitive to ionising radiation. By way of comparison, HD-V2 is sensitive to doses of between 10 to 1000 Grays (Gy), whereas EBT2 is sensitive in the region of 1 cGy to 10 Gy [256, 257]. As a result, when multiple layers of RCF are stacked to measure the energy spectrum of an accelerated proton beam, HD-V2 layers are arranged towards the front. The spatial resolution of HD-V2 film is $\sim$5 μm, compared to a resolution of 100 μm for EBT2, though this number is limited by the system used to digitise the film for analysis (discussed later in this section). Furthermore, as shown in figure 4.10, HD-V2 is asymmetric and thus, care must be taken to orient the film such that the active layer is oriented towards the oncoming proton beam; EBT2 does not suffer from this issue.

Stacking multiple layers of HD-V2 and EBT2 enables the energy spectrum of the accelerated proton beam to be measured, in addition to diagnosis of the evolution of the spatial-intensity distribution and beam divergence. Arranging a stack consisting of purely HD-V2 and EBT2 allows for a maximum energy resolution of $\sim$ 1 MeV. However, such a design would require excessive quantities of film to be used. Consequently, it is common for metallic or plastic filters to be interleaved into the design. This enables the proton beam to be sampled at discrete energy intervals $>$ 1 MeV. The intervals can be tailored to allow higher or lower energy resolution by adjusting the thickness or material of the filters. Moreover, by careful choice of the filters used in the stack, these can also be employed as complimentary diagnostics, i.e copper activation and imaging [258, 259]. An illustration

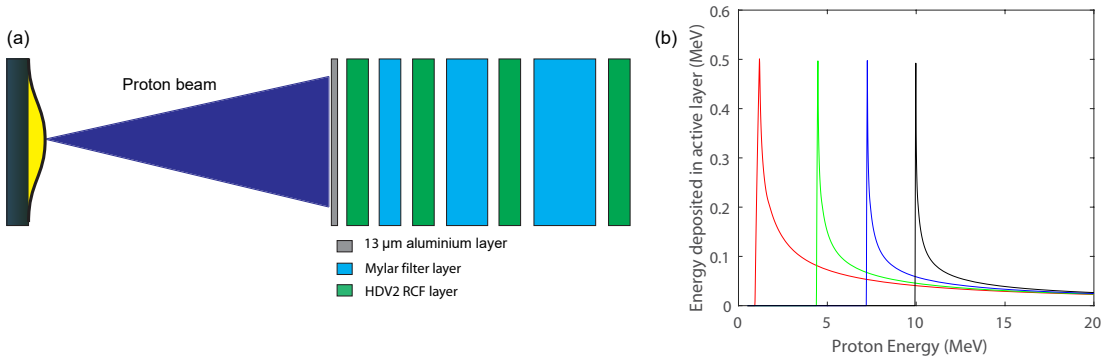

Figure 4.11: (a) Illustration of the design of a stacked RCF diagnostic. (b) Example response curves generated via a MATLAB code based on data from the Monte-Carlo SRIM code.

of stacked RCF is shown in figure 4.11(a).

The spatial profile of the proton beam can be energy resolved due to the Bragg stopping characteristics of ions in matter, as illustrated in figure 4.11(b). The Bragg peak is explained by the interaction cross-section between the protons and the RCF increasing as the proton energy decreases.

After exposure, the self-developed RCF is digitised for analysis. An optical scanner, in transmission mode is used for this purpose. The dose level is quantified by the optical density of the film, where the optical density is defined as $OD = log_{10}\frac{I}{I_o}$, i.e. the ratio of the level of light transmitted through the film to the intensity of the light source. This technique has been calibrated by scanning samples of film exposed to a known proton dose from a conventional RF accelerator [260, 261].

4.3.3 Imaging plate

Whilst RCF is sensitive to energy deposition by the accelerated proton beam, electrons accelerated in the interaction typically only deposit a small amount of energy in the stacked dosimetry diagnostic. As such the use of imaging plates are necessary to image the accelerated electron population. Imaging plates are a propriety particle-imaging diagnostic produced by Fujifilm and, in the case of laser-solid interaction experiments, can be used in tandem with RCF stacks to experimentally measure the energy-resolved, two-dimensional spatial-intensity profile of the accelerated electrons escaping laser-solid interactions.

Imaging plates (IP) are composed of a photostimulable phosphor layer [$BaF(BrI) : Eu^{2+}$], which is supported by a steel-paper backing [262]. A schematic of the composition of IP is shown in figure 4.12. Various types of IP are commercially available, each with

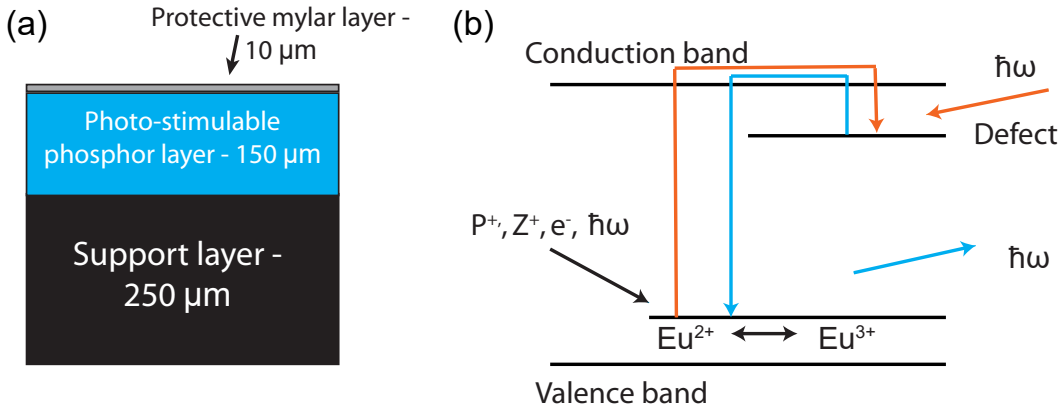

Figure 4.12: (a) Composition of Fujifilm BAS IP-SR image plate; (b) Electron transitions which occur during the exposure (red) and scanning (blue) processes.

variations on the above composition, for example: IP biological analysis system (BAS) - SR possesses a protective mylar layer which prevents excessive damage to the photostimulable phosphor layer; whilst BAS-TR plates do not have this layer, rendering them more sensitive to low-energy X-rays at a cost of increased fragility [263, 264].

X-rays, or ionising radiation including electrons, incident on the phosphor plate ionise Eu^{2+} to Eu^{3+}. The resultant photoelectron emitted moves to the conduction band of the phosphor crystals, where they are trapped in Br^- and F^- vacancies (called F^+ centres) [262,263,265]. These F^+ centres are actually intentional lattice defects introduced in manufacturing, and the holding of the electrons in these states is metastable. The photoelectrons can then be extracted via photo-stimulation by employing a HeNe scanning laser operating at a wavelength of $\lambda = 632$ nm. As the metastable state decays, an ultraviolet photon ($\lambda = 390$ nm) is ejected from the IP, and is detected by a photomultiplier tube. This also has the consequence that IPs must be shielded from light sources after exposure in the interaction until they are ready to be digitised. This process is typically carried out in a proprietary Fujifilm scanning system [266]. Moreover, once the data has been extracted, exposure to a white light source will erase any signal left by depopulating the metastable states, enabling future re-use.

The digitisation process also places a limit on the resolution of the extracted image: the minimum focal spot size that can be achieved with the scanning laser is 25 μm. Although this is lower resolution than can be achieved with x-ray film (5 μm) [263], it is sufficient for use many in laser-plasma interaction experiments.

4.3.4 Plasma diagnostics

The diagnostics discussed in the previous section focused on the measurement of particles emitted from the interaction, in order to diagnose the dynamics occurring during the interaction. In this section, diagnostic techniques that attempt to measure the plasma dynamics and properties through external optical probing of the interaction will be discussed.

Optical probing techniques are commonly employed in laser-plasma interaction experiments. These involve directing a second, lower-energy laser pulse, or a "pick-off" of the main driver-pulse, towards the target. This probe beam can be directed transverse to the target, or reflected off the desired surface, before being typically sent to a CCD to be imaged. The energy content of the probe-pulse is typically much lower than that of the main pulse to avoid influencing the interaction to a significant degree. Typically, the light in the probe-beam is frequency doubled prior to reaching the interaction region, such that it can probe to higher electron densities (as discussed in **chapter 2**) and to enable differentiation from scattered light from the interaction, at the laser central wavelength. Furthermore, before being sent towards the target, the probe pulse is first directed via a "*timing-slide*" which enables variable delay between the arrival of the main pulse and the probe beam, thus enabling the probing of various temporal regions of the interaction.

Several different approaches of inferring plasma dynamics and properties through optical probing have been employed successfully by a number of research groups in relation to laser-solid interactions. Two different methods of diagnosing the plasma dynamics are relevant to this thesis: shadowgraphy and polarimetry. Shadowgraphy is simply the technique of backlighting the expansion of overdense plasma from the interaction. When the probe light encounters an overdense region of plasma, it is absorbed, or refracted out of the line-of-sight by gradients in the refractive index. Thus, quantities such as the plasma expansion distance, and profile, can be inferred through this method. The approach of polarimetry is a relatively more complex topic, and so will be discussed in greater detail in the following section.

Optical probe polarimetry

Optical probe polarimetry is often used in conjunction with interferometric methods of measuring electron density distributions in plasma, as a means to characterise the strength of the magnetic field generated by the motion of fast electron currents in the interaction

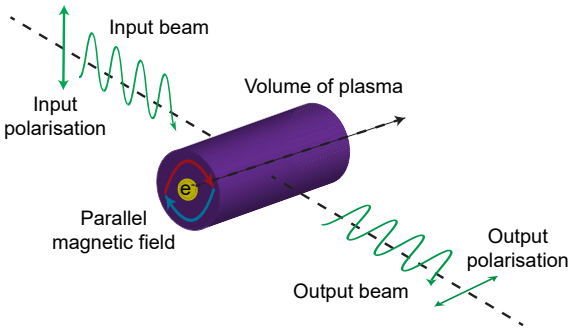

Figure 4.13: Illustration of the Faraday effect. The polarisation plane of a input linear wave is rotated an angle ϕ when it travels through a parallel magnetic field.

of a solid-density foil and an intense laser pulse. For the polarimetry techniques discussed in this thesis, the approach taken to measure the magnetic field strength in the expanding plasma was the analysis of the Faraday rotation of the polarisation plane of the linear wave of an optical probe pulse after traversing a parallel magnetic field. Figure 4.13 illustrates this effect.

The strength of the magnetic field, related to the rotation angle of the polarisation of the probe pulse, is given by the following:

$$\phi = VBL \tag{4.5}$$

where ϕ is the Faraday rotation angle, V is the Verdet constant of the material being probed [267], B is the magnetic field strength, and L is the thickness of the target. The Verdet constant is measured in units of deg/G/cm. Considering an example magnetic field strength, B, of 1 MG, $V = 4 \times 10^{-4}$ deg/G/cm, and $L = 0.05$ cm, the Faraday rotation angle would be calculated as $\phi \sim 20^{o}$ [268]. Equation 4.5 can be easily rearranged to obtain the magnetic field strength, if the rotated angle ϕ is known and experimentally measured.

To measure ϕ experimentally, a two-channel polarimetry setup is employed with a linear polariser, set at $\pm$ an angle θ placed in front of each channel, respectively. A typical schematic of such a setup is shown in figure 4.14

The optical behaviour of both polarisers is described by Malus's law (equation (4.6)):

$$I_{D_{1,2}} = \alpha_{1,2} I_0 [1 - \beta_{1,2} sin^2(\theta_{1,2})] \tag{4.6}$$

where $I_{D_{1,2}}$ is the intensity detected on the CCDs used to image the probe; $\alpha_{1,2}$ are the

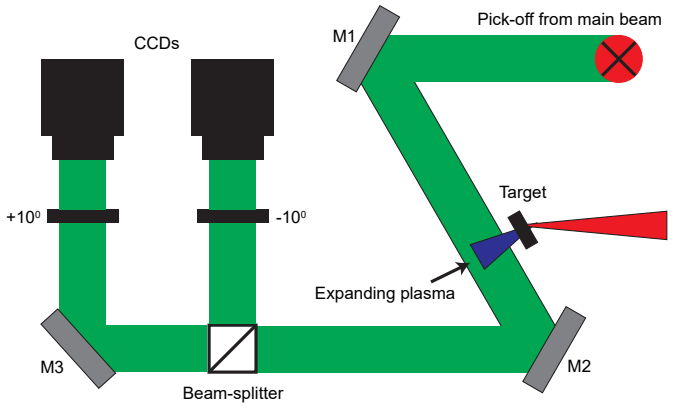

Figure 4.14: Simplified illustration of a typical polarimetry probe beam set-up used to transversely probe the rear-surface plasma dynamics in laser-solid interaction experiments, and characterise the Faraday rotation due to magnetic fields.

transmission coefficients for both polarisers, respectively; I_0 is the intensity of the input beam; $\beta_{1,2}$ are the extinction ratios of the polarisers; and finally, $\theta_{1,2}$ is the angle set for each polariser.

If the probe beam passes through a parallel magnetic field as it propagates through the interaction, the final intensity from equation 4.6 must be corrected as:

$$I_{D_{1,2}} = \alpha_{1,2} I_0 [1 - \beta_{1,2} sin^2(\theta_{1,2} \pm \phi)] \tag{4.7}$$

The positive sign corresponds to areas where the probe light has encountered a parallel magnetic field, whereas a negative sign corresponds to regions with an anti-parallel magnetic field. This is manifested as brighter and darker regions (with respect to background) on the final obtained images. As two channels are used, with polarisers set at $\pm\ \theta$, the response on each polariser will be the opposite with respect to the other channel, enabling the detection of an azimuthal magnetic field distribution due to the difference of intensities between the two channels. Furthermore, another reason for using a two-channel setup is that, in order to obtain ϕ from the presence of a magnetic field (from equation (4.7)), it is simply the ratio of intensities from both polarisers which is required. Terms including the initial probe beam intensity, and the transmission coefficients and extinction ratios of the polarisers, which are similar across both channels, disappear from the relation. Further characterisation of the polarisers used is required to determine the values of the transmission coefficients and extinction ratios.

Thus, equation (4.7) can be solved to provide an expression for the Faraday rotation

angle, ϕ, as follows:

$$I_0 = \frac{I_{D_{1,2}}}{\alpha_{1,2}[1 - \beta_{1,2} sin^2(\theta_{1,2} \pm \phi)]} \tag{4.8}$$

Rearranging the above to obtain a ratio of intensities gives:

$$\frac{I_1 \alpha_1}{I_2 \alpha_2} = \frac{1 - \beta_1 sin^2(\theta_1 + \phi)}{1 - \beta_1 sin^2(\theta_2 - \phi)} = A \tag{4.9}$$

The values of $\alpha_{1,2}$ cancel, and so can be removed from the above, and the remaining ratio I_1/I_2 is denoted as "A" for simplification. Here, it can be seen that the negative angle identity for the sine function can be applied, i.e. that $sin(-x) = -sin(x)$. This is the reason for choosing polariser angles such that $\theta_2 = -\theta_1$. In the case for equation (4.9), this means that we effectively have $sin(-\theta - \phi) = -sin(\theta + \phi)$. This leads to equation (4.9) being rewritten as:

$$A = \frac{1 - \beta_1 sin^2(\theta_1 + \phi)}{1 + \beta_1 sin^2(\theta_1 + \phi)} \tag{4.10}$$

Through further algebraic manipulation, equation (4.10), can be finally rearranged to give the Faraday rotation angle:

$$\phi = \arcsin \sqrt{\frac{1 - A}{A\beta_2 - \beta_1}} \tag{4.11}$$

However, in the experimental campaigns presented in this thesis, the probe beam propagates through an underdense plasma generated in vacuum. Hence, the relation presented in equation 4.5 cannot simply be used to calculate the magnetic field strength in the plasma. Instead, an Abel inversion method demonstrated in Flacco *et al.* [269, 270] must be employed. Thus, the final 2D map of the magnetic field strength is obtained from the following integral transform:

$$(n_e B_\phi)(r, x) = \frac{2 m_e c n_c}{\pi e} \frac{\partial}{\partial r} \int_r^{r_0} \frac{\phi_{rot}(y, x)}{\sqrt{y^2 - r^2}} \tag{4.12}$$

The process of Abel inversion was carried out on the assumptions that the effects of refraction on the probe beam were negligible and that the density of the plasma under consideration is much less than the critical density.

By knowing the distance through which the probe light propagates through the expanding plasma (which, if cylindrical symmetry is assumed, can be measured directly from

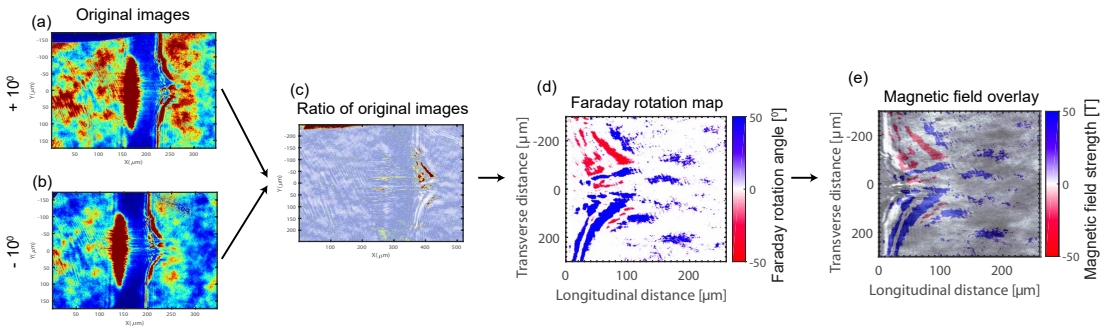

Figure 4.15: Typical steps of Faraday rotation analysis, where (a) and (b) are the original polarimetry images obtained from experiment for $+20^0$ and -20^0, respectively; (c) is the image obtained by calculating the ratio of the intensities of the images; (d) is the calculated Faraday rotation, obtained via equation 4.11; and (e) is the map of magnetic field overlaid over an experimentally obtained probe image.

the original image), in conjunction with the electron density through which it travels, the magnetic field strength can be estimated accordingly. Figure 4.15 illustrates the steps involved in the production of a magnetic field map obtained via Faraday rotation.

4.4 Numerical Modelling

Experimental observations and measurements provide the foundation upon which our understanding of laser-solid interactions is built. However, in intense laser-solid interactions, there are many processes which occur on timescales unresolvable by current, state-of-the-art experimental diagnostic techniques. Moreover, experimental campaigns continue to suffer from issues of repeatability due to shot-to-shot fluctuations, for example, with thermal processes in the laser chain presenting limitations on the performance of the laser throughout the day. Furthermore, other issues such as solid target alignment and beam-time restrictions present other constraints to experimental measurements.

The use of numerical studies has become ubiquitous in the laser-solid target interactions community due to their ability to complement experiments with detailed insight into the underlying physics of laser-solid interactions. Such tools have become more and more commonplace and useful with advancements in high power computing enabling larger and more complex simulation studies to be carried out. The resources required to perform numerical modelling can vary greatly between the situation being studied, and the type of code selected to carry out the operation: certain models may run in seconds on a single processor, or desktop computer; whereas other, more intense simulation studies may take weeks on national, parallelised, high performance computer clusters.

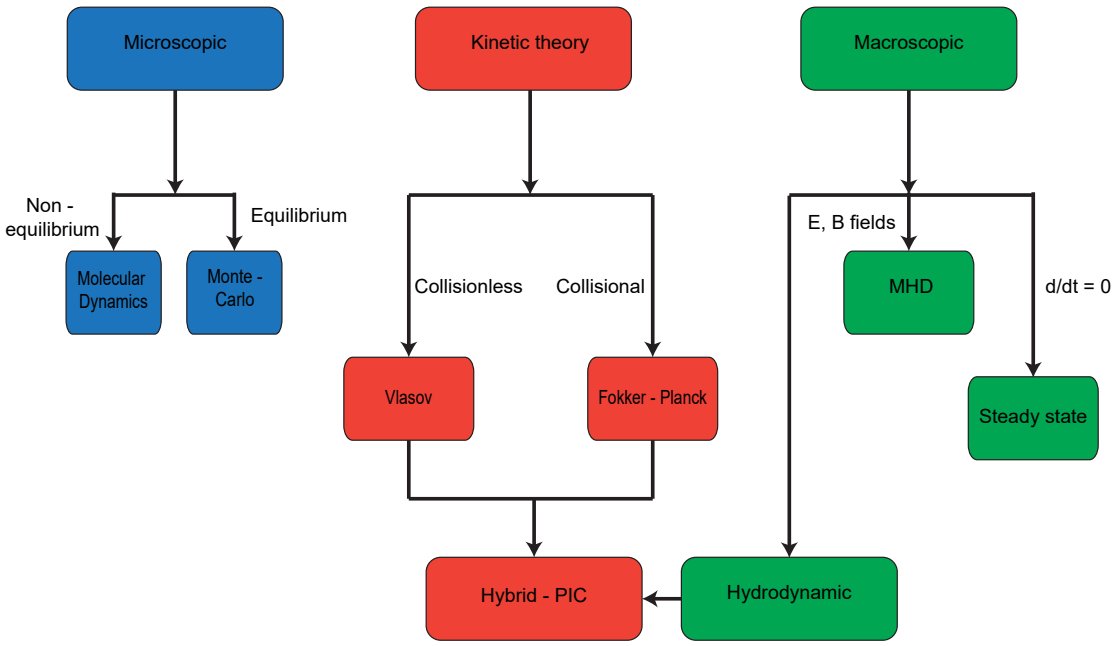

Figure 4.16: Illustration of the various branches of numerical codes routinely used in simulation studies of laser-solid interactions. Adapted from P. Gibbon, Short pulse laser interactions with matter, Imperial College Press, 2005.

There are three main types of code employed in simulation studies of laser-solid interactions. These are summarised by Gibbon [89] into the categories of 1) microscopic, 2) kinetic (i.e. particle), and 3) macroscopic (i.e. fluid). These are illustrated in figure 4.16, (adapted from Gibbon [89]).

The kinetic theory and macroscopic methods are highly relevant to laser-solid interactions, and thus are the two regimes of numerical modelling used to investigate the underlying physics of the investigations presented in this thesis. More specifically, a combination of kinetic modelling, and a hybrid scheme of kinetic and macroscopic methods are employed, and will be discussed in detail over the following sections. Microscopic methods remain useful for studying the stopping of particles in matter or for investigating the molecular dynamics of materials under the effects of intense laser irradiation. In addition, microscopic modelling offers an insight into the evolution of the target's electrical resistivity - temperature relationship to be characterised. Furthermore, simulations of particle stopping are utilised heavily to design diagnostics for experimental measurements, including the RCF diagnostic described in section 4.3.2.

Particle-in-cell codes: EPOCH

Kinetic or, most relevant to this thesis, particle-in-cell (PIC) methods are commonly used in the field of laser-solid interactions for the simulation of collisionless plasma kinetics [271]. Studies of PIC algorithms have been performed for almost 30 years [272, 273], and are still extensively used as a tool for investigating the underlying physics of laser-solid interactions [274].

The core of the PIC method is the use of a single particle velocity distribution, $f(\mathbf{r}, \mathbf{v})$ to describe the plasma. The evolution of this distribution in space, and time, is given by the Vlasov equation [168]:

$$\frac{\partial f}{\partial t} + \mathbf{v} \cdot \frac{\partial f}{\partial x} + q \left(\mathbf{E} + \frac{\mathbf{v}}{c} \times \mathbf{B} \cdot \frac{\partial f}{\partial \mathbf{p}} \right) = 0 \tag{4.13}$$

where $\mathbf{E}$ is the electric field, $\mathbf{B}$ is the magnetic field, $\mathbf{p}$ is the momentum, $\mathbf{v}$ is the velocity, and $\mathbf{r}$ in $f(\mathbf{r}, \mathbf{v})$ is the spatial dimensions of the system, of which there are three. Moreover, there are in fact three spatial and three velocity dimensions to consider when attempting to solve the distribution function $f(\mathbf{r}, \mathbf{v})$, and hence the general solution of equation (4.13) is too complex and computationally intensive to solve with current state-of-the-art high power computing technology [168]. In order to circumvent this, PIC methods represent large groupings of single particles with discrete, statistically weighted approximations of "macroparticles", where each macroparticle is described by a charge, q_i, and mass, m_i and i is the number of particles comprising each macroparticle.

Solving the Vlasov equation (equation (4.13)) for macroparticles results in a *collisionless* PIC code. By extension of the Vlasov equation to include collisonal Fokker-Planck operators, effects such as collisions and electrical resistivity can be included [275].

The algorithm central to the PIC method is as follows: initially the macroparticles are moved according to the Lorentz equation [89]:

$$\frac{d}{dt}(\gamma_i \mathbf{v}_i) = \frac{q_i}{m_i} \left(\mathbf{E} + \frac{\mathbf{v}_i}{c} \times \mathbf{B} \right) \tag{4.14}$$

The positions of the macroparticles are then mapped onto a simulation grid, in order to obtain the associated current densities. Once the position and current density are known, Faraday's and Ampére's laws are used to solve for the resulting electric and magnetic fields. The calculated field values are then used to interpolate from the grid and update the momentum of the macroparticles, resulting in new positions for each macroparticle. These

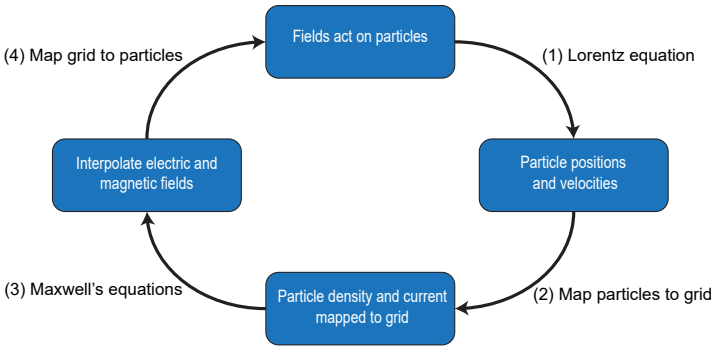

Figure 4.17: Schematic illustrating the PIC algorithm.

new values of momentum are then input into the Lorentz equation, and new positions for the macroparticles are found, and subsequently mapped onto the grid. This process continues for the duration of the simulation. This algorithm is demonstrated graphically in figure 4.17.

The PIC code used to generate and conduct simulations presented in this thesis was the EPOCH code [271, 276]. EPOCH follows the same implementation of the PIC algorithm as other available PIC codes, and as such will generate results that are consistent with the other available codes.

Although PIC codes have become extremely powerful and useful tools for investigating the underlying physics of laser-solid interactions, there are a number of pitfalls qhich may occur when using them. For example, the representation of the particle distriubtion function, and its "resolvability" in phase space are both dependent on the number of macroparticles initialised per cell, N_{pc}, at the onset of the simulation. The level of non-physical, statistical noise present in the outputs of simulations is also interlinked with N_{pc}. The results of simulations may be obscured by such noise if N_{pc} has too small a value. Even if non-physical behaviour has been considered prior to initiating a simulation, additional effects may occur, for example, if the Debye length is not properly resolved (and is smaller than the spatial size of the cells that comprise the simulation grid) then issues such as self-heating of the plasma can occur.

Hybrid-PIC fast electron transport simulations: ZEPHYROS

One method which has been used to overcome these issues, whilst also dealing with the computational demands of studying the transport of fast electrons, with long mean free paths, propagating through an initially cold, dense plasma is hybrid-PIC codes.

Hybrid-PIC methods are, essentially, an extension of the traditional PIC method that incorporates several assumptions which reduce the degree of accuracy associated with full-PIC simulations. These assumptions produce a, relatively, less computationally intensive model of laser-solid interactions that can include collisional operators in the Vlasov equation (equation (4.13)), allowing target resistivity, and its effects, such as magnetic field generation, to be modelled.

The key assumptions made by hybrid-PIC models are that there is a small population of fast electrons generated in the initial laser-solid interaction, where the fast electron population is much smaller than the background, cold electron population, i.e. $n_f << n_b$, where n_f and n_b are the number densities of the fast and background electron populations, respectively. This enables the background to be treated independently to the fast population, with quasi-neutrality assumed. Moreover, hybrid codes assume that a fluid description of the background plasma is valid on the spatial and temporal timescales of interest. This assumption results in the comparably smaller length- and time- scales of the background plasma being ignored in calculations, enabling larger simulation time-steps to be utilised. In addition, if the population of fast electrons is kept small over the collisionless skin depth of the background electrons, then electrostatic and magnetostatic arguments for the conservation of current neutrality is:

$$\mathbf{j}_f + \mathbf{j}_b = \frac{\nabla \times \mathbf{B}}{\mu_0} \tag{4.15}$$

Furthermore, Ohm's law is used to calculate the electric field, given by the following:

$$\mathbf{E} = \eta \mathbf{j}_b \tag{4.16}$$

in which, if current neutrality is assumed, results in:

$$\mathbf{E} = -\eta \mathbf{j}_f + \frac{\eta}{\mu_0} \nabla \times \mathbf{B} \tag{4.17}$$

and, if we neglect the contributions from the $\nabla \times \mathbf{B}$ term, equation (4.17) can be written as:

$$\mathbf{E} = -\eta \mathbf{j}_f \tag{4.18}$$

The final assumption made is that the use of Ohm's law to determine the electric field,

leads to Faraday's law expressing the resistive generation of a magnetic field around a population of fast electrons, being reduced, i.e.

$$\frac{\partial \mathbf{B}}{\partial t} = \nabla \times -\eta \mathbf{j}_f \tag{4.19}$$

$$\frac{\partial \mathbf{B}}{\partial t} = \eta \nabla \times \mathbf{j}_f + \nabla \eta \times \mathbf{j}_f \tag{4.20}$$

The contribution of $\nabla \times \mathbf{B}$ term in equation (4.17) corresponds to the resistive diffusion of magnetic field, which in the limit of strong-heating (i.e. KeV temperatures) becomes negliglible. Thus, equation (4.20) can be reduced to the form shown.

The background plasma is treated hydrodynamically, that is to say, it is deemed analogous to a fluid. Thus, it may be described using macroscopic variables of density, pressure and fluid velocity, with the caveat that it is close to a state of local thermal equilibrium (LTE), i.e. its particle distribution functions are Maxwellian, with well defined temperatures for the electron and ion populations. In contrast, the fast electron population is governed by the Vlasov equation, with the inclusion of Fokker-Planck collisional operators, and is solved via the PIC method outlined previously. The effects of drag generated by the background electrons on the fast electron population are also modelled. Furthermore, energy deposition due to the slowing down of the fast electrons and Ohmic heating induced by the return current are used to determine the temperature evolution within the target.

The inclusion of collisions in hybrid-PIC models leads to the important addition of the target's electrical resistivity- temperature relation to be incorporated into the simulation. This can take the form of a theoretical model of resistivity, such as the Lee-More or Spitzer models [119,120]; or a "hybrid" model derived from a combination of both simulation and theory, as outlined by McKenna *et al.* [54] and Maclellan *et al.* [128]. A full discussion of the method behind this can be found in reference [277].

Moreover, as the target temperature is relatively cold at the beginning of the simulation, the hybrid-PIC method enables the effects of electrical resistivity at low-temperatures to be investigated [115, 278].

Although a number of hybrid-PIC codes have been developed in recent years, including the first hybrid-PIC code applied to fast electron transport in solids by Davies *et al.* [279] and PARIS by Gremillet *et al.* [117] amongst others [280, 281], the results presented in this thesis were performed by employing the hybrid-PIC code ZEPHYROS, written and

developed by Dr. A. P. L. Robinson, and has been employed extensively to simulate conditions relevant to fast electron transport in dense plasma [282, 283].

Chapter 5

Role of resistive self-generated magnetic fields in relativistic electron beam propagation in solids

5.1 Introduction

In this chapter, results from experimental and numerical investigations are presented, which examine the role played by the low-temperature resistivity, on influencing the growth of self-generated magnetic fields and the resistive filamentation of the beam of fast electrons propagating within the material. Cases of targets comprised of a single material and, targets comprised of ordered and disordered allotropes of carbon, arrayed in a "layered" configuration, are considered.

Qualifying the dependency of the growth of instabilities on a material's low-temperature resistivity is a critical study, not only of fundamental interest, but also for envisioned applications where controlled, tunable particle beams are required. For example, in studies involving producing transient states of WDM [116, 203, 284] and in the FI scheme of ICF [19, 285].

Laboratory investigations of WDM states are relevant to multiple astrophysical scenarios [116, 203, 284], with one salient example being that of brown dwarf physics [32]. Brown dwarfs are objects with mass in the range of 0.013 and 0.072 solar masses. In this range,

some nuclear burning will still occur, but not at a rate sufficient for star formation [182]. These objects are comparable in size to Jupiter. Brown dwarfs present conditions similar to those created in intense laser-foil interactions, with temperatures and mass densities of ∼200 eV and 10^2-10^3 g/cm^3, respectively [286]. The transport of heat and electron currents in brown dwarfs is governed by the viscosity of the plasma [287]. The viscosity of brown dwarf plasma and the resistivity of a laser-produced plasma are both dependent on electron collisions (see section 2.6.3). Therefore, investigations of the role of the low-temperature resistivity on fast electron dynamics in intense laser-solid interactions are relevant to studies of the viscosity of matter in brown dwarfs. Understanding the role of the viscosity of electron dynamics in brown dwarfs will offer insight into the transport of heat from the central regions to the outer atmosphere of such objects.

Previous studies have confirmed that electrical resistivity at low-temperatures (i.e. below 100 eV) plays a key role in defining the characteristics of fast electron transport through solid density targets, via its role in defining resistive magnetic fields. It also results in the growth of resistive instabilities and defines the transverse transport patterns which are, in turn, mapped into the rear-sheath accelerated proton beams [53, 54, 128, 282]. The work presented in this chapter expands to experimental and numerical studies into the influence of low-temperature resistivity in silicon [128] and carbon [54]. Furthermore, the role of the material lattice structure in defining the onset of the resistive filamentation instability is investigated via the utilisation of double-layered, ordered (diamond) and disordered (vitreous) carbon targets. Additionally, it is demonstrated that the thickness of the layer of disordered material is crucial in defining the beam filamentation pattern.

Spatial-intensity distributions of the beam of protons accelerated from the rear-surface of targets via the TNSA mechanism are used to diagnose the fast electron transport within the target. These are subsequently compared to numerical simulations performed using the 3D hybrid-PIC code Zephryos. A model is developed to investigate the two-dimensional mapping of the sheath electron density (from simulations) into the spatial-intensity distribution of the accelerated protons [53, 128, 288, 289].

The chapter is broadly organised as follows; in section 5.2, the results of a numerical investigation into the role of low-temperature electrical resistivity in defining the transport properties of fast electrons in solids are presented. Section 5.2.2 discusses the role played by the shape and magnitude of the low-temperature resistivity-temperature profile of lithium, in various states of lattice disorder. Following this, section 5.2.2 presents a

further numerical study focusing on silicon for comparison. Finally, an extension of these investigations to parameters relevant to the FI scheme for ICF is also reported in section 5.2.2.

The case of solid targets composed of layers of ordered (diamond) and disordered (vitreous) carbon allotropes is then considered in section 5.3. Firstly, experimental results from an investigation at PHELIX, GSI will be discussed in section 5.3.1. Comparative numerical modelling is examined in section 5.3.2, before the effects of a variation of the thickness and position of the vitreous carbon layer are explored in section 5.3.3. These results are discussed in the context of linear resistive instability theory. The investigations presented in this chapter have been published in two papers in *Plasma Physics and Controlled Fusion* [115, 278]

5.2 Influence of low-temperature resistivity on fast electron transport in lithium and silicon

The control of mega-Ampere currents of fast electrons in solids, driven by relativistically intense laser pulses, underpins many applications of high power lasers, including the FI approach to ICF [19], and the generation of intense x-ray [24, 25, 290] and ion sources [22, 291]. These applications require control of the fast electron beam transport, and thus, it is critical to understand the role played by self-generated resistive magnetic fields in defining the properties of fast electron propagation and the onset of transport instabilities. As discussed in section 2.7.1, the growth of these self-generated magnetic fields is governed by:

$$\frac{\partial \mathbf{B}}{\partial t} = \eta \nabla \times \mathbf{j}_f + \nabla \eta \times \mathbf{j}_f \tag{5.1}$$

where η is the background electrical resistivity and $\mathbf{j}_f$ is the fast electron density. The first term on the right hand side drives electrons to regions of higher current density, whereas the second term pushes electrons into regions of higher resistivity.

Previous studies have tended to neglect the influence of the electrical resistivity at low temperatures, below 20 eV, and have instead been based on Spitzer resistivity [119]. As such, experimental investigations have often utilised relatively thin targets, tens-of-microns thick, where substantial heating occurs over the entirety of the target bulk. Investigations by our group have demonstrated that the electrical resistivity at low temperatures, in the few-to-tens of eV range, plays a defining role in driving the self-generation of strong

resistive magnetic fields and hence, establishing the degree of filamentation of the fast electron beam [54, 288] and the onset of annular structure [116, 128, 292].

Here, targets with thicknesses of the order of hundreds of microns are employed, and so, reduced heating of the target bulk is observed. Thus, the evolution of the resistivity-temperature profile of the target material at low temperatures must be considered.

In the following sections, numerical simulations of the sensitivity of fast electron transport dynamics to the shape, and magnitude, of the low temperature $\eta - T$ profile for lithium and silicon (an example metal and semiconductor, respectively) are presented. Intermediate $\eta - T$ profiles were generated between limits set by the cases of ordered and disordered lattice structures for both materials. The resultant changes to the self-generated resistive magnetic field, and its role in defining fast electron propagation is investigated using the 3D hybrid-PIC code discussed in section 4.4.

5.2.1 Modelling

The hybrid-PIC code (Zephyros) was used to simulate the three-dimensional relativistic motion of electrons under the influence of self-generated resistive magnetic fields, and collisions within the target. The electrical resistivity is obtained from tabulated values of $\eta - T$, defined as an input parameter to the code. Values for the low-temperature resistivity of lithium and silicon were determined via *ab initio* quantum molecular dynamics (QMD) simulations based on density functional theory (DFT). The Vienna *Ab initio* Simulation Program (VASP) plane-wave DFT code [122, 123] was used to perform the QMD calculations, as conducted by Dr M. P. Desjarlais of Sandia National Laboratory, via the method laid out in reference [54]. This process can be summarised as follows: Resistivity-temperature profiles corresponding to well-ordered lattice structures were generated by performing DFT simulations at an initial temperature of 300 K. This value was selected as it corresponds to ionic structure at room temperature. These simulations resulted in the calculation of the $\eta - T$ profiles shown in figures 5.2 and 5.5 (a).

Following this, the electronic temperature of the system was varied from 0.025 to 20 eV in subsequent Kubo-Greenwood resistivity calculations [122, 124]. These calculations were performed for ordered and disordered lattice structures, for both lithium and silicon. To obtain the $\eta - T$ profiles for the disordered cases, the atomic configurations were simulated at a higher temperature of ~ 47000 K (~ 4 eV).

As discussed in **Chapter 2**, the level of lattice order affects both the shape and mag-

nitude of the electrical resistivity at low temperatures. This arises from the fact that the resistivity is strongly determined by the electron mean free path in the material [293]. A high level of lattice disorder leads to increased incoherent electron scattering, and a reduction of the electron mean free path (MFP), resulting in higher resistivity. Conversely, a material demonstrating an ordered lattice structure exhibits constructive interference of the wave function of the electron scattering from multiple ions. This leads to an effective MFP that is significantly longer than the mean interatomic distance [54]. Hence, the magnitude of the electrical resistivity is much smaller for a material comprised of an ordered lattice structure, than the same material, with a lower degree of lattice order.

If the electronic temperature is increased substantially, then the material enters the Spitzer resistivity regime [119] and is substantially heated, where the electron MFP increases with increasing temperature. The temperature at which a given material enters the Spitzer regime is dependent on the characteristics of the material itself, but for the specific cases of lithium and silicon, the threshold is in the region of ~ 20 eV and ~ 60 eV, respectively.

The differences in the QMD-Kubo-Greenwood resistivity-temperature profiles between the ordered and disordered cases for each material, as well as between lithium and silicon, in the low-temperature regime arises from the following. For the case of lithium (and all metallic materials) at room temperature, the electrical resistivity is low due to the presence of free electrons. As the temperature of the material is increased, the resistivity increases due to an increased number of free electrons present in the conduction band, resulting in an increased rate of electron-phonon scattering. The electrical resistivity increases to a peak value when the electron MFP in the plasma is approximately equal to the interatomic spacing of the ions. Comparing disordered and ordered lithium, the maximum value of the resistivity is 4.2×10^{-6} Ωm and 1.9×10^{-6} Ωm, respectively. The maximum value of resistivity is determined by the level of lattice disorder, as the minimum MFP cannot physically be shorter than the mean interatomic spacing. As the temperature of the material is increased yet further, the resistivity decreases due to a decrease in the collisional cross-section with increasing electron velocity, corresponding to the Spitzer regime [119]. Figure 5.1 illustrates the differences between the different cases. Also plotted are intermediate resistivity-temperature profiles, corresponding to varying degrees of lattice melt. These were calculated via the choice of a "lattice parameter", a, that took the value of an integer between one (for the ordered case) and n (for the

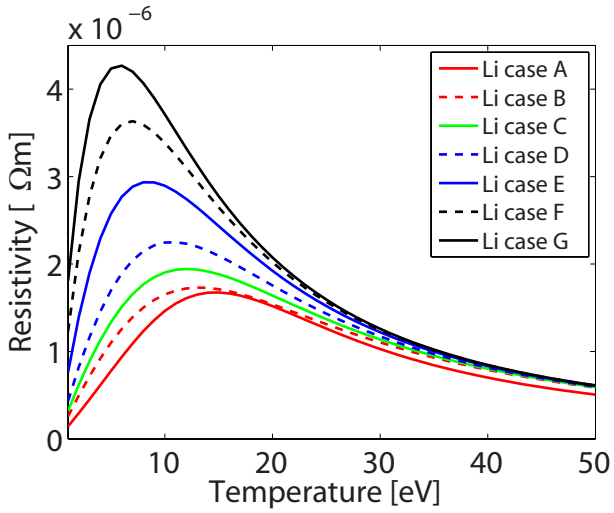

*Figure 5.1: Resistivity-temperature profiles for ordered (case **A**) and disordered lithium (case **G**), plotted alongside modelled intermediate resistivity curves, calculated via choice of a "lattice parameter".*

disordered scenario), that was inserted as a coefficient into the fit for the ordered $\eta - T$ curve obtained via QMD simulations. In the case of lithium, the "lattice parameter" was varied between one and seven, corresponding to cases **A** to **G**, respectively.

Conversely, silicon is a semiconductor and thus possesses a high electrical resistivity at room temperature. For the case of ordered silicon, a small increase in temperature results in a rapid decrease in the value of the target resistivity (see figure 5.5 (a), leading to a minimum value at $\sim$ 3.5 eV. This minimum point arises due to the excitation and ionisation of the outer valence electrons above silicon's bandgap ($\sim$ 1.12 eV). This promotes the generation of an increased number of free charge carriers in the conduction band of the material, and thus, a reduction in the electrical resistivity. Following this, the resistivity is observed to increase to a peak value at $\sim$ 50 eV. This peak corresponds to the similar situation for lithium, where a minimum in the electron MFP leads to an increased rate of electron-ion collisions. Beyond this, the collisional cross-section decreases and the resistivity falls off sharply, again corresponding to the Spitzer regime.

The highly-ordered face-centred cubic diamond crystal structure of ordered silicon (as is also the case with ordered lithium) has a strong influence on the mean free path of the target electrons, and thus, the material resistivity in the transient warm dense matter state [54]. Furthermore, as the degree of lattice disorder increases, and the electron MFP decreases, the presence of the "dip" is seen to disappear, and the target resistivity remains high until it enters the Spitzer regime. Figure 5.5 (a) illustrates the differences between

the two scenarios of ordered and disordered silicon, where cases **A** and **D** correspond to ordered and disordered silicon, respectively. A similar "lattice parameter" was defined for silicon, as described for lithium, in order to model intermediate $\eta - T$ profiles from the fits to the QMD results. This value, a, was varied between values of 1 and 4 in this instance and will be discussed further in section 5.2.2.

Simulations were performed on a grid with spatial dimensions X = 200 μm × Y = 400 μm × Z = 400 μm, with a cell resolution of ΔX = ΔY = ΔZ = 0.5 μm. The total number of macroparticles injected into each simulation was 2×10^8, which results in 4×10^7 macroparticles being injected into the simulation grid every timestep (of 0.2 ps), up to a pulse duration of 1 ps. Simulation box boundaries were transmissive, with the exception of the X = 0 and X = X_{max} boundaries, which were reflective in order to mimic the effects of fast electron refluxing due to the sheath fields formed at the target rear surface in experiments. However, the simulation outputs were sampled just after the bulk of the fast electron population had reached the rear surface boundary (1.4 ps), and thus reflected electrons did not significantly influence the fast electron transport pattern. The background plasma temperature was initialised at 1 eV.

The fast electron macroparticles were injected at [X,Y,Z] = [0,0,0], uniformly over a cone with half-angle equal to 50° [294]. The electrons were given an exponential energy distribution: $\exp(-E_f/kT_f)$. Wilk's scaling [97] is assumed for the determination of T_f. The fast electrons were injected uniformly over the laser pulse duration and possessed a Gaussian spatial-intensity distribution and, finally, a laser-to-fast electron energy conversion efficiency of 30% was chosen. This value is based on the results of previous investigations of energy absorption and coupling to electrons for similar laser parameters [176, 295].

The simulations in the discussion at the end of section 5.2.2 were performed with the majority of the same parameters (as in sections 5.2.2 and 5.2.2) with the exception that size of the simulation grid was varied for four different cases: X = 50, 100, 200, and 400 μm. The cell resolution, defined earlier, was maintained throughout for each case. Furthermore, these simulations were performed with 1×10^7 macroparticles injected every 1 ps, with the total duration of the pulse increased to 20 ps, and a peak laser intensity of 4×10^{20} W/cm^2. The simulation outputs were sampled at a time of 5 ps, in order to minimise the level of lattice melt.

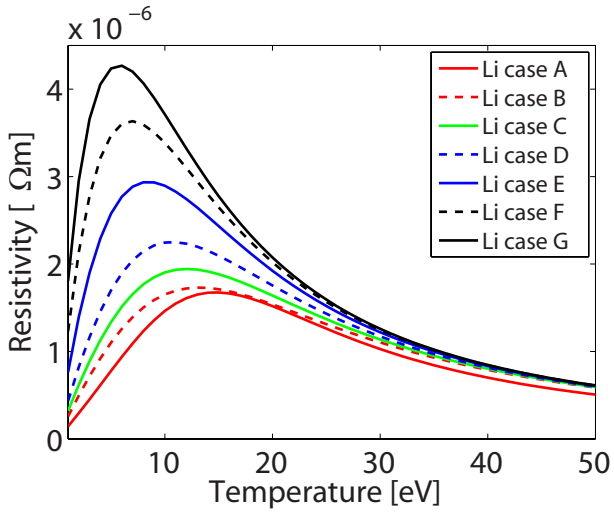

*Figure 5.2: Resistivity-temperature profiles for ordered (case **A**) and disordered lithium (case **G**), plotted alongside modelled intermediate resistivity curves, calculated via choice of a "lattice parameter".*

5.2.2 Results

Onset of beam filamentation in lithium

Lithium was chosen as a sample material for various reasons, including: its resistivity-temperature profile is characteristic of metallic materials, as discussed previously. Moreover, the aforementioned resistivity peak occurs at low temperatures compared to higher Z metals ($\sim 5-15$ eV, in the same temperature region as the resistivity dip that occurs in silicon). Furthermore, the position and the magnitude of the peak of the resistivity-temperature profile for lithium has been measured to vary significantly with the level of lattice disorder of the material.

Figure 5.2 presents the range of lithium resistivity-temperature profiles investigated, ranging from case **A** (ordered lattice structure) to case **G** (disordered lattice structure). Cases **A** and **G** were calculated via the method based on *ab initio* QMD calculations coupled with the Kubo-Greenwood equation discussed in section 5.2.1. The remainder of the intermediate profiles were modelled by using numerical fits to the low-temperature region of both the ordered and disordered curves, via the choice of lattice parameter, and are plotted alongside the resistivity-temperature profiles obtained via the *ab initio* QMD-Kubo-Greenwood method.

Transport simulations were run for all seven cases and four representative examples cases are shown, corresponding to cases **A**, **D**, **E**, and **F**, i.e. ordered and disordered lithium,

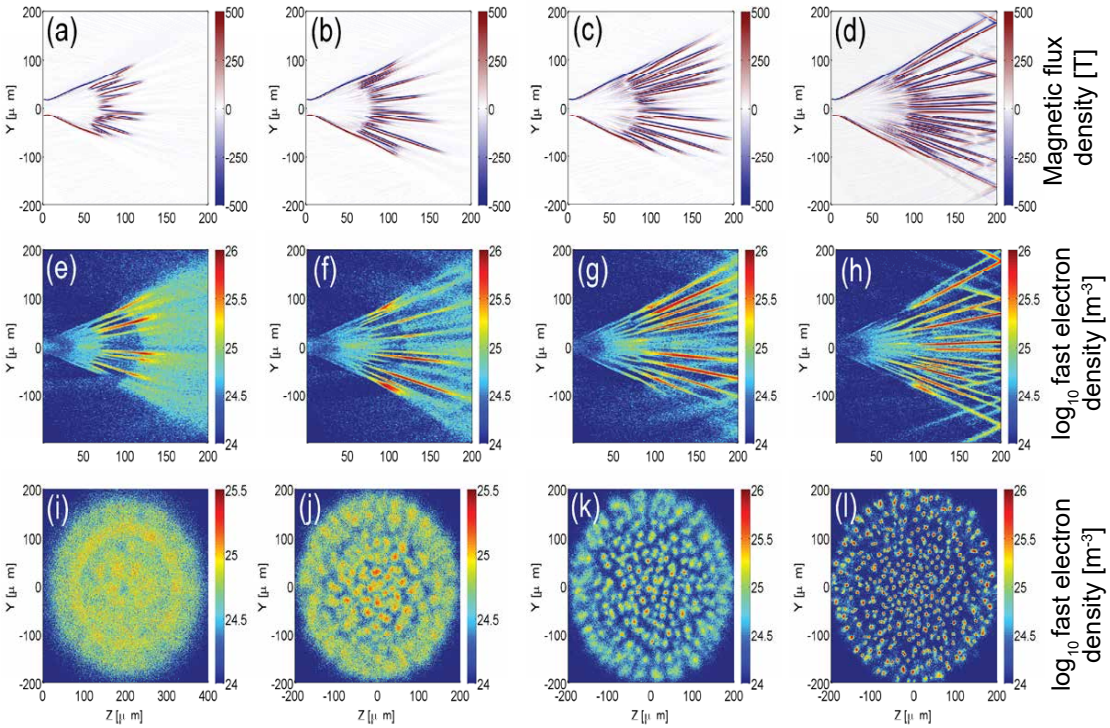

Figure 5.3: Hybrid-PIC simulation results, 1.4 ps after the start of the electron injection, showing: Top row: [X-Y] mid-plane 2D maps of the magnetic flux density (B_z component) for (a) case A; (b) case D; (c) case E, and (d) case G; Middle row: Corresponding results showing log_{10} fast electron density maps in the [X-Y] mid-plane; Bottom row: Corresponding results showing log_{10} fast electron density maps at the rear-surface [Y-Z] plane (X=200 μm).

and two intermediate cases. Thus, the evolution in fast electron transport is investigated at discrete points over the transition from ordered to disordered ion structure. Simulations results showing the B_Z component of the magnetic flux density, and two-dimensional maps of the fast electron density in the [X-Y] and [Y-Z] planes are shown in figure 5.3.

Concentrating initially on the results showing the fast electron density maps at the rear surface plane, an evolution of the fast electron transport pattern from relatively smooth, for ordered Li (case **A**) to a strongly filamented beam for case **G**, can be observed. In all cases, resistive filamentation is observed to occur at a distance between $50 - 100$ μm into the target, although for cases **A** and **D**, where the material lattice is relatively more ordered, these filamentary structures are seen to coalesce into larger scale structures by the time they propagate to the rear surface. Furthermore, the number of observable filaments increases with the level of lattice disorder. This is explained by considering the equation governing the evolution of self-generated magnetic fields (equation (5.1)). As target heating is identical in each case, the temperature at ~ 50 μm will be of the order of 10 eV. it is in this region of the $\eta - T$ profile that the largest change in η occur and thus there

is a strong degree of variation in the degree of resistive instabilities occurring [117,152,296].

Further into the target, the electron temperature continues to decrease, resulting in a drop in the electrical resistivity. Due to this, the strength of the self-generated magnetic field in this region decreases accordingly. This is particularly prevalent for the "more ordered" scenario (case **A**, figure 5.3 (e) and (i)). In these cases, the strength of the "pinching" force of this field, acting to collimate the filaments, is reduced and they expand transversely, leading to them merging, due to the attraction of like currents, and the relatively smoother transport pattern observed at the rear-surface (figure 5.3 (i)). In contrast, in case **G** the resistive, self-generated magnetic fields surrounding the filaments are observed to remain relatively strong in the deeper regions of the target, illustrated in figure 5.3 (d). In this example, η in this region is relatively higher than for case **A** and, as such, the magnitude of the self-generated magnetic fields collimating the fast electron current does not dissipate to the degree observed for ordered lithium (figure 5.3 (l)). Considering the [X-Y] midplane maps of magnetic flux density within the target (figure 5.3 (a-d)), the influence of the low-temperature resistivity and material lattice structure on the growth of self-generated magnetic fields and the resistive filamentation instability can be clearly seen. For example, as the degree of lattice disorder is increased, the distance to which strong magnetic fields are found in the target increases because of the increase in η at lower T.

The degree of beam filamentation was quantified via calculation of the percentage variance of the beam density at the rear surface of the target (i.e. at $X = 200$ μm). The fast electron beam variance was sampled over an area corresponding to 30% of the total beam area, centered at $Y = 0$, $Z = 0$. The level of inhomogeneities in the fast electron transport patten in this region is shown, as a function of the peak electrical resistivity of the corresponding resistivity-temperature relation for lithium, in figure 5.4.

There is clear evidence of increasing inhomogeneity and disorder in the transport pattern with increasing magnitude of the peak electrical resistivity. This is consistent with the growth of the resistive filamentation instability [117].

Onset of beam filamentation in silicon

The previous section was concerned with investigating fast electron transport in lithium. In this section, silicon is considered. Being a relatively poor conductor at room temperature, silicon has a distinctly different electrical resistivity-temperature relation [128] and

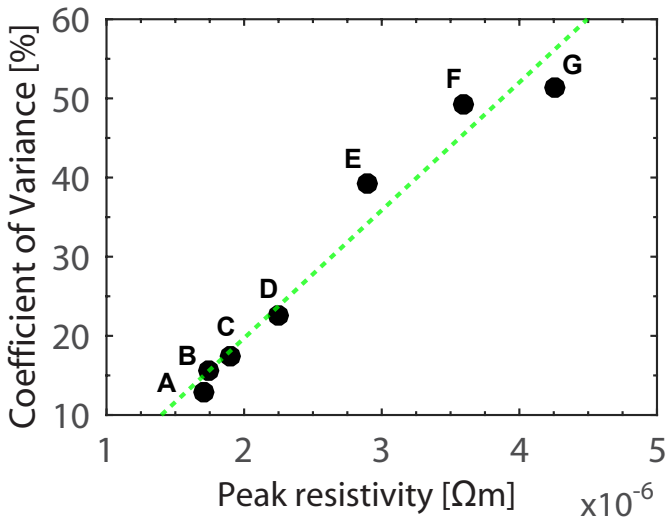

*Figure 5.4: Coefficent of variation in the fast electron density at the rear-surface [Y-Z] plane of the target ($X = 200\mu m$) in the simulation results for lithium, as a function of the magnitude of the peak of the resistivity-temperature relation for cases **A**-**G***

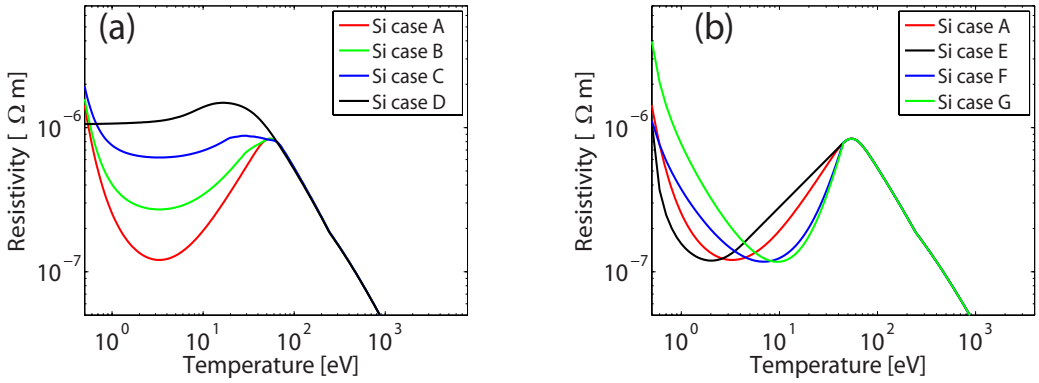

*Figure 5.5: (a) Electrical resistivity of silicon as a function of target temperature for ordered (case **A**) and disordered (case **D**) silicon, determined via ab initio QMD-Kubo-Greenwood calculations. Cases **C** and **D** correspond to modelled, intermediate electrical resistivity curves, calculated via choice of "lattice parameter". (b) Cases **E** - **G** correspond to devised η-T profiles for which the temperature at which the η dip occurs is varied to enable investigation of the resulting effect on fast electron transport.*

possesses an initially high electrical resistivity value at room temperatures. The electrical resistivity-temperature relation for ordered silicon is shown in figure 5.5 (a).

As discussed in section 5.2.1, the magnitude of the electrical resistivity decreases sharply with a small increase in temperature due to excitation of electrons above the band gap. As the temperature increases further, the resistivity gradient reverses and η increases again, peaking at $T \sim 50$ eV. MacLellan *et al.* [128] first demonstrated that the subsequent dip in the electrical resistivity of silicon at low temperatures leads to a reversal of the resistivity

gradient, $\Delta\eta$, at the edge of the beam. The consequence is a reversal in the direction of the self-generated magnetic field (from equation (5.1)), acting to pinch the fast electron beam. However, the azimuthal field encircling the beam continues to force the electrons radially inwards, and so the combined action of both opposite forces results in the fast electrons being driven into an annular pattern (i.e. a ring distribution), with an increased electron density found in the region of the resulting ring formation. The increased electron density in the region of the ring leads to an increase in localised Ohmic heating (see section 2.6.3), bringing the temperature into the Spitzer regime of plasma resistivity [119], reducing the resistivity. This decrease in resistivity leads to strong positive feedback, sustaining the annular pattern of the beam as it propagates through the target.

As before, the cases corresponding to ordered and disordered lattice structures were calculated via the method based on *ab initio* QMD calculations coupled with the Kubo-Greenwood equation discussed in section 5.2.1. The intermediate η-T profiles were determined via numerical fits to the low-temperature regions of the results of the QMD simulations for both the ordered (case **A**) and disordered (case **D**) curves. A model equation was formulated which scales the resistivity between the ordered and disordered curves for an appropriate choice of "lattice order" parameter, a, with the following form [277]:

$$\eta(T) = \beta\frac{\Gamma(T)}{\Omega(T)} \tag{5.2}$$

where η is the resistivity of the material, β is equal to 0.11, and Γ and Ω are defined by:

$$\Gamma(T) = (C_1 a^3 T^3) - (C_2 a^5 T^3) - (C_3 a^4 T^4) - (C_4 a^6 T^2) + (C_5 a^6 T) + (C_6 a^9) + C_7 \tag{5.3}$$

$$\Omega(T) = (C_8 a^3 T^2) + (C_9 a^6 T) + (C_{10} a^8) \tag{5.4}$$

where $C_1 = 1.2 \times 10^7, C_2 = 1.1 \times 10^9, C_3 = 1.2 \times 10^{10}, C_4 = 1 \times 10^9, C_5 = 1.33 \times 10^6, C_6 = 9 \times 10^9, C_7 = 4 \times 10^7, C_8 = 0.75, C_9 = 8 \times 10^2$ and $C_{10} = 1 \times 10^2$.

The modelled fits to the QMD simulations were obtained via a curve-fitting analysis and arise from requiring a fit that could represent a range of $\eta - T$ profiles via selection of an appropriate lattice parameter, a. In this case of silicon, a was varied between one and four, which corresponds to cases **A** and **D**, respectively. The sensitivity of the annular fast electron transport pattern to the influence of the varying magnitude of the minima in the low-temperature η-T relation is investigated over the course of this section. Furthermore,

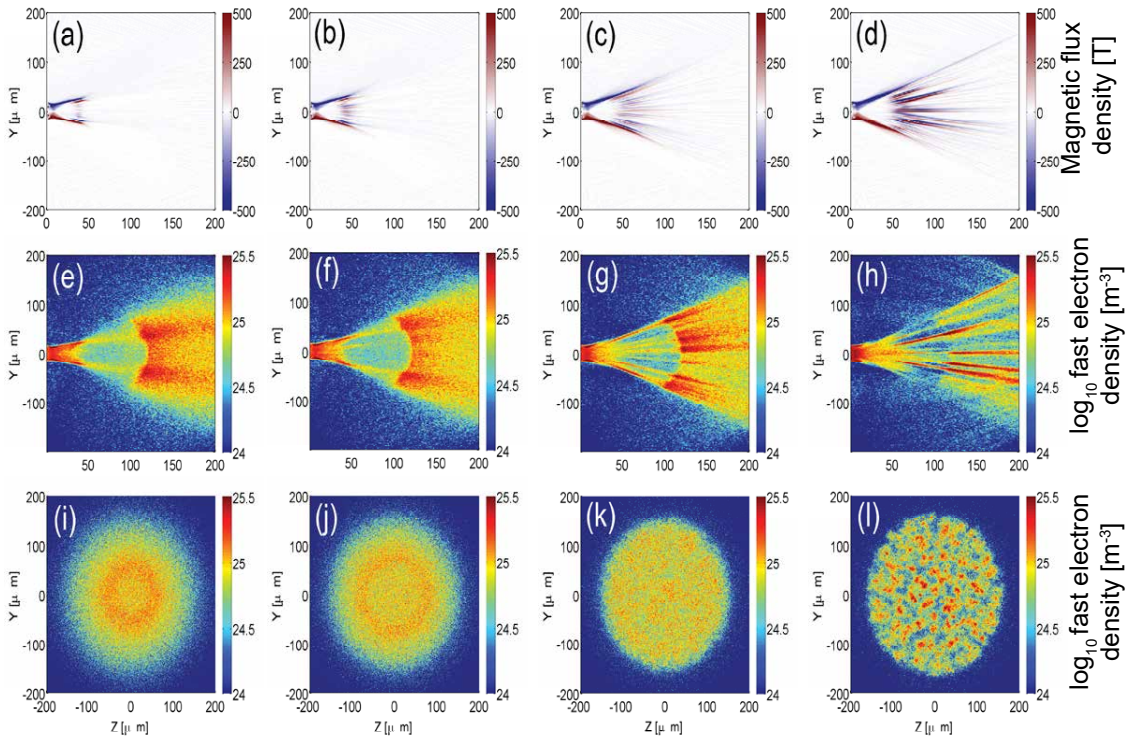

Figure 5.6: Hybrid-PIC simulation results, 1.4 ps after the start of the electron injection showing: Top row: [X-Y] mid-plane 2D maps of the magnetic flux density for (a) case A; (b) case D; (c) case E, and (d) case G; Middle row: Corresponding results showing fast electron density maps, in the [X-Y] mid-plane; Bottom row: Corresponding results showing fast electron density maps, at the rear-surface [Y-Z] plane (X=200 μm).

the influence of varying the temperature at which the minima of electrical resistivity occurs is also investigated.

Considering the influence of the variation of the magnitude of the electrical resistivity dip at low temperatures initially, figure 5.6 shows the fast electron transport patterns obtained for each case in figure 5.5 (a). The minima of the dip in resistivity, and thus, the level of lattice disorder, is increased from left to right (i.e. case **A** to **D**).

Looking at the [X-Y] and [Y-Z] fast electron density maps figure 5.6 (e)-(h) and (i)-(l), the ordered lattice (case **A**) is observed to produce an annular transport pattern (as described in MacLellan *et al.* [128, 297]). Increasing the level of disorder in the lattice structure is observed to, first, disperse the ring feature in case **B**, before evidence of the onset of filamentation is seen in case **C**. For the fully disordered case (case **D**), the beam is completely filamented, with large filaments seen propagating towards the target rear. The filaments remain relatively large in comparison to those observed for the corresponding case for lithium. This can be explained by considering the magnetic field strength map in figure 5.6 (d). In the case of lithium (figure 5.3) (d), the resistively-generated

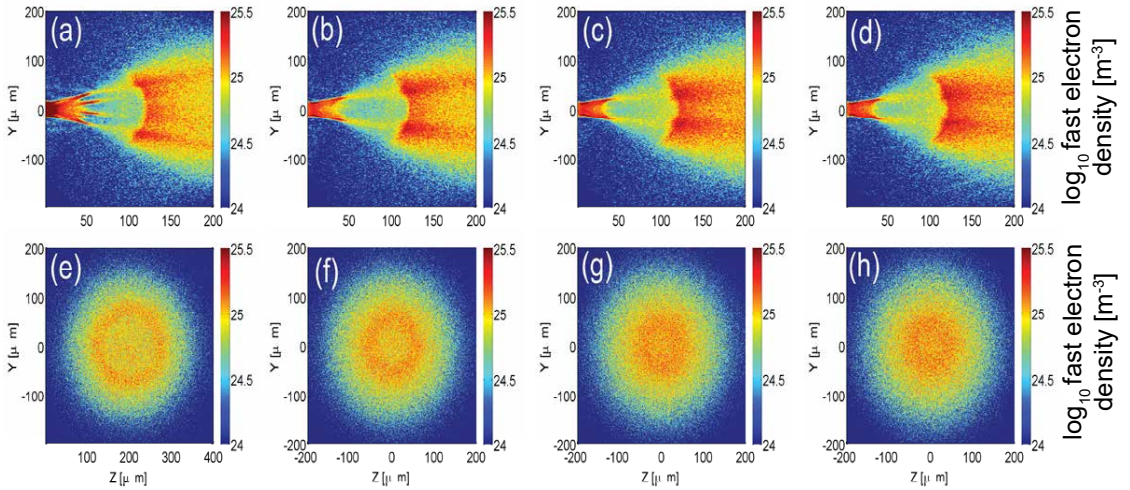

Figure 5.7: Fast electron density maps, in the [X-Y] mid-plane and rear-surface [Y-Z] plane for (a) Si case E, (b) Si case A, (c) Si case F and (d) Si case G.

magnetic fields extend to the rear boundary, acting to collimate the filamented fast electron populations. In contrast, the magnetic fields in case **D** for silicon are significantly diminished approximately 50 μm prior to the target rear, and thus, the filaments expand transversely. The relatively high resistivity of disordered lithium at low temperatures ($\sim$ 10 eV), when compared to disordered silicon (in a similar temperature range) is the source for the stronger magnetic field growth, at a greater extent from the fast electron source.

In summary, similarly to the lithium investigation, the magnitude of the dip in electrical resistivity, at low temperatures, has a defining effect on the transport pattern of the fast electron transport and generation of resistive magnetic fields.

Following on from the above investigation, the influence of the variation of the temperature at which the minima of resistivity occurs was examined (as shown in figure 5.5 (b)). Here, case **A** corresponds to the case of ordered silicon (case **A** in the investigation of the influence of varying the magnitude of the dip in the low-temperature electrical resistivity profile). Cases **E** to **G** were devised such that the minima of the resistivity-temperature profile occurred at higher and lower temperatures (2, 7 and 9.5 eV, for cases **E**, **F** and **G**, respectively). The results, obtained via three-dimensional hybrid-PIC simulations are shown in figure 5.7. Looking from (a) to (d) in figure 5.7, the fast electron density maps are shown in the order of increasing minima temperature, i.e. cases **E**, **A**, **F** and **G**.

It was observed that increasing the temperature at which the dip in electrical resistivity occurs leads to a reduction on the radius of the annular feature. This is particularly evident when examining the [Y-Z] rear-surface maps of fast electron density in figures 5.7

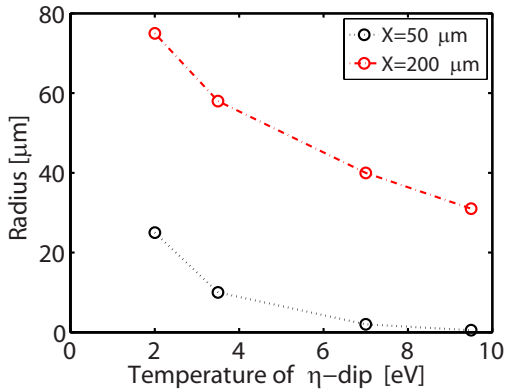

Figure 5.8: Radius of the annulus at the target rear side (X=200 μm) and at X=50 μm (at which the reversal in the B-field occurs) as a function of the temperature of the centre of the η-dip.

(e)-(h). This size reduction of the annular feature arises because the radius at which the reversal in the self-generated magnetic field occurs decreases with increasing background electron temperature. Thus, increasing the temperature at which the dip occurs results in the gradient of the resistivity reversing at increased background temperatures, leading to the radius of the annular feature being reduced. This process is highlighted in figure 5.8, which displays the sensitivity of the radius of the final annular transport pattern to the radius of the annular profile at the point at which it is seeded.

It should be noted that, in order to maintain the characteristics of the parabolic profile of the electrical resistivity profile at low temperatures, the magnitude of the resistivity at approximately 1 eV is varied, depending on the location of the dip. The initial resistivity value is increased as the temperature at which the dip occurs is increased. As can be seen in figure 5.7, the presence of resistive filamentation is not evident and thus, the transport of the fast electrons is not significantly affected by this small shift in η.

It is also important to note that the intermediate, modelled $\eta - T$ profiles presented were generated purely to investigate the growth of self-generated resistive magnetic fields, at discrete intervals of the degree of lattice structure of silicon and do not correspond to real allotropes of silicon. The feasibility of the creation of an allotrope of silicon where the lattice structure of the material remains relatively ordered, but the position of the minima of the low-temperature $\eta - T$ profile varies, is a matter beyond the scope of this thesis. However, recent investigations [116] explored the possibility of employing resistivity gradients via melting the lattice structure of a target by isochoric heating using laser-accelerated protons [298–300]. MacLellan *et al.* [116] showed through the tailoring

of the heating profile, the self-generated resistive magnetic fields which strongly influence the propagation of fast electrons, could be manipulated. This was demonstrated in the context of the variation of annular structure mapped into spatial-intensity profile of TNSA-accelerated protons from silicon targets that were unheated (prior to the interaction) and targets that had been proton heated for tens of picoseconds (to temperatures up to ~ 2 eV) prior to the arrival of the irradiating pulse. Other viable options for control of the resistive magnetic fields which influence fast electron transport may include doping of the target materials with free electrons. In semiconductors, doping (replacing silicon atoms with atoms of another element, i.e boron), is frequently used to control the material resistivity/conductivity. Doping may be used to locally manipulate the the behaviour of the electrical resistivity, by decreasing the mobility of the charge carriers in the semiconductor [301]. The mobility of the charge carriers is dependent on both temperature and the concentration of dopant atoms [302]. Through this process, it may be possible to tailor the resistivity-temperature profile to induce desired transport effects.

The results presented in this chapter demonstrate the influence of the low-temperature resistivity profile on the generation of unique spatial distributions within the beam of fast electrons. By subtle manipulation of the target's $\eta - T$ profile, a level of control of the fast electron population can be achieved. The potential for control of fast electrons generated in laser-solid interactions, and thus control of the protons accelerated via the TNSA mechanism (see section 2.9.1) is a matter of significant interest within the scientific community. The potential for employing annular fast electron beams as a mechanism for depositing energy in the FI scheme for ICF is discussed in this section.

In the FI scheme, a giga-Ampere current of electrons is required to propagate through the compressed fuel capsule from the fast electron source at the edge of the capsule (a distance of approximately $100 - 200$ μm) and deposit its energy at the in the compressed fuel for ignition to occur. Alternative methods of FI involve inserting a hollow cone inside the capsule. The cone enables the drive-pulse to propagate closer to the compressed fuel, but the fast electrons must additionally propagate through the rear wall of the solid cone, typically located at a distance of 100 μm from the core [303]. The parameters of the drive pulse are governed by the energy requirements of the fast electron beam: it must be high enough to minimise scattering losses over the propagation distance, but also be of the order that the majority of the energy is deposited in the region of the compressed fuel [304,305]. This leads to a required intensity on the order to 10^{20} W/cm^2 [97]. Furthermore, the

laser parameters are additionally dependent on the density of the compressed fuel capsule. Typical fuel densities in FI schemes are of the order of 300 g/cm^3 post-compression, dropping to $\sim$ a few g/cm^3 near the tip of the cone [303]. To achieve ignition with fuel densities of this order, require $\sim$ 20 kJ of total electron energy to be deposited within the core (approximately 20 μm radius) before the capsule disassembles (typically on timescales of $\sim$ 20 ps).

Annular beams are particularly attractive for FI as the maximum current transported can be increased compared to the case of a uniform beam. This is possible due to the Alfvén limit increasing by a factor of $r/\Delta r$, where r and Δr are the radius and width of the annular structure, respectively [107]. In addition, Davies [292] showed that one potential method of mitigating the rapid resistive decay of the return current in FI scenarios would be the utilisation of annular fast electron beams. Furthermore, Hatchett *et al.* [165] numerically demonstrated reduced ignition energy requirements when employing annular beams for FI.

Re-entrant cones employed in FI schemes are often hollow and made of high density materials, purely to allow clean entry of the ignition pulse to the compressed fuel assembly. Thus, modifications would have to made to existing models to enable the addition of a silicon target into the assembly to enable the annular beam to be generated. In addition, the importance of the low-temperature resistivity profile has already been shown to be of utmost importance to the formation of the annular structure. Thus, some method of protecting the silicon insert from pre-heating during compression would need to be devised. In the case of sub-kJ energy laser pulses for which the annular transport profiles in silicon have been experimentally verified [128] radiation heating has little effect. However, the higher radiation flux produced in the case of FI-relevant pulses may influence the formation of these patterns and should be considered in a more detailed assessment of this scheme. It should be noted that this discussion is merely an investigation into the feasability of generating annular beams in environments relevant to FI, not a detailed analysis of their utilisation for ignition or the engineering of the fuel assembly. A schematic of the envisioned fuel assembly is shown in figure 5.9 (a).

A typical deposited electron energy of $\sim$ 20 kJ (corresponding for example to an ignition laser pulse energy equal to 100 kJ and 20% conversion efficiency to fast electrons) and a pulse duration equal to 20 ps (the capsule disassembly timescale) were utilised in 3D hybrid-PIC simulations of silicon targets representing the silicon insert to the re-entrant

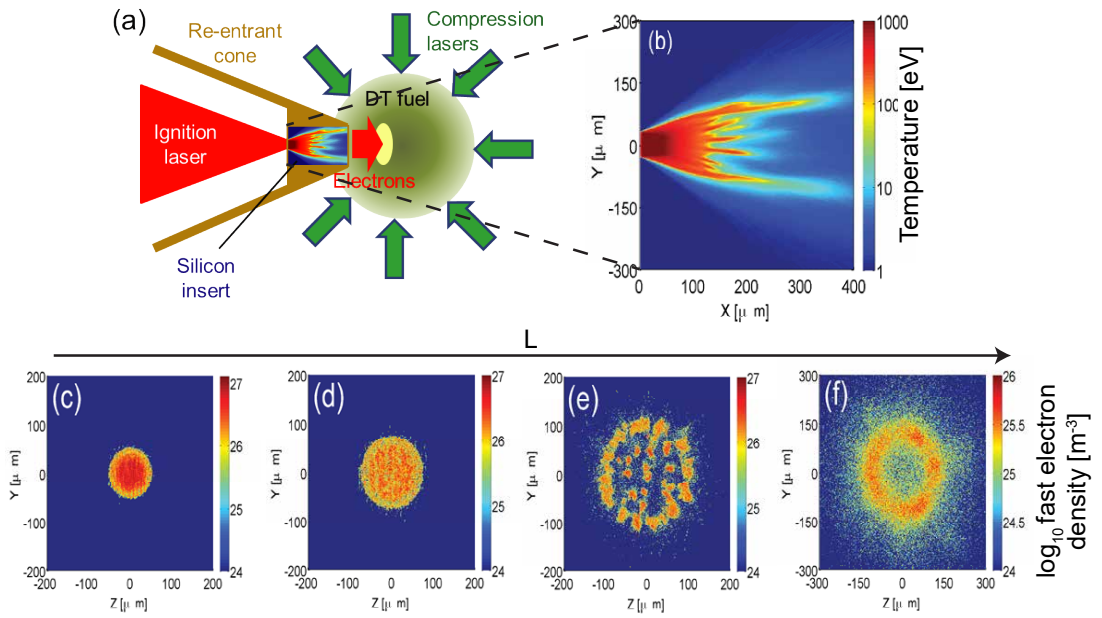

Figure 5.9: (a) Schematic illustrating a cone FI target scheme with a silicon insert to induce an annular fast electron beam transport pattern. (b) Background target temperature in the [X-Y] mid-plane for the L=400 μm case. (c)-(f): Fast electron density maps at the rear-surface [Y-Z] plane, for (c) L=50 μm; (d) L=100 μm; (e) L=200 μm; and (f) L=400 μm;.

cone. These parameters resulted in a peak laser intensity equal to $4{\times}10^{20}$ Wcm^{-2} (to minimise scattering, but enable the majority of electron energy to be deposited within the central hot spot). These ignition pulse parameters are typical for DT fuel compression to a peak density of ∼300 g.cm^{-3} [19]. The silicon resistivity-temperature profile was defined to be case **A** (see section 5.2).

Figure 5.9 (c)-(f) show simulation results at a timestep of 5 ps after initialisation, selected to minimise the effects of lattice melt, which (as MacLellan *et al.* [116] demonstrated) will change the profile of the electrical resistivity-temperature relation.

The annular profile observed in section 5.2 (figures 5.6 and 5.7) is only present in figures 5.9 (e) and (f). In figures 5.9 (c) and (d), evidence of an annular fast electron beam is visible, however the presence of an annular structure is not yet present at the rear. Thus, there must be requirement for the growth of the annular structure. As this feature is generated via the action of self-generated resistive magnetic fields and the reversal of the resistivity gradient at low temperatures, the temperatures present within the first 100 μm of the target must be sufficiently high enough that low-temperature resistivity effects are negligible. This is demonstrated in the corresponding target temperature map (in the [X-Y] mid-plane) in figure 5.9 (b) for the L=400 μm case. Therefore, the silicon insert would be required to be of the order of, $\geq$ 200 μm in thickness for the formation of annular

fast electron currents that could penetrate the compressed fuel.

5.3 Role of low-temperature resistivity on magnetic field generation and fast electron transport in carbon

This section discusses an experimental and numerical investigation of the role of lattice structure in defining the growth of self-generated magnetic fields and the onset of the resistive filamentation instability specific to carbon targets. Double-layer targets comprised of ordered (diamond, D) and disordered (vitreous carbon, VC) allotropes of carbon were employed, with the layer thickness varied. The use of exotic targets with resistivity or material boundaries has previously been explored as schemes for controlling the propagation of fast electron currents. [132, 282, 283, 306, 307]. The utilisation of layered targets constructed of different allotropes of carbon ensured that any dependence on atomic number was removed, and the influence of the low-temperature resistivity of carbon could be isolated. The investigation presented here builds upon the work reported in McKenna *et al.* [54] and MacLellan *et al.* [277, 288] and furthers the discussion presented in sections 5.2.2 and 5.2.2.

5.3.1 Experimental results

The experiment used the PHELIX high power laser (see section 4.2.9), which produced S-polarised pulses with a central wavelength equal to 1.053 μm, with duration (725$\pm$100) fs and energy (180$\pm$10) J. The beam was focussed using an F/1.5 off-axis parabola into a 2.5 μm diameter (FWHM) spot, resulting in calculated peak intensity of $\sim 7\times10^{20}$ Wcm^{-2}, at the front side of the target.

The targets were either single material or double-layer carbon samples (D and VC), all with total thickness L=200 μm. The double-layer targets had equal thickness (100 μm) layers of VC and D pressed together with negligibly thin layer of adhesive. They were irradiated with the layers reversed on alternative shots. Relatively thick targets were chosen to minimise fast electron refluxing, due to the strong effects of refluxing on magnetic field generation [289].

The fast electron transport, and subsequent sheath dynamics were diagnosed by measuring the spatial-intensity distribution of the beam of multi-MeV protons accelerated at the target rear surface. The proton beam distribution is sensitive to modulations in the

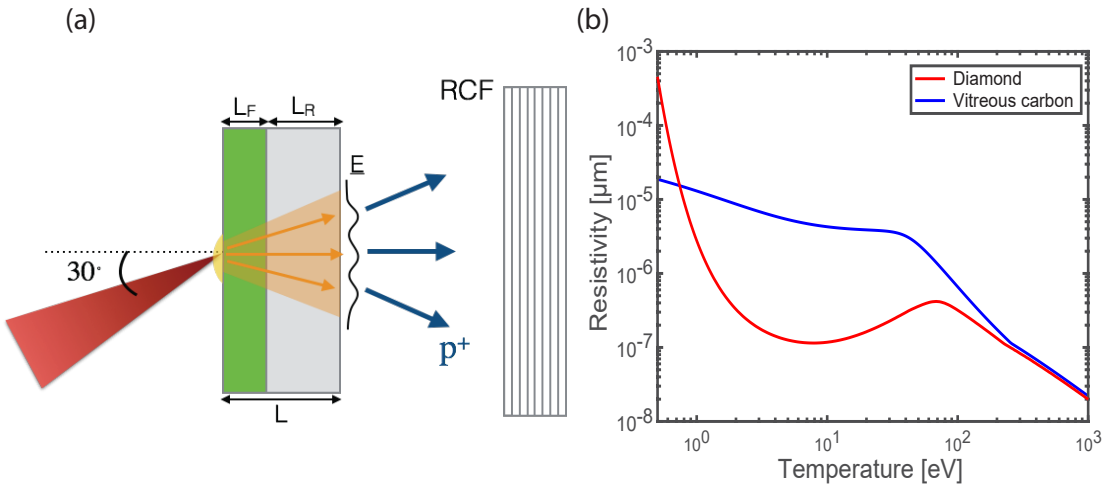

Figure 5.10: (a) Schematic illustrating the experimental arrangement; (b) Electrical resistivity as a function of temperature for ordered and disordered forms of carbon

sheath field produced by variations in the density distribution of fast electrons arriving at the target rear. The distribution was measured at discrete proton energies using stacked dosimetry film positioned 5 cm from the target rear. The stack configuration enabled discrete proton energies beyond 2 MeV up to 40 MeV to be detected. Figure 5.10 (a) shows a schematic of the experimental arrangement, whilst figure 5.10 (b) illustrates the $\eta - T$ profiles obtained via fits to the results of QMD simulations for ordered and disordered allotropes of carbon (discussed in section 5.3.2).

Figures 5.11 (a) and (b) show representative measured spatial-intensity distributions (at 10 MeV) of the beam of protons accelerated from 200 μm thick samples of VC and D, respectively. In agreement with similar results presented in reference [54], the disordered form of carbon produces a proton beam with significant cusp-like modulations, reflecting modulation of the fast-electron distribution due to transport instabilities. Conversely, the proton beam produced with diamond is smooth, except for a localised region of structure near the centre (as also observed previously in reference [288]). Equivalent measurements for the double-layer targets, corresponding to 100 μm VC/100 μm D and 100 μm D/100 μm VC are shown in figures 5.11 (c) and (d), respectively. The thickness of each layer was fixed at 100 μm thick such that a total thickness of $L = 200$ μm was conserved. In both cases evidence of filamentation is observed, but to varying degrees. The cusp-like structures in the proton beam are larger when vitreous carbon is at the target front layer compared to the reverse scenario.

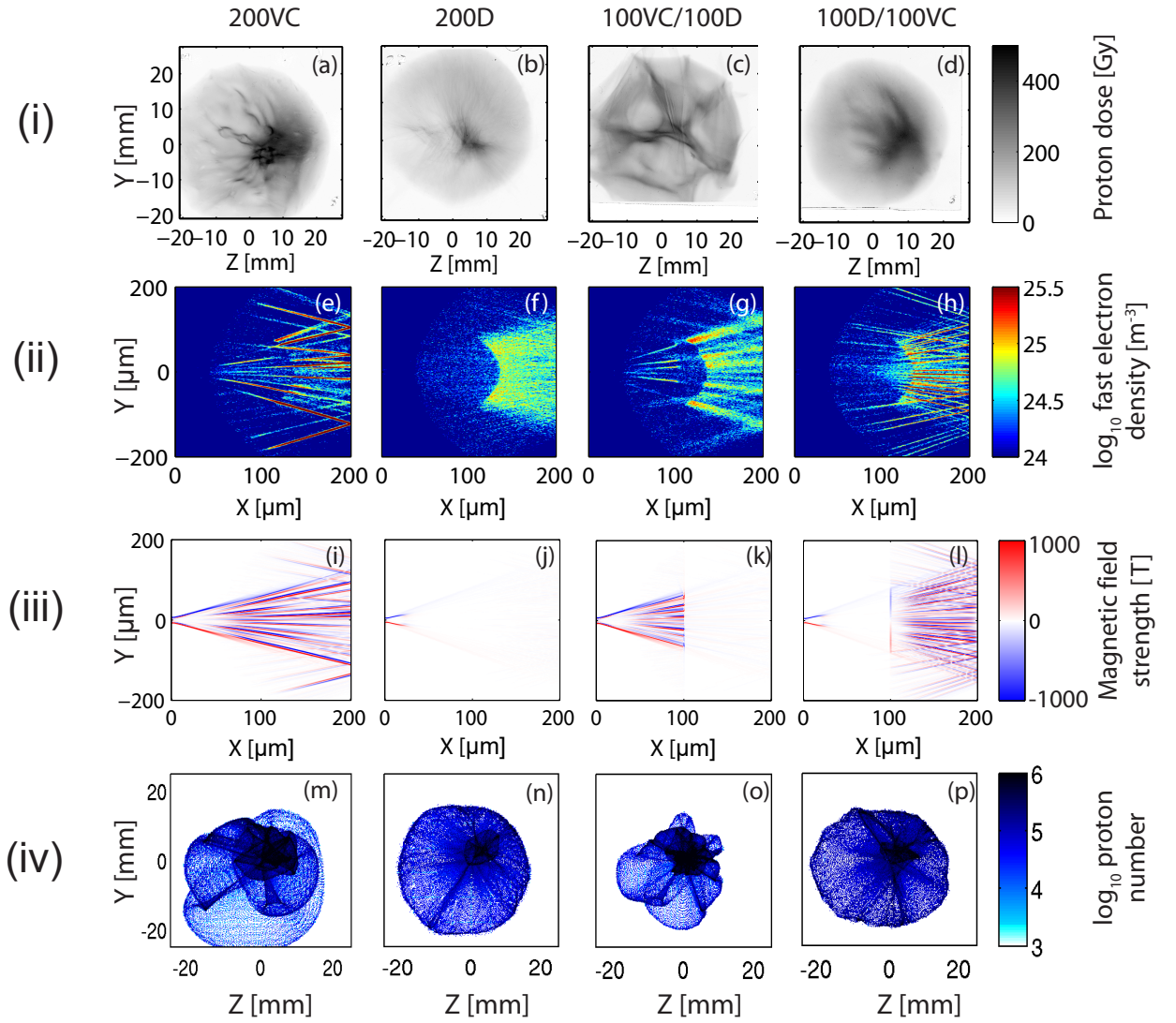

Figure 5.11: Row (i): Measured proton spatial-intensity dose profiles (Gy) for: (a) L=200 μm VC; (b) L=200 μm D; (c) L_F=100 μm VC and L_R=100 μm D; (d) L_F=100 μm D and L_R=100 μm VC; Row (ii): Corresponding fast electron density maps in the [X-Y] plane, from 3D hybrid-PIC simulations at 1.2 ps from the start of the electron injection; Row (iii): Corresponding [X-Y] mid-plane 2D maps of the magnetic flux density (B_z component); Row (iv): Corresponding modelled proton spatial-intensity maps, calculated using the rear-side fast electron density maps obtained from (e)-(h).

5.3.2 Modelling the experiment

To investigate the underlying transport physics, simulations of fast electron transport were performed using Zephyros. The electrical resistivity as a function of temperature for D and VC are shown in figure 5.10 (b). These were obtained via the method laid out in section 5.2.1. In order to obtain a fit to the $\eta - T$ curves such that the effects of resistivity boundaries could be implemented in the numerical simulations, a polynomial fit to the

results of QMD simulations, similar to the one described in section 5.2.2, was determined, where the selection of a "lattice parameter" enabled the degree of lattice order to be chosen. This was necessary in order to define discrete regions of the target corresponding to either ordered, or disordered, carbon in the numerical simulations of the double-layer targets. The lattice parameter is an integer whose minimum and maximum values correspond to the ordered and disordered $\eta - T$ profiles of the target material, respectively. By selecting values of this parameter intermediate to these limits, intermediate $\eta - T$ profiles could be investigated.

The same grid was used for all the simulations and had dimensions 400 μm $\times$ 400 μm $\times$ 200 μm, with each cell of a size of ΔX = ΔY = ΔZ = 1 μm. A total of 2×10^8 macro-particles were injected over the duration of the 725 fs pulse. The side boundaries were defined as transmissive to avoid any potential artificial effects due to the transverse size of the simulation box and the rear boundary was set as reflective to mimic the reflection effect on the fast electrons of the sheath field formed on the target rear surface. The simulation outputs are sampled just after the bulk of the fast electrons have reached the rear boundary; approximately 500 fs after the end of the pulse and therefore the reflected electrons have little effect on the main fast electron transport dynamics.

The fast electron population was injected uniformly at [X, Y, Z] = [0, 0, 0], where they then propagate in the longitudinal direction, defined as the X-direction, over a cone with half-angle equal to 40° (informed by reference [294]). The electrons have an exponential energy distribution, exp(-E_f/kT_f). A 30% laser-to-fast-electron energy conversion efficiency is assumed [295].

Simulations were performed to match the experimental parameters and the results are shown in figure 5.11 (e)-(l). Initially considering the case of the single-layer targets, figures 5.11 (e) and (f) appear to be in good agreement with the experimental measurements in figures 5.11 (a) and (b), respectively. A two-dimensional slice of the fast electron density distribution, sampled at the rear-surface in the [Y-Z] plane, was used to model the evolution of the sheath field and subsequent TNSA protons, using the method first demonstrated in reference [53]. This technique has the following steps: the electric field profile at the target rear is determined via the fast electron density map output from the hybrid-PIC simulations; this is mapped onto a two-dimensional spatial grid of 1000 x 1000 cells, with a cell resolution of 1 μm. The fast electron distribution then expands transversely across the grid, with an initial velocity of $v_\perp = c$ (defined via studies of sheath

expansion for similar laser conditions [308,309]). The value of $v_\perp$ decreases exponentially with time with $1/e = 1.6$ ps, consistent with measurements of sheath expansion detailed in reference [310]. The spatial distribution of the sheath field was measured every 100 fs of its expansion up until 1.2 ps. The magnitude of the field $E_0 G(t)$ increases with the Gaussian temporal profile, $G(t)$, of the laser pulse to a maximum value of E_0 at $t_p = \tau_L$. Thereafter, the field strength follows an exponential decrease with $1/e = 1.6$ ps, as reported in reference [309]. The filaments evolve radially along the grid over this time, gradually merging to form a total electric sheath field $F(x, y, t)$:

$$F(x, y, t) = \sum_{i=1}^{n_s} f_i(x, y, t) \tag{5.5}$$

where n_s is the number of filaments with an initial size $\geq 80\%$ of the maximum filament size. The spatial and temporal evolution of the sheath field magnitude, $E(x, y, t)$ is calculated using:

$$E(x, y, t) = E_0 G(t) F(x, y, t) \tag{5.6}$$

A uniform layer of hydrogen is then defined on the target rear surface and is ionised by the electric field $E(x, y, t)$ in order to produce protons for acceleration. The resulting protons are accelerated in each 100 fs timestep, perpendicular to the local orientation of the sheath. The energy gained by each proton is determined by the magnitude of the local region of the sheath from which it was accelerated. The protons are translated from the target rear surface to a detector by using polar coordinates to extrapolate the local gradients from the ion front surface into angular mapping of the protons. The detector was defined as a 5 cm x 5 cm grid, located 5 cm away from the target, i.e. identical parameters to that of the experiment. The predicted spatial-intensity distributions of the sheath-accelerated proton beams are shown in figures 5.11 (m) and (n). The modelled proton beam distributions are in good qualitative agreement with the experimentally measured proton beams, with D possessing a relatively smooth profile with a small degree of structure at the centre, and VC showing evidence of cusp-like features.

Considering the double-layer targets, there is good agreement in the similarities between the measurements and numerical simulations. The RCF images in figures 5.11 (c) and (d) exhibit a small number of large, cusp-like features when VC is at the target front side, and a larger number of smaller filaments for the opposite scenario. These features are reproduced to a good qualitative degree in figures 5.11 (g) and (h). Strong filamentation

is observed in both orientations of the VC layer, however when it is at the target rear, strong filamentation can be observed over the full 100 μm layer thickness. In contrast, when the VC layer is placed at the front side of the target, filamentation is only observed after a depth of $\sim$ 30 μm due to the low electrical resistivity in the high temperature Spitzer region at the electron source. Thus, a smaller number of filaments are produced before the beam propagates into the D layer. Thus, when the ordered D lattice is located at the target rear side, the strength of the resistively-generated magnetic fields is greatly reduced compared to the case when VC is at the target rear. Therefore, the filaments experience some degree of transverse spreading and merging as they propagate, resulting in fewer larger filaments reaching the rear surface (figure 5.11 (g)), in comparison to the contrasting case in figure 5.11 (h). Thus, although large-scale filamentary structure is most evident in figure 5.11 (c), the number of filaments produced in the corresponding simulation is the lowest of all the target structure scenarios presented. This highlights a limitation of the proton spatial-profile diagnostic: a small number of large, well-defined filaments leads to large modulations in the spatial-profile of the sheath field, which is easily diagnosed via the stacked RCF diagnostic. Conversely, a large number of small filaments in close proximity results in the transverse spreading of the sheath field, in effect reducing the magnitude of any modulations.

In order to quantify and compare the degree of filamentation of the fast electron beam in the simulations with the structure in the measured proton dose, an analysis of the variation in the rear-surface fast electron density from the numerical simulations was performed. This was compared with a similar analysis of the structure measured in the proton spatial-profile. The results of this analysis are shown in figure 5.12. The process of quantifying the degree of filamentation is as follows: the density distribution of the fast electron beam at $X = 200$ μm is transformed into polar coordinates $[r, \theta]$, where $r = 0$ is the beam centre. Radial line-outs are then taken every 1^o in order to extract the electron densities. The root-mean-square deviation (RSMD) with respect to the average beam density is calculated and the average over all angles determined to produce a single quantity, $\bar{S}$. This procedure is repeated for five time steps in the simulation (centered around 1.2 ps). This is to mimic the fact that proton spectroscopy is a time-integrated diagnostic. The final $\bar{S}$ value is the mean of the variation measured at the five sampled time steps. The same approach is applied to quantify the experimental measurements obtained via RCF spectroscopy.

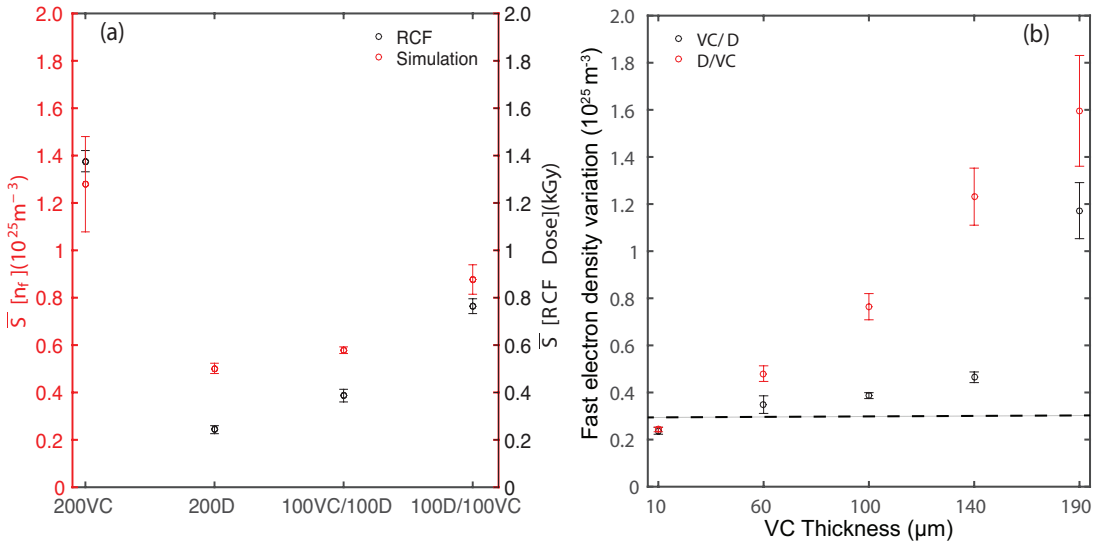

Figure 5.12: (a) Variation in the rear-surface fast electron density in the simulation results and the measured proton dose for the four given target types; (b) Variation in the fast electron density as a function of the thickness of the VC layer, both for the layer at the front and at the rear. The dotted line signifies the point at which filamentary structure is no longer visible. Details of the methodology are given in the text.

The degree of variation in the measured proton dose for the four target types is in good agreement with the degree of fast electron filamentation, obtained from simulation, as shown in figure 5.12 (a). The degree of structure in the experimental proton measurements is clearly correlated with the degree of change in the filamentation predicted in the fast electron transport simulations.

5.3.3 Variation of vitreous carbon layer thickness

The results presented in the previous section demonstrated that, although the growth of self-generated magnetic fields is dependent on position of the VC layer, the onset of resistive filamentation is not. In this section, the sensitivity of the growth of the resistive filamentation instability to thickness of the VC layer is investigated.

A series of simulations were performed for double-layer targets (with identical simulation parameters as in section 5.3.2) where the thickness of the VC layer was varied between $L_{VC} = 10$ μm and 190 μm. The effect of having the VC layer positioned at the front and rear of the target was examined. Firstly, the case where the VC layer is located at the target front surface is considered. The results are shown in figure 5.13. It is observed that as the thickness of the VC layer is increased, from (a) to (e), that the degree of filamentation increases. When the thickness of the VC layer is < 50 μm, the

fast electron transport remains relatively smooth. However, at $L_{VC} \sim 50 - 60$ μm, the onset of filamentation is observed. The level of filamentation increases further as L_{VC} is increased.

The corresponding, modelled proton spatial-intensity distributions, obtained via the two-dimensional, rear surface fast electron density maps are shown in figures 5.13 (p)-(t). The degree of structure present in the proton beam is observed to increase as the thickness of L_{VC} increases and thus, the level of filamentation increases.

Reversing the order of the layers, corresponding simulations were performed with D now located at the target front side. All other parameters remained constant, and the resulting simulation outputs are shown in figure 5.14. In this case, the thickness of L_{VC} is reduced from (a) to (e), resulting in the number and transverse size of the filaments produced increasing with the level of filamentation reduced for $L_{VC} < 60$ μm. The dependence on the VC-layer thickness is not connected to the strong heating at the interaction region in this case, and the differences in the level of filamentation are connected purely to the time-scale required for the resistive filamentation instability to grow.

It is notable that, although the dependence on the thickness of the VC layer is similarly irrespective of its location in the target, there are differences in the size of the filamentary structure depending on whether the VC layer is at the front or the rear side. This is illustrated in figure 5.12 (b), where the values of $\bar{S}$ are typically higher when VC is located at the rear of the target. This is due to the VC layer being located away from the high temperatures at the electron source. Thus, the electrical resistivity in the VC remains relatively high, resulting in strong filamentation occurring over the full thickness of the layer.

Finally, the scenario in which the VC layer is buried within a target, referred to as "sandwiched" between two layers of diamond was investigated. The thickness of the VC was varied between 10 and 100 μm. The results are shown in figure 5.15. In each case, some degree of filamentation is evident, with more distinct filaments present when the thickness of the VC layer is increased. The diamond layer washes out any fine scale filamentary structure at the target rear surface, which (as previously discussed) results in the transverse expansion of the filaments. A transverse magnetic field is induced at the interface between the layers, as shown in figures 5.15 (e)-(h). Previous studies involving buried layers of materials with significantly different atomic numbers [311, 312] have concluded that significant transverse spreading of the fast electron beam can be produced by strong

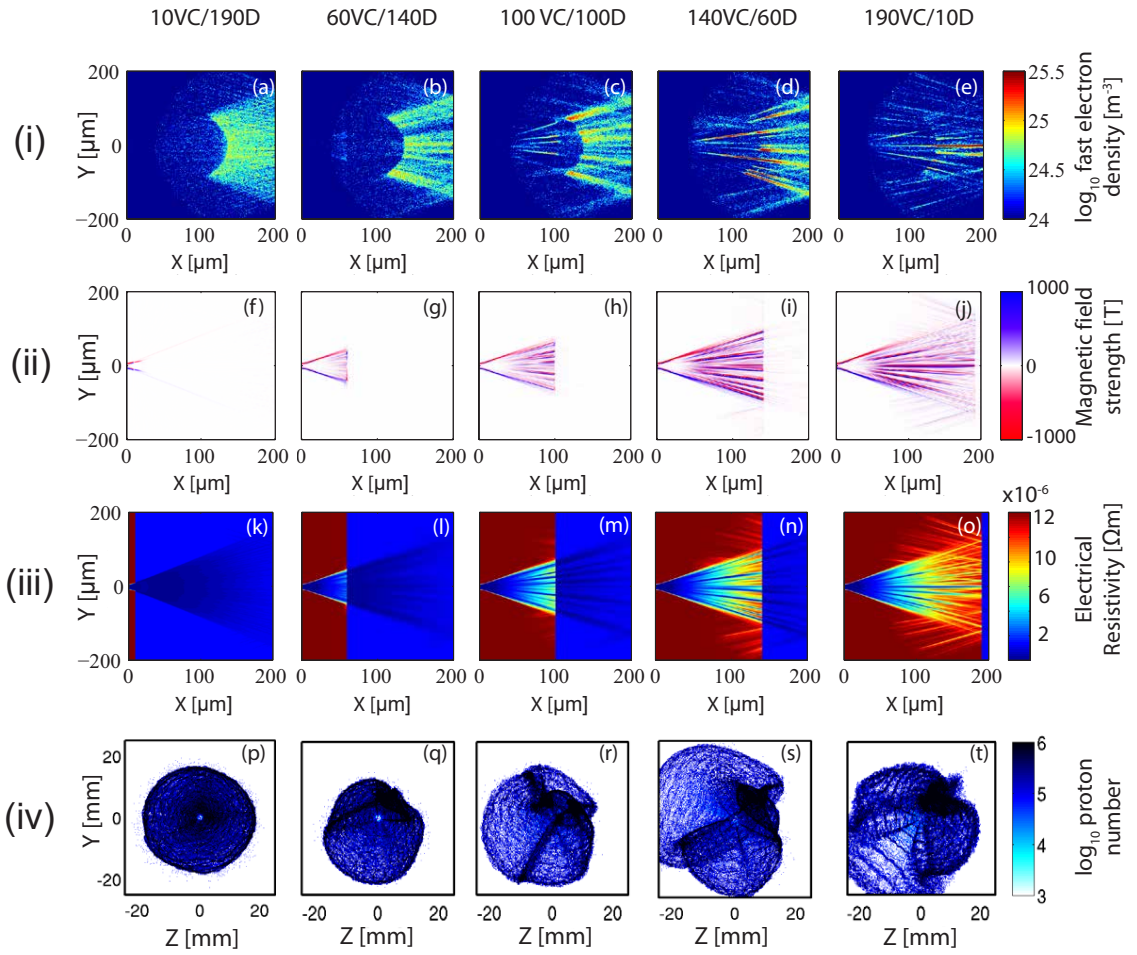

Figure 5.13: Hybrid-PIC simulation results for double layer targets with VC as the front layer and D as the rear. Row (i): Fast electron density maps, in the [X-Y] mid-plane, for: (a) L_{VC}=10 μm; (b) L_{VC}=50 μm; (c) L_{VC}=100 μm; (d) L_{VC}=140 μm; (e) L_{VC}=190 μm; Row (ii): Corresponding 2D maps of the magnetic flux density (B_z component); Row (iii): Corresponding 2D maps of electrical resistivity; Row (iv): Corresponding modelled proton spatial-intensity maps, calculated using the rear-side fast electron density maps obtained from (a)-(d).

field generation at the interface, i.e. at the resistivity boundary. However, the magnitude of this field is measured to be lower than the resistively-generated field generated around the filaments and the azimuthal field produced at the interaction region. Furthermore, the beam divergence and transport does not appear to be altered as a result of the interface field.

5.3.4 Resistive instability growth rate

Finally, a linear resistivity analysis, based on the work of Gremillet *et al.* [117] and Robinson *et al.* [148] was performed in order to explain the dependency of the VC layer thickness on the degree of filamentation observed in the simulations. This analysis estimated the

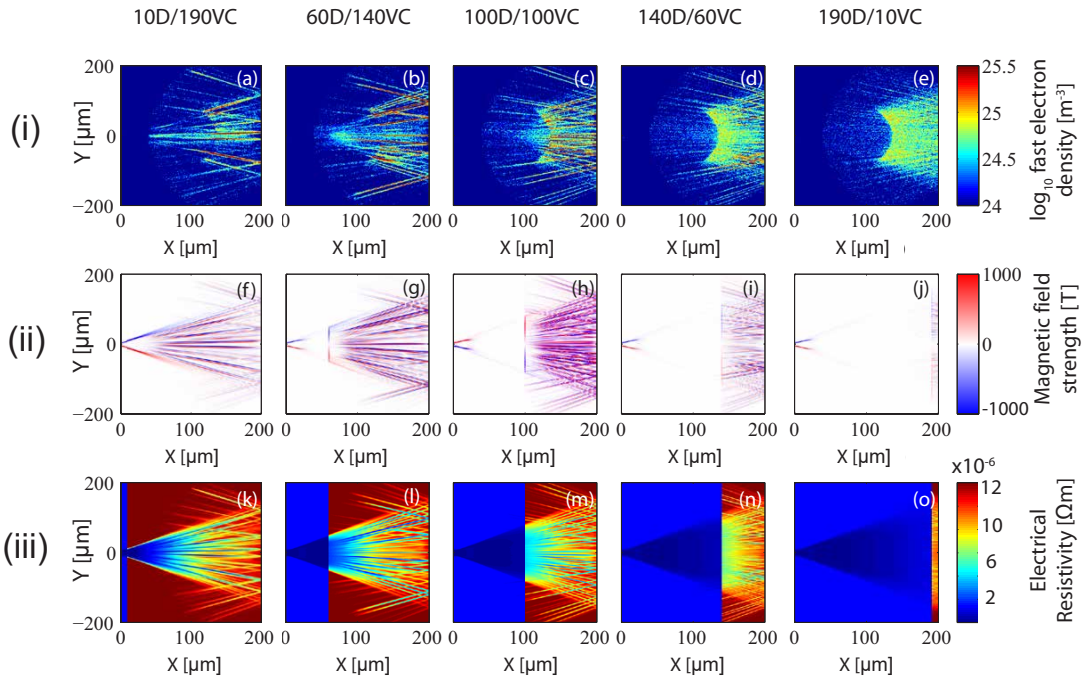

Figure 5.14: Hybrid-PIC simulation results for double layer targets with D as the front layer and VC as the rear. Row (i): Fast electron density maps , in the [X-Y] mid-plane, for: (a) L_{VC}=10 μm; (b) L_{VC}=50 μm; (c) L_{VC}=100 μm; (d) L_{VC}=140 μm; (e) L_{VC}=190 μm; Row (ii): Corresponding 2D maps of the magnetic flux density (B_z component); Row (iii): Corresponding 2D maps of electrical resistivity.

growth rate of the resistive filamentation instability in both D and VC, both as a function of wavenumber and the background temperature of the target. Thus, the seemingly independent nature of the position of the VC layer within the target was also investigated. The model made several simplifying assumptions for ease-of-use, including uniformity of the background electrical resistivity and does not take into account the resistivity evolution, as discussed in section 5.2 and references [116] and [115]. Even with these assumptions, the analysis is still useful in providing an estimate of the local growth rate of the resistive filamentation instability in the two carbon allotropes under consideration.

The model approach is as follows: the fast electrons are given a fluid description, via the linearised fluid equations presented in reference [148]. The beam filamentation has an exponentially growing mode, $\exp(\Gamma t)$, where t is the time and Γ is the growth rate of the resistive filamentation, given by [148]:

$$\Gamma = \left(\frac{\alpha}{2} + \sqrt{D}\right)^{1/3} - \left(\sqrt{D} - \frac{\alpha}{2}\right)^{1/3} \tag{5.7}$$

where $D = (\beta/3)^3 + (\alpha/2)^2$, $\alpha = e^2 u_{x,0}^2 n_{f,0} k_p^2 \eta / \gamma m_e$, $\beta = k_p^2 e T_{f,\perp} / \gamma m_e$ and $k_p = 2\pi/\lambda$

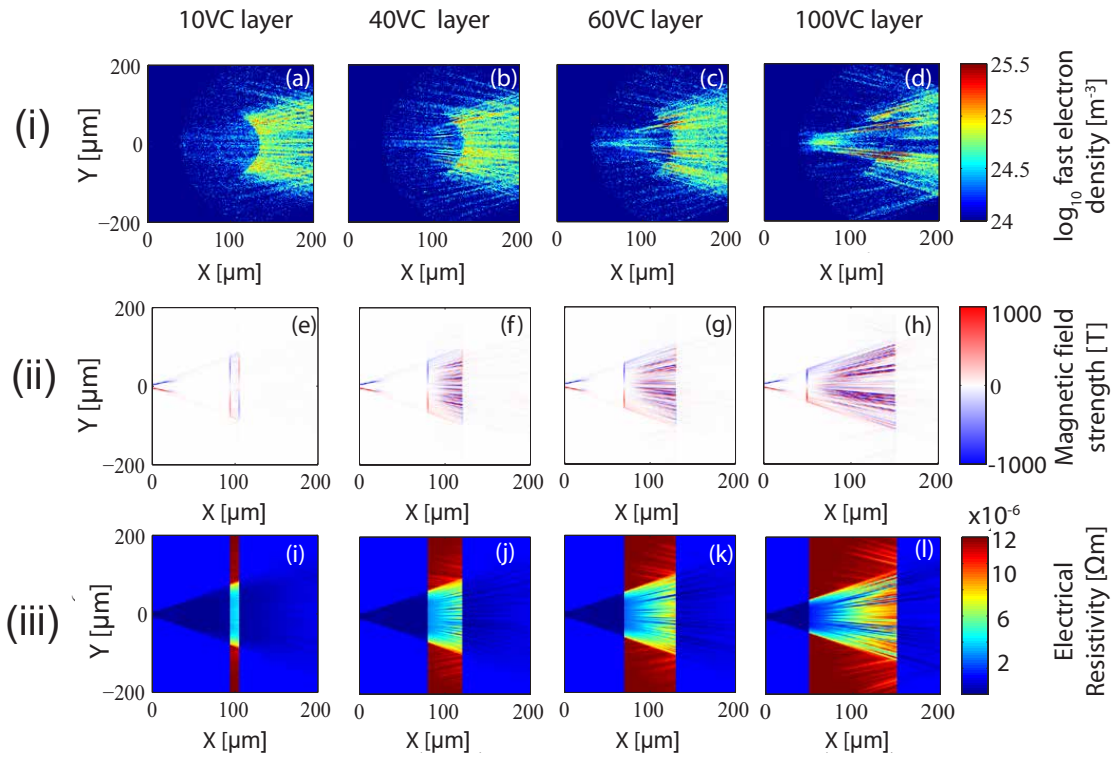

Figure 5.15: Hybrid-PIC simulation results for a triple layer target comprising a VC layer at the centre of a D target, with overall length L=200 μm: Row (i) Fast electron density maps, in the [X-Y] mid-plane; Row (ii) Corresponding 2D map of the magnetic flux density (B_z component); Row (iii) Corresponding 2D map of electrical resistivity.

is the wavenumber of the perturbation and $T_{f,\perp}$ is the transverse temperature of the beam. The fast electron density, $n_{f,0}$, and velocity, $u_{x,0}$, are estimated as 10^{26} m^{-3} and c, respectively. The importance of the transverse temperature on the growth of the resistive filamentation instability was discussed in section 2.7.4 and in reference [152].

Figure 5.16 shows the results of the linear resistivity analysis. Figure 5.16 (a) highlights the growth of the instability as a function of k_p at three example $T_{f,\perp}$ values for D and VC. The magnitude of η, in equation 5.7, for D and VC was determined by calculating the average η value between 1 and 50 eV, i.e. within the low-temperature range for carbon. The values were determined to be 4×10^{-6} Ωm and 2×10^{-7} Ωm, respectively. The resistive filamentation growth rate is approximately an order of magnitude higher in VC than in D, over the full range of parameters explored. Thus, it is shown that the beam will filament relatively faster in VC compared to D. The e-folding time (the time for which the filamentation grows by a factor equal to Euler's number) for VC varies from tens to hundreds of femtoseconds across the range of k_p values considered. The stated minimum thickness of VC for visible filamentation to be present ($\sim$ 60 μm) corresponds

to a propagation time of ~ 200 fs for a relativistic electron beam. Thus, several e-foldings may occur in the timescale over which the beam traverses the VC layer, in agreement for the conditions in which strong fast electron beam filamentation will occur. The growth of resistive filamentation as a function of $T_{f,\perp}$ was then investigated (shown in figure 5.16 (b)). The results show that the growth rate of resistive filamentation is significantly larger for a large fraction of the temperature range from ~ 1 eV to ~ 80 eV, the start of the Spitzer regime of resistivity. Lastly, figure 5.16 (c) shows an example two-dimensional map of electron temperature within a D target, for the same simulation parameters employed throughout this chapter. Figure 5.16 (c) highlights that, excluding the first ~ 50 μm of the target where Spitzer resistivity regime dominates due to the strong heating by the laser, the majority of the remainder of the target has a temperature in the range of $1 \text{ eV} \leqslant T_e \leqslant 80$ eV. The resistivity of VC is high over this temperature range, as illustrated in figure 5.10 (b), and thus, it can be inferred that the location of the VC layer is inconsequential to the degree of filamentation.

It should be noted that the focus of this analysis is the growth rate of the resistive filamentation instability, and the influence of other beam transport instabilities (see section 2.7.4) have been neglected. For example, the ionisation instability has been shown to be responsible for macroscopic transverse filamentation of fast electron beams in previous studies performed for insulator targets [313,314]. Thus, in the scenarios studied, ionisation would be required to provide free electrons for the return current. Since the targets in this investigation are comprised of different allotropes of the same chemical element, the ionisation potential across the target remains the same, irrespective of the permutation of the VC layer position or thickness. Therefore, the filamentation rate across D and VC cannot be explained via the ionisation instability. The main parameter varying between D and VC is the $\eta - T$ profile, which the resistive filamentation instability is particularly sensitive to. Thus, resistive filamentation is considered to be the prime driver for the observed filamentation findings.

5.4 Conclusions

The influence of self-generated resistive magnetic fields, and specifically the role of low temperature resistivity in defining magnetic fields has been investigated for the example materials, lithium and silicon. The results demonstrate that the transport of the fast

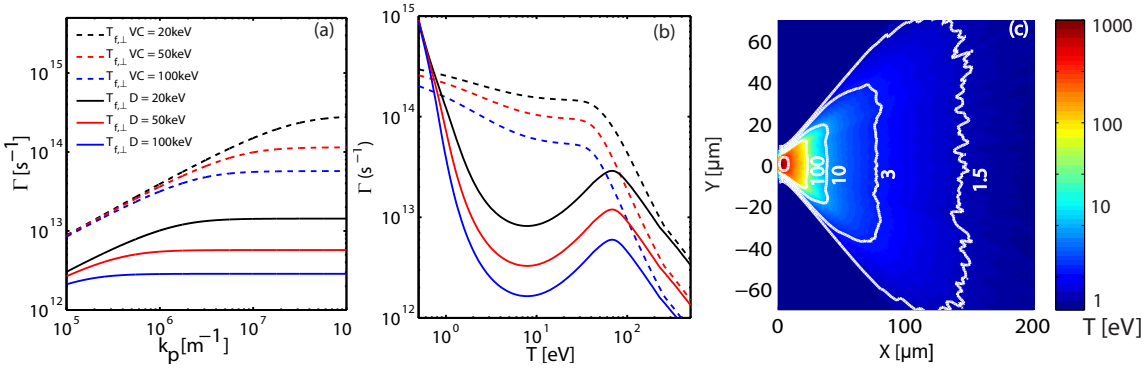

Figure 5.16: Resistive instability growth rate as a function of (a) wave number and (b) temperature, for VC and D, at three example beam transverse temperatures (as indicated). The dashed lines correspond to VC and the solid lines are for D; (c) Example 2D temperature map in the [X-Y] mid-plane at 1.2 ps. Contours are drawn for isothermals corresponding to 1.5, 3, 10 and 100 eV.

electron currents generated is strongly influenced by the low-temperature $\eta - T$ profile. In the case of lithium, an example metal, the magnitude of the electrical resistivity peak determines the growth rate of the resistive filamentation instability. This results in enhanced structure in the fast electron transport pattern at the rear surface of the target, and thus the beam of accelerated protons.

For semiconductors (in this case silicon) the size of the bandgap results in the presence of a parabolic dip in the $\eta - T$ profile. This leads to the formation of annular structure in the beam. It has been demonstrated that, as the minima of the dip and thus, the degree of lattice disorder, is increased, the fast electron transport pattern is observed to change from that of an annular structure to a filamented beam. It was also demonstrated that the temperature at which the dip occurs significantly influences the diameter of the ring. The diameter is inversely proportional to the temperature at which the reversal in the resistivity gradient occurs.

In addition, a discussion on the feasibility of scaling interactions of this kind up to those employed in FI scenarios is presented. The potential application of employing a laser generated annular fast electron beam for the purpose of achieving ignition is explored, and the engineering considerations for such a scheme briefly discussed.

Furthermore, the role of lattice structure in defining the growth of self-generated magnetic fields and the onset of the resistive filamentation instability in single-, and multi-layered targets comprised of ordered and disordered allotropes of carbon has been investigated, both experimentally and numerically. Experimental measurements of the TNSA-accelerated proton beam, accelerated from single-layer carbon targets, were found to be

consistent with measurements previously obtained via the same stacked RCF diagnostic, using the Vulcan laser, with comparable experimental parameters [54].

The sensitivity of the onset of fast electron filamentation to the thickness of the vitreous carbon layer and its position were investigated. It was found that the growth of the resistive filamentation instability was strongly dependent on the thickness of vitreous carbon present, and that strong filamentation could be observed when it was of the order of $\gtrsim 60$ μm. This was consistent with the predictions of a linear resistive analysis, which indicated that a propagation distance of 60 μm in vitreous carbon corresponded to several e-folding times, consistent with the conditions for strong fast electron beam filamentation. The linear resistivity analysis also accounted for the differences in resistivity between vitreous carbon and diamond, and it was shown that the growth rate of the resistive filamentation instability was an order of magnitude greater for vitreous carbon than diamond for a range of spatial frequencies of the perturbations of the filamentation instability. It was also shown that the magnitude of resistive filamentation in vitreous carbon is significantly higher than for diamond for the majority of the low-temperature regime (~ 1 eV to ~ 80 eV). Finally, the location of the vitreous carbon layer was found to be inconsequential to the degree of filamentation and, outwith the first ~ 50 μm of the target, filamented electron transport is produced provided the thickness of the vitreous carbon layer is $\gtrsim 60$ μm.

The results presented in this chapter demonstrate the defining role that cold material properties play on the transport of fast electrons produced in laser-solid interactions. The properties of fast electron beams resulting from the growth of self-generated magnetic fields and associated resistive instabilities has a key impact on defining the properties of ion acceleration deriving from the TNSA scheme, and thus, the potential use of laser-driven ions for applications, including FI fusion. The relevance of the generation of magnetic fields via the transport and dynamics of energetic electrons, in states of WDM, to astronomical scenarios will be discussed further in **Chapter 7**.

Chapter 6

Generation of astrophysically relevant magnetic field structures in expanding foils

6.1 Introduction

As discussed in **Chapter 3**, the generation of strong magnetic fields is prevalent in numerous scenarios and systems across the known universe, commonly associated with stellar prominences: filaments of matter extending into stellar atmospheres along magnetic field lines related to coronal mass ejections [182]; accretion mechanisms and the dynamo mechanism. The magnetic fields required for the formation of phenomena such as plasma jets or collisionless shocks may be initially present, for example in supernova remnants or young galaxies, or they may be self-generated in systems such as inward-flowing accretion mechanisms [45]. Another known mechanism resulting in the self-generation of magnetic fields, even in the absence of a seed field, is the Weibel instability. In section 2.7.3, the growth of the Weibel instability as a result of two counter-propagating currents is discussed in the context of fast electron propagation and a counter-propagating, neutralising return current. In this scenario, small modulations in the density profile of one of the populations leads to perturbations in the local self-generated magnetic field, resulting in the filamentation of the population of fast electrons. However, Weibel [129] also considered the case of the growth of an instability driven by velocity anisotropies in a fast electron beam, propagating into a background of a resting ion population. As in the case

of two counter-propagating electron beams, the resultant fast electron transport pattern is filamented. The scenario of a collisionless, relativistic electron population propagating into a static ion population is particularly relevant for laser-solid interaction physics (as discussed in section 2.6.3).

This chapter focuses on two cases of strong magnetic field generation in intense laser-solid interactions with thin foils which expand to near-critical densities during the interaction. These are: (i) the generation of a directed jet of relativistic electrons via direct acceleration by laser light transmitted through an ultrathin foil, and the subsequent collimation by an azimuthal magnetic field; and (ii) the role played by the Weibel instability in the growth of self-generated magnetic fields. Both of these cases are relevant to modelling relativistic plasma astrophysics phenomena.

(i) Relativistic plasma jets

Directed jets of relativistic plasma are prevalent in many astrophysical systems, including young stellar objects (YSOs) [56], gamma ray bursts (GRBs) [204] and active galactic nuclei (AGNs) [55]. Such jets are associated with compact central objects, surrounded by a strongly magnetised accretion disk. Jets represent some of the largest continuous structures in the observable universe, with propagation distances of the order of 10^6 parsecs observed from AGNs [315], whilst YSOs launch jets which are considerably smaller (0.01 to 1 pc). These phenomena can be arranged into several classes according to their properties: AGN jets are described as highly relativistic with velocities approaching $\sim 0.99c$ [316], whilst the velocity of YSO jets have been measured to be in the region of hundreds of km/s. Despite the vast differences between the physical properties of jets arising from the multitude of astronomical sources, they all share common properties; they are highly-collimated and, in most cases, symmetrical on either side of the accretion disk (as shown in figure 6.1). They originate in dense objects, and are associated with magnetic fields and the accretion of matter onto the central object via an accretion disk. Hence a similar launching mechanism for all astrophysical jets has been postulated, as discussed in **Chapter 3**.

The lifetime of astrophysical jets presents an issue for the observation and measurement of the evolution of such structures: shorter-lived YSO jets have typical lifetimes of 10,000 years [315], whilst jets launched from AGNs propagate for $\sim 10^7$-10^8 years. Furthermore, complications including extinction due to interstellar gas clouds can also obscure measurements. Laboratory-produced jets, generated in laser-driven plasma flows, may enable

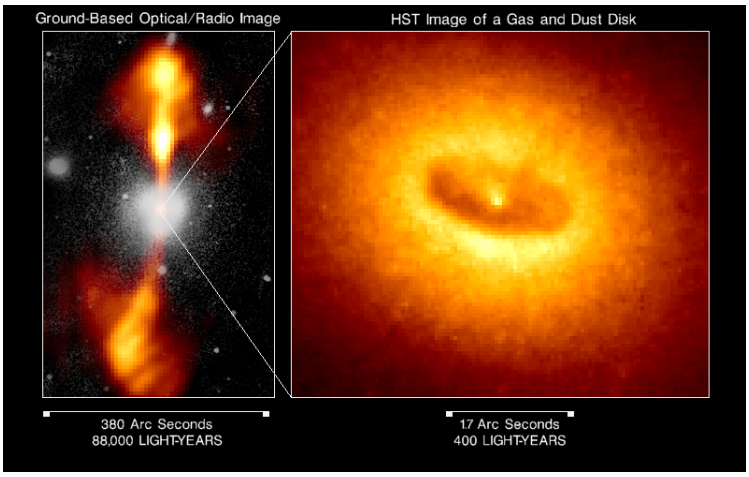

Figure 6.1: A Hubble Space Telescope (HST) and ground-based view of the core of galaxy NGC 4261. A bi-polar jet, emanating to ~ 70000 *light years from the galactic core, is visible in the radio image. Credit HST/NASA.*

astrophysical phenomena to be reproduced on far smaller temporal and spatial scales, and with a wide variety of diagnostic tools available to obtain relevant information on the underlying physics. Numerical simulations of such phenomena are similarly problematic; the non-linear and widely-varying scale of such systems mean that a full numerical investigation of their dynamics is beyond the capability of current computational techniques [62].

Laser-solid interaction experiments have previously been employed as laboratory analogues of astrophysical phenomena. For example, supersonic, collimated jets of plasma have been observed from high-power laser interactions with solid foil targets [317, 318]. The jets produced in these studies were formed via the radiative cooling of the particles accelerated in the interaction: Mizuta *et al.* [223] demonstrated that the effect of radiating heat from the region of an accelerated ion population enhances the collimation of the beam. Other mechanisms for the formation of laboratory jets include the ablation of a target foil driving a shock wave into the resultant plasma, producing a collimated jet at the target rear [201]. Furthermore, the onset of RSIT in expanding ultrathin foils (see section 2.9.3) has been shown to drive the formation of a jet of superthermal electrons [34, 253, 319]. In this concept, electrons are directly accelerated by a fraction of the transmitted pulse, and collimated by a global self-generated, azimuthal magnetic field. The characterisation of such jet formation will be the focus of the first section of this chapter (section 6.2).

(ii) Weibel instability-induced magnetic fields

The growth of the Weibel instability (see section 2.7.3) in laser-induced plasma expansion scenarios has been investigated [45, 141]. It has been suggested to play an important role in the generation of magnetic fields and the acceleration of particles in relativistic shocks [320,321]. The role of the WI in the generation of strong, sustained magnetic fields supporting astrophysical jets has also been discussed previously [141]. Recent studies have focused on the growth of WI-generated magnetic fields [136, 144, 322]. The second half of this chapter (section 6.4) features an experimental and numerical investigation exploring the role of the WI on the filamentation of relativistic electron beams produced in intense laser-foil interactions, and the subsequent influence on proton acceleration. The sensitivity of the growth of the WI to the degree of target decompression (i.e. density gradients) is also investigated, and a transition from large-scale, azimuthal magnetic field structures, to filamented, smaller-scale fields is observed.

6.2 Plasma jet formation in ultrathin foils undergoing transparency

The focus of the work reported in this section is the generation of relativistic electron jets from ultrathin (tens to hundreds of nanometres thick) foils. The interaction of intense laser pulses with ultrathin foils is investigated widely in the context of new mechanisms for the acceleration of ions based on laser radiation pressure. If the target foil is thin enough, then it can become relativistically transparent when heated and expanded by the laser pulse (see section 2.9.3).

During the process of transparency a population of superthermal electrons can be directly accelerated by the laser pulse as it propagates through the target [34]. These electrons are collimated via the presence of a self-generated azimuthal magnetic field, generated via the Biermann battery mechanism (see section 2.7.2), that bounds the plasma expanding from the rear surface of the target. This process occurs as follows: the intense laser pulse possesses a temporal and spatial intensity profile (see section 4.2). The interaction of the leading edge of the pulse with a foil heats electrons, inducing an expansion of the plasma. Ions are accelerated from the target rear via the TNSA mechanism (see section 2.9.1). As the intensity of the pulse increases with time, the radiation pressure of the laser begins to dominate, driving the plasma electrons inwards to higher energies.

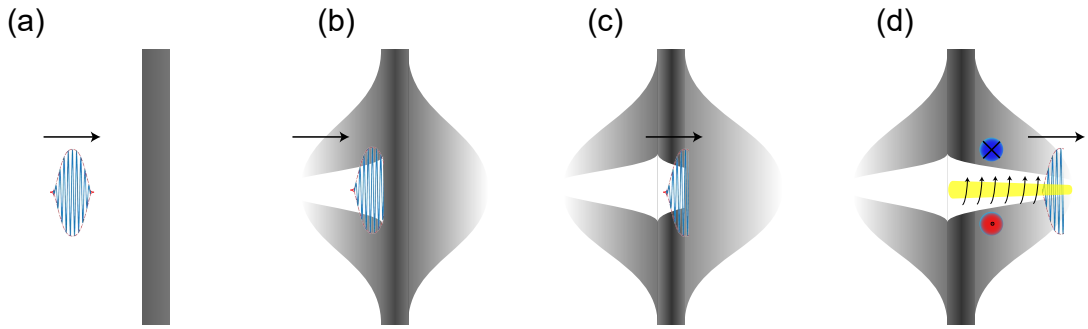

Figure 6.2: Schematic of the process of the formation of a relativistic electron jet upon the onset of RSIT. (a) An intense laser pulse is incident on the front surface of a solid density foil; (b) The foil is heated and expands to near-critical density. As the intensity of the pulse increases with time, electrons are driven to relativistic energies; (c) For a sufficiently thin target, the combination of target expansion and electron relativistic mass increase results in the target undergoing RSIT, and a fraction of the pulse is transmitted; (d) The transmitted portion of the pulse directly accelerates electrons in its vicinity. A self-generated magnetic field is produced via the Biermann battery mechanism. This confines the electrons in a plasma channel.

For a suffiently thin target, the combination of target expansion and electron heating to high energies results in the target becoming relativistically transparent to the laser pulse (see section 2.9.3). Volumetric acceleration of the plasma electrons in the vicinity of the transmitted portion of the laser pulse then occurs. The electrons are confined in a plasma channel, collimated by the self-generation of a quasi-static azimuthal magnetic field via the Biermann battery mechanism. The confined electrons co-propagate with the laser, forming a relativistic electron jet, resulting in electron energies significantly higher than the surrounding plasma. This process is detailed schematically in figure 6.2.

Numerical simulations, using the EPOCH PIC code in 2D3V (previously discussed in section 4.4) [271], demonstrate the formation of a relativistic electron jet in intense laser-foil interactions. Example findings from these simulations are shown in figure 6.3. It was observed, as previously described, that the onset of RSIT was accompanied by the formation of a jet of superthermal electrons, with kinetic energies much greater than that of the background electron population (figure 6.3 (b)). This jet extends into the expanding plasma layers. The jet is supported by a self-generated, azimuthal magnetic field that acts to collimate as it extends out to the plasma boundary (figure 6.3 (c)). Beyond this point, the jet is susceptible to hosing-like instabilities, due to a lack of background electrons from which to draw a return current.

Due to co-propagation of a significant fraction of the transmitted laser pulse with the jet, the electrons comprising this feature experience a direct acceleration over the distance which they co-propagate, resulting in electron energies higher than the background value,

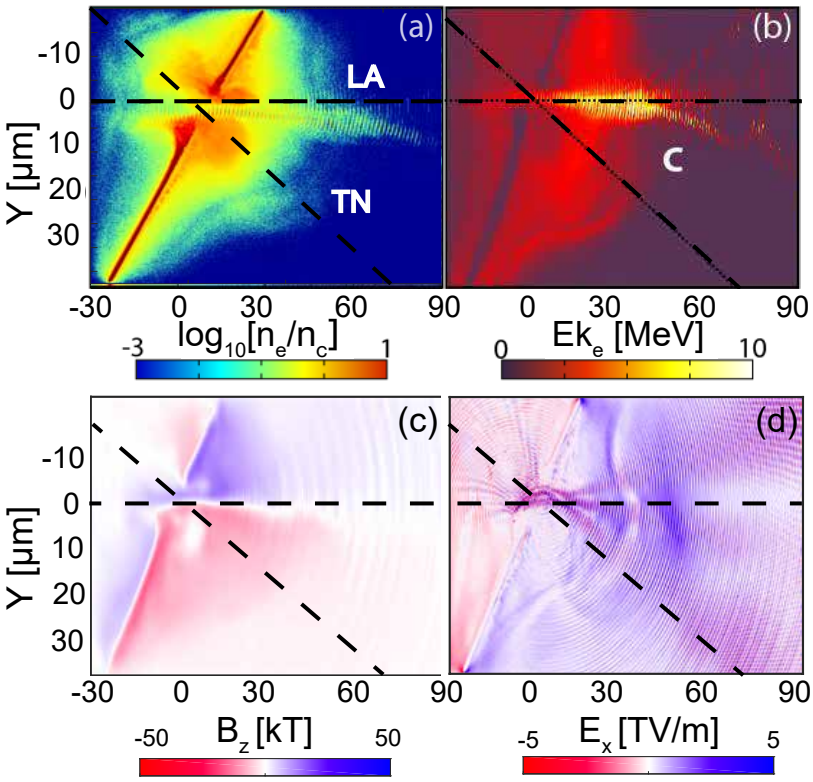

*Figure 6.3: Two dimensional PIC simulation results, showing (a) The electron density; (b) The kinetic energy of the electron population, (c) The magnetic field strength in the region of the rear of the target, and; (d) The longitudinal electric field strength. Feature **C** represents the relativistic electron jet.*

by approximately a factor of 2. The high energy electrons in the jet then couple additional energy to the protons in its vicinity, enhancing the maximum proton energy. This occurs because the longitudinal electrostatic field is enhanced in the region of the jet, as shown in figure 6.3 (d).

It is not possible to directly observe the jet in an experiment. However, evidence of jet formation was noted in measurements of the plasma expansion made using a transverse optical probe, as shown in figure 6.4. An optical probe measurement of the rear-surface plasma expansion for an l =40 nm Al target is shown in figure 6.4 (b). A feature consistent with the late time remnant of an electron jet is observed and labelled **C**. Additional evidence, in the form of spatial-intensity distributions of proton beams obtained from two example aluminium targets, of thickness l = 10 and l = 40 nm, is also shown in figure 6.4 (c) and (d) [34]. Both targets were irradiated at an incidence angle of 30° from the target normal in order to angularly separate proton populations directed along laser and target normal axes, as marked on the figure. Three separate populations of

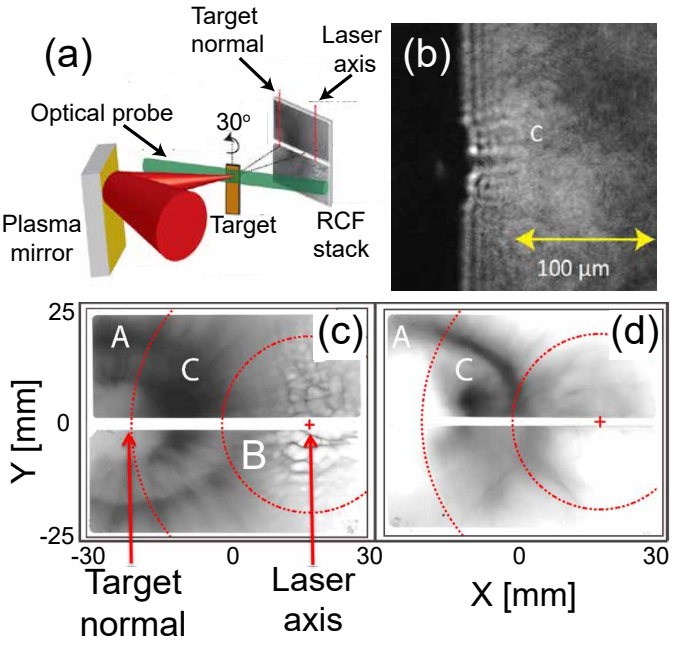

*Figure 6.4: (a) Schematic illustrating the experimental arrangement; (b) Example optical probe image of rear-surface plasma expansion for a $l = 40$ nm target, 10 ps after the interaction. A feature consistent with a channel, and associated jet formation is shown (feature **C**); (c) Example measured spatial-intensity distributions of the beam of accelerated protons from a $l = 10$ nm thick aluminium target undergoing relativistic induced transparency; (d) Same, but for a $l = 40$ nm thick target. The salient features are labelled as: (**A**) proton ring distribution arising from a buffered sheath acceleration process [193]; (**B**) Instability-driven filamentation of the proton distribution (discussed in section 6.4); and (**C**) a low-divergence, high energy proton component consistent with a relativistic electron jet.*

accelerated protons are observed and interpreted with reference to detailed simulations using the EPOCH PIC code. The first feature, denoted **A**, is an annular distribution of low-energy, radially deflected, sheath accelerated protons, driven from the laser focal region during the hole-boring phase of RPA. This is discussed in detail in Padda *et al.* [197] and Powell *et al.* [34,323]. The bubble-like structures observed in population **B** have been postulated to arise from Rayleigh-Taylor-like instabilities during the RPA phase of the interaction [44, 159, 324]. An alternative explanation for the formation of these bubbles, arising from the WI will be presented in the second half of this chapter (section 6.4). However, it is feature **C** that is of direct relevance to the topic of this section. Population **C** is a high energy, low divergence proton component directed at an angle between target normal and laser axis. This feature occurs for the target expansion conditions for which the remnants of the plasma jet are observed in the transverse optical probe, and is therefore linked to the physics of the jet. The direction of this component was observed to vary on a shot-to-shot basis, consistent with hosing of the jet.

The investigation laid out in the following sections builds upon the work reported in Powell *et al.* [34] and King *et al.* [253], and aims to characterise the properties of this electron jet, and its dependency on the onset of RSIT, through variation of the target foil thickness. The time at which RSIT occurs is dependent on the target areal density, as previously discussed in section 2.4.3. It was observed, in PIC simulations that the onset of RSIT is crucial to jet formation, and hence a degree of target decompression is required. However, excessive target expansion leads to numerous relativistic effects (as discussed in section 2.4.2), and jet formation is prevented, or the energy transfer to electrons via direct acceleration is minimised.

It should be noted that although the case presented in **Chapter 5** also featured a dense current of propagating electrons, collimated by an azimuthal magnetic field, the fundamental physical processes involved are quite different. The previous case involved solids which were of the order of hundreds of microns thick. In that case, the laser pulse does not propagate beyond the front surface. By contrast, for the physics discussed this chapter, the electron jet under consideration is directly driven by the laser pulse as it propagates through the target undergoing RSIT. Furthermore, the targets employed are approximately four orders of magnitude thinner than in the previous chapter, and thus are subject to a high level of heating over the target volume (termed "volumetric heating"). Upon the onset of RSIT, electrons throughout the target volume that the laser pulse interacts within undergo direct acceleration, enhancing their energy. The electrons stream through a cloud of energetic, expanding ions, influencing their motion and acceleration.

Furthermore, despite both this investigation and the results presented in section 6.4 being concerned with the growth of magnetic fields in ultra-thin target (thicknesses on the scale of 10-100 nm) it should be stated that the driver for magnetic field generation differs for each case. Gode *et al.* [144] demonstrates the influence of target decompression on the driving mechanism of magnetic field growth. In section 6.2, the level of target decompression is reduced by increasing the target thickness employed and the growth of magnetic fields is governed by the large-scale, global Biermann battery mechanism [136]. In section 6.4, the targets employed are of thicknesses 10-40 nm. In this scenario, a transition from Biermann battery to WI-governed magnetic fields is observed as the target thickness is decreased, and the associated level of plasma expansion is increased.

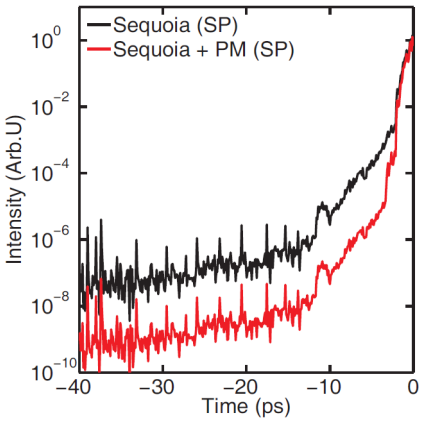

Figure 6.5: Third order cross-correlator measurement of the rising edge profile of the laser pulse (black). Modelled temporal intensity contrast enhancement due to the plasma mirror (red).

6.2.1 Experimental techniques specific to this investigation

The Vulcan Petawatt laser (see section 4.2.8), delivering P-polarised pulses with a central wavelength equal to 1.053 μm, duration (900±100) fs and energy (210±40) J was used in this study. The beam was focused using an F/3 OAP to a 3 μm diameter (FWHM) spot, with ∼30% of the pulse energy contained within the area defined by the FWHM, resulting in a calculated peak intensity of $\sim(3\pm2)\times10^{20}$ Wcm^{-2}, at the front side of the target sample. A planar plasma mirror was employed for contrast enhancement (see section 4.2.5). Figure 6.5 shows the measured temporal intensity contrast and modelled enhancement via the utilisation of a plasma mirror [34]. The inherent pulse contrast was diagnosed by a third order cross-correlator measuring low-power pulses without a plasma mirror present. The enhancement of the temporal intensity contrast could not be measured using this same method due to the requirement of full power pulses to ionise the plasma optics. Thus, experimental characterisation of the plasma mirror reflectivity were employed to enable modelling of the enhancement. Figure 6.6 (a) illustrates the experimental setup.

The targets employed were thin planar plastic (CH) foils, with thicknesses, l, in the range 40-1500 nm. They were irradiated at 30° with respect to the target normal, such that proton beam components directed along the laser and target normal axes could be spatially resolved using the stacked RCF detector (see section 4.3.2). This diagnostic was located 5 cm downstream, shown in figure 6.6 (a). Layers of imaging plate (see section 4.3.3) were interleaved towards the rear of the RCF stack, in order to characterise the electron acceleration.

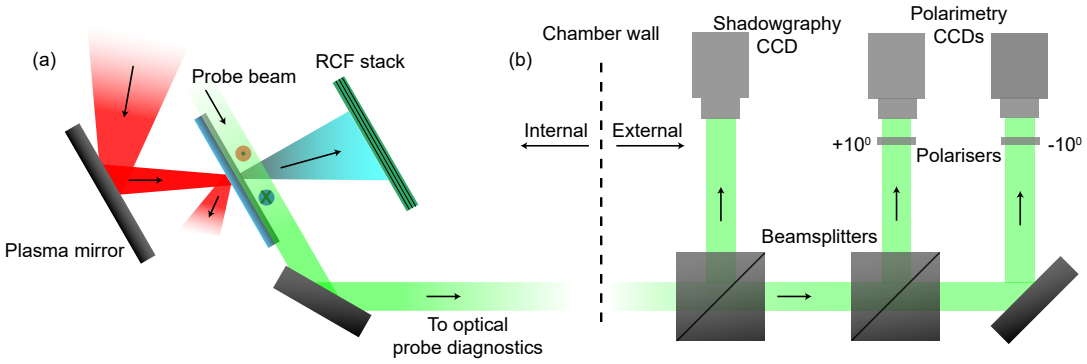

Figure 6.6: (a) Schematic of experimental setup employed in the experimental campaign. The drive-pulse was focused by an F/3 OAP, and reflected off a plasma mirror onto the target foils. The spatial-intensity distribution of the beam of accelerated protons was measured using a stacked RCF diagnostic. Shadowgraphy and polarimetry measurements were made using a frequency-doubled pick-off from the main pulse; (b) Post-target probe diagnostic schematic. The polarimetry CCDs were Andor Neo cameras, whilst the shadowgraphy CCD was a Starlight Trius SX35 camera.

The main diagnostic employed for the characterisation of the electron jet and the collimating magnetic field structures was a transverse optical probe setup. This consisted of shadowgraphy, and polarimetry imaging lines (see section 4.3.4). The optical probe was produced via a pick-off from the main TAP pulse, after the final turning mirror, inside the vacuum chamber. This was then frequency-doubled ($2\omega = 525$ nm). Following this, the probe beam was split into two orthogonal components in order to achieve measurements in the horizontal and vertical planes of the target rear. The two transverse probes were then directed towards the target, as shown in figure 6.7. The spatial resolution of the probe was of the order of two-to-three microns, as determined by the optical system. The temporal separation between the beams was varied, with picosecond resolution, via the use of independent timing slides. Thus, the expansion of the jet could be characterised on the picosecond timescale of its formation. Timing was characterised, intially, through the use of a fast diode and scope, enabling temporal characterisation on timescales of hundreds of picoseconds. A streak camera was then utilised to enable characterisation on the picosecond timescale.

The transverse probe results presented in the following sections come from the horizontal probe line. There were difficulties in implementing the vertical probe. Due to the high magnification and relatively small field-of-view of the imaging lines, any small angle in the target orientation renders the diagnostic unusable, despite extremely precise target manufacture. This was more prevalent in the employment of the vertical probe than the horizontal as a rigorous pre-alignment procedure was employed to guarantee precise

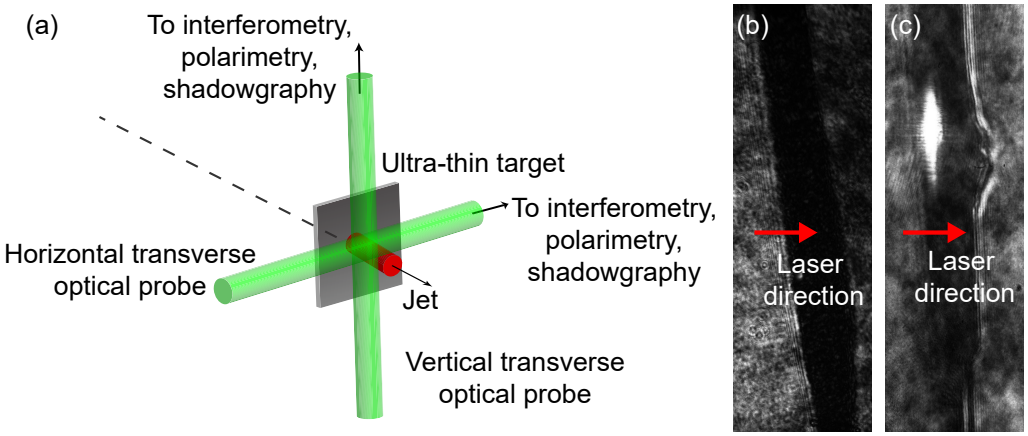

Figure 6.7: (a) Schematic of transverse optical probe imaging lines. The probe beams were produced via a pick-off from the main pulse after the final turning mirror. The frequency-doubled pulse was then split into orthogonal components and directed across the target rear surface; (b) Example shadowgraphy image obtained via the horizontal probe line, showing plasma expansion of the target rear side; (c) Example shadowgraphy image, obtained from the same shot as (b), but for the vertical probe line. No expansion is visible due to masking of the data via warping of the target.

orientation of the target. However, rotation of the target angle was only possible in the horizontal plane, thus any warps or misalignments in the vertical were unable to be corrected. Figures 6.7 (b) and (c) demonstrate the comparison between the horizontal and vertical lines, respectively, and the effect of probing along the rear surface of a warped target.

The polarimetry measurements were obtained via a two-channel setup (as described in section 4.3.4), where the values of the polarisers were set at $\pm 10°$, in order to simplify analysis post-experiment. The polarisers employed were all calibrated using a reference Glan-Laser polariser, set to allow only light polarised in the same plane as the TAP pulse pass. The process of converting the measured intensities in each camera was complicated by the absence of the complimentary measurements from the interferometry diagnostic. The same process as laid out in section 4.3.4 was followed until the stage where the Faraday rotation measurement was calculated, as demonstrated in figure 4.15 (d).

Due to difficulties implementing an interferometry diagnostic to measure electron densities, the electron density encountered by the probe was calculated to be $n_e \sim 0.1\ n_c$. Rather than performing the Abel inversion process with measured electron densities, the magnetic field strength was determined via the following process: the extent of the plasma through which the the probe pulse propagated was measured via an assumption of the cylindrical symmetry of the expanding plasma and the strength of the magnetic field distribution was

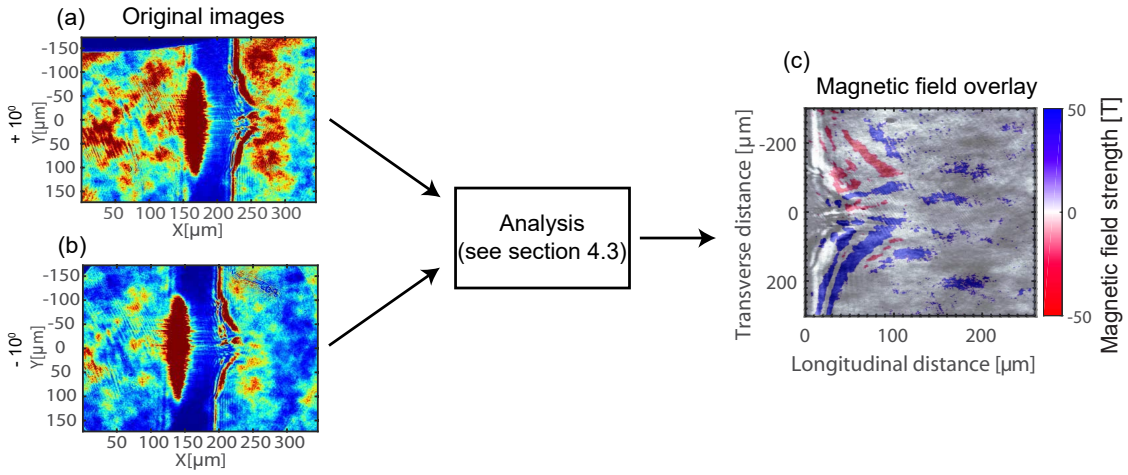

Figure 6.8: Typical steps of Faraday rotation analysis, where (a) and (b) are the original polarimetry images obtained from experiment for +10° and −10°, respectively; and (c) is the post-analysis map of magnetic field overlaid over a measured probe image. The analysis process is detailed in section 4.3.4.

then calculated via:

$$B = \frac{\phi}{n_e L} \tag{6.1}$$

where ϕ is the Faraday rotation angle, n_e is the electron density and L is the propagation distance of the probe pulse through the plasma. The magnitude of the resultant magnetic field is consistent with two-dimensional PIC simulations, as discussed in section 6.2.3.

6.2.2 Experimental results

The plasma expansion profile as a function of target thickness was characterised using the transverse optical probe. Figure 6.9 shows example images obtained.

The shadowgraphy images (figure 6.9) were acquired ∼25 ps after the arrival of the main drive laser. Jet formation and propagation occurs on the timescales of the laser pulse and thus it is the remnants of the radial expansion of the jet that are observed in the probe images. It is clear that the level of self-emission (corresponding to the dark regions) surrounding the expanding plasma is greatly increased at an optimum target thickness of l =90 nm (Figure 6.9 (c)). The shadowed regions are still visible as the target thickness is further increased.

For thicknesses below l =90 nm, the formation of the jet is inhibited as the level of transmission through the target increases. This has been attributed to the onset of RSIT occurring too early in the interaction for optimum coupling of the laser energy to the

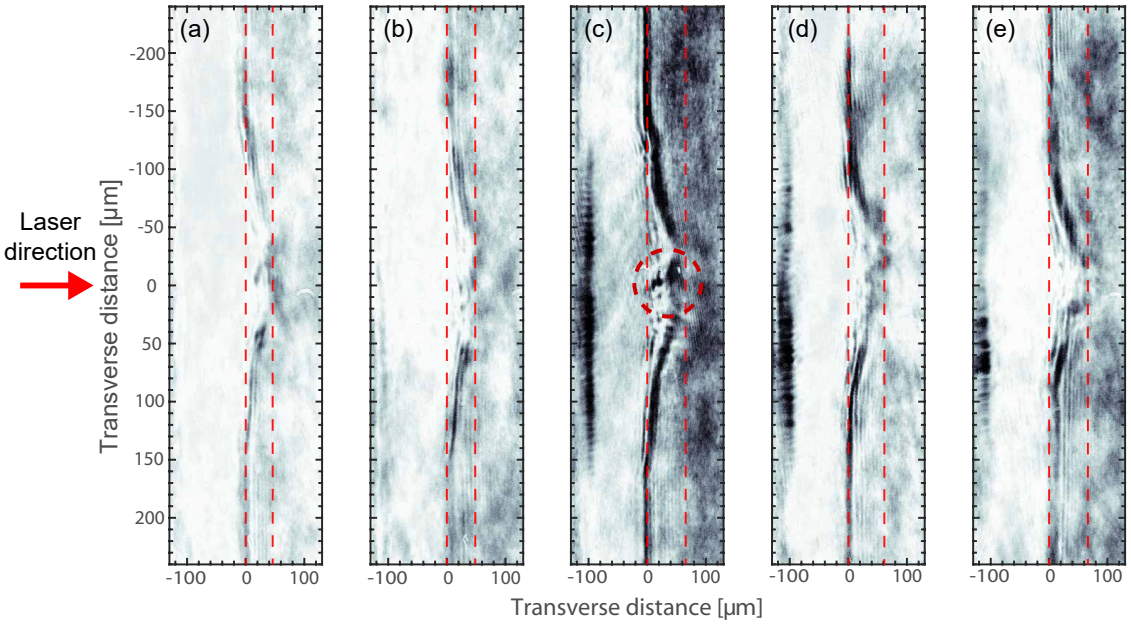

Figure 6.9: Images obtained via transverse shadowgraphy of CH targets, obtained 25 ps after the arrival of the main pulse, for varying thickness of: (a) 40 nm; (b) 75 nm; (c) 90 nm; (d) 300 nm; and (e) 1500 nm. The darker regions surrounding the expanding plasma correspond to regions of self emission. Visible in (c) is the remnants of a plasma channel. The dashed red lines indicate the longitudinal extent of the plasma expansion.

electrons to occur. In the case of the l =40 nm target shown in figure 6.9 (a), the level of decompression is increased, and thus the reduced electron density results in RSIT occuring on the rising edge of the pulse, rather than at the intensity peak, as in the optimal condition. Notably, as the target thickness is increased >100 nm, the level of transmission through the target decreases. The reduction in the level of laser light propagating through the target, volumetrically heating the electrons and driving a localised energy enhancement, leads to disappearance of the jet and the low-divergence enhanced proton population (feature **C** in figure 6.4). Furthermore, the TNSA scheme for ion acceleration begins to dominate at these thicknesses (see section 2.9.1) and the sheath field longitudinal expansion generated at the rear surface acts to confine electrons to the target. The degree of expansion for the bulk of the rear-surface plasma was measured as a function of target thickness and is shown in figure 6.10.

There is evidence of a channel visible at the target rear surface in figure 6.9 (c). This is produced by the laser propagating through the target rear and is observed for conditions at which the jet is produced. This feature, combined with the presence of higher levels of self-emission would appear to indicate the optimum conditions for plasma jet formation. This behaviour was observed on multiple occasions for each target thickness, indicating

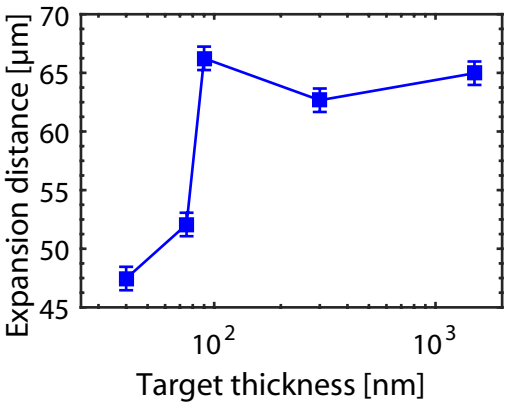

Figure 6.10: Measured values of the longitudinal expansion distance of the bulk plasma at the rear-surface of CH targets for various target thicknesses, at a time of 25 ps after the interaction. The extent of the plasma was only able to be imaged if it sufficiently impeded the path of the optical probe pulse.

that the phenomena investigated here were reproducible. Furthermore, the presence of a plasma jet has been measured on multiple experimental campaigns, on a number of high-power laser systems, for these target and laser parameters [33, 34, 253].

Polarimetry measurements were conducted in order to further examine the strength and extent of the magnetic fields present at the target rear-surface. Example measurements of the magnetic field strength, processed via the method detailed in section 4.3.4, are shown in figure 6.11. It can be seen that the azimuthal magnetic field distribution closely follows the plasma expansion, with the measurement for the l =90 nm CH target extending to the greatest distance from the target rear (figure 6.11 (c)). This azimuthal magnetic field component is likely to be acting to collimate the plasma jet.

For each case, the mean magnetic field strength was measured. This is plotted in figure 6.12 (a). There is a clear increase in the strength of the azimuthal magnetic field for l =90 nm, i.e. the thickness at which the longitudinal plasma expansion shows signatures of a channel. It is also the thickness for which the maximum energy protons are measured, over a narrow angular range between laser axis and target normal. The image plate located at the rear of the stacked RCF diagnostic shows a large increase in the number of escaping electrons from the target at this thickness, in comparison to the other thicknesses investigated. It is postulated that for the thinnest targets, the onset of RSIT occurs too early in the interaction for efficient acceleration of electrons to occur, whilst for targets of increased thickness the TNSA scheme of ion acceleration dominates and a greater number of electrons are reflected by the sheath field at the rear of the target. The measured

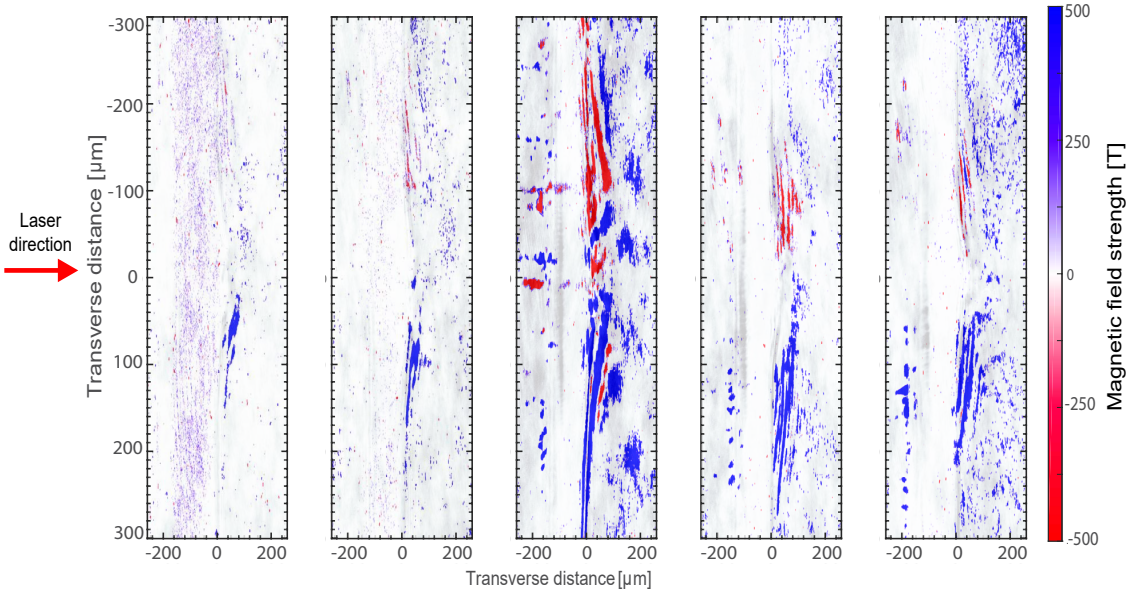

Figure 6.11: Example measurements of the magnetic field strength measured at the surfaces of CH targets, obtained 25 ps after the arrival of the main pulse, for thickness: (a) l =40 nm; (b) l =75 nm; (c) l =90 nm; (d) l =300 nm; and (e) l =1500 nm. The magnetic field maps are overlaid on top of the corresponding shadowgraphy images presented in figure 6.9.

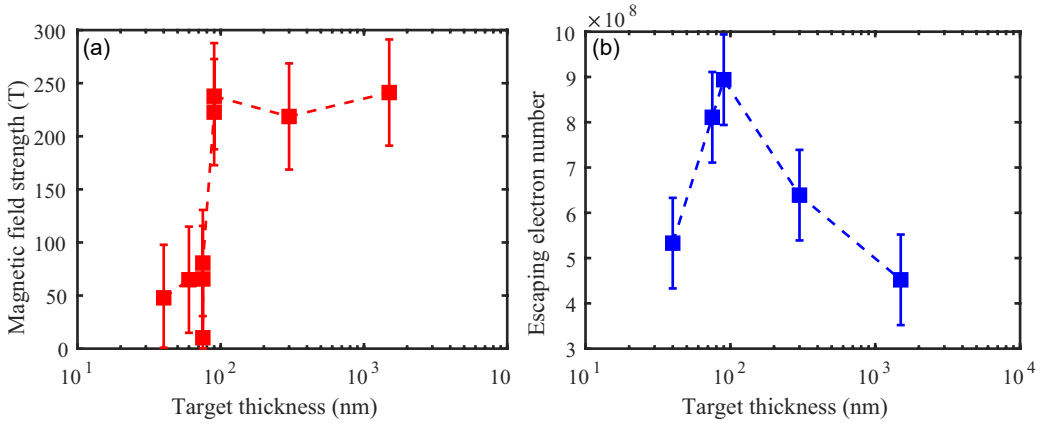

Figure 6.12: (a) Average magnetic field strength calculated from Faraday rotation measurements. A large increase in magnetic field strength is observed with increasing target thickness, starting at 90 nm. This corresponds to the optimum conditions for enhanced proton acceleration and jet production; (b) Number of escaping electrons as a function of target thickness. There is a clear peak observed at the optimal target thickness of 90 nm.

numbers of escaping electrons, obtained via the stacked IP diagnostic (see sections 4.3.3 and 6.2.1), as a function of target thickness are shown in figure 6.12 (b). Thus, all measured parameters demonstrate an optimum target thickness for which laser energy coupling to fast particles and magnetic fields is enhanced.

Analysis of the accelerated proton spatial-intensity profiles, obtained via the stacked RCF diagnostic, enabled quick diagnosis of the presence of the jet and an indication of its

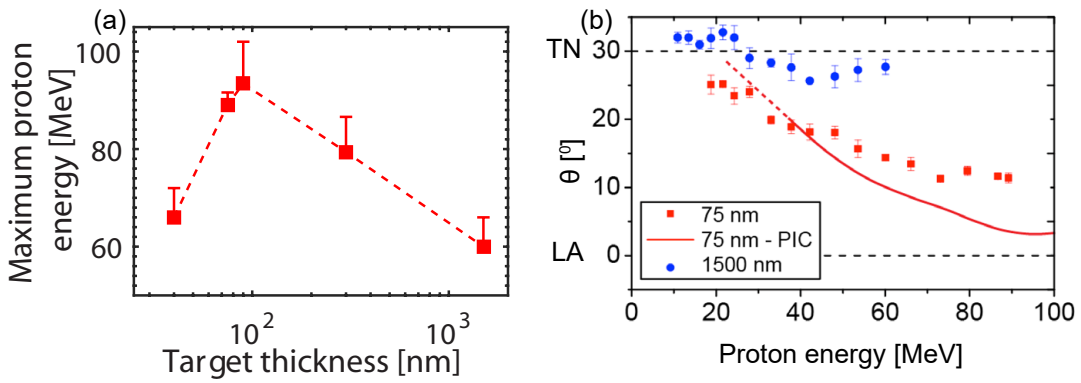

Figure 6.13: (a) Dependence of target thickness on the maximum proton energy; (b) Directionality of the proton beam as a function of energy for two example target thicknesses of 75 nm and 1.5 μm. Results of example PIC simulations are included for comparison.

directionality. As discussed previously, the enhanced-energy ion population is observed in the general direction of the electron jet. Figure 6.13 (a) shows measurements of the effect of the jet on the directionality of the proton beam for two cases; one where the target is of sufficient thickness that RSIT does not occur, and the other of optimal condition for the enhancement of the proton population. The steering of the proton beam is explained due to the high electron current density within the jet, leading to the production of an axial electric field which pulls protons in its vicinity. The protons drawn towards the jet experience an enhancement in acceleration due to the enhanced longitudinal electric field component in this region, and are boosted to higher energies with the respect the surrounding sheath accelerated population. As such, with increasing proton energy, a transition from a target-normal centered proton beam to one directed at an angle between the target normal and the laser axis is observed [200]. Notably, this dependence is not observed for targets that do not experience the onset of RSIT, as there is no jet formation in this scenario. Corresponding measurements of the maximum proton energy are plotted in 6.13 (b) to demonstrate the influence of the formation of the relativistic electron jet. Measurements of the longitudinal plasma expansion are plotted alongside these values. In both cases, a peak is measured at the optimum target thickness value of l =90 nm.

It is seen that a trend exists between all measured parameters at a target thickness of l =90 nm. Together with measurements of the presence of a plasma channel, only at this thickness, these measurements provide an indication of the optimum conditions for the generation of a relativistic electron jet.

6.2.3 Modelling

To investigate the underlying physics of the formation of the plasma jet, simulations were performed using the fully relativistic PIC code, EPOCH (see section 4.4) [271] in two dimensions. The simulation box was defined as 160 μm $\times$ 70 μm, with 26000 $\times$ 5760 simulation cells, giving a mesh cell size of 5 $\times$ 12 nm. The boundaries of the simulation box were all defined as free-space. The CH targets employed in the experimental investigation were initialised as a uniform mixture of C^{6+} and H^{+} ions, with densities of $60n_c$. A layer of contaminants was defined on the front and rear surface of the targets, with a depth of 120 nm. A population of electrons was defined to neutralise the ions appropriately, with an initial temperature of 1 keV. The initial target thickness, l, was varied over the range 75 nm to 1 μm. The laser pulse temporal and spatial profiles were both Gaussian, with FWHM of 570 fs and 5 μm, respectively, with a peak laser intensity of $2{\times}10^{20}$ W/cm^2. The pulse was incident at an angle of 30^0 with respect to the target normal axis.

Figure 6.14 shows the results of two example simulations which highlight that the generation of a plasma jet only occurs at the onset of RSIT. Figure 6.14 (a) and (c) show example outputs from a simulation of 75 nm CH, at a time of 1 ps after start of the simulation, where (a) shows the electron density and (c) shows the proton density. Here, the onset of transparency is clearly visible, with a higher density, collimated population of electrons observed propagating, initially, along the laser axis direction. As this population propagates away from the target, it is observed to begin to sweep across to an angle in between the laser axis and target normal directions. Furthermore, the electrons in this region are observed to propagate out to a distance of $\sim$ 50 μm; approximately 20 μm further than the bulk electron population, indicating a higher velocity due to direct acceleration from the transmitted pulse. The location of this jet of electrons is seen to coincide with the presence of a high density population of protons. This corresponds to the low-divergence, high-energy feature observed in measurements of the spatial-intensity profile of accelerated proton beams.

Figure 6.14 (b)-(d) show corresponding results for the case of a target with $l = 1$ μm. In this case, no transparency is observed, and there is no clear signature of a plasma jet in the electron density map (figure 6.14 (b)). Here, the electron population appears to expand relatively homogeneously in comparison. Similarly, there is no evidence of a higher density proton region in figure 6.14 (d), and the sheath-accelerated protons are observed to expand with a gaussian spatial profile.

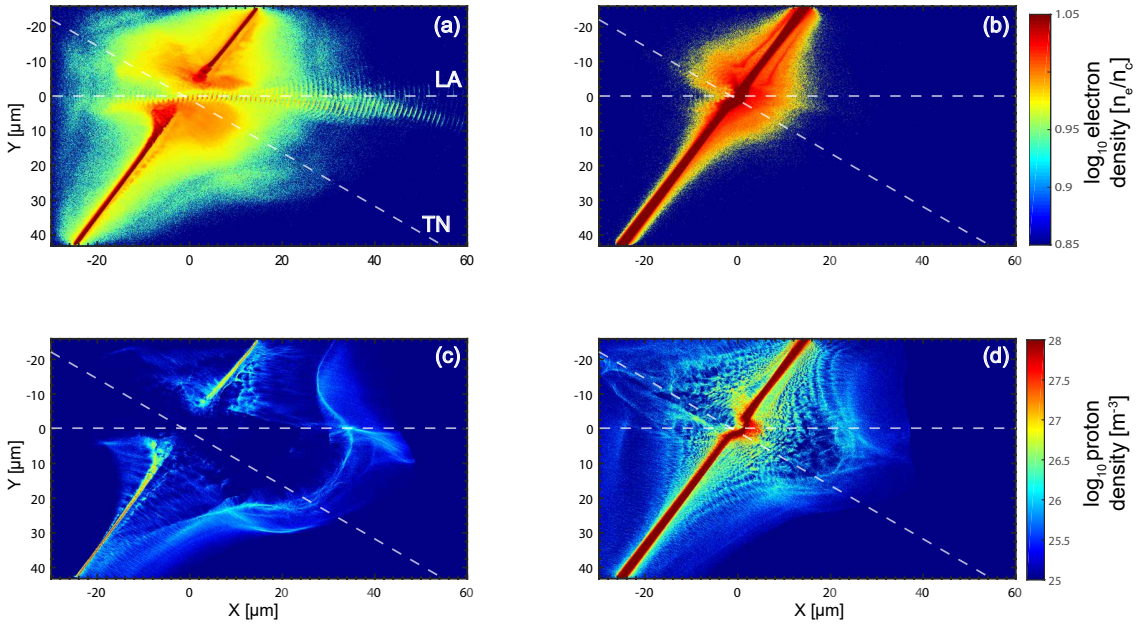

Figure 6.14: Example particle density maps obtained via 2D PIC simulations investigating jet formation showing (a) Electron density for a CH target, where $l = 75$ nm and (b) for $l = 1$ μm; (c)-(d) Same, but showing the proton density. Outputs were sampled at a time of 1 ps. LA denotes the laser axis, whilst TN denotes the target normal direction.

The numerical simulations also highlight an enhancement in the longitudinal electric field generated by the jet. The action of this field accelerates protons drawn towards the jet by an axial electric field [200]. The structure of this electric field is shown in figure 6.14 (a), for the interaction with a 75 nm CH target viewed 1 ps after the start of the simulation. When compared to figure 6.14 (b) (for a 1 μm thick CH target), there is a clear enhancement in the longitudinal electric field strength in the region of the jet. A sheath-field is also seen, at a distance of ~ 30 μm from the target rear. In the case of the $l = 1$ μm target, the rear-surface electric field is observed to be generated by the action of fast electrons propagating to the target rear and setting up a sheath field, with the centre of the electric field distribution directed along the target normal direction. In figure 6.15 (c), the magnetic field distribution is shown for a 75 nm CH target. A clear channel is visible, directed along the laser axis, in the region of the electron jet, enveloping by an azimuthal, collimated magnetic field. Also visible are two regions of null field, one on either side of the plasma channel. These may be a signature of relativistic electron vortices [325, 326]: localised structures consisting of electrons encompassing a quasi-static magnetic field inside the cavity, formed by the interaction of a high-intensity pulse with underdense plasma. The presence of a channel appears to be in agreement

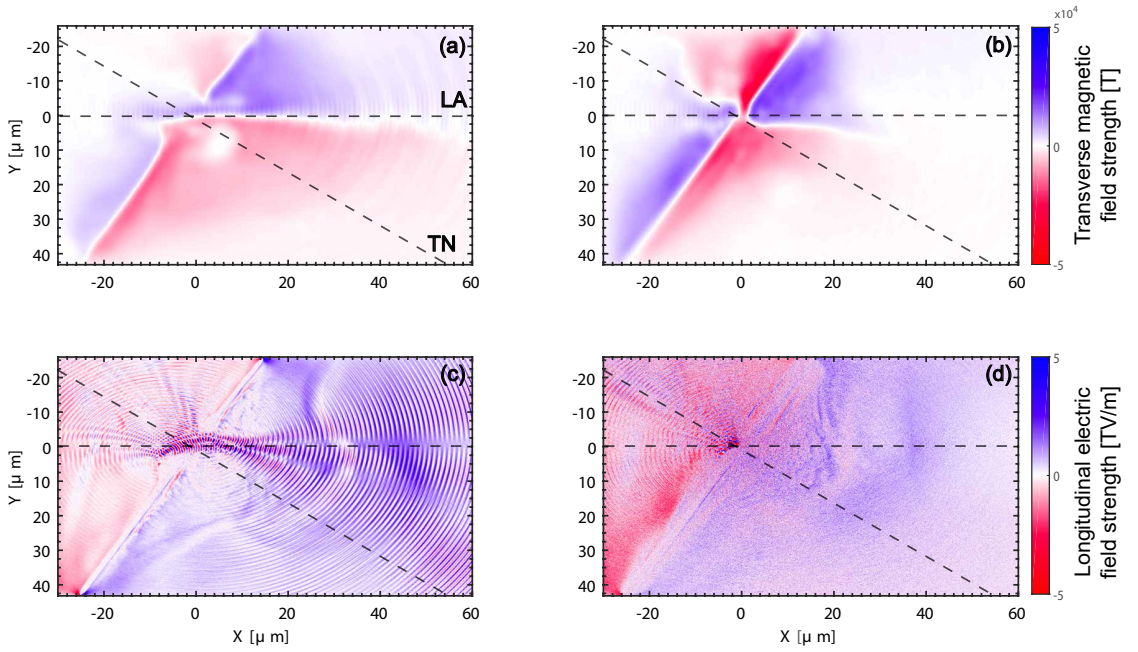

Figure 6.15: Example electric and magnetic field maps obtained via 2D PIC simulations investigating jet formation showing (a) Transverse (B_z) magnetic field strength for a CH target, where $l = 75$ nm and (b) for $l = 1$ μm; (c)-(d) Same, but showing the longitudinal (E_x) electric field . Outputs were sampled at a time of 300 fs after the peak of the pulse. LA denotes the laser axis, whilst TN denotes the target normal direction.

with the observation in figure 6.9 (c) of a visible plasma channel present in the expanding rear-surface plasma. Furthermore, the magnetic field distribution appears to be extended in the region of the laser axis, corresponding to the increased propagation distance of the electron jet, and the higher density proton population, in this region. In the micron-thick target case presented in figure 6.15 (d), there appears to be no such asymmetry in the magnetic field distribution. The electron vortex structures have disappeared in this case, and the magnetic field strength is increased over the $l = 75$ nm case. This is likely due to the increased numbers of electrons present in the target, accumulating at the rear-surface sheath field.

The simulation results are all presented at an example time of 300 fs after the peak of the pulse, whereas experimentally, the optical probe results were obtained at a time of 25 ps after the interaction commenced. The time over which the simulations were run was limited due to computational limitations in the utilisation of such tools (see section 4.4). To account for the differences in time, the magnetic field strengths from the simulations were extrapolated to the same time as the experimental measurements. This was done via a power-law fit to the evolution of the mean and maximum magnetic field

strengths over the simulation time. The extrapolated values of magnetic field demonstrate relatively good agreement with the experimental measurements for thicker targets, but not at small thicknesses. This is postulated to be due to the number of electrons present in the simulation when l is small, leading to lower currents and thus, weaker magnetic fields. Conversely, when l is larger, the magnetic fields grow to higher values, with the trend appearing to continuously increase, rather than exhibiting the plateau behaviour seen with the experimental measurements.

6.3 Magnetic field scaling

As previously discussed in **Chapter 3**, if the basic laws describing the behaviour of plasmas are invariant under a given transformation, then any scaling laws derived from these must also be invariant for the same transformation. A discussion of scaling relations, from Ryutov *et al.* [220, 221] was presented that demonstrated that if a scale factor can be determined between two systems for one parameter describing both systems, for example L^*, p^* or ρ^*, the spatial scale, pressure and density, respectively, then this same scale factor also applies to a parameter such as velocity, $\mathbf{v}$, or magnetic field strength, $\mathbf{B}$. An example of scaling between a laboratory plasma beam, generated via an intense laser-solid interaction [64, 225], and an example astrophysical jet, launched from the AGN 3C 273, was discussed (see section 3.3). The systems in this example were found to be comparable by the following method: a length scale ratio was determined by comparison of the spatial extent of both plasmas (1 pc vs 15 μm). Making the assumption that the velocity of both beams was comparable ($\sim c$) it was shown that, by applying the length scale ratio to the lifetimes of the AGN jet ($1{\times}10^8$ s) a laboratory interaction timescale of 50 fs was calculated. This was in very good agreement with the experimental pulse duration (40 fs).

The results presented in section 6.2 offer a potential avenue for studies of laboratory astrophysics performed via intense laser-solid interactions. The generation of magnetically-collimated plasma jets and the interplay between magnetic field generation mechanisms, such as the Biermann Battery and WI, in a laboratory environment, is of deep interest to the field of astrophysics. This is especially valid for investigations of the collimating and launching mechanisms of jets formed in YSOs and AGNs, where observations of the central core are difficult partly due to the complex physical processes occurring, and partly due to the obscuring nature of the accretion disk and intergalactic clouds of dust and gas.

Parameter	Vulcan PW	AGN	YSO
L (m)	$\sim 50 \times 10^{6}$	10^{21}	10^{15}
t (s)	1×10^{-12}	10^{15}	10^{11}
$\mathbf{v}$ (m/s)	$\sim c$	$\sim$c	$\sim 10^{5}$
$\mathbf{B}$ (T)	250	10^{-10}	10^{-4}

Table 6.1: Comparison of parameters measured for laboratory jets, and astrophysical jets originating from two example phenomena associated with jet formation, Active Galactic Nuclei (AGNs) and Young Stellar Objects (YSOs).

Such investigations would benefit from the potential to field a suite of diagnostics probing the interaction, whilst also enabling many data points to be acquired over the course of an experimental campaign, providing useful statistical data.

6.3.1 Applicability of scaling: plasma jets

Considering the investigation presented in section 6.2, the plasma jet generated at the onset of transparency in the interaction of an intense laser pulse with an ultrathin target appears superficially similar to those observed in astrophysical scenarios. The current and magnetic field structures that collimate the jet could be used to generate laboratory analogues of astrophysical phenomena. A comparison of the measured parameters for the scenarios of intense laser-solid interactions, AGN and YSOs are outlined in table 6.1. In this section, a similar scaling analysis to that performed in Gonzalez-Izquierdo *et al.* [64], is performed for these investigations in order to quantitatively compare the systems.

The measurements for Vulcan petawatt in table 6.1 were acquired from the experiment presented in section 6.2.2. The spatial extent of the jet, L was determined from the measurements of the rear-surface plasma expansion (figure 6.10). The approximate value of 50 μm was chosen from measurements of the plasma expansion for targets in the range of 75-90 nm thickness, i.e. where the features of the plasma jet are most strongly inferred. The typical pulse duration for Vulcan petawatt was selected as the timescale for the lifetime, t of the jet. After this time, the jet is no longer being driven by the transmitted portion of the pulse, and thus, dissipates. The magnetic field strength, $\mathbf{B}$ was measured via the polarimetry diagnostic $\sim$25 ps after the main interaction, and the number shown is the mean magnetic field strength at this time. The jet is assumed to propagate with a velocity, $\mathbf{v}$, approaching c, defined via studies of sheath expansion [308, 309].

The properties of the jets launched by AGNs were obtained from various observations on a range of objects. The magnetic field strength within a sub-parsec region of the compact

source object was measured as 10^{-6} G in Safarzadeh *et al.* [327], whilst the spatial extent and velocity were measured in dal Pino *et al.* [315], on the scale of Mega-parsecs (1 parsec $\sim 3\times10^{16}$ m) and $\sim c$, respectively. In contrast, YSO jets are typically on the order of a parsec in length, with velocities of hundreds of kilometres/second, i.e. $\sim 10^{-3}c$ [328, 329]. The magnetic field strength in the region near to the source was measured to be $\sim 10^{-4}$ T in Ray *et al.* [215].

Performing the same methodology as used in Gonzalez-Izquierdo *et al.* [64], a length scale-ratio was calculated between the laboratory experiment and the astrophysical cases. Considering first the comparison between the intense laser-driven plasma jet and the typical YSO parameters, $L^*=6\times10^{22}$. The magnitude of this number demonstrates the massive differences in scale between the two scenarios. The velocity of the jets in these instances are vastly different: with the laser-driven jet propagating at $\sim c$, and the YSO jet having a velocity in the region of $0.001c$. Thus, the timescale-ratio of these two jets cannot be assumed to be similar. The scaling ratios of other parameters must be employed to obtain information on the possibility of scaling. Examining the relative magnetic field strength between the two scenarios, the ratio is $B^*=2.5\times10^6$. However, it should be noted that the value for the magnetic field strength near the jet launch region in the laboratory experiment was measured at a time of 25 ps after the interaction. At this time, the interaction is no longer being driven by the pulse. As demonstrated in Antici [310], the velocity of electrons in rear-surface sheath fields decreases exponentially with time with $1/e$ =1.6 ps. As the magnetic field is generated by the motion of charged particles, it is assumed that the magnetic field will decay in a similar fashion. Performing a rudimentary analysis to interpolate the magnetic field strength back to a time of 1 ps (approximately the pulse duration employed in the interaction), the magnetic field was calculated to be $\sim$1.5 kT. Repeating the scaling analysis for this magnetic field strength returned the ratio $B^*=1.5\times10^7$. Although, the interpolated magnetic field strength was in good agreement with the two-dimensional PIC simulations performed in conjunction with the experiment, this analysis was rudimentary. Detailed, early-time (comparable with the pulse duration) experimental measurements of the magnetic field strengths in the region of jet formation are necessary to obtain a full description of the applicability of the scaling of plasma jets originating in solid foils undergoing RSIT. Currently however, these results indicate that the parameters employed in the experiment presented in section 6.2 do not present scaled-down laboratory analogues to jets originating from YSOs. Several experimental campaigns have been un-

dertaken that have produced jets in intense laser-solid interactions with relevance to YSOs and HH objects. Shigemori *et al.* [330] employed conical targets, under irradiation by an intense pulse, in order to focus the plasma expansion into a jet-like feature at the target's axis of symmetry. Scaling analysis demonstrated that experimental measurements of the Mach number of the jet (the ratio of the jet velocity to the sound speed inside the jet) were in good agreement with astrophysical jets launched from YSOs. This demonstrates a method by which the experimental parameters could be varied to tailor the investigation to the study of a specific example of astrophysical phenomena. This same discussion was presented in Gregory *et al.* [62], where it was suggested that targets of different Z may be selected in order to study the transition between radiative and adiabatic flows.

Examining the scaling of laboratory analogues to jets originating in AGNs is now considered. A length scale-ratio of $L^*=2\times10^{27}$ was calculated, employing the parameters detailed in table 6.1. As the jet velocity in each case is now directly comparable (both $\sim c$), then the timescale ratio t^* should compare to L^* [228]. Applying this ratio to the jet lifetime (1×10^{15} s), results in an interaction time of 5×10^{-13} s, or 500fs. This is in good agreement with the experimental pulse duration and thus, interaction time, of the laboratory-produced jet. These parameters demonstrate the applicability of scaling laws to the results presented in section 6.2 in future laboratory testing of the formation of analogues of astrophysical jet structures. Finally, the scaling-ratio determined for this case of the AGN jet was applied to the measured magnetic field strength from the experimental campaign. Taking the previously interpolated value at a time of 1 ps resulted in a magnetic field strength of 7.5×10^{-25} T, in the sub-parsec region of an AGN jet. Clearly, this value does not agree with measurements performed of such structures [327] and thus, this highlights the necessity of detailed, earlier-time measurements of the magnetic field strength in laboratory experiments. Despite this difference, the laboratory simulation of a relativistic plasma jet offers an important tool for modelling the characterisation of astrophysical analogues to those launched from accreting, astrophysical phenomena.

In the astrophysical scenarios presented here, gravity is the main driver of the phenomena observed: the motion of accreting or contracting matter results in the generation of high temperatures and magnetic field growth. However, in laboratory experiments the role of gravity is drastically reduced: the laser is the driver of the interaction and transfers energy to the particles it interacts with, resulting in the growth of high temperature environments and strong self-generated magnetic fields. In both cases, the phenomena

under investigation in this thesis are results of the initial interaction, and thus, despite the main driving mechanism being different in both scenarios, the validity of regarding both to be similar is justifiable.

Finally, it should be noted that, in this study, the jet produced upon the onset of RSIT is primarily populated by electrons and protons. Thus, laboratory analogues of lepton-baryon were investigated. However, the basic nature of relativistic astrophysical jets is still unclear, and there exists the possibility of leptonic jets, being composed of electrons and positrons, being prevalent throughout the universe [331]. Electron-positron beams are believed to play a key role in astrophysical phenomena [332], and have been postulated to be a driver for GRBs [70, 71]. Previous studies have concluded that jets originating from AGNs must be composed of electron-proton plasma [333], whilst others have argued that they are leptonic in nature due to their kinetic luminosity [331].

6.4 Evidence of the Weibel instability in the growth of self-generated magnetic fields

In **Chapter 5**, filamentation of beams of fast electrons propagating through solid targets of thickness, l, of the order of hundreds of microns was characterised via measurements of the degree of modulation in the spatial-intensity profile of the beam of sheath-accelerated protons. The dominant mechanism for the filamentation of the electron beam in that scenario is the resistive filamentation instability arising from self-generated resistive magnetic field growth.

The use of ultrathin targets for novel ion acceleration schemes [186, 334] has also been shown to result in strong spatial modulations, in the form of bubble structures, in the spatial intensity profile of the beam of accelerated protons [34, 44, 159]. In this case however, the modulations have been attributed to Rayleigh-Taylor-like (RT-like) transverse instabilities during laser interaction with the target front side (see feature **B** in figure 6.4). In Powell *et al.* [34] it was reported that these bubbles are observed in the proton population directed along the laser axis, which means that they are less likely to be associated with TNSA, and more likely to be produced by instabilities in the RPA mechanism. These measurements involved expanding ultrathin Al foil targets.

In the present work, proton beam measurements made using the Vulcan Petawatt laser show the notable presence of bubble structures only on shots for which a controlled pre-

pulse is employed to expand the target foil prior to the arrival of the main laser pulse. This was achieved by splitting the laser pulse into two pulses and applying a temporal separation between them, with control of the relative amplitude ratio of the pulses. The temporal separation is short and thus the two pulses overlap such that the "pre-pulse" merges with the rising edge of the "main" pulse. Changing the pre-pulse thus effectively changes the rising edge profile of the main pulse. The value of the intensity on the rising edge at a selected time t =-1.5 ps, is denoted hereafter as I_{RE}. This technique is described in detail in section 6.4.1. It is noted that, even with a plasma mirror, the minimum value of I_{RE} achieved was $\sim 0.04 I_L$, defined by the inherent contrast of the Vulcan laser.

The absence of bubble structures in the case of $I_{RE} = 0.04 I_L$ (i.e. with no controlled target pre-expansion) appears to contradict the hypothesis that bubble-like structures are generated by RT-like instabilities. As discussed in section 2.8, the RT instability is a transverse instability at the interface between two fluids of different densities. The interface is initially flat, with the two fluid layers being plane parallel [157]. Small localised perturbations at the interface results in pressure variations, leading to the growth of the perturbations, producing the characteristic bubble-like structures. Thus, the case when no controlled pre-pulse is employed should present a greater degree of an initially plane-parallel interface between the heavy fluid (the target) and the light fluid (the pulse), resulting in RT-like instability growth.

On the other hand, recent studies [45, 136, 144] have demonstrated that the presence of a rear-surface expansion in relatively thick foils results in the formation of bubble-like structures in the accelerated proton population, as seen in figure 6.4. Instead of RT-like instabilities, it is postulated that the spatial modulations observed in the proton beam are a result of filamentary magnetic field structures arising from the WI. By performing an analytical analysis of the growth rate of the WI, Göde *et al.* [144] demonstrates that the magnetic field strength at the target rear can be greater than that generated inside the target. As will be discussed later in this section, the bubble-like structures observed in the case of expanding ultrathin foils are likely to be generated by this same mechanism. The resistive filamentation instability, previously investigated as the driver for electron filamentation in **Chapter 5**, is not considered as a potential candidate due to the fact that the timescale for this instability to grow requires propagation distances far greater than the target thicknesses employed in references [34] and [44].

This section features an experimental and numerical investigation into the role of the WI

on the filamentation of the beam of energetic electrons accelerated in laser-foil interactions, and the subsequent influence on proton acceleration. The sensitivity of the growth of the WI to the degree of target decompression is also investigated. A transition from large-scale, azimuthal magnetic field structures, to filamented, smaller-scale fields is observed.

6.4.1 Details of the specific experiment

The Vulcan Petawatt laser (see section 4.2.8) was employed to deliver P-polarised pulses with a central wavelength of 1.053 μm and energy (on target), E =(200±15) J. The targets were aluminium foils, with l =10-40 nm. The pulse duration was ∼(1±0.1) ps (FWHM). The focal spot diameter was 7.3 μm (FWHM), resulting in a peak intensity, I_L, of ∼2×10^{20} W/cm^2. The incidence angle was 30° with respect to target normal.

A single planar plasma mirror was employed to enhance the temporal intensity contrast. Figure 6.5 shows the measured temporal intensity contrast and enhancement produced via the utilisation of this plasma mirror configuration. The application of dual pulsing in conjunction with a plasma mirror is discussed in Scott *et al.* [244]. The experimental setup is similar to the one presented in section 6.6. The Vulcan petawatt laser can operate in a dual pulse mode, implemented by splitting the main pulse after the picosecond OPCPA pre-amplification stage (see section 4.2.8). This mode of operation has been previously been employed for dual pulse experiments on ion acceleration in the TNSA regime [176, 247]. In the present investigation, it was employed to vary the intensity on the rising edge of the main laser pulse and thus, induce controlled pre-expansion the interaction foil to near-critical densities. The total pulse energy was fixed throughout, i.e. the energy ratio between the two pulses was varied. The pulses were temporally separated by (1.5±0.1) ps.

The dual pulse was generated by first splitting the pulse into two, prior to stretching and amplification, and then applying a temporal separation, as illustrated in figure 6.16 (b). The dual-pulser arrangement operates as follows. The input beam enters the setup and encounters an interferometer, coupled with a polariser and polarising beam splitter. The interferometer allows relative control of the amplitude of the two pulses (and thus I_{RE}). Through a change in the polarised reflectivity at the beam splitter, a fraction of the pulse is reflected to form the pre-pulse, and has a polarisation determined by the polariser at the input to the dual-pulser. Both the pre-pulse and main pulse arms of the setup have separate timing mechanisms for independent control of the pulse arrival time

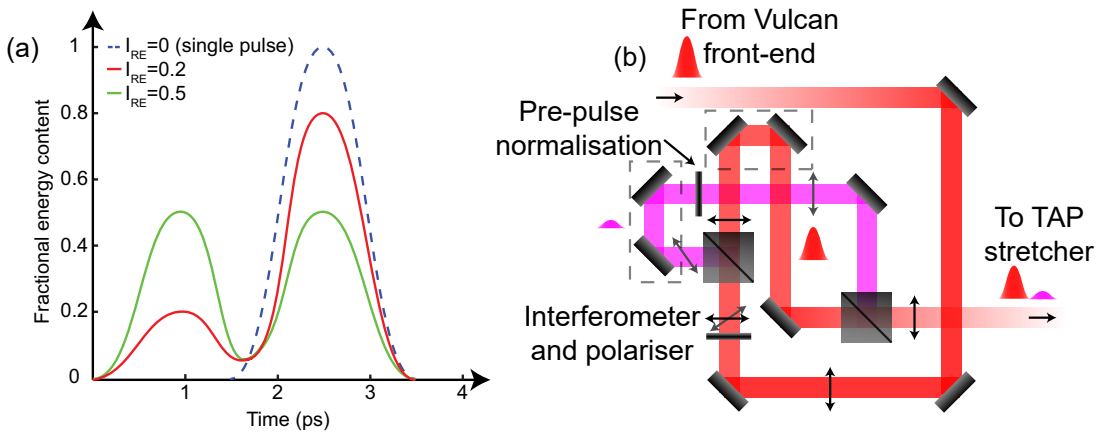

Figure 6.16: (a) Plot of the double-pulse arrangement employed in the experimental campaign. The drive-pulse was focused by a F/3 OAP, and reflected off a PPM onto the target foil. The temporal spacing between the pulses was 1.5 ps from peak-to-peak; (b) Schematic of the TAP "double-pulser" system. The seed pulse is split into two arms by a polarised beam splitter. Each arm has a separate timing slide for independent timing of each pulse. Following the delay stage, the pre-pulse is re-normalised and the pulses are recombined.

at the target and thus the temporal separation. Following the delay stage, the pre-pulse polarisation is rotated to its original state with a second polariser. Both pulses are finally propagated through a non-polarising beam splitter where they are recombined and sent to the stretching and amplification stages of the Vulcan petawatt system (section 4.2.8).

To define the pulse temporal separation, both pulses must first be overlapped, spatially and temporally. Spatial overlap was achieved by adjustment of the final two turning mirrors prior to the stretcher. The near- and far-field stretcher diagnostics were utilised to perform this alignment. The pulses were temporally overlapped by the introduction of a spatial tilt to the pulse which introduced fringes to the near field only when the two pulses were overlapped spatially and temporally. Thus, the zero delay condition was defined. I_{RE} was varied up to $0.5I_L$, with I_L reduced so as to maintain a fixed pulse energy.

The two-dimensional spatial-intensity distribution of the accelerated proton beam was measured using the stacked RCF diagnostic (see section 4.3.2). The diagnostic was positioned ~75 mm from the target rear, and was composed of two 25×65 mm "half stacks" (sampling the top and bottom of the beam) enabling an angular range of -10° to 35^o to be measured, with respect to the laser propagation axis. This large angular range enabled both the target-normal and laser-axis directed components of the proton beam to be resolved. The gap between the two RCF half-stacks enabled proton spectra measurements to be obtained via a suite of high resolution Thomson parabola spectrometers. The spectral measurements are not discussed here but are presented in reference [34].

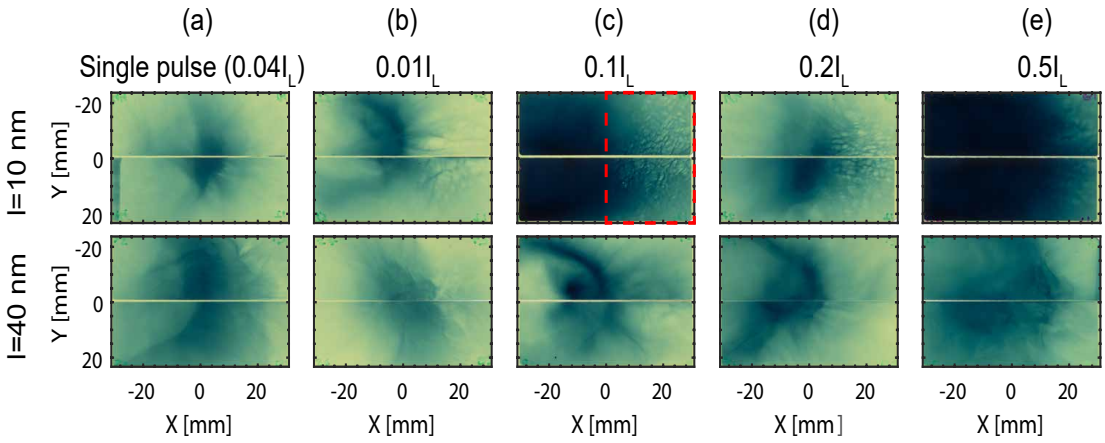

Figure 6.17: Example spatial-intensity distribution measurement of the proton beam for (top row) l =10 nm and (bottom row) l =40 nm Al targets, and a variety of pre-pulse intensities, showing (a) No pre-pulse; (b) I_{RE} =0.01I_L; (c) I_{RE} =0.1I_L; (d) I_{RE} =0.2I_L; (e) I_{RE} =0.5I_L. The area marked by the dashed red line in figure 6.17 (c) is presented in greater detail in figure 6.18 (a).

6.4.2 Experimental results

Figure 6.17 shows example proton beam spatial-intensity profiles measured for targets of l =10 nm and l =40 nm. The proton beams are sampled at an example energy of 7 MeV. The bubble-like structures are clearly visible in the beams obtained from the l =10 nm targets when a pre-pulse is applied. Bubble features are only faintly present in the l =40 nm target case. The bubble features are most clearly observed at optimum pre-pulse levels of I_{RE} =0.1I_L and 0.2I_L. Whereas the jet, discussed in section 6.2, is supported by a global, azimuthal magnetic field driven by the Biermann battery mechanism, the bubble-like structures are formed by local perturbations of the magnetic field, generated by the growth of the WI. As the target thickness increases the level of decompression of the target prior to the arrival of the main pulse decreases accordingly. The magnetic field perturbations are thus clearly dependent on the scale length of the expanding plasma. This hypothesis is further supported by the fact that for l =10 nm, in the case of a single pulse (0.04I_L), there are no bubble-like structures present in the accelerated proton population. The area marked by the dashed red line in figure 6.17 (c) is presented in greater detail in figure 6.18 (a).

For l =10 nm, the number of bubbles is found to to increase with I_{RE} up to 0.1I_L, and decrease for higher I_{RE}, as shown in figure 6.18. This is in qualitative agreement with both the 2D and 3D simulation studies presented in section 6.4.3. For l =40 nm, a similar trend in the number of bubbles measured in the proton beam is shown in figure 6.18 (albeit that the numbers of bubbles are far smaller). An optimum I_{RE}(=0.1I_L) is

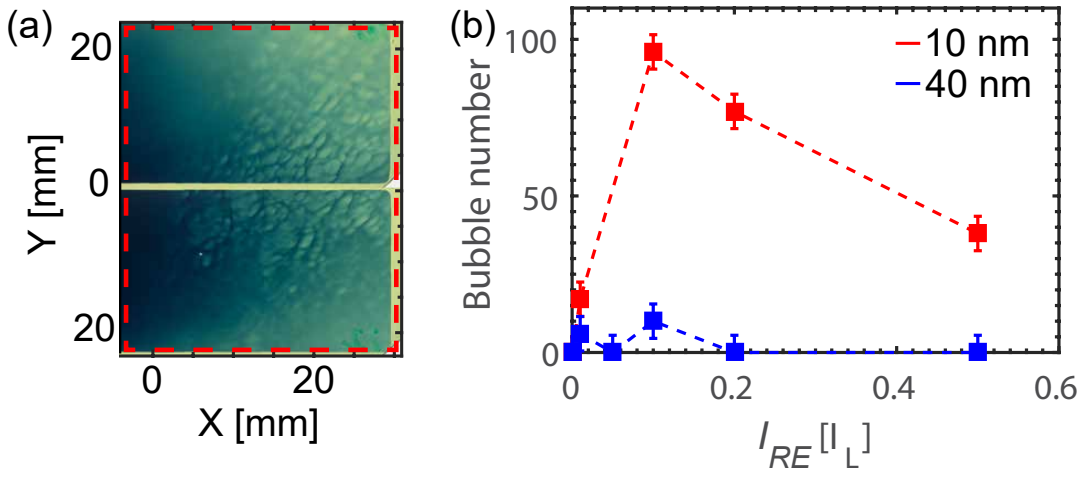

Figure 6.18: (a) Example spatial-intensity distribution measurements of the proton beam for l =10 nm Al, with I_{RE} =0.1I_L, corresponding to the dashed-red area in figure 6.17 (c); (b)The number of bubble-like structures observed in the proton beam as a function of pre-pulse intensity.

again observed.

These results suggest that l =10 nm and I_{RE} =0.1I_L produces the optimum expansion and thus timescale for the growth of the WI. The growth rate of this instability is indirectly proportional to the electron density of the plasma (as discussed in section 2.7.3):

$$\Gamma_{WI} = \omega_{pf}\sqrt{\left(\frac{n_f}{\gamma n_e}\right)} \times \frac{v_f}{c} \tag{6.2}$$

where ω_{pf} is the plasma frequency of the fast electrons, n_f is the number density of fast electrons, n_e is the target electron density and v_f is the fast electron velocity. Figure 6.19 plots the growth rate as a function of electron density and the Lorentz factor of the fast electrons.

The growth rate of the WI increases with decreasing electron density, which would thus correspond to a greater degree of beam filamentation. In the next section, a numerical investigation of the generation of bubble structures is presented. The hypothesis that, for lower degrees of target expansion the filamented magnetic field structures do not grow fast enough to be measurable using stacked RCF diagnostics is examined. The location in the target at which filamented magnetic field growth occurs in also explored. Locating the position of the onset of filamentation would help to resolve the driving mechanism: RT-like instabilities are initiated at the front surface, whereas WI-driven filamentation is produced in the expanding plasma at the target rear.

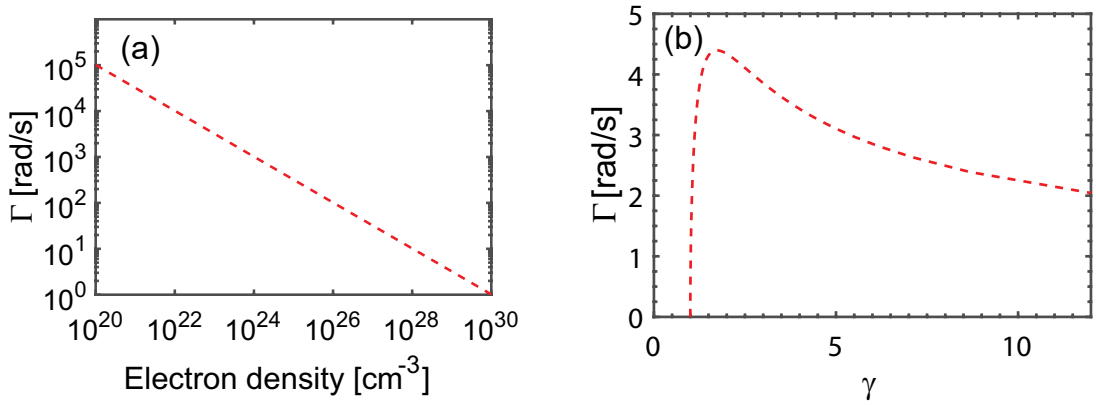

Figure 6.19: Growth rate of the Weibel instability as a function of (a) electron density and (b) plasma electron Lorentz factor. The growth rate of the instability is observed to decrease as a function of increasing electron density, consistent with the observation that a greater degree of target decompression results in the generation of bubble-like, filamentary structures in the proton beam.

6.4.3 Modelling

A numerical investigation of magnetic field growth for l =20 nm aluminium targets was performed using the fully relativistic PIC code, EPOCH (see section 4.4) [271]. A thickness of 20 nm was chosen, rather than l =10 nm at which the bubble-like structures had been observed experimentally, due to computational constraints of the resolution required for this thickness. Simulations were performed in both 2D and 3D to ensure that the behaviour observed is independent of dimensionality and to discount the impact of any potential asymmetric effects driven by the linear polarisation of the laser light (e.g. as explored in references [198, 199]).

To determine whether structures similar to those observed experimentally are present, 3D simulations were first performed. Due to computational constraints, the numerically intensive 3D simulations used a 60 μm×20 μm×20 μm box with 3000×360×360 simulation cells. The mesh cell size was 20×55×55 nm. To compensate for the low resolution, the target consisted of the equivalent of 20 nm Al^{11+} at a density of $60n_c$, expanded to a Gaussian profile with a peak density of $5n_c$. The FWHM in all cases was 200 nm. Similarly, the H^+ and C^{6+} contaminant layers on the surfaces were expanded to a peak density of $5n_c$ and $1.67n_c$, respectively. A population of electrons, initialised at a temperature of 10 keV, was defined to appropriately neutralise the ions. The focal spot size was defined as 6 μm (FWHM), and the pulse duration was set to 200 fs (FWHM) to make the 3D simulations feasible. The degree of pre-expansion of the target was controlled by variation of the rising edge profile of the pulse. This was varied by using a pre-pulse of the same duration, with

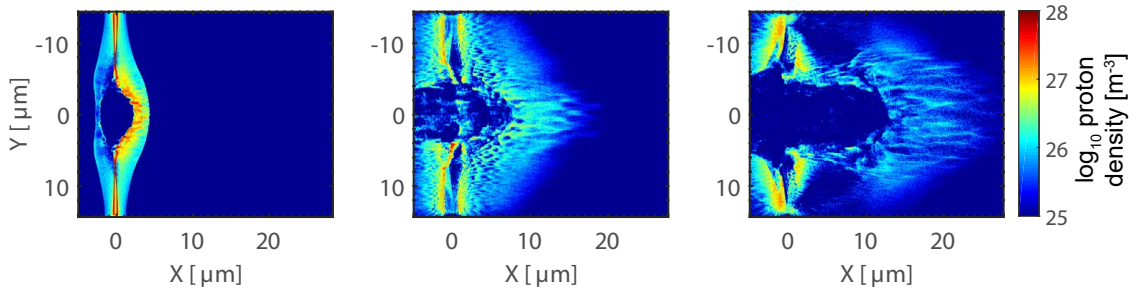

Figure 6.20: Proton density maps, from 3D PIC simulations, in the [X-Y] plane, of the irradiation of l =20 nm Al targets, for the cases of (a) a single pulse; (b) I_{RE} =0.05I_L; and (c) I_{RE} =0.2I_L. The number of filaments is seen to decrease from (a) to (c).

peak-to-peak separation of 1 ps (i.e. similar to the experiment). The previously defined intensity ratio, I_{RE}, is again employed to quantify the changes to the rising edge intensity profile of the main pulse.

Outputs were sampled just prior to the peak of the main pulse. Bubble-like features were observed in all cases, including the scenario with no pre-pulse due to the pre-expansion in all simulations. The degree of pre-expansion for the no pre-pulse case is likely to correspond to the optimum expansion, as observed experimentally for $0.1I_L$. A higher intensity pre-pulse results in a greater degree of target decompression prior to the arrival of the main pulse. This leads to the size of the filamentary structures in the proton density increasing, whilst the number of filaments generated is seen to decrease. In order to directly compare the results of the numerical simulations with experimental measurements, a projection of the accelerated protons was sampled downstream of the target, approximately 3 μm from the target rear surface, to give an indication of how the structures evolve. As I_{RE} increases (from (a)-(c)), the area with the bubble structures appears to grow accordingly, although the specific features are difficult to resolve. In agreement with the measurements discussed above, the number of filamentary structures is seen to decrease, as shown in figure 6.21. Assuming the pre-expansion for the single pulse case is approximately the optimal expansion condition, this agrees with the experimental results (for I_{RE} >0.1I_L).

In the simulations featured in this section, a plasma jet is not observed. The large degree of target decompression, due to the decreased target areal density, in addition to the pre-expansion generated by the pre-pulse, is postulated to result in a transition of the dominant magnetic field generation mechanism from the global Biermann battery to the spatially localised WI growth [136]. As the degree of decompression is increased from the target parameters investigated in section 6.2, the global collimating magnetic

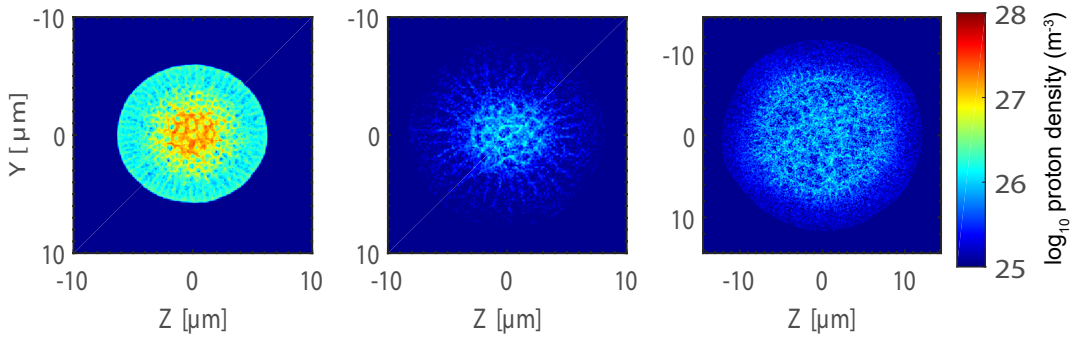

Figure 6.21: Proton density maps in the [Y-Z] plane, sampled ∼ 3 μm from the target rear, from 3D PIC simulations of the irradiation of l =20 nm Al targets, for the cases of (a) a single pulse; (b) I_{RE} =0.05I_L; and (c) I_{RE} =0.2I_L. The number of clearly defined bubbles decreases from (a) to (c).

field structures, driven by the Biermann battery, are replaced by magnetic field structures arising from the WI. This gives rise to the filamentation of protons, manifesting in bubble structures.

Next, a numerical investigation of the driver of these filamentary patterns was performed in 2D. The reduced dimensionality enables a wider parameter space to be explored, with relaxed requirements for temporal and spatial resolution. As such, the box for the 2D simulations was defined as 2 μm×23 μm, using 2001×11520 simulation cells, giving a mesh cell size of 1 nm×2 nm. The boundaries of the simulation box were all defined as free space. Aluminium targets with l =20 nm were employed, with various degrees of pre-expansion applied, such that the density takes a Gaussian profile. This represents the expansion induced by the dual pulse. Scenarios of no expansion, and FWHM expansions of 250 nm, 500 nm and 750 nm (prior to the arrival of the pulse) were simulated. The targets were initialised as a population of electrons expanded to a perfect Gaussian, with FWHM corresponding to the degree of pre-expansion. An electron temperature of 10 keV was selected to be low enough to minimise further pre-expansion of the target prior to the arrival of the pulse, but high enough to resolve the Debye length as closely as possible. A population of $60n_c$ Al^{11+} ions and a layer of contaminants, located on both the front and rear target surfaces, composed of $60n_c$ H^+ and $20n_c$ C^{6+} were defined to neutralise the electrons appropriately. This is illustrated in figure 6.22. The laser pulse temporal and spatial profiles were both Gaussian, with FWHM of 500 fs and 6 μm, respectively, with a peak laser intensity of I_L =2×10^{20} W/cm^2. The pulse was incident along the target normal axis.

Considering initially the electron behaviour, the transverse momentum was studied for

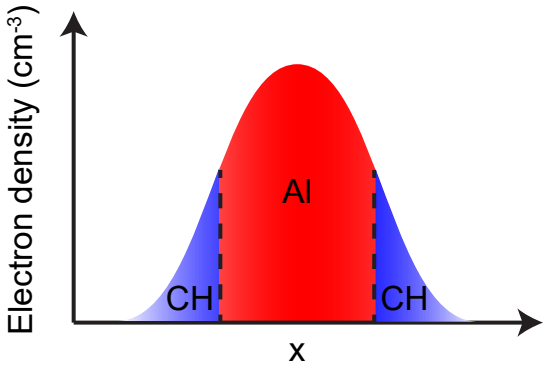

Figure 6.22: Schematic illustration of the target initialisation in the 2D PIC simulations. Aluminium ions were defined comprising the target bulk, and contaminant layers of hydrogen and carbon ions were initialised on the front and rear surfaces in order to neutralise the Gaussian electron population appropriately.

varying degrees of target pre-expansion, as shown in figure 6.23. The momentum was sampled at a distance of 10 nm, centered on the laser axis (i.e. X=0 μm). The outputs were obtained at a time of 50 fs after the start of the simulation. The results demonstrate that when minimal pre-expansion of the target has occurred, the electron transverse momentum is negligible and thus no bubble-like structures are generated. As the target is pre-expanded further (to 250 nm FWHM, figure 6.23 (b)), distinct sinusoidal ripples are observed over a 4 μm diameter region. The amplitude of these ripples is measured as $\sim 5 \times 10^{-22}$ kg m/s, resulting in a velocity of $\sim 5.5 \times 10^{7}$ m/s. The transverse expulsion of the proton population in this scenario is proposed to result in the formation of the bubble-like structures, as seen in figure 6.17. Further pre-expansion (to 500 nm, figure 6.23 (c)) leads to the measurement of longer wavelength ripples in the same region. These modulations are postulated to result in the formation of similar bubble structures to those observed previously, however with larger magnitude and a comparably lower number. The average magnitude of the momentum is comparable to the 250 nm expansion case, but the wavelength is approximately two times larger in comparison: 0.20 nm compared to 0.46 nm. As the degree of pre-expansion increases, the sinusoidal ripples are seen to disappear again. However, rather than the variation in the momentum being negligible (as seen in the case with no expansion), the wavelength of the modulation is now sufficiently large that any small scale features have been diminished. It is unlikely that this would produce measurable proton bubble structures. Furthermore, an important point to note is the apparent lack of momentum modulation for the case of no pre-expansion. This may be explained by the modulations being of a shorter wavelength and amplitude than any of

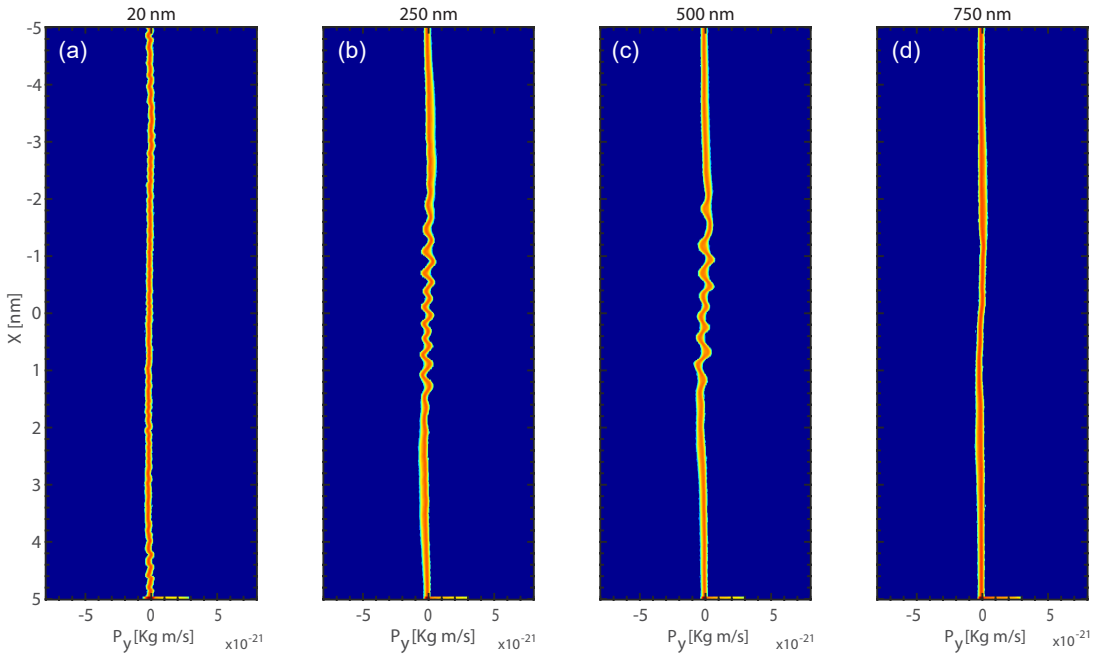

Figure 6.23: Two dimensional electron momentum phase space plots for varying degrees of target pre-expansion, sampled over a 10 μm distance for (a) No pre-expansion and (b)-(d) Gaussian density profiles with FWHM equal to (b) 250 nm, (c) 500 nm and (d) 750 nm. Modulations in the transverse momentum are observed as the level of pre-expansion is increased. The wavelength of the modulations is observed to grow.

the other cases studied, as discussed in section 6.4.2.

The resultant behaviour of the protons, responding to the transverse expulsion of electrons, was then investigated in 2D. The proton density distribution was sampled at a later time of 75 fs after the start of the simulation, for the same cases of target pre-expansion presented above. Sample outputs are presented in figure 6.24, and are in agreement with the hypothesis that any modulations present in the case of no target pre-expansion are too short in wavelength and amplitude to be measurable. There are a large number of small density perturbations visible in figure 6.24 (a). In a similar argument to that presented in **Chapter 5**, the scenario of a large number of small filaments of a fast electron beam in close proximity to each other at the target rear, acts to reduce the magnitude of any modulations in the measured proton beam. It is postulated that the high spatial-frequency of the density perturbations observed in this case also reduces the observable effects of the growth of the WI.

As the degree of pre-expansion increases, a clear transition to highly filamented proton density distributions emerges in figures 6.24 (b) and (c). As previously shown in figures 6.23 (b) and (c), the wavelength of the perturbations is seen to be comparatively smaller for the case of a 250 nm pre-expansion than 500 nm. In addition, the width of the filaments

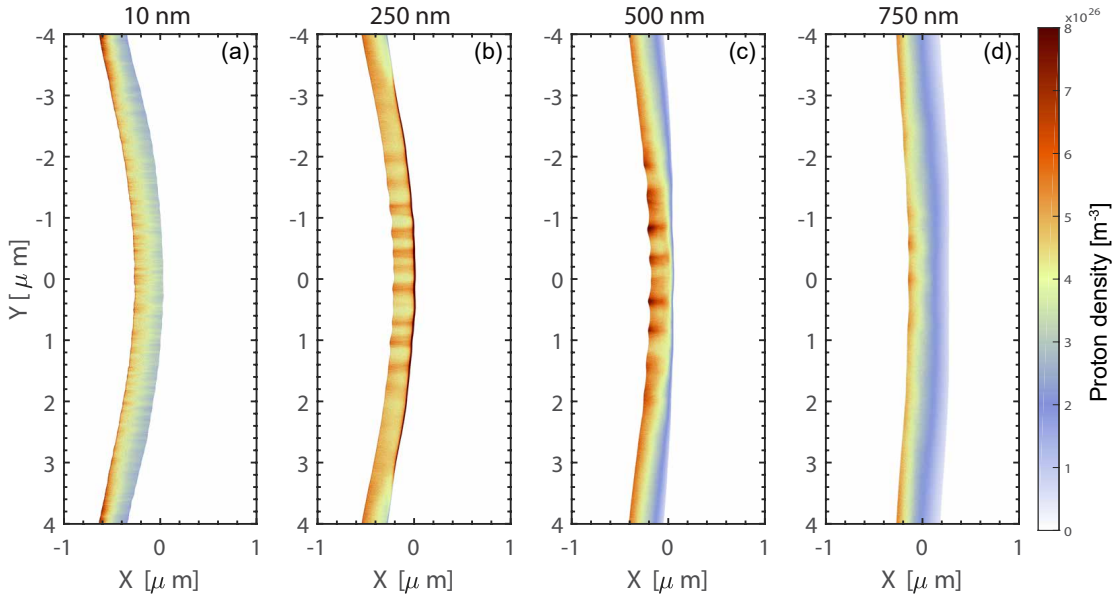

Figure 6.24: 2D PIC simulation results of proton density for varying degrees of target pre-expansion. (a) No pre-expansion and (b)-(d) Gaussian density profiles with FWHM equal to (b) 250 nm, (c) 500 nm and (d) 750 nm. Modulations in the proton density are observed as the level of pre-expansion is increased, but decrease again at 750 nm.

in figure 6.24 (c) was measured to be 0.2 μm, i.e. twice that of the filaments in figure 6.24 (b). Similarly, the average void-width was found to be $\sim$0.2 μm in (b) and $\sim$0.32 μm in (c), and the number of filaments formed is found to be greater in (b) than in (c). Further increase of the target pre-expansion, shown in figure 6.24 (d), again results in the filaments disappearing. Thus, the long wavelength modulation of the transverse electron momentum exhibited in figure 6.23 (d) leads to negligible filamentation of the proton beam.

6.4.4 Effect of target decompression on filamentary magnetic field growth

Finally, the effect of target density decompression on the structure of the self-generated magnetic fields produced in the interaction was investigated via 2D PIC simulations. The presence of rear-side plasma results in strong filamentary patterns in both the electron and proton populations, and is shown by Göde *et al.* [144] to develop via the relativistic WI. The effect of varying the degree of decompression on magnetic field growth is now examined; in particular, the transition from the Biermann battery mechanism to the WI as the progenitor of self-generated magnetic fields [143].

The magnetic fields were sampled at a time of 50 fs after the simulation was initialised, and lineouts of the magnetic field distribution were extracted at a distance of 190 nm

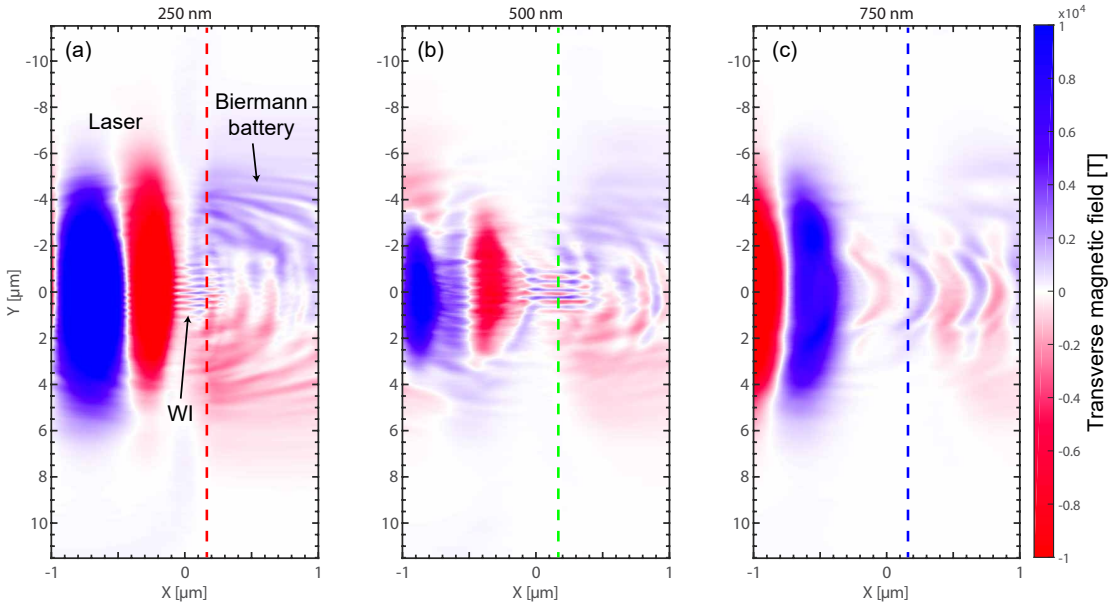

Figure 6.25: Magnetic field maps obtained from 2D PIC simulations, sampled at a time of 50 fs. The target was pre-expanded to (a) 250 nm; (b) 500 nm; and (c) 750 nm. As the degree of decompression increases from (a) to (b), the WI-driven filament size observed along the Y=0 axis increases. No filaments are observed in (c).

from the target front surface. This position was selected as it was located in the centre of the observed filamented magnetic field distributions. Simulation results in the [X-Y] plane are shown in figure 6.25. For the case of target decompression to 250 nm (figure 6.25 (a)), a large number of fine filaments are visible in the sample region, weakly extending out to the far end of the simulation box. A large scale, azimuthal magnetic field is also observed extending from the rear of the target. The degree of decompression in this case is comparatively smaller than in figures 6.25 (b) and (c). Thus, large scale, azimuthal fields, such as those associated with the Biermann battery mechanism are observed. The high electron density due to the small degree of decompression results in the generation of a large number of small filaments, with the result being many, small bubble-like structures measured downstream of the target. The low level of decompression for the 250 nm case also results in the generation of global magnetic fields driven by the Biermann battery mechanism, which given the correct conditions, will result in the generation of a collimated electron jet [34]. The strength of the Biermann battery-driven magnetic fields appears to exceed those of the WI-driven fields. As the degree of pre-expansion increases to 500 nm, the number of filaments generated decreases. The filament number is approximately halved and the transverse size of the filaments increases, in agreement with the experimental data (figure 6.17). The filamentary magnetic field in this case extends out to both edges of the

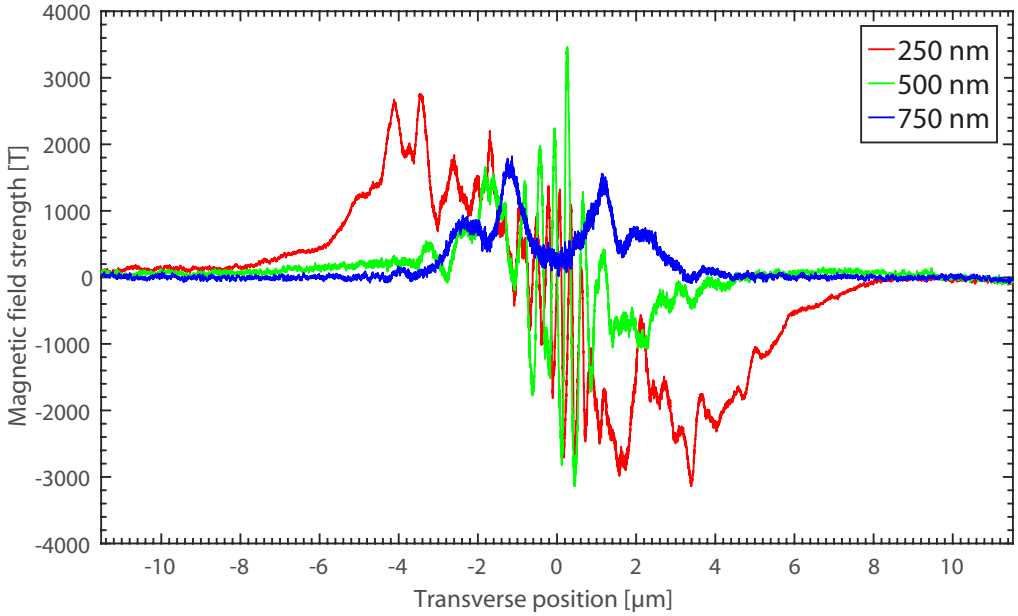

Figure 6.26: Lineouts sampled from the magnetic field maps in figure 6.25. The colours of the plots correspond to the dashed lines indicating the sampled regions in figure 6.25.

simulation box. The presence of a global, azimuthal magnetic field is still observed at the target rear, but it is relatively weaker than the WI-driven field. Further increasing the degree of compression to 750 nm (figure 6.25 (c)), results in the disappearance of the magnetic field structures driven by both mechanisms. The differences, between the cases presented in figure 6.25, are quantified via the lineouts in figure 6.26, which correspond to the coloured dashed lines in figure 6.25. This clearly demonstrates that the frequency of the magnetic modulations in the region at the centre of the target is greatest for the low expansion case. In addition, the extent of the global azimuthal Biermann battery-driven magnetic fields is also measured to be highest for this expansion case.

The frequency of the perturbations is observed to decrease as the target is pre-expanded to 500 nm, with the WI-driven magnetic fields centred on the middle of the target being of a longer wavelength than for the 250 nm case. Here, the magnetic field strengths generated in this region are also comparatively higher than for a target decompression of 250 nm. Similar periodic modulations are observed in the large-scale magnetic field as before, but the transverse extent of the field is decreased from those seen previously. The reduction of the signatures of the Biermann battery mechanism indicates the dominance of the WI as the mechanism for the self-generation of magnetic fields with increased target decompression, in agreement with the findings of Schoeffler *et al.* [136, 143] and Göde

et al. [144]. In the final case, of pre-expansion of 750 nm, no signatures of either the WI or Biermann battery mechanisms are evident. This is clear from the lack of high frequency modulations present at the zero position corresponding to the centre of the target (indicative of WI-driven magnetic fields). Thus, it can be seen that if the degree of target decompression is too large, then the conditions for the self-generation of magnetic fields are not optimal.

6.5 Conclusions

To conclude, the generation of astrophysically relevant magnetic field structures has been investigated in intense laser-plasma interactions with ultrathin foils expanded to near-critical density. The first half of this chapter (section 6.2) focused on the production of a jet of superthermal electrons, formed at the onset of RSIT. Whilst previous work was concerned with the influence of the jet on the maximum energy and spatial-intensity profile of the beam of accelerated protons [200], the present investigation focused on the characterisation of the jet properties and specifically, the azimuthal magnetic field surrounding it. This study was carried out using transverse optical probe diagnostics, utilising shadowgraphy and polarimetry techniques. The results demonstrate that a strong azimuthal magnetic field acts to collimate the electron jet. Electrons within the jet are directly accelerated by the co-propagating part of the laser pulse. This results in an enhancement in the electrostatic field, and hence the energy of the protons located in its vicinity. The direct observation of a plasma channel, a few microns wide, suggested the remnants of an expanding plasma jet. Direct imaging of the jet was not possible due to the late timescales at which the interaction was probed. The presence of the strongest magnetic fields and the plasma channel were observed for the case of CH targets with a thickness, l =90 nm. For l <90 nm, the target decompression occurs very rapidly and the onset of transparency occurs too early in the interaction for efficient volumetric heating of the electron population to occur. In such a scenario, additional acceleration of the proton population in the vicinity of the jet will not take place. For l >90 nm, the degree of transmission through the target rapidly decreases and the jet is not formed.

The scaling of the plasma jet parameters was considered to explore the possibility to use jets generated upon the onset of RSIT in intense laser-solid experiments with ultrathin foils as a platform for laboratory investigations of relativistic plasma astrophysics. The

analysis performed was based on the method employed in Gonzalez-Izquierdo *et al.* [64] with reference to the work in Ryutov *et al.* [221]. It was demonstrated via dimensionless scaling that the electron jet produced in the experimental campaign could not be compared to astrophysical jets launched from YSOs. However, through careful selection of the experimental parameters [62, 330] the interaction could be tailored in such a way that enables electron jets generated at the onset of RSIT to be employed as laboratory analogues of jets expelled from YSOs. It was then demonstrated that scaling laws could be applied to the laboratory scenario that would enable comparison with jets collimated by AGNs. The scaling-ratio determined through the use of these laws was applied to determine the expected magnetic field strength in the experiment. However, the value does not agree well with the measured magnetic field [327]. The measured magnetic field was probed at a time of 25 ps after the interaction, when the field is decreasing (no longer supported by the 1 ps laser pulse). This highlights the necessity of earlier-time measurements, in order to characterise the peak magnetic field strength.

The second half of this chapter (section 6.4) concerns the role of the WI in the growth of self-generated magnetic fields. The presence of bubble-like structures in proton beams accelerated from ultrathin targets (l =10 nm Al) was observed in several experimental investigations of ion acceleration. This had previously been attributed to Rayleigh-Taylor-like transverse instabilities at the front of the target [44, 159]. However, recent investigations [45, 143, 144] have shown that the presence of a rear-surface pre-plasma during the course of high power laser-plasma interactions can result in the formation of spatial modulations in the beam of accelerated protons, leading to bubble-like structures, as described in references [44] and [159]. These observations appeared to be in good agreement with experimental results reported here which show that bubbles are produced only on shots for which a controlled pre-pulse was employed to decompress the target prior to the arrival of the main intense pulse. It was demonstrated that bubble-like structures are strongest for an optimum target decompression. These observations are in agreement with the findings of Gode *et al.* [144], which report that the dominant mechanism for the generation of magnetic fields is dependent on the degree of decompression of the target. Targets subject to a low-level of pre-expansion exhibit signatures of the Biermann battery process, whereas the dominant mechanism in highly decompressed targets is the Weibel instability. The degree of the partition of energy between the controlled pre-pulse and the main interaction pulse was used to alter the dynamics of plasma expansion such that the number of the

bubble-like structures was varied.

A numerical study, performed to investigate the underlying physics of the growth of self-generated magnetic fields with parameters relevant to the experimental investigation, demonstrates that the degree of target pre-expansion plays a significant role on the degree of filamentation of the electron and proton populations. It was found that modulations in the magnetic field distributions, and the electron momenta and consequently proton densities, decrease in frequency as the degree of target decompression is increased. This results in a higher number of small filaments being produced for low degrees of pre-expansion, leading to the production of a large number of small bubble-like structures in projected proton beam. As the level of pre-expansion is increased, the number of filaments, and thus bubbles, decrease, whilst the size of both increases accordingly. Simulations of the magnetic field distribution for varying degrees of target decompression demonstrate an interplay between the Biermann battery and the WI magnetic field generation mechanisms. Increasing the degree of pre-expansion reduces the presence and extent of global, azimuthal magnetic fields (such as those generated by the Biermann battery), whilst WI-generated fields began to dominate.

The process by which magnetic fields are seeded from initially unmagnetised plasma is a pertinent question in both the astrophysical and laboratory scenarios. In some systems, seed fields may already be present, for example in supernova remnants or quasars [335]. In the early universe however, there was an absence of magnetic fields [138]. The Biermann battery mechanism has been invoked as the progenitor of magnetic fields in the absence of a seed, and has been confirmed as a driver for self-generated magnetic fields in the context of laser-plasma interaction experiments [336]. Weibel-like instabilities have been previously shown to generate, and amplify, strong magnetic fields in astrophysical scenarios [129], particularly in supporting the propagation of astrophysical jets [141].

The large-scale, azimuthal magnetic field collimating relativistic astrophysical jets [131] is believed to arise from the motion of accretion disks that are associated with the compact objects from which the jet is launched. The distribution of the fields generated by these structures is qualitatively similar to those observed in this investigation at the target rear surface when the production of plasma jets has been inferred.

Chapter 7

Conclusions and discussion

7.1 Summary of results

The underlying theme of this thesis is the investigation of the generation of strong magnetic fields in intense laser-solid interactions. This was explored via experimental and numerical investigations of self-generated magnetic field growth. The first part (**Chapter 5**) focused on investigating resistive self-generated magnetic fields in relatively thick solid foils and their influence on fast electron dynamics. The target bulk is heated to produce a transient state of warm dense matter, with equivalent temperatures to those at the core of some planets. This was then followed, in **Chapter 6**, by two interlinked investigations of magnetic field generation in ultrathin foils expanding to near-critical densities. The former involved the production of a jet of superthermal electrons formed upon the onset of RSIT, and confined by a magnetic field produced by the Biermann battery mechanism. The latter explored the role of the WI on the growth of self-generated magnetic fields in targets subject to a significant degree of decompression prior to the arrival of the intense pulse.

The conditions measured in the investigations presented in **Chapter 5** and in the latter portion of **Chapter 6** resemble warm dense matter (WDM) states found in planetary or brown dwarf interiors, and planetary nebulae and supernova (SNe) remnants, respectively. In addition, measurements of the electron jet in **Chapter 6** presented an opportunity to examine the feasibility of employing this experimental set-up to produce analogues of relativistic plasma jets observed in astrophysical scenarios.

This final chapter summarises the key results from each investigation and discusses the main conclusions, together with potential directions for future research.

7.2 Role of resistive self-generated magnetic fields in relativistic electron beam propagation in dense plasma

The investigations presented in **Chapter 5** built upon previous studies of fast electron transport in solid targets [53, 54, 128, 288] by investigating the influence of material lattice structure and the profile of the electrical resistivity at low temperatures (i.e. below 100 eV) on the production of self-generated resistive magnetic fields. In section 5.2, the transport of fast electrons was explored via three-dimensional hybrid-particle-in-cell (PIC) simulations in single-species lithium and silicon targets. This addressed a major factor influencing the global fast electron transport properties in solid density targets, namely the importance of the shape of the resistivity-temperature (η-T) profile. This was investigated by varying the magnitude of the peak resistivity for lithium; and the magnitude and position of the minimum resistivity for silicon. In the case of lithium, it was demonstrated that, as the magnitude of η increases, there is a transition from an ordered to a disordered fast electron spatial-intensity distribution, with increasing degree of filamentary structure. Similarly, for silicon, a transition from an annular to a filamented fast electron transport spatial-intensity distribution was observed as the minimum value of η, at the characteristic η-dip associated with semiconductor materials, increased. Furthermore, it was shown that the temperature at which this dip is located is a major influence on the diameter of the annular fast electron beam structure previously observed in ordered silicon targets [128, 288]. Thus, it was concluded that even subtle features in the η-T profile, at low temperatures, profoundly alters fast electron transport, due to the resulting changes in the self-generated resistive magnetic fields.

Following this, a discussion on the feasibility of scaling the annular fast electron beams produced in silicon targets to the parameters required for the fast ignition (FI) scheme for inertial confinement fusion (ICF) was presented. Davies [292] previously showed that the propagation of an annular fast electron beam, with the parameters required for FI, enabled the maximum current transported to be increased compared to that of a uniform beam, in addition to mitigating the rapid resistive decay of the return current. Furthermore, Hatchett *et al.* [165] numerically demonstrated reduced driver energy requirements when employing annular beams for FI.

In section 5.3, the influence of low temperature resistivity on the onset of the resistive filamentation instability in carbon targets was investigated. The targets employed

were composed of layers of ordered and disordered carbon. Experimental measurements of the spatial-intensity distributions of the TNSA proton beams were employed to infer that the thickness of the disordered carbon layer influences the degree of filamentation of the fast electron beam for an electron distribution driven by a sub-picosecond, mid-10^{20} W/cm^2 pulse. Corresponding three-dimensional hybrid-PIC simulations, combined with analytical modelling of the subsequent ion acceleration, provided good agreement with the experimental measurements. Further simulations were performed investigating the dependence of the thickness of the disordered carbon layer on the growth of the resistive filamentation instability. Strong filamentation was measured if the thickness of the layer was of the order of 60 μm or greater. Moreover, the location of the layer within the target was found to be inconsequential to the growth of resistive filamentation. This was demonstrated to be consistent with the predictions of a simple linear resistive instability model [117, 148], taking into account the differences in filamentation observed in the two allotropes of carbon.

7.3 Generation of astrophysically relevant magnetic field structures in expanding foils

In **Chapter 6**, two studies investigating the influence of self-generated magnetic fields on the dynamics of fast electrons in the interaction of intense laser pulses with ultrathin foils expanding to near-critical density were presented, building upon previous studies of ion acceleration from ultrathin solid targets [34, 253]. The salient outcome of these studies was that the onset of RSIT is accompanied by the formation of a jet of superthermal electrons extending into the sheath-accelerated ions, collimated by a strong, azimuthal magnetic field. Due to the co-propagation of the transmitted portion of the intense laser pulse with this jet, the electrons are directly accelerated to energies significantly higher than the background plasma. Sheath-accelerated protons in the vicinity of the jet are subsequently driven to increased energies, compared to those of the TNSA regime, resulting in the the measurement of a low-divergence, high-energy component of the proton beam. Furthermore, the presence of bubble-like filamentary structures was measured in beams of accelerated protons from targets that had undergone significant decompression prior to the arrival of the main pulse.

The motivation for the investigations presented in **Chapter 6** was threefold: (1) the

characterisation of the self-generated magnetic fields produced in the interaction, and their influence on the relativistic plasma jet; (2) investigation of the mechanism by which magnetic fields are generated in intense laser-solid interactions; and (3) exploration of the extension of the resulting measurements to analogues of astrophysical phenomena.

The investigation presented in section 6.2 explored characterisation of the jet and the conditions under which it is produced during the onset of RSIT. Optimal target conditions were determined for the most efficient coupling of energy from the electrons in the jet to the sheath-accelerated protons. It was demonstrated that, in this optimal target thickness range, RSIT occurs at the peak of the incident pulse and thus, the most intense portion of the pulse is transmitted upon the onset of RSIT. This produces a greater direct acceleration than if RSIT occurrs early in the interaction (in which case the majority of the laser light is transmitted without efficient coupling to electrons) or later (in which case, a lower intensity portion of the pulse would be transmitted). Furthermore, the level of target decompression for target thicknesses less than the optimal range results in the dominant mechanism for the generation of strong magnetic fields transitioning from the Biermann battery mechanism to the Weibel instability [136, 143].

Unfortunately, direct imaging of the electron jet was not possible due to the late timescales at which the interaction was probed, though its presence was inferred by measurements of a low-divergence proton population in proton radiography measurements and the observation of a channel, formed in the plasma expanding from the target rear. Transverse optical probe polarimetry measurements were used to characterise the azimuthal magnetic field strength surrounding the electron jet, and it was demonstrated that the strongest magnetic fields were measured in the optimum range of target thickness for RSIT occuring near the laser pulse peak. Measurements of the flux of electrons accelerated in the interaction show a similar trend to the measurement of magnetic field strength as a function of target thickness. These results demonstrate the requirement for further, detailed measurements on the generation and evolution of the electron jet. More specifically, earlier-time, transverse optical measurements of the interaction are needed to directly the image the structure of the jet itself in order to enable the indirect experimental evidence of the presence of an electron jet to be reconciled with direct imaging of the phenomena.

An analysis of the measured parameters of the electron jet was performed to test the potential future employment of intense laser-ultrathin foil interactions as a laboratory platform for the generation of analogues of astrophysical relativistic plasma jet phenomena.

An analysis based on the magnetohydrodynamic scaling in Ryutov *et al.* [220, 221] was performed on the relativistic electron jet. The jet was compared to two astrophysical scenarios: parsec-scale jets typical of those launched from young stellar objects (YSOs) and Mega-parsec, relativistic jets associated with active galactic nuclei (AGNs). Common to both scenarios, regardless of the progenitor, is the association of jet formation with rotating accretion disks, generating large-scale magnetic field structures that act to collimate the matter ejected from the parent object. Similarly, the presence of a strong, azimuthal magnetic field extending from the target rear was measured experimentally, providing analogous mechanisms for the collimation of the laboratory jets. The relatively slower YSO jets were found to not present a great deal of similarity to the laboratory analogues. However, good agreement was shown to exist with AGN jets. A length scale-ratio between the two cases of $L*=2\times10^{27}$ was determined. Applying this ratio to the lifetime of the AGN jet resulted in a laboratory interaction timescale of 500 fs which is in good agreement with the experiment pulse duration. This demonstrates that there may be sufficient similarities to enable future laboratory exploration of the physics of the formation of jets originating from AGNs. Further application of this scaling to the magnetic field strengths did not reproduce the fields measured experimentally. However, the measurement was made at a late time, long after the interaction, which accounts for the disagreement. This highlights the requirement for further, detailed measurements on the generation and evolution of the relativistic electron jet.

Following this, an investigation of the role of the Weibel instability on the growth of self-generated magnetic fields was presented, in section 6.4. Bubble-like filamentary structures were measured in the spatial-intensity distribution of protons in intense laser interactions with ultrathin, solid density targets [34, 44]. The generation of these structures had been attributed to Rayleigh-Taylor-like instabilities in the interaction region [44]. However, recent investigations [45, 143, 144] have postulated that the dominant mechanism for the formation of these structures is the growth of the Weibel instability. This was postulated as a result of the observation that bubble-like structures in the proton beam were only observed when there was a degree of decompression of the target, and thus the presence of a pre-plasma prior to the arrival of the main intense pulse. The experimental measurements in section 6.4.2 are in good agreement with this hypothesis.

A numerical investigation of the underlying physics of the formation of the filamentary proton structures was undertaken. It was demonstrated that target decompression plays

a key role in the self-generation of magnetic fields during the interaction: the Biermann battery mechanism dominates for the case of a small degree of decompression, whilst the Weibel instability dominates for large pre-expansion, in agreement with the findings of Gode *et al.* [144]. Filamentary magnetic fields, similar in appearance to those generated by the Weibel instability were observed for large degrees of target decompression. These structures disappeared when targets with minimal pre-expansion were investigated. Thus, it is concluded that the Weibel instability mechanism drives the filamentation of the fast electrons, and subsequently protons, in targets exhibiting significant decompression prior to the main pulse.

7.4 Future work

The field of high intensity laser-foil interaction physics is closely intertwined with developments in laser technology. As new techniques and mechanisms are developed, enabling peak intensities in the range of 10^{22}-10^{23} W/cm^2, new avenues of research will be opened will up. The advent of new, multi-Petawatt facilities such as the Extreme Light Infrastructure (ELI) [15], APOLLON [337] and the proposed Omega EP OPAL upgrade [16] will enable new regimes of ion acceleration and high-energy radiation production to be investigated.

In **Chapter 5**, it was demonstrated that the shape and magnitude of the resistivity-temperature profile at temperatures has a significant influence on the growth of self-generated resistive magnetic fields, and therefore resistive instabilities, during the propagation of fast electrons through the target. One potential method for experimentally exploring the role played by the low-temperature η could be to introduce dopants, artificially tailoring the η-T profile. A detailed study of fast electron transport employing both pure and doped semiconductor targets could be undertaken. A similar investigation of the dependence of fast electron beam filamentation on the laser parameters would also provide critical information on the growth of resistive instabilities. Thus, the material and laser parameters which reduce (or enhance) the impact of fast electron beam filamentation could be verified; this is a topic of great importance for various applications, including the FI approach to ICF.

Furthermore, the deployment of double-layer targets, comprising different allotropes of the same material, with orientations parallel to the fast electron propagation direction

present a potential mechanism for control of the fast electron beam properties. Utilising the differential growth rates of the resistive filamentation instability in the layers, and associated magnetic field growth at their boundaries, could provide a tool for enacting control over the fast electron divergence, without recourse to varying the laser parameters.

In **Chapter 6**, characterisation of the formation of a jet of superthermal electrons, generated at the onset of RSIT, was presented. Presently, the jet forms only up to the plasma boundary and is subject to hosing instabilities which affect its directionality. The injection of the jet into a secondary target or background plasma may present a method by which the length of the jet could be extended and its directionality controlled. By injecting the jet into a micron-thick solid target, collimated fast electron transport may be induced, which may be of interest as a possible driver for advanced fusion schemes. In addition, the injection of the jet into an ambient medium or foam target may enable further exploration of laboratory analogues of astrophysical phenomena, via the simulation of astrophysical jets into, for example, interstellar media or planetary nebulae, producing phenomena such as streaming instabilities or collisionless shocks.

Furthermore, a detailed investigation on the mechanism of magnetic field generation in intense laser interactions with near-critical density targets would enable an experimental verification of the conditions corresponding to the specific mechanisms for the generation of the magnetic field to be determined. The dependence of the Biermann battery and the Weibel instability on the laser and target parameters could be investigated via extensive measurements of the magnetic field distribution. Thus, the dominant mechanism for the generation of the magnetic field could be determined. The structures arising from the action of the magnetic fields are qualitatively similar to those observed in astrophysical scenarios, such as supernova remnants. Therefore, characterisation of the features measured in the laboratory could be of great interest to the field of laboratory astrophysics.

Bibliography

[1] M. Brand, S. Neaves, *et al.* Lodestone. Museum of Electricity and Magnetism, Mag Lab U. US National High Magnetic Field Laboratory., 1995. Last accessed 13/11/2017.

[2] E. Whittaker. A History of the Theories of Aether and Electricity: Vol. I: The Classical Theories; Vol. II: The Modern Theories, 1900-1926, volume 1. Courier Dover Publications, 1951.

[3] J. Maxwell. On physical lines of force. *The London, Edinburgh, and Dublin Philosophical Magazine and Journal of Science*, 21 & 23(140):14,15, 1864.

[4] M. Borghesi, A. J. Mackinnon, *et al.* Large quasistatic magnetic fields generated by a relativistically intense laser pulse propagating in a preionized plasma. *Phys. Rev. Lett.*, 80:5137–5140, 1998.

[5] R. J. Mason and M. Tabak. Magnetic field generation in high-intensity-laser˘matter interactions. *Phys. Rev. Lett.*, 80:524–527, 1998.

[6] A. Einstein. Zur quantentheorie der strahlung. *Phys. Z.*, 18:121–128, 1917.

[7] T. H. Maiman. Stimulated optical radiation in ruby. *Nature*, 187(4736):493–494, 1960.

[8] J. P. Gordon, H. J. Zeiger, *et al.* The maser - new type of microwave amplifier, frequency standard, and spectrometer. *Phys. Rev.*, 99:1264–1274, 1955.

[9] A. Javan, W. R. Bennett, *et al.* Population inversion and continuous optical maser oscillation in a gas discharge containing a He-Ne mixture. *Phys. Rev. Lett.*, 6:106–110, 1961.

[10] R. N. Hall, G. E. Fenner, *et al.* Coherent light emission from GaAs junctions. *Phys. Rev. Lett.*, 9:366–368, 1962.

[11] F. McClung and R. Hellwarth. Giant optical pulsations from ruby. *Appl. Opt.*, 1(101):103–105, 1962.

[12] L. Hargrove, R. L. Fork, *et al.* Locking of He–Ne laser modes induced by synchronous intracavity modulation. *Appl. Phys. Lett.*, 5(1):4–5, 1964.

[13] C. Joshi, M. Richardson, *et al.* Quantitative measurements of fast ions from CO2 laser-produced plasmas. *Appl. Phys. Lett.*, 34(10):625–627, 1979.

[14] D. Strickland and G. Mourou. Compression of amplified chirped optical pulses. *Opt. Commun.*, 56(3):219 – 221, 1985.

[15] G. Korn, B. LeGarrec, *et al.* ELI extreme light infrastructure science and technology with ultra-intense lasers. In *CLEO: 2013*, page CTu2D.7. Optical Society of America, 2013.

[16] J. D. Zuegel. Status of high-energy opcpa at lle and future prospects. In *CLEO: 2014*, page JTh4L.4. Optical Society of America, 2014.

[17] J. Nuckolls, L. Wood, *et al.* Laser compression of matter to super-high densities: Thermonuclear (CTR) applications. *Nature*, 239(5368):139–142, 1972.

[18] J. Lindl. Development of the indirect-drive approach to inertial confinement fusion and the target physics basis for ignition and gain. *Phys. Plasmas*, 2(11):3933–4024, 1995.

[19] M. Tabak, J. Hammer, *et al.* Ignition and high gain with ultrapowerful lasers. *Phys. Plasmas*, 1(5):1626–1634, 1994.

[20] P. Norreys, R. Allott, *et al.* Experimental studies of the advanced fast ignitor scheme. *Phys. Plasmas*, 7(9):3721–3726, 2000.

[21] R. l. Kodama, H. Shiraga, *et al.* Nuclear fusion: Fast heating scalable to laser fusion ignition. *Nature*, 418(6901):933–934, 2002.

[22] A. Macchi, M. Borghesi, *et al.* Ion acceleration by superintense laser-plasma interaction. *Rev. Mod. Phys.*, 85(2):751–793, 2013.

[23] M. Borghesi and A. Macchi. Laser-Driven Ion Accelerators: State of the Art and Applications, pages 221–247. Springer International Publishing, Cham, 2016.

[24] C. M. Brenner, S. R. Mirfayzi, *et al.* Laser-driven x-ray and neutron source development for industrial applications of plasma accelerators. *Plasma Phys. Controlled Fusion*, 58(1):014039, 2015.

[25] C. P. Jones, C. M. Brenner, *et al.* Evaluating laser-driven bremsstrahlung radiation sources for imaging and analysis of nuclear waste packages. *J. Hazard. Mater.*, 318:694–701, 2016.

[26] R. Deas, L. Wilson, *et al.* A laser driven pulsed x-ray backscatter technique for enhanced penetrative imaging. *J. Xray Sci*, 23(6):791–797, 2015.

[27] B. A. Remington. Laboratory astrophysics on high power lasers and pulsed power facilities. In *American Association Advancement of Science Annual Meeting and Science Innovation Exposition*, 2002.

[28] R. Drake. Laboratory experiments to simulate the hydrodynamics of supernova remnants and supernovae. *J. Geophys. Res.: Space Physics*, 104(A7):14505–14515, 1999.

[29] S. Rose. High-power laser-produced plasmas and astrophysics. *Laser Part. Beams*, 9(4):869–879, 1991.

[30] H. Takabe. Astrophysics with intense and ultra-intense lasers laser astrophysics. *Progr. Theor. Exp. Phys. Supplement*, 143:202–265, 2001.

[31] B. A. Remington, R. P. Drake, *et al.* Experimental astrophysics with high power lasers and z pinches. *Rev. Mod. Phys.*, 78(3):755–807, 2006.

[32] N. Booth, A. Robinson, *et al.* Laboratory measurements of resistivity in warm dense plasmas relevant to the microphysics of brown dwarfs. *Nat Commun.*, 6, 2015.

[33] S. Palaniyappan, C. Huang, *et al.* Efficient quasi-monoenergetic ion beams from laser-driven relativistic plasmas. *Nat. Commun.*, 6:10170, 2015.

[34] H. W. Powell, M. King, *et al.* Proton acceleration enhanced by a plasma jet in expanding foils undergoing relativistic transparency. *New J. Phys.*, 17(10):103033, 2015.

[35] E. Oks, E. Dalimier, *et al.* Using x-ray spectroscopy of relativistic laser plasma interaction to reveal parametric decay instabilities: a modeling tool for astrophysics. *Opt. Express*, 25(3):1958, 2017.

[36] J. Colgan, A. Y. Faenov, *et al.* Evidence of high-n hollow ion emission from si ions pumped by ultraintense x-rays from relativistic laser plasma. *Europhys. Lett.*, 114(3), 2016.

[37] S.-C. Yoon and N. Langer. Helium accreting CO white dwarfs with rotation: Helium novae instead of double detonation. *Astron. Astrophys.*, 419(2):645–652, 2004.

[38] F. J. Rogers, C. A. Iglesias, *et al.* Astrophysical opacity. *Science*, 263(5143):50–54, 1994.

[39] T. Perry, S. Davidson, *et al.* Opacity measurements in a hot dense medium. *Phys. Rev. Lett.*, 67(27):3784, 1991.

[40] P. Springer, K. Wong, *et al.* Laboratory measurement of opacity for stellar envelopes. *J. Quant. Spectrosc. Radiat. Transfer*, 58(4-6):927–935, 1997.

[41] E. J. Lentz, E. Baron, *et al.* Analysis of type iin sn 1998s: effects of circumstellar interaction on observed spectra. *Astrophys. J*, 547(1):406, 2001.

[42] E. Fermi. On the origin of the cosmic radiation. *Phys. Rev.*, 75(8):1169, 1949.

[43] V. Ginzburg and S. Syrovatskii. The secondary electron component of cosmic rays and the spectrum of general galactic radio emission. *Soviet Astronomy*, 8:342, 1964.

[44] C. A. J. Palmer, J. Schreiber, *et al.* Rayleigh-taylor instability of an ultrathin foil accelerated by the radiation pressure of an intense laser. *Phys. Rev. Lett.*, 108(22), 2012.

[45] C. M. Huntington, F. Fiuza, *et al.* Observation of magnetic field generation via the weibel instability in interpenetrating plasma flows. *Nat. Phys.*, 11(2):173–176, 2015.

[46] J. J. Hester, J. M. Stone, *et al.* WFPC2 studies of the crab nebula. III. magnetic rayleigh-taylor instabilities and the origin of the filaments. *Astrophys. J.*, 456:225, 1996.

[47] R. Drake, S. Glendinning, *et al.* Observation of forward shocks and stagnated ejecta driven by high-energy-density plasma flow. *Phys Rev Lett*, 81(10):2068, 1998.

[48] G. Gregori, A. Ravasio, *et al.* Generation of scaled protogalactic seed magnetic fields in laser-produced shock waves. *Nature*, 481(7382):480, 2012.

[49] J. Meinecke, H. Doyle, *et al.* Turbulent amplification of magnetic fields in laboratory laser-produced shock waves. *Nat. Phys.*, 10(7):520–524, 2014.

[50] H. Ahmed, M. E. Dieckmann, *et al.* Time-resolved characterization of the formation of a collisionless shock. *Phys. Rev. Lett.*, 110:205001, 2013.

[51] T. Lay, J. Hernlund, *et al.* Core–mantle boundary heat flow. *Nat. Geosci.*, 1(1):25–32, 2008.

[52] A. Denoeud, N. Ozaki, *et al.* Dynamic x-ray diffraction observation of shocked solid iron up to 170 gpa. *Proc. Natl. Acad. Sci. U.S.A*, 113(28):7745–7749, 2016.

[53] M. N. Quinn, D. C. Carroll, *et al.* On the investigation of fast electron beam filamentation in laser-irradiated solid targets using multi-mev proton emission. *Plasma Phys. Cont. Fusion*, 53(12):124012, 2011.

[54] P. McKenna, A. P. L. Robinson, *et al.* Effect of lattice structure on energetic electron transport in solids irradiated by ultraintense laser pulses. *Phys. Rev. Lett.*, 106(18), 2011.

[55] R. Laing, A. Bridle, *et al.* Physics of energy transport in radio galaxies. In *NRAO Workshop no. 9*, page 90. NRAO, 1984.

[56] T. Bührke, R. Mundt, *et al.* A detailed study of HH 34 and its associated jet. *Astron. Astrophys.*, 200:99–119, 1988.

[57] R. Blandford and D. Payne. Hydromagnetic flows from accretion discs and the production of radio jets. *Mon. Not. R. Astron. Soc.*, 199(4):883–903, 1982.

[58] K. Asada, M. Inoue, *et al.* A helical magnetic field in the jet of 3c 273. *Publ. Astron. Soc. Jpn.*, 54(3):L39–L43, 2002.

[59] L. Logory, P. Miller, *et al.* Nova high-speed jet experiments. *Astrophys. J. Supplement Series*, 127(2):423, 2000.

[60] J. Foster, B. Wilde, *et al.* High-energy-density laboratory astrophysics studies of jets and bow shocks. *Astrophys. J. Lett.*, 634(1):L77, 2005.

[61] P. Nilson, L. Willingale, *et al.* Magnetic reconnection and plasma dynamics in two-beam laser-solid interactions. *Phys Rev Lett*, 97(25):255001, 2006.

[62] C. D. Gregory, J. Howe, *et al.* Astrophysical jet experiments with colliding laser-produced plasmas. *Astrophys. J.*, 676(1):420, 2008.

[63] G. Sarri, A. Macchi, *et al.* Dynamics of self-generated, large amplitude magnetic fields following high-intensity laser matter interaction. *Phys. Rev. Lett.*, 109:205002, 2012.

[64] B. Gonzalez-Izquierdo, R. J. Gray, *et al.* Optically controlled dense current structures driven by relativistic plasma aperture-induced diffraction. *Nat Phys*, 12(5):505–512, 2016.

[65] M. W. Pound. Molecular gas in the eagle nebula. *The Astrophysical Journal Letters*, 493(2):L113, 1998.

[66] E. Waxman and B. T. Draine. Dust sublimation by gamma-ray bursts and its implications. *The Astrophysical Journal*, 537(2):796, 2000.

[67] R. I. Klein, K. S. Budil, *et al.* Interaction of supernova remnants with interstellar clouds: From the nova laser to the galaxy. *The Astrophysical Journal Supplement Series*, 127(2):379, 2000.

[68] H. F. Robey, T. S. Perry, *et al.* Experimental investigation of the three-dimensional interaction of a strong shock with a spherical density inhomogeneity. *Phys. Rev. Lett.*, 89:085001, 2002.

[69] A. Gruzinov. Gamma-ray burst phenomenology, shock dynamo, and the first magnetic fields. *The Astrophysical Journal Letters*, 563(1):L15, 2001.

[70] G. Sarri, K. Poder, *et al.* Generation of neutral and high-density electron–positron pair plasmas in the laboratory. *Nat Commun*, 6, 2015.

[71] J. Warwick, T. Dzelzainis, *et al.* Experimental observation of a current-driven instability in a neutral electron-positron beam. *Phys. Rev. Lett.*, 119:185002, 2017.

[72] J. C. Maxwell. A dynamical theory of the electromagnetic field. *Philosophical Transactions of the Royal Society of London*, 155:459–512, 1865.

[73] P. A. Sturrock. Plasma Physics: An Introduction to the Theory of Astrophysical, Geophysical and Laboratory Plasmas. Cambridge University Press, 1994.

[74] R. D. Hazeltine and F. L. Waelbroeck. The Framework Of Plasma Physics (Frontiers in Physics). Westview Press, 1998.

[75] S. Eliezer. The Interaction of High-Power Lasers with Plasmas (Series in Plasma Physics). CRC Press, 2002.

[76] L. V. Keldysh. Ionization in the field of a strong electromagnetic wave. *J. Exp. Theor. Phys.*, 20(5):1307 – 1314, 1965.

[77] V. S. Popov. Tunnel and multiphoton ionization of atoms and ions in a strong laser field (keldysh theory). *Physics - Uspekhi*, 47(9):855 – 885, 2004.

[78] D. A. Hammer and N. Rostoker. Propagation of high current relativistic electron beams. *Phys. Fluids*, 13(7):1831–1850, 1970.

[79] F. N. Beg, A. R. Bell, *et al.* A study of picosecond laser-solid interactions up to 10^{19} Wcm^{-2}. *Phys. Plasmas*, 4(2):447–457, 1997.

[80] S. C. Wilks, A. B. Langdon, *et al.* Energetic proton generation in ultra-intense laser-solid interactions. *Phys. Plasmas*, 8(2):542–549, 2001.

[81] M. Hegelich, S. Karsch, *et al.* MeV ion jets from short-pulse-laser interaction with thin foils. *Phys. Rev. Lett.*, 89:085002, 2002.

[82] M. Roth, A. Blazevic, *et al.* Energetic ions generated by laser pulses: A detailed study on target properties. *Phys. Rev. ST Accel. Beams*, 5:061301, 2002.

[83] T. Topcu and F. Robicheaux. Dichotomy between tunneling and multiphoton ionization in atomic photoionization: Keldysh parameter γ versus scaled frequency Ω. *Phys. Rev. A*, 86:053407, 2012.

[84] O. Lundh, F. Lindau, *et al.* Influence of shock waves on laser-driven proton acceleration. *Phys. Rev. E*, 76:026404, 2007.

[85] L. Landau and E. Lifshitz. The theory of classical fields, 1962.

[86] J. E. Gunn and J. P. Ostriker. On the motion and radiation of charged particles in strong electromagnetic waves. I. motion in plane and spherical waves. *Astrophys. J.*, 165:523, 1971.

[87] J. S. Roman, L. Roso, *et al.* Evolution of a relativistic wavepacket describing a free electron in a very intense laser field. *J. Phys. B. At. Mol. Opt. Phys.*, 33(10):1869, 2000.

[88] J. D. Lawson. Lasers and accelerators. *IEEE Trans. Nucl. Sci.*, 26(3):4217–4219, 1979.

[89] P. Gibbon. Short Pulse Laser Interactions with Matter. Imperial College Press, 2005.

[90] A. Macchi. A Superintense Laser-Plasma Interaction Theory Primer. Springer Netherlands, 2013.

[91] J. Fuchs, J. C. Adam, *et al.* Transmission through highly overdense plasma slabs with a subpicosecond relativistic laser pulse. *Phys. Rev. Lett.*, 80:2326–2329, 1998.

[92] J. Fuchs, J. C. Adam, *et al.* Experimental study of laser penetration in overdense plasmas at relativistic intensities. II: Explosion of thin foils by laser driven fast electrons. *Phys. Plasmas*, 6(6):2569–2578, 1999.

[93] S. Palaniyappan, B. M. Hegelich, *et al.* Dynamics of relativistic transparency and optical shuttering in expanding overdense plasmas. *Nat. Phys.*, 8:763–769, 2012.

[94] A. Macchi, S. Veghini, *et al.* "Light sail" acceleration reexamined. *Phys. Rev. Lett.*, 103:085003, 2009.

[95] V. A. Vshivkov, N. M. Naumova, *et al.* Nonlinear electrodynamics of the interaction of ultra-intense laser pulses with a thin foil. *Physics of Plasmas*, 5(7):2727–2741, 1998.

[96] D. F. Price, R. M. More, *et al.* Absorption of ultrashort laser pulses by solid targets heated rapidly to temperatures 1-1000 eV. *Phys. Rev. Lett.*, 75:252–255, 1995.

[97] S. Wilks and W. Kruer. Absorption of ultrashort, ultra-intense laser light by solids and overdense plasmas. *IEEE J. Quantum Electron.*, 33(11):1954–1968, 1997.

[98] W. L. Kruer and K. Estabrook. JxB heating by very intense laser light. *The Physics of Fluids*, 28(1):430–432, 1985.

[99] J. R. Davies, M. Fajardo, *et al.* Filamented plasmas in laser ablation of solids. *Plasma Physics and Controlled Fusion*, 51(3):035013, 2009.

[100] W. Kruer. The physics of laser plasma interactions. Addison-Wesley Pub. Co. Inc.,Reading, MA, 1988.

[101] S. C. Wilks, W. L. Kruer, *et al.* Absorption of ultra-intense laser pulses. *Phys. Rev. Lett.*, 69:1383–1386, 1992.

[102] F. Brunel. Not-so-resonant, resonant absorption. *Phys. Rev. Lett.*, 59:52–55, 1987.

[103] L. M. Chen, J. Zhang, *et al.* Hot electron generation via vacuum heating process in femtosecond laser-solid interactions. *Phys. Plasmas*, 8(6):2925–2929, 2001.

[104] Y. Ping, R. Shepherd, *et al.* Absorption of short laser pulses on solid targets in the ultrarelativistic regime. *Phys. Rev. Lett.*, 100(8), 2008.

[105] P. Gibbon and A. R. Bell. Collisionless absorption in sharp-edged plasmas. *Phys. Rev. Lett.*, 68:1535–1538, 1992.

[106] A. R. Bell, J. R. Davies, *et al.* Fast-electron transport in high-intensity short-pulse laser-solid experiments. *Plasma Phys. Cont. Fusion*, 39(5):653, 1997.

[107] H. Alfven. On the motion and of cosmic and rays in interstellar and space. *Phys. Rev.*, 55(5):425–429, 1939.

[108] P. Norreys, D. Batani, *et al.* Fast electron energy transport in solid density and compressed plasma. *Nucl. Fusion*, 54(5):054004, 2014.

[109] V. T. Tikhonchuk. Interaction of a beam of fast electrons with solids. *Phys. Plasmas*, 9(4):1416–1421, 2002.

[110] A. R. Bell, A. P. L. Robinson, *et al.* Fast electron transport in laser-produced plasmas and the KALOS code for solution of the Vlasov-Fokker-Planck equation. *Plasma Phys. Cont. Fusion*, 48(3):R37, 2006.

[111] O. Embrus, A. Stahl, *et al.* Effect of bremsstrahlung radiation emission on fast electrons in plasmas. *New J. Phys.*, 18(9):093023, 2016.

[112] M. J. Berger, J. S. Coursey, *et al.* ESTAR, PSTAR, and ASTAR: Computer Programs for Calculating Stopping-Power and Range Tables for Electrons, Protons, and Helium Ions. NIST Physics Laboratory Gaithersburg, MD, 1999.

[113] S. Mazevet, J. Clérouin, *et al.* Ab-initio simulations of the optical properties of warm dense gold. *Phys. Rev. Lett.*, 95:085002, 2005.

[114] V. Recoules, J. Clérouin, *et al.* Effect of intense laser irradiation on the lattice stability of semiconductors and metals. *Phys. Rev. Lett.*, 96:055503, 2006.

[115] P. McKenna, D. A. MacLellan, *et al.* Influence of low-temperature resistivity on fast electron transport in solids: scaling to fast ignition electron beam parameters. *Plasma Phys. Cont. Fusion*, 57(6):064001, 2015.

[116] D. A. MacLellan, D. C. Carroll, *et al.* Tunable mega-ampere electron current propagation in solids by dynamic control of lattice melt. *Phys. Rev. Lett.*, 113(18), 2014.

[117] L. Gremillet, G. Bonnaud, *et al.* Filamented transport of laser-generated relativistic electrons penetrating a solid target. *Phys. Plasmas*, 9(3):941–948, 2002.

[118] A. R. Bell and R. J. Kingham. Resistive collimation of electron beams in laser-produced plasmas. *Phys. Rev. Lett.*, 91(3), 2003.

[119] L. Spitzer and R. Härm. Transport phenomena in a completely ionized gas. *Phys. Rev.*, 89(5):977–981, 1953.

[120] Y. T. Lee and R. M. More. An electron conductivity model for dense plasmas. *Phys. Fluids*, 27(5):1273, 1984.

[121] R. W. Lee, S. J. Moon, *et al.* Finite temperature dense matter studies on next-generation light sources. *J. Opt. Soc. Am. B*, 20(4):770–778, 2003.

[122] G. Kresse and J. Hafner. Ab initio molecular dynamics for liquid metals. *Phys. Rev. B*, 47(1):558–561, 1993.

[123] G. Kresse and J. Furthmüller. Efficiency of ab-initio total energy calculations for metals and semiconductors using a plane-wave basis set. *Comput. Mater. Sci.*, 6(1):15–50, 1996.

[124] M. P. Desjarlais, J. D. Kress, *et al.* Electrical conductivity for warm, dense aluminum plasmas and liquids. *Phys. Rev. E*, 66(2), 2002.

[125] J. A. Stamper, K. Papadopoulos, *et al.* Spontaneous magnetic fields in laser-produced plasmas. *Phys. Rev. Lett.*, 26:1012–1015, 1971.

[126] J. A. Stamper, E. A. McLean, *et al.* Studies of spontaneous magnetic fields in laser-produced plasmas by faraday rotation. *Phys. Rev. Lett.*, 40:1177–1181, 1978.

[127] B. Albertazzi, E. dHumires, *et al.* A compact broadband ion beam focusing device based on laser-driven megagauss thermoelectric magnetic fields. *Review of Scientific Instruments*, 86(4):043502, 2015.

[128] D. A. MacLellan, D. C. Carroll, *et al.* Annular fast electron transport in silicon arising from low-temperature resistivity. *Phys. Rev. Lett.*, 111(9), 2013.

[129] E. S. Weibel. Spontaneously growing transverse waves in a plasma due to an anisotropic velocity distribution. *Phys. Rev. Lett.*, 2:83–84, 1959.

[130] L. Biermann and A. Schlüter. Cosmic radiation and cosmic magnetic fields. ii. origin of cosmic magnetic fields. *Phys. Rev.*, 82:863–868, 1951.

[131] V. Icke, G. Mellema, *et al.* Collimation of astrophysical jets by inertial confinement. *Nature*, 355(6360):524, 1992.

[132] A. P. L. Robinson and M. Sherlock. Magnetic collimation of fast electrons produced by ultraintense laser irradiation by structuring the target composition. *Phys. Plasmas*, 14(8):083105, 2007.

[133] J. R. Davies. Electric and magnetic field generation and target heating by laser-generated fast electrons. *Phys. Rev. E*, 68:056404, 2003.

[134] J. R. Davies, J. S. Green, *et al.* Electron beam hollowing in laser-solid interactions. *Plasma Phys. Cont. Fusion*, 48(8):1181, 2006.

[135] P. A. Norreys, J. S. Green, *et al.* Observation of annular electron beam transport in multi-TeraWatt laser-solid interactions. *Plasma Phys. Cont. Fusion*, 48(2):L11, 2006.

[136] K. M. Schoeffler, N. F. Loureiro, *et al.* The generation of magnetic fields by the biermann battery and the interplay with the Weibel instability. *Phys. Plasmas*, 23(5):056304, 2016.

[137] M. V. Medvedev and A. Loeb. Generation of magnetic fields in the relativistic shock of gamma-ray burst sources. *The Astrophysical Journal*, 526(2):697, 1999.

[138] R. M. Kulsrud and E. G. Zweibel. On the origin of cosmic magnetic fields. *Rep. Prog. Phys.*, 71(4):046901, 2008.

[139] Y. T. Li, X. H. Yuan, *et al.* Observation of a fast electron beam emitted along the surface of a target irradiated by intense femtosecond laser pulses. *Physical Review Letters*, 96(16), 2006.

[140] M. G. Haines. Saturation mechanisms for the generated magnetic field in nonuniform laser-matter irradiation. *Phys. Rev. Lett.*, 78:254–257, 1997.

[141] K. Quinn, L. Romagnani, *et al.* Weibel-induced filamentation during an ultrafast laser-driven plasma expansion. *Phys. Rev. Lett.*, 108:135001, 2012.

[142] F. Pegoraro, S. V. Bulanov, *et al.* Nonlinear development of the weibel instability and magnetic field generation in collisionless plasmas. *Physica Scripta*, 1996(T63):262, 1996.

[143] K. M. Schoeffler, N. F. Loureiro, *et al.* Magnetic-field generation and amplification in an expanding plasma. *Phys. Rev. Lett.*, 112:175001, 2014.

[144] S. Göde, C. Rödel, *et al.* Relativistic electron streaming instabilities modulate proton beams accelerated in laser-plasma interactions. *Phys. Rev. Lett.*, 118:194801, 2017.

[145] A. Ramani and G. Laval. Heat flux reduction by electromagnetic instabilities. *The Physics of Fluids*, 21(6):980–991, 1978.

[146] M. King, R. J. Gray, *et al.* Energy exchange via multi-species streaming in laser-driven ion acceleration. *Plasma Phys. Cont. Fusion*, 59(1):014003, 2016.

[147] B. Albright, L. Yin, *et al.* Relativistic buneman instability in the laser breakout afterburner. *Physics of Plasmas*, 14(9):094502, 2007.

[148] A. P. L. Robinson, R. J. Kingham, *et al.* Effect of transverse density modulations on fast electron transport in dense plasmas. *Plasma Phys. Cont. Fusion*, 50(6):065019, 2008.

[149] S. I. Krasheninnikov, A. V. Kim, *et al.* Intense electron beam propagation through insulators: Ionization front structure and stability. *Phys. Plasmas*, 12(7):073105, 2005.

[150] A. Debayle, J. J. Honrubia, *et al.* Divergence of laser-driven relativistic electron beams. *Phys. Rev. E*, 82:036405, 2010.

[151] R. G. Evans. Modelling electron transport for fast ignition. *Plasma Phys. Cont. Fusion*, 49(12B):B87, 2007.

[152] L. O. Silva, R. A. Fonseca, *et al.* On the role of the purely transverse Weibel instability in fast ignitor scenarios. *Phys. Plasmas*, 9(6):2458–2461, 2002.

[153] D. R. Blackman, A. P. L. Robinson, *et al.* Role of low temperature resistivity on fast electron transport in disordered aluminium and copper. *Phys. Plasmas*, 22(8):083108, 2015.

[154] W. H. Bennett. Magnetically self-focussing streams. *Phys. Rev.*, 45:890–897, 1934.

[155] J. Freeman, M. Clauser, *et al.* Rayleigh-Taylor instabilities in inertial-confinement fusion targets. *Nucl. Fusion*, 17(2):223, 1977.

[156] O. Porth, S. S. Komissarov, *et al.* Rayleigh-Taylor instability in magnetohydrodynamic simulations of the Crab nebula. *Mon. Not. R. Astron. Soc.*, 443(1):547–558, 2014.

[157] D. Sharp. An overview of Rayleigh-Taylor instability. *Physica D*, 12(1):3 – 18, 1984.

[158] F. Pegoraro and S. V. Bulanov. Photon bubbles and ion acceleration in a plasma dominated by the radiation pressure of an electromagnetic pulse. *Physical Review Letters*, 99(6), 2007.

[159] A. Sgattoni, S. Sinigardi, *et al.* Laser-driven Rayleigh-Taylor instability: Plasmonic effects and three-dimensional structures. *Phys. Rev. E*, 91(1), 2015.

[160] R. A. Snavely, M. H. Key, *et al.* Intense high-energy proton beams from petawatt-laser irradiation of solids. *Phys. Rev. Lett.*, 85:2945–2948, 2000.

[161] E. L. Clark, K. Krushelnick, *et al.* Measurements of energetic proton transport through magnetized plasma from intense laser interactions with solids. *Phys. Rev. Lett.*, 84:670–673, 2000.

[162] A. Maksimchuk, S. Gu, *et al.* Forward ion acceleration in thin films driven by a high-intensity laser. *Phys. Rev. Lett.*, 84:4108–4111, 2000.

[163] J. Fuchs, Y. Sentoku, *et al.* Comparison of laser ion acceleration from the front and rear surfaces of thin foils. *Phys. Rev. Lett.*, 94:045004, 2005.

[164] L. Robson, P. Simpson, *et al.* Scaling of proton acceleration driven by petawatt-laser–plasma interactions. *Nat. Phys.*, 3(1):58–62, 2007.

[165] S. P. Hatchett, C. G. Brown, *et al.* Electron, photon, and ion beams from the relativistic interaction of petawatt laser pulses with solid targets. *Phys. Plasmas*, 7(5):2076–2082, 2000.

[166] M. Borghesi, J. Fuchs, *et al.* Fast ion generation by high-intensity laser irradiation of solid targets and applications. *Fusion Sci. Technol.*, 49(3):412–439, 2006.

[167] J. Fuchs, P. Antici, *et al.* Laser-driven proton scaling laws and new paths towards energy increase. *Nat. Phys.*, 2(1):48–54, 2006.

[168] P. McKenna, D. Neely, *et al.*, editors. Laser-Plasma Interactions and Applications. Scottish Graduate Series. Springer, 2013.

[169] B. M. Hegelich, B. Albright, *et al.* Laser acceleration of quasi-monoenergetic MeV ion beams. *Nature*, 439(7075):441, 2006.

[170] P. Mora. Plasma expansion into a vacuum. *Phys. Rev. Lett.*, 90(18):185002, 2003.

[171] P. Mora. Thin-foil expansion into a vacuum. *Phys. Rev. E*, 72:056401, 2005.

[172] L. Willingale, S. P. D. Mangles, *et al.* Collimated multi-MeV ion beams from high-intensity laser interactions with underdense plasma. *Phys. Rev. Lett.*, 96:245002, 2006.

[173] M. Passoni and M. Lontano. Theory of light-ion acceleration driven by a strong charge separation. *Phys. Rev. Lett.*, 101:115001, 2008.

[174] A. Pukhov. Three-dimensional simulations of ion acceleration from a foil irradiated by a short-pulse laser. *Phys. Rev. Lett.*, 86:3562–3565, 2001.

[175] V. Kovalev, V. Y. Bychenkov, *et al.* Particle dynamics during adiabatic expansion of a plasma bunch. *J. Exp. Theor. Phys.*, 95(2):226–241, 2002.

[176] C. M. Brenner, A. P. L. Robinson, *et al.* High energy conversion efficiency in laser-proton acceleration by controlling laser-energy deposition onto thin foil targets. *Appl. Phys. Lett.*, 104(8):081123, 2014.

[177] F. Wagner, O. Deppert, *et al.* Maximum proton energy above 85 mev from the relativistic interaction of laser pulses with micrometer thick ch_2 targets. *Phys. Rev. Lett.*, 116:205002, 2016.

[178] M. Borghesi, A. J. Mackinnon, *et al.* Multi-MeV proton source investigations in ultraintense laser-foil interactions. *Phys. Rev. Lett.*, 92(5):055003, 2004.

[179] M. Borghesi, D. H. Campbell, *et al.* Electric field detection in laser-plasma interaction experiments via the proton imaging technique. *Phys. Plasmas*, 9(5):2214–2220, 2002.

[180] G. Marx. Interstellar vehicle propelled by terrestrial laser beam. *Nature*, 211(5044):22–23, 1966.

[181] R. Heller, M. Hippke, *et al.* Optimized trajectories to the nearest stars using lightweight high-velocity photon sails. *Astron. J.*, 154(3):115, 2017.

[182] B. W. Carroll and D. A. Ostlie. Introduction to Modern Astrophysics, An: Pearson New International Edition. Pearson Education Limited, 2013.

[183] D. Heinzeller and W. J. Duschl. On the eddington limit in accretion discs. *Mon. Not. R. Astron. Soc.*, 374(3):1146–1154, 2007.

[184] A. Robinson, M. Zepf, *et al.* Radiation pressure acceleration of thin foils with circularly polarized laser pulses. *New J. Phys.*, 10(1):013021, 2008.

[185] T. Esirkepov, M. Borghesi, *et al.* Highly efficient relativistic-ion generation in the laser-piston regime. *Phys. Rev. Lett.*, 92:175003, 2004.

[186] A. Macchi, S. Veghini, *et al.* Radiation pressure acceleration of ultrathin foils. *New J. Phys.*, 12(4):045013, 2010.

[187] A. Macchi and C. Benedetti. Ion acceleration by radiation pressure in thin and thick targets. *Nucl. Instrum. Methods Phys. Res., Sect. A*, 620(1):41–45, 2010.

[188] C. Scullion, D. Doria, *et al.* Polarization dependence of bulk ion acceleration from ultrathin foils irradiated by high intensity, ultrashort laser pulses. *Phys. Rev. Lett.*, 119:054814, 2017.

[189] A. Robinson, P. Gibbon, *et al.* Relativistically correct hole-boring and ion acceleration by circularly polarized laser pulses. *Plasma Phys. Cont. Fusion*, 51(2):024004, 2009.

[190] X. Zhang, B. Shen, *et al.* Efficient GeV ion generation by ultraintense circularly polarized laser pulse. *Phys. Plasmas*, 14(12):123108, 2007.

[191] X. Q. Yan, C. Lin, *et al.* Generating high-current monoenergetic proton beams by a circularly polarized laser pulse in the phase-stable acceleration regime. *Phys. Rev. Lett.*, 100:135003, 2008.

[192] X. Zhang, B. Shen, *et al.* Multistaged acceleration of ions by circularly polarized laser pulse: Monoenergetic ion beam generation. *Phys. Plasmas*, 14(7):073101, 2007.

[193] O. Klimo, J. Psikal, *et al.* Monoenergetic ion beams from ultrathin foils irradiated by ultrahigh-contrast circularly polarized laser pulses. *Phys. Rev. Spec. Top. Accel Beams*, 11(3):031301, 2008.

[194] B. Qiao, M. Zepf, *et al.* Stable GeV ion-beam acceleration from thin foils by circularly polarized laser pulses. *Phys. Rev. Lett.*, 102:145002, 2009.

[195] S. Kar, K. F. Kakolee, *et al.* Ion acceleration in multispecies targets driven by intense laser radiation pressure. *Phys. Rev. Lett.*, 109:185006, 2012.

[196] V. Eremin, A. Korzhimanov, *et al.* Relativistic self-induced transparency effect during ultraintense laser interaction with overdense plasmas: Why it occurs and its use for ultrashort electron bunch generation. *Phys. Plasmas*, 17(4):043102, 2010.

[197] H. Padda, M. King, *et al.* Intra-pulse transition between ion acceleration mechanisms in intense laser-foil interactions. *Phys. Plasmas*, 23(6):063116, 2016.

[198] L. Yin, B. Albright, *et al.* GeV laser ion acceleration from ultrathin targets: The laser break-out afterburner. *Laser Part. Beams*, 24(2):291–298, 2006.

[199] D. Jung, B. Albright, *et al.* Beam profiles of proton and carbon ions in the relativistic transparency regime. *New J. Phys.*, 15(12):123035, 2013.

[200] A. Higginson, R. J. Gray, *et al.* Near - 100 MeV protons via an enhanced hybrid laser-ion acceleration mechansism. *Nat. Commun.*, 9(724), 2018.

[201] J. Meinecke, P. Tzeferacos, *et al.* Developed turbulence and nonlinear amplification of magnetic fields in laboratory and astrophysical plasmas. *Proc. Natl. Acad. Sci. U.S.A*, 112(27):8211–8215, 2015.

[202] H. Schmitz and A. Robinson. Investigation of jet formation from the blast wave of a locally heated laser-irradiated target. *High Energy Density Phys.*, 15(Supplement C):82 – 92, 2015.

[203] A. Benuzzi-Mounaix, S. Mazevet, *et al.* Progress in warm dense matter study with applications to planetology. *Phys. Scr.*, 2014(T161):014060, 2014.

[204] M. V. Medvedev, L. O. Silva, *et al.* Generation of magnetic fields in cosmological shocks. *J. Kor. Astron. Soc.*, 37:533–541, 2004.

[205] E. G. Blackman. Distinguishing propagation vs. launch physics of astrophysical jets and the role of experiments. *Astrophys. Space Sci.*, 307(1):7–10, 2007.

[206] M. Cohen, J. Emerson, *et al.* A reexamination of luminosity sources in T Tauri stars. I-Taurus-Auriga. *Astrophys. J.*, 339:455–473, 1989.

[207] P. Hartigan. Shock waves in outflows from young stars. *Astrophys. Space Sci.*, 287(1):111–122, 2003.

[208] M. Livio. Astrophysical jets. *Baltic Astronomy*, 13:273–279, 2004.

[209] D. Lynden-Bell. On why discs generate magnetic towers and collimate jets. *Mon. Not. R. Astron. Soc.*, 341(4):1360–1372, 2003.

[210] G. S. Bisnovatyi-Kogan, N. V. Ardelyan, *et al.* Jet formation from rotating magnetized objects. *AIP Conference Proceedings*, 586(1):439–444, 2001.

[211] P. Hartigan, J. A. Morse, *et al.* Mass-loss rates, ionization fractions, shock velocities, and magnetic fields of stellar jets. *Astrophys. J.*, 436:125–143, 1994.

[212] J. C. Wheeler, D. L. Meier, *et al.* Asymmetric supernovae from magnetocentrifugal jets. *Astrophys. J.*, 568(2):807, 2002.

[213] S. Matt, A. Frank, *et al.* The last hurrah: PPN formation by a magnetic explosion. In B. B. Margaret Meixner, Joel H. Kastner and N. Soker, editors, *Asymmetrical Planetary Nebulae III:*, volume 313 of *ASP Conference Proceedings*, page 449. Astronomical Society of the Pacific, 2004.

[214] S. G. Moiseenko and G. Bisnovatyi-Kogan. Magnetorotational supernovae. *AIP Conference Proceedings*, 937(1):275–279, 2007.

[215] T. Ray, T. Muxlow, *et al.* Large-scale magnetic fields in the outflow from the young stellar object T Tauri S. *Nature*, 385(6615):415, 1997.

[216] Y. Uchida and K. Shibata. Magnetodynamical acceleration of CO and optical bipolar flows from the region of star formation. *Publ. Astron. Soc. Jpn.*, 37:515–535, 1985.

[217] J. C. McKinney and R. D. Blandford. Stability of relativistic jets from rotating, accreting black holes via fully three-dimensional magnetohydrodynamic simulations. *Mon. Not. R. Astron. Soc.: Letters*, 394(1):L126–L130, 2009.

[218] J. W. Connor and J. B. Taylor. Scaling laws for plasma confinement. *Nucl. Fusion*, 17:1047–1055, 1977.

[219] D. C. McDonald, L. Laborde, *et al.* JET confinement studies and their scaling to high βN , ITER scenarios. *Plasma Phys. Cont. Fusion*, 50(12):124013, 2008.

[220] D. Ryutov, B. Remington, *et al.* Magnetohydrodynamic scaling: From astrophysics to the laboratory. *Phys. Plasmas*, 8(5):1804–1816, 2001.

[221] D. Ryutov, R. Drake, *et al.* Similarity criteria for the laboratory simulation of supernova hydrodynamics. *Astrophys. J.*, 518(2):821, 1999.

[222] R. P. Drake. High-Energy-Density Physics: Fundamentals, Intertial Fusion and Experimental Astrophysics. Springer Berlin Heidelberg, 1 edition, 2006.

[223] A. Mizuta, S. Yamada, *et al.* Numerical analysis of jets produced by intense laser. *Astrophys. J.*, 567(1):635, 2002.

[224] P. Rosen, J. Foster, *et al.* Laboratory experiments to study supersonic astrophysical flows interacting with clumpy environments. *Astrophys. Space Sci.*, 322(1-4):101, 2009.

[225] B. Gonzalez-Izquierdo, M. King, *et al.* Towards optical polarization control of laser-driven proton acceleration in foils undergoing relativistic transparency. *Nat. Commun.*, 7:12891, 2016.

[226] G. Ghisellini, F. Tavecchio, *et al.* Structured jets in TeV BL Lac objects and radiogalaxies - implications for the observed properties. *Astron. Astrophys.*, 432(2):401–410, 2005.

[227] M. Zamaninasab, E. Clausen-Brown, *et al.* Dynamically important magnetic fields near accreting supermassive black holes. *Nature*, 510(7503):126, 2014.

[228] S. Bouquet, E. Falize, *et al.* From lasers to the universe: Scaling laws in laboratory astrophysics. *High Energy Density Phys.*, 6(4):368–380, 2010.

[229] D. E. Spence, J. M. Evans, *et al.* Regeneratively initiated self-mode-locked Ti:Sapphire laser. *Opt. Lett.*, 16(22):1762–1764, 1991.

[230] I. N. Ross, P. Matousek, *et al.* Analysis and optimization of optical parametric chirped pulse amplification. *J. Opt. Soc. Am. B*, 19(12):2945–2956, 2002.

[231] M. S. Webb, P. F. Moulton, *et al.* High-average-power KTiOAsO4 optical parametric oscillator. *Opt. Lett.*, 23(15):1161–1163, 1998.

[232] C. Webb and S. Hooker. Laser Physics. Oxford University Press, 2010.

[233] A. Dubietis, R. Butkus, *et al.* Trends in chirped pulse optical parametric amplification. *IEEE J. Sel. Top. Quantum Electron.*, 12(2):163–172, 2006.

[234] I. Musgrave, W. Shaikh, *et al.* Picosecond optical parametric chirped pulse amplifier as a preamplifier to generate high-energy seed pulses for contrast enhancement. *Appl. Opt.*, 49(33):6558–6562, 2010.

[235] V. Bagnoud, B. Aurand, *et al.* Commissioning and early experiments of the phelix facility. *Appl. Phys. B*, 100(1):137–150, 2010.

[236] G. Doumy, F. Quéré, *et al.* Complete characterization of a plasma mirror for the production of high-contrast ultraintense laser pulses. *Phys. Rev. E*, 69:026402, 2004.

[237] D. Neely, P. Foster, *et al.* Enhanced proton beams from ultrathin targets driven by high contrast laser pulses. *Appl. Phys. Lett.*, 89(2):021502, 2006.

[238] R. Wilson, M. King, *et al.* Ellipsoidal plasma mirror focusing of high power laser pulses to ultra-high intensities. *Phys. Plasmas*, 23(3):033106, 2016.

[239] P. Gibbon. Plasma physics: Cleaner petawatts with plasma optics. *Nat Phys*, 3(6):369–370, 2007.

[240] A. Kon, M. Nakatsutsumi, *et al.* Geometrical optimization of an ellipsoidal plasma mirror toward tight focusing of ultra-intense laser pulse. *J. Phys. Conf. Ser.*, 244(3):032008, 2010.

[241] M. Nakatsutsumi, A. Kon, *et al.* Fast focusing of short-pulse lasers by innovative plasma optics toward extreme intensity. *Opt. Lett.*, 35(13):2314–2316, 2010.

[242] B. Dromey, S. Kar, *et al.* The plasma mirror—a subpicosecond optical switch for ultrahigh power lasers. *Rev. Sci. Instrum.*, 75(3):645–649, 2004.

[243] C. Ziener, P. S. Foster, *et al.* Specular reflectivity of plasma mirrors as a function of intensity, pulse duration, and angle of incidence. *J. Appl. Phys.*, 93(1):768–770, 2003.

[244] G. G. Scott, V. Bagnoud, *et al.* Optimization of plasma mirror reflectivity and optical quality using double laser pulses. *New J. Phys.*, 17(3):033027, 2015.

[245] C. Hernandez-Gomez, J. L. Collier, *et al.* Wave-front control of a large-aperture laser system by use of a static phase corrector. *Appl. Opt.*, 39(12):1954–1961, 2000.

[246] Thorlabs shack hartmann tutorial. `https://www.thorlabs.com/newgrouppage9.cfm?objectgroup_id=2946`. Accessed: 2017-05-17.

[247] K. Markey, P. McKenna, *et al.* Spectral enhancement in the double pulse regime of laser proton acceleration. *Phys. Rev. Lett.*, 105:195008, 2010.

[248] Phelix laser facility webpage. `https://www.gsi.de/en/work/research/appamml/plasma_physicsphelix/phelix.htm`. Accessed 2017-05-17.

[249] J. Fuchs, T. E. Cowan, *et al.* Spatial uniformity of laser-accelerated ultrahigh-current MeV electron propagation in metals and insulators. *Phys. Rev. Lett.*, 91(25), 2003.

[250] F. Nürnberg, M. Schollmeier, *et al.* Radiochromic film imaging spectroscopy of laser-accelerated proton beams. *Rev. Sci. Instrum.*, 80(3):033301, 2009.

[251] P. Bolton, M. Borghesi, *et al.* Instrumentation for diagnostics and control of laser-accelerated proton (ion) beams. *Physica Med.*, 30(3):255–270, 2014.

[252] H. W. Powell. Ion acceleration in ultra-thin foils undergoing relativistically induced transparency. PhD thesis, University of Strathclyde, 2015.

[253] M. King, R. Gray, *et al.* Ion acceleration and plasma jet formation in ultra-thin foils undergoing expansion and relativistic transparency. *Nucl. Instrum. Methods Phys. Res., Sect. A*, 829:163–166, 2016.

[254] S. Palaniyappan, C. Huang, *et al.* Efficient quasi-monoenergetic ion beams from laser-driven relativistic plasmas. *Nat. Commun.*, 6:10170, 2015.

[255] Gafchromic. Gafchromic EBT3 Scan Handling Guide.

[256] Gafchromic. Gafchromic HD-V2 Film Specification and User Guide.

[257] Gafchromic. Gafchromic EBT2 Dosimetry Film.

[258] R. J. Clarke, P. T. Simpson, *et al.* Nuclear activation as a high dynamic range diagnostic of laser–plasma interactions. *Nucl. Instrum. Methods Phys. Res., Sect. A*, 585(3):117–120, 2008.

[259] P. McKenna, K. W. D. Ledingham, *et al.* Characterization of proton and heavier ion acceleration in ultrahigh-intensity laser interactions with heated target foils. *Phys. Rev. E*, 70(3), 2004.

[260] D. Kirby, S. Green, *et al.* LET dependence of GafChromic films and an ion chamber in low-energy proton dosimetry. *Phys. Med. Biol.*, 55(2):417–433, 2009.

[261] D. Kirby, S. Green, *et al.* Radiochromic film spectroscopy of laser-accelerated proton beams using the FLUKA code and dosimetry traceable to primary standards. *Laser Part. Beams*, 29(02):231–239, 2011.

[262] I. J. Paterson, R. J. Clarke, *et al.* Image plate response for conditions relevant to laser–plasma interaction experiments. *Meas. Sci. Technol.*, 19(9):095301, 2008.

[263] S. G. Gales and C. D. Bentley. Image plates as x-ray detectors in plasma physics experiments. *Rev. Sci. Instrum.*, 75(10):4001–4003, 2004.

[264] K. Zeil, S. D. Kraft, *et al.* Absolute response of Fuji imaging plate detectors to picosecond-electron bunches. *Rev. Sci. Instrum.*, 81(1):013307, 2010.

[265] B. Gonzalez-Izquierdo. Collective Charged Particle Dynamics in Relativistically Transparent Laser-Plasma Interactions. PhD thesis, University of Strathclyde, 2016.

[266] F. Ingenito, P. Andreoli, *et al.* Comparative calibration of IP scanning equipment. *J. Instrum.*, 11(05):C05012, 2016.

[267] A. Jain, J. Kumar, *et al.* A simple experiment for determining verdet constants using alternating current magnetic fields. *Am. J. Phys*, 67(8):714–717, 1999.

[268] G. S. Sarkisov, V. V. Ivanov, *et al.* Propagation of a laser-driven relativistic electron beam inside a solid dielectric. *Phys. Rev. E*, 86(3), 2012.

[269] A. Flacco, J. Vieira, *et al.* Persistence of magnetic field driven by relativistic electrons in a plasma. *Nat. Phys.*, 11(5):409–413, 2015.

[270] A. Flacco, J.-M. Rax, *et al.* Reconstruction of polar magnetic field from single axis tomography of Faraday rotation in plasmas. *Phys. Plasmas*, 19(10):103107, 2012.

[271] T. D. Arber, K. Bennett, *et al.* Contemporary particle-in-cell approach to laser-plasma modelling. *Plasma Phys. Cont. Fusion*, 57(11):113001, 2015.

[272] C. K. Birdsall and A. B. Langdon. Plasma Physics via Computer Simulation. CRC Press, 1991.

[273] R. W. Hockney and J. W. Eastwood. Computer simulation using particles. CRC Press, 1988.

[274] A. Pukhov. Particle-in-cell codes for plasma-based particle acceleration. *CERN Yellow Reports*, 1:181, 2016.

[275] Y. Sentoku, K. Mima, *et al.* Three-dimensional particle-in-cell simulations of energetic electron generation and transport with relativistic laser pulses in overdense plasmas. *Phys. Rev. E*, 65(4), 2002.

[276] Epoch source code. `https://cfsa-pmw.warwick.ac.uk/users/sign_in`. Accessed 2017-05-18.

[277] D. A. Maclellan. Effects of Electrical Resistivity on Fast Electron Transport in Relativistic Laser-Solid Interactions. PhD thesis, University of Strathclyde, 2014.

[278] R. J. Dance, N. M. H. Butler, *et al.* Role of lattice structure and low temperature resistivity in fast-electron-beam filamentation in carbon. *Plasma Phys. Cont. Fusion*, 58(1):014027, 2016.

[279] J. R. Davies, A. R. Bell, *et al.* Short-pulse high-intensity laser-generated fast electron transport into thick solid targets. *Phys. Rev. E*, 56(6), 1997.

[280] D. R. Welch, D. V. Rose, *et al.* Simulations of intense heavy ion beams propagating through a gaseous fusion target chamber. *Phys. Plasmas*, 9(5):2344–2353, 2002.

[281] J. Honrubia and J. M. ter Vehn. Three-dimensional fast electron transport for ignition-scale inertial fusion capsules. *Nucl. Fusion*, 46(11):L25, 2006.

[282] A. P. L. Robinson, M. H. Key, *et al.* Focusing of relativistic electrons in dense plasma using a resistivity-gradient-generated magnetic switchyard. *Phys. Rev. Lett.*, 108(12), 2012.

[283] S. Kar, A. P. L. Robinson, *et al.* Guiding of relativistic electron beams in solid targets by resistively controlled magnetic fields. *Phys. Rev. Lett.*, 102:055001, 2009.

[284] E. G. Saiz, G. Gregori, *et al.* Probing warm dense lithium by inelastic X-ray scattering. *Nat. Phys.*, 4(12):940, 2008.

[285] M. Roth, T. Cowan, *et al.* Fast ignition by intense laser-accelerated proton beams. *Phys. Rev. Lett.*, 86(3):436, 2001.

[286] S. Ichimaru and H. Kitamura. Pycnonuclear reactions in dense astrophysical and fusion plasmas. *Physics of Plasmas*, 6(7):2649–2671, 1999.

[287] S. Mohanty, G. Basri, *et al.* Activity in very cool stars: Magnetic dissipation in late m and l dwarf atmospheres. *The Astrophysical Journal*, 571(1):469, 2002.

[288] D. A. MacLellan, D. C. Carroll, *et al.* Fast electron transport patterns in intense laser-irradiated solids diagnosed by modeling measured multi-MeV proton beams. *Laser Part. Beams*, 31(03):475–480, 2013.

[289] X. H. Yuan, A. P. L. Robinson, *et al.* Effect of self-generated magnetic fields on fast-electron beam divergence in solid targets. *New J. Phys.*, 12(6):063018, 2010.

[290] H. Chen, S. C. Wilks, *et al.* Hot electron energy distributions from ultraintense laser solid interactions. *Phys. Plasmas*, 16(2):020705, 2009.

[291] H. Daido, M. Nishiuchi, *et al.* Review of laser-driven ion sources and their applications. *Rep. Prog. Phys.*, 75(5):056401, 2012.

[292] J. R. Davies. Alfvén limit in fast ignition. *Phys. Rev. E*, 69(6), 2004.

[293] J. Ziman. The electron transport properties of pure liquid metals. *Adv. Phys.*, 16(64):551–580, 1967.

[294] M. Coury, D. C. Carroll, *et al.* Injection and transport properties of fast electrons in ultraintense laser-solid interactions. *Phys. Plasmas*, 20(4):043104, 2013.

[295] M. Nakatsutsumi, J. R. Davies, *et al.* Space and time resolved measurements of the heating of solids to ten million kelvin by a petawatt laser. *New J. Phys.*, 10(4):043046, 2008.

[296] A. P. L. Robinson, M. Sherlock, *et al.* Artificial collimation of fast-electron beams with two laser pulses. *Phys. Rev. Lett.*, 100(2), 2008.

[297] D. A. MacLellan, D. C. Carroll, *et al.* Influence of laser-drive parameters on annular fast electron transport in silicon. *Plasma Phys. Cont. Fusion*, 56(8):084002, 2014.

[298] A. Mančić, A. Lévy, *et al.* Picosecond short-range disordering in isochorically heated aluminum at solid density. *Phys. Rev. Lett.*, 104:035002, 2010.

[299] A. Pelka, G. Gregori, *et al.* Ultrafast melting of carbon induced by intense proton beams. *Phys. Rev. Lett.*, 105:265701, 2010.

[300] W. Bang, B. Albright, *et al.* Visualization of expanding warm dense gold and diamond heated rapidly by laser-generated ion beams. *Sci. Rep.*, 5, 2015.

[301] W. Callister. Materials Science And Engineering: An Introduction. John Wiley & Sons, 2007.

[302] W. W. Gartner. Temperature dependence of junction transistor parameters. *Proc. IRE*, 45(5):662–680, 1957.

[303] R. l. Kodama, P. Norreys, *et al.* Fast heating of ultrahigh-density plasma as a step towards laser fusion ignition. *Nature*, 412(6849):798, 2001.

[304] S. Atzeni. Inertial fusion fast ignitor: Igniting pulse parameter window vs the penetration depth of the heating particles and the density of the precompressed fuel. *Phys. Plasmas*, 6(8):3316–3326, 1999.

[305] S. Atzeni, A. Schiavi, *et al.* Targets for direct-drive fast ignition at total laser energy of 200-400kJ. *Phys. Plasmas*, 14(5):052702, 2007.

[306] B. Ramakrishna, S. Kar, *et al.* Laser-driven fast electron collimation in targets with resistivity boundary. *Phys. Rev. Lett.*, 105(13), 2010.

[307] H. Schmitz, R. Lloyd, *et al.* Collisional particle-in-cell modelling of the generation and control of relativistic electron beams produced by ultra-intense laser pulses. *Plasma Phys. Cont. Fusion*, 54(8):085016, 2012.

[308] E. Brambrink, J. Schreiber, *et al.* Transverse characteristics of short-pulse laser-produced ion beams: A study of the acceleration dynamics. *Phys. Rev. Lett.*, 96:154801, 2006.

[309] P. McKenna, D. C. Carroll, *et al.* Lateral electron transport in high-intensity laser-irradiated foils diagnosed by ion emission. *Phys. Rev. Lett.*, 98(14), 2007.

[310] P. Antici. Laser-acceleration of high-energy short proton beams and applications. PhD thesis, École Polytechnique, 2007.

[311] X. H. Yang, H. B. Zhuo, *et al.* Effects of resistive magnetic field on fast electron divergence measured in experiments. *Plasma Phys. Cont. Fusion*, 57(2):025011, 2015.

[312] A. Bell, J. Davies, *et al.* Magnetic field in short-pulse high-intensity laser-solid experiments. *Phys. Rev. E*, 58(2):2471, 1998.

[313] R. Jung, J. Osterholz, *et al.* Study of electron-beam propagation through preionized dense foam plasmas. *Phys. Rev. Lett.*, 94:195001, 2005.

[314] A. Debayle and V. T. Tikhonchuk. Ionization instability of a relativistic electron beam propagating through a dielectric target. *Eur. Phys. J. Special Topics*, 175(1):127–132, 2009.

[315] E. M. de Gouveia Dal Pino. Astrophysical jets and outflows. *Adv. Space Res.*, 35(5):908 – 924, 2005.

[316] C. B. Singh, Y. Mizuno, *et al.* Spatial growth of current-driven instability in relativistic rotating jets and the search for magnetic reconnection. *Astrophys. J.*, 824(1):48, 2016.

[317] A. Bell, F. Beg, *et al.* Observation of plasma confinement in picosecond laser-plasma interactions. *Phys. Rev. E*, 48(3):2087, 1993.

[318] P. Nicolaï, V. T. Tikhonchuk, *et al.* Plasma jets produced in a single laser beam interaction with a planar target. *Phys. Plasmas*, 13(6):062701, 2006.

[319] L. Yin, B. J. Albright, *et al.* Three-dimensional dynamics of breakout afterburner ion acceleration using high-contrast short-pulse laser and nanoscale targets. *Phys. Rev. Lett.*, 107:045003, 2011.

[320] S. Tomita and Y. Ohira. Weibel instability driven by spatially anisotropic density structures. *Astrophys. J.*, 825(2):103, 2016.

[321] W. Fox, G. Fiksel, *et al.* Filamentation instability of counterstreaming laser-driven plasmas. *Phys. Rev. Lett.*, 111(22):225002, 2013.

[322] F. Fiuza, R. A. Fonseca, *et al.* Weibel-instability-mediated collisionless shocks in the laboratory with ultraintense lasers. *Phys. Rev. Lett.*, 108:235004, 2012.

[323] N. P. Dover, C. A. J. Palmer, *et al.* Buffered high charge spectrally-peaked proton beams in the relativistic-transparency regime. *New J. Phys.*, 18(1):013038, 2016.

[324] F. Pegoraro and S. V. Bulanov. Ion acceleration and stability in the radiation pressure dominated regime. *Laser Phys.*, 19(2):222–227, 2009.

[325] L. Romagnani, A. Bigongiari, *et al.* Observation of magnetized soliton remnants in the wake of intense laser pulse propagation through plasmas. *Phys. Rev. Lett.*, 105(17), 2010.

[326] K. V. Lezhnin, F. F. Kamenets, *et al.* Explosion of relativistic electron vortices in laser plasmas. *Phys. Plasmas*, 23(9):093116, 2016.

[327] M. Safarzadeh, S. Naoz, *et al.* Generation of toroidal magnetic fields in accretion disks. *arXiv preprint*, 1701.03800, 2017.

[328] B. Reipurth and J. Bally. Herbig-haro flows: Probes of early stellar evolution. *Annu. Rev. Astron. Astrophys.*, 39(1):403–455, 2001.

[329] G. A. Kyrala. High energy density laboratory astrophysics. Springer, 2005.

[330] K. Shigemori, R. Kodama, *et al.* Experiments on radiative collapse in laser-produced plasmas relevant to astrophysical jets. *Phys. Rev. E*, 62:8838–8841, 2000.

[331] C. S. Reynolds, T. Di Matteo, *et al.* The quiescent black hole in M87. *Mon. Not. R. Astron. Soc.*, 283(4):L111–L116, 1996.

[332] R. D. Blandford and R. L. Znajek. Electromagnetic extraction of energy from kerr black holes. *Mon. Not. R. Astron. Soc.*, 179(3):433–456, 1977.

[333] A. Celotti and A. C. Fabian. The kinetic power and luminosity of parsec-scale radio jets an argument for heavy jets. *Mon. Not. R. Astron. Soc.*, 264(1):228–236, 1993.

[334] L. Yin, B. J. Albright, *et al.* Monoenergetic and GeV ion acceleration from the laser breakout afterburner using ultrathin targets. *Phys. Plasmas*, 14(5):056706, 2007.

[335] M. L. Bernet, F. Miniati, *et al.* Strong magnetic fields in normal galaxies at high redshift. *Nature*, 454(7202):302–304, 2008.

[336] C. K. Li, F. H. Séguin, *et al.* Observation of the decay dynamics and instabilities of Megagauss field structures in laser-produced plasmas. *Phys. Rev. Lett.*, 99(1), 2007.

[337] J. Zou, C. Le Blanc, *et al.* Design and current progress of the apollon10pwproject. *High Power Laser Science and Engineering*, 3, 2015.